Blood velocity reconstruction with contrast enhanced X-ray CT

Shusong Huang

N°d'ordre NNT : 2024ISAL0009

THESE de DOCTORAT DE L'INSA LYON,
membre de l'UNIVERSITE DE LYON

Ecole Doctorale N° 160
Électronique, Électrotechnique, Automatique (EEA)

Spécialité / discipline de doctorat :
Traitment du Signal et de l'Image

Soutenue publiquement le 25/01/2024, par :
Shusong HUANG

Blood velocity reconstruction with contrast enhanced X-ray CT

Devant le jury composé de :

Aurélia FRAYSSE	Maître de conférence HDR	Université Paris-Saclay	Rapportrice
Thomas RODET	Professeur	ENS Paris-Saclay	Rapporteur
Franck NICOUD	Professeur	Université de Montpellier	Examinateur
Yuemin ZHU	Directeur de recherche CNRS	INSA Lyon	Examinateur
Bruno SIXOU	Maître de conférence HDR	INSA Lyon	Directeur de thèse
Monica SIGOVAN	Chargés de recherche	CNRS	Co-directrice de thèse

INSTITUT NATIONAL DES SCIENCES APPLIQUÉES LYON

Département de la Formation par la Recherche et des Études Doctorales (**FEDORA**)

Bâtiment INSA direction, 1er étage
37, av. J. Capelle
69621 Villeurbanne Cédex
fedora@insa-lyon.fr

Référence : TH1072_HUANG Shusong

L'INSA Lyon a mis en place une procédure de contrôle systématique via un outil de détection de similitudes (logiciel Compilatio). Après le dépôt du manuscrit de thèse, celui-ci est analysé par l'outil. Pour tout taux de similarité supérieur à 10%, le manuscrit est vérifié par l'équipe de FEDORA. Il s'agit notamment d'exclure les auto-citations, à condition qu'elles soient correctement référencées avec citation expresse dans le manuscrit.

Par ce document, il est attesté que ce manuscrit, dans la forme communiquée par la personne doctorante à l'INSA Lyon, satisfait aux exigences de l'Etablissement concernant le taux maximal de similitude admissible.

INSA LYON
Campus LyonTech La Doua
20, avenue Albert Einstein - 69621 Villeurbanne cedex - France
Tél. +33 (0)4 72 43 83 83 - Fax +33 (0)4 72 43 85 00
www.insa-lyon.fr

Département FEDORA – INSA Lyon - Ecoles Doctorales

SIGLE	ECOLE DOCTORALE	NOM ET COORDONNEES DU RESPONSABLE
ED 206 CHIMIE	**CHIMIE DE LYON** https://www.edchimie-lyon.fr Sec. : Renée EL MELHEM Bât. Blaise PASCAL, 3e étage secretariat@edchimie-lyon.fr	**M. Stéphane DANIELE** C2P2-CPE LYON-UMR 5265 Bâtiment F308, BP 2077 43 Boulevard du 11 novembre 1918 69616 Villeurbanne directeur@edchimie-lyon.fr
ED 341 E2M2	**ÉVOLUTION, ÉCOSYSTÈME, MICROBIOLOGIE, MODÉLISATION** http://e2m2.universite-lyon.fr Sec. : Bénédicte LANZA Bât. Atrium, UCB Lyon 1 Tél : 04.72.44.83.62 secretariat.e2m2@univ-lyon1.fr	**Mme Sandrine CHARLES** Université Claude Bernard Lyon 1 UFR Biosciences Bâtiment Mendel 43, boulevard du 11 Novembre 1918 69622 Villeurbanne CEDEX e2m2.codir@listes.univ-lyon1.fr
ED 205 EDISS	**INTERDISCIPLINAIRE SCIENCES-SANTÉ** http://ediss.universite-lyon.fr Sec. : Bénédicte LANZA Bât. Atrium, UCB Lyon 1 Tél : 04.72.44.83.62 secretariat.ediss@univ-lyon1.fr	**Mme Sylvie RICARD-BLUM** Laboratoire ICBMS - UMR 5246 CNRS - Université Lyon 1 Bâtiment Raulin - 2ème étage Nord 43 Boulevard du 11 novembre 1918 69622 Villeurbanne Cedex Tél : +33(0)4 72 44 82 32 sylvie.ricard-blum@univ-lyon1.fr
ED 34 EDML	**MATÉRIAUX DE LYON** http://ed34.universite-lyon.fr Sec. : Yann DE ORDENANA Tél : 04.72.18.62.44 yann.de-ordenana@ec-lyon.fr	**M. Stéphane BENAYOUN** Ecole Centrale de Lyon Laboratoire LTDS 36 avenue Guy de Collongue 69134 Ecully CEDEX Tél : 04.72.18.64.37 stephane.benayoun@ec-lyon.fr
ED 160 EEA	**ÉLECTRONIQUE, ÉLECTROTECHNIQUE, AUTOMATIQUE** https://edeea.universite-lyon.fr Sec. : Philomène TRECOURT Bâtiment Direction INSA Lyon Tél : 04.72.43.71.70 secretariat.edeea@insa-lyon.fr	**M. Philippe DELACHARTRE** INSA LYON Laboratoire CREATIS Bâtiment Blaise Pascal, 7 avenue Jean Capelle 69621 Villeurbanne CEDEX Tél : 04.72.43.88.63 philippe.delachartre@insa-lyon.fr
ED 512 INFOMATHS	**INFORMATIQUE ET MATHÉMATIQUES** http://edinfomaths.universite-lyon.fr Sec. : Renée EL MELHEM Bât. Blaise PASCAL, 3e étage Tél : 04.72.43.80.46 infomaths@univ-lyon1.fr	**M. Hamamache KHEDDOUCI** Université Claude Bernard Lyon 1 Bât. Nautibus 43, Boulevard du 11 novembre 1918 69 622 Villeurbanne Cedex France Tél : 04.72.44.83.69 direction.infomaths@listes.univ-lyon1.fr
ED 162 MEGA	**MÉCANIQUE, ÉNERGÉTIQUE, GÉNIE CIVIL, ACOUSTIQUE** http://edmega.universite-lyon.fr Sec. : Philomène TRECOURT Tél : 04.72.43.71.70 Bâtiment Direction INSA Lyon mega@insa-lyon.fr	**M. Etienne PARIZET** INSA Lyon Laboratoire LVA Bâtiment St. Exupéry 25 bis av. Jean Capelle 69621 Villeurbanne CEDEX etienne.parizet@insa-lyon.fr
ED 483 ScSo	**ScSo**[1] https://edsciencessociales.universite-lyon.fr Sec. : Mélina FAVETON Tél : 04.78.69.77.79 melina.faveton@univ-lyon2.fr	**M. Bruno MILLY** (INSA : J.Y. TOUSSAINT) Univ. Lyon 2 Campus Berges du Rhône 18, quai Claude Bernard 69365 LYON CEDEX 07 Bureau BEL 319 bruno.milly@univ-lyon2.fr

[1] ScSo : Histoire, Géographie, Aménagement, Urbanisme, Archéologie, Science politique, Sociologie, Anthropologie

Remerciements

Firstly, I would like to express my sincere gratitude to the all of jury members of my PhD thesis, Aurélia FRAYSSE, Thomas RODET, Franck NICOUD, and Yuemin ZHU, for spending valuable time reading and providing constructive criticism.

Furthermore, I would like to especially acknowledge my doctoral supervisor, Dr. Bruno SIXOU, and Dr. Monica SIGOVAN. They have been incredibly patient and very friendly, and with their dedicated guidance and assistance, I completed this doctoral work and wrote my PhD thesis. I wish them success in their work and happiness in their lives.

Next, I want to express my gratitude to le sang, the big big boss Nicola Pinon vient de Strasbourg et de champagne, and the mushroom boss Pierre Rougé. As representatives of kind-hearted bosses, they have indirectly influenced me, encouraged me, and enabled me to improve myself, learning how to be a better person. They remind me of a Cantonese song, 'Always Have Your Encouragement,' which I would like to share with my friends. Here, I hope the big big boss becomes an even bigger boss, influencing more people, and I wish them joy in both work and life. To the mushroom boss from Marseille, keep going, 'Marseille, beyond.' You are a boss from Marseille, and I wish you happiness and fulfillment. 'When you get old' (Chinese song), don't forget to take your mushroom noir, 'gantianwo' please.

After that, I would like to express my sincere thanks to the big office 19. Many thanks to boss Marta from Italy, always dressed in stylish Italian beauty fashion, for your encouragement and smiles. Special thanks to dance patronne Maylis, dumpling boss Morgane, new Phd babyfoot boss Célia, 'kuangyede' boss Séréna. Moreover, I would like to appreciate the kind athletics sports boss Robin with gentille parents des professor qui enseignez des fils, and I hope he wins the kind sports championship. Many thanks to the 'don't hesitate helpful boss' Nathan and the Canadian-flavored boss Thierry, from Canada. Thanks to Hangjung, the representative boss from Malaysia. In addition, thanks to Pierre-Elliott company's boss, the seat-empty-like-new boss Raphael who has a cute bebe, hope for a happy family, and a growing baby. Thanks to the departed one babyfoot boss Rémi, the climbing boss Gaspart, the silent focus on hardworking Yamil, and intern Amine.

Furthermore, I want to express my deep gratitude to the babyfoot team bosses. Many thanks to the kind babyfoot bosses, Frog Prince Dr Alexandre, Happy Nut Valentin, double kind twin Nom Romain, Master babyfoot patron Benoît and also tres fort for climbing, tall Thomas with a litter junk, nice danser et babyfoot boss Axel, incredibly smart Tokin Jean zay boss Jean-Baptiste with few hairs, nice smile hangs on the face every time Lyon boss Thibaut with never give up. Also, thanks to baby Barbie Candice, wish a good future, Spanish strong and independent friend boss Celia 'Pablo please doesn't do that,' Monaco beauty Naziha, come on, dear jeune Colombian friend Pablo wish a nice future, kind Lucas wishing good health, Anders from Norway keep going climbing and biking, Amine starting the doctoral process, Some interns bosses Astree, Hippolyte, 'tao,' Louise, Leo, tall circle Maxence, Slim from Tunisia wishes you good luck for looking a job, and the unnamed colleague in memory. Thanks for bringing joy. I wish all of you a pleasant work and life.

Thanks to the doctoral bosses, particularly the couple bosses from Iran, Samaneh and Mehdi, for sharing language learning methods and much help. Thanks to the new Iranian boss Mahshid. Many thanks to the always smiling and incredibly happy GANGNAM 'Jiangnan' style Sophie, Dr Louise with a shit frowning'meitoujincu' PhD boss, I wish her to be happy without frowning, je va parle franse avec Louise sans accent oh non, avec Marseille accent 'Tabon bien', slim beauty and sportster fort Julia from Spain, smiling with french style beauty dimple Juliette female Michael Jackson, mysterious 'shenlongjianshoubujianwei' Flora keeping fishes boss, basketball-loving Célestine, special boss Dr Valentine, going to Japan Meghane, singer boss Ludmilla, Daria, intern Maria. Thanks to the kind brother Kannara, I wish all your wishes come true, '9 pm break' Cyril, NBA candidate Dr Charles, 'special smile gege' Matthis, climbing boss l'escalade Dr Frank, I hope you climb your dreams dans ton vie. Thanks to the one trying to go abroad, Emile. Thanks to classic danser boss Valentin M. Many thanks to the postdoctoral bosses Baptiste, and Spanish danser models Lorena and Tatiana. Thanks to kind colleague Angèle Houmeau in HCL Louis Pradel. Thanks to the non-doctoral bosses, IT master Pierre, Cluster master Fabrice, Pierre Ecarlat who has been to Japan, humor and funny Chef Anthony, and the laboratory secretaries and so on. Also, thanks to the help and companionship of fellow Chinoises, 'local tyrant' Ruifen, Yuhan with a happy family, Yunyun, 'happiness' Yulei, Xuhao, Zexian 'wish you find a good job,' Jiqing 'master chef,' Yunlong, Youcong 'basketball pioneer,' hefeng, Kevin, Qilin crossing Grenoble, Liutong, Haosheng couple. Thanks to Enyi, Zinan, Zhiyuan, Xuefeng in Creatis. Also, thanks to those who came together with me in INSA, apple Cuidi, 'local tyrant' Jingjing, Sichuan sister Yiping brother, Yufei, Zhaojiao brother, Xi'an Huiru, brothers Shandong strong Qiaohu, brothers Sichuan chef Junxiong. Thanks to basketball friends especially Lan. Thanks to professeur de French Dominique, Marie in INSA. Thanks to the master's supervisor and friend Xuqu, I wish you a happy work and life. Thanks to the help provided by Xingyi. Thanks to the ex-girlfriend. Thanks to CSC for funding support. Thanks to colleagues in Creatis. Thanks to the friends from years ago. In the past, I'm sorry.

Thanks to my parents, sister and relatives. Thanks to the encounters occasion, the days in France, I have been influenced and attracted by French culture, bringing priceless wealth to myself and helping me understand myself. No one is shameless enough to thank oneself, donc je me merci my completely bad self 'chouloudezhanan'. Thanks to 'tiandao,' the 'yaoyuan-dejiushizhu.' Le sang 'Looking back again' expresses my current feelings. In conclusion, the heart cannot be obtained in the past, present, and future.

Shusong HUANG, à Villeurbanne le 5 Decembre 2023, modifie 6 Decembre 2023 et le 11 Janvier 2024

Contents

List of Figures

List of Tables

Introduction

Hemodynamics and cardiovascular diseases

Cardiovascular diseases are the main cause of mortality worldwide. The development of diagnosis methods is thus a crucial issue. The hemodynamics i.e the dynamics of blood flows is closely related to these cardiovascular diseases with the development of aneurysms or stenoses for example. Thus, blood velocity plays a crucial role as a clinical parameter in the vascular system for diagnosing cardiovascular diseases. (Crosetto et al., 2011; Shi et al., 2011; Quarteroni et al., 2017). Furthermore, it is important for the understanding of the physiological processes in these cardiovascular diseases. Atherosclerosis is a vessel obstruction that accelerates the blood flow locally and leads to an increase in the wall shear stress. Pressure drop is also a very useful biomarker for stenosis. An aneurysm is a local dilatation of an arterial wall. Its evolution depends on the stresses exerted by the blood flow on the wall. Other diseases such as aortic dissection may be detected by measuring the hemodynamics parameters. Aortic dissections can be diagnosed by the presence of velocity with inverse direction. Hemodynamic parameters are thus very pertinent for the diagnosis of cardiovascular diseases. A crucial parameter for hemodynamics is the Reynolds number $Re = \frac{UL}{\nu}$ where U is the blood velocity, L a characteristic length, for example the vessel radius, and ν the kinematic viscosity. Within a cardiac cycle, it varies roughly in the range [0,4000]. A low Reynolds number corresponds to the laminar regime where the viscous effects dominate. For $Re > 2000$, turbulent features can appear. Blood which contains platelets, red blood cells, and white blood cells exhibits a non-Newtonian behavior. Variations in the vessel structure and vessel wall motion have a large impact on the hemodynamic response. Therefore the understanding of the blood flow is a very complex and challenging field.

In-vivo blood flow measurements

Doppler and MRI measurement techniques

The introduction of a pressure probe in the artery is a well-known clinical method to obtain a direct measurement of the pressure. Non-invasive medical imaging techniques, for example, ultrasounds and phase-contrast magnetic resonance imaging (MRI), enable the measurement of blood flow velocity. Additionally, there are more advanced techniques available for very precise velocity measurements such as laser Doppler velocimetry, laser speckle techniques, particle image velocimetry (Lusby et al., 1981; Briers, 2001; Lotz et al., 2002; Vennemann et al., 2007; Daly and Leahy, 2013; Tarbell et al., 2014; Vaz et al., 2016; Poelma, 2017; Engelhard et al., 2018; Bouillot et al., 2019).

Here, we will introduce the advantages and limitations of typical medical imaging techniques such as ultrasound, magnetic resonance imaging, and CT for the measurement of blood velocity. The researchers classify blood flow measurement using ultrasounds into three groups

such as time-of-flight(TOF) methods, Doppler methods, and correlation-based methods. These approaches are presented in some review papers (Hoskins, 1999; Poelma, 2017; Suñol et al., 2018). The TOF method in ultrasounds involves the propagation of an ultrasound wave pulse into the flowing medium, while the propagation time can be affected by the mean flow velocity. On the other hand, the Doppler method detects the variation in a reflected pulse to measure the velocity component in the direction of the ultrasound beam. A scattering material is essential in the blood flow causing a frequency shift that measures blood flow velocity. The correlation methods in ultrasound blood flow measurement are based on tracking the speckle patterns produced by blood to measure the blood velocity (Trahey et al., 1987; Meunier and Bertrand, 1995). The major advantage of the ultrasound technology is that it is non-invasive and instantaneous. However, there are some limitations to consider. In TOF methods of ultrasound imaging, assumptions about the velocity profile need to be made to obtain the mean velocity along the wave pulse path. In the medical field, the Doppler method faces drawbacks such as aliasing, where local velocities can exceed the detectable range set by the pulse repetition frequency, resulting in phase shifts. Moreover, the Doppler method only provides some information about the magnitude of the velocity and it lacks the comprehensive characterization of all the directions of the velocity field. An important limitation is that it only gives access to velocity components oriented along the ultrasonic beam. The correlation approach is unsuitable for real-time application in clinical settings because it is very computationally intensive. (Wang and Shung, 1996). One breakthrough that enables access to real-time applications has been presented by (Zheng et al., 2006), but its drawback includes low spatial accuracy and resolution, and inherently low frame rates that restrict the range of measurable velocities. Additionally, the low frame rate is a drawback when measuring the 3D blood flow. (Poelma, 2017) Other techniques like speckle tracking or Vector Doppler techniques have been developed recently to reconstruct a two dimensional velocity field.

After the introduction of ultrasounds, MRI medical imaging technology for blood flow measurement will be presented. There are some researchers who have already done complete reviews in blood flow measurement with MRI (Calamante et al., 1999; Sakuma et al., 1999; Jahng et al., 2014; MacDonald and Frayne, 2015). MRI measures the relaxation properties of some specific atoms subjected to high-frequency variations of magnetic fields. Especially, the advanced 4D MRI technique has been proposed to measure blood flow. It has the capability to determine velocity magnitude and its components in clinical applications and it has been reviewed by (Azarine et al., 2019; Soulat et al., 2020; Morgan et al., 2021; Kamada et al., 2022).* In the phase-contrast MRI methods, applications of gradient pulses produce phase shifts in magnetic moments of moving protons that can be used to determine the velocity (Lotz et al., 2002; Srichai et al., 2009). With phase-contrast MRI, there is simple relationship between the phase of the measured signal and the velocity of the protons which is useful to reconstruct the blood velocity field. With 4D Flow MRI, the spatio-temporal description of the velocity field in the three spatial directions can be obtained, as well as the morphology of the region of interest. Some quantities like the pressure field or wall shear stresses can be estimated, which are crucial for medical diagnosis and very difficult to evaluate with other modalities.

There are several typical categories of methods to measure blood flow with MRI which include time-of-flight methods, contrast-enhanced approaches and MR bolus approaches. The time-of-flight technique to measure blood velocity by MRI uses selective exciting and refocusing radio-frequency pulses to affect planes oriented in orthogonal directions in space. Specifically, the region of excitation is positioned perpendicular to the blood flow, while the refocusing region is oriented parallel to the flow and including it (Axel et al., 1986). The time-of-flight approach is used by other researchers (Wehrli et al., 1986; Wagner et al., 2004; Pates et al., 2010). Furthermore, the contrast agent MR angiography is based on contrast agents such as the most

commonly used gadolinium-containing through injection into the blood (Kato et al., 2002; Sourbron and Buckley, 2013). Additionally, the MRI bolus methods such as dynamic susceptibility contrast (DSC)-MRI, and dynamic contrast-enhanced (DCE)-MRI are widely applied in clinical applications with a contrast agent (Lia et al., 2000; Østergaard, 2005; Jahng et al., 2014). One of the novel perfusion methods known as the Arterial Spin Labeling technique uses blood water as the endogenous tracer for blood flow measurement without a contrast agent injection and without ionizing radiation (Fan et al., 2016; Zhang et al., 2017).

The major advantage of MRI medical imaging technology is that it is non-invasive but the limitations are its cost and the long time for examination (MacDonald and Frayne, 2015). The main drawback of utilizing the TOF approach is the lack of sensitivity to slow blood flows indicated and reviewed by this researcher (Pipe, 2001). The major limitation of contrast agent MRI is the intravenous administration (MacDonald and Frayne, 2015). For the MRI bolus methods, there are limitations such as bolus delay (Calamante et al., 2002). One limitation of phase-contrast MRI is the lack of a standard protocol when measuring blood flow. And another drawback of this technique is that it is not possible to provide velocity in real-time (Lotz et al., 2002). The spatio-temporal resolution may be too low for a precise flow description. The measurements depend on the hardware and software settings.

Computed tomography measurements

In this work, we aim to focus on the reconstruction of blood flow using the Computed Tomography (CT) technique. A review presenting insights into CT imaging technology and its applications is provided by Cnudde et al. (Cnudde and Boone, 2013). One notable advantage of this medical technique is its non-invasive nature. Additionally, CT imaging has the potential to give high temporal and spatial resolution (Prevrhal et al., 2011), which is another advantageous feature. However, in the past two decades, there are few research works concentrating on in vivo blood velocity measurement with X-ray CT. These research articles associated with blood velocity reconstruction with CT are presented below in chronological order based on their publication time.

Lu et al. employed the CT technique to obtain the data on blood motion within a hollow fiber dialyzer and subsequently evaluated the mean blood velocity by image processing methods (Lu and Lu, 2010).Barfett et al. used 4D CT angiography with contrast boluses injection to measure the average blood velocity and compared the results with in vivo MR angiography (Barfett et al., 2010). Then, they considered a time of flight (TOF) approach with contrast-enhanced volumetric and time-resolved CT to study the average blood velocity (Barfett et al., 2014). Prevrhal et al. present constant flow velocity measured by CT projection data. The mean velocity can be obtained by the ratio of the distance between CT detector rows and the time of propagation (Prevrhal et al., 2011). Dubsky et al. used Computed Tomographic X-ray velocimetry to measure the blood velocity and at the same time the structure of a vessel. They performed synchrotron experiments for assessment of the blood velocity within a complex geometric configuration of the vessel (Dubsky et al., 2012). Jong et al. measured the mean blood flow velocity with perfusion CT in a master thesis. The method is based on the direct-flow principle that considers the geodesic distance and time delay of bolus arrival (Jong, 2015). Korporaal et al. investigated an approach to estimate the average blood velocity by applying CT with a contrast agent. The average velocity can be measured by the contrast agent density gradients and their changes with time (Korporaal et al., 2016). Boonen et al. proposed time-resolved CT angiography to measure blood velocity by arterial segmentation and estimation of the bolus arrival time locally in one conference paper (Boonen et al., 2018). Furthermore, they also performed experiments to measure the average blood velocity by time-resolved CT in another conference paper (Boonen et al., 2020). Bouillot et al. investigated four-dimensional

CT angiography (4D-CTA) to reconstruct blood velocity. The average velocity is obtained from the spatial displacement of the time-intensity curves (TICs) (Bouillot et al., 2019).

The use of numerical simulations to improve blood flow characterization

Computational Fluid Dynamics has been widely used for blood flow prediction and simulation in the cardiovascular system. Coupled CFD-MRI methods have been investigated to improve the diagnosis and for validation. Computational fluid dynamics simulations can provide higher spatio-temporal resolution and an easy derivation of hemodynamic parameters. Computational fluid dynamics simulations are based on many modeling assumptions and numerical approximations. The inlet velocity boundary conditions are assumed to be perfectly known, the wall motion and fluid-structure interactions are often neglected, the outflow pressure is often assumed to be zero, and the blood is often assumed to be a Newtonian fluid. The numerical solvers have to be chosen carefully, especially for challenging turbulent structures. Yet, computational fluid dynamics simulations can be very useful to validate some approaches for the reconstruction of the blood flow and to improve the diagnosis.

Recently, some previous works in our team have studied a new approach to reconstruct this velocity field with contrast-enhanced X-ray CT (Sixou et al., 2016, 2018; Sixou, 2019). It has been validated with simulations. The acquisition of 2D CT projections perpendicular to the major flow propagation direction is considered for the reconstruction of blood flow, with a tracer injected into the vessel. In order to solve the inverse problem of contrast-enhanced CT reconstruction of vascular blood flow, a functional is minimized with a data term taken into account the projections coupled with a partial differential equation (PDE) describing the transport of the tracer used as a constraint. The PDE models the propagation of the contrast agent with a density or tracer concentration expressed by $f(\mathbf{X}, t)$ with a convection term depending on a flow field $\mathbf{V}(\mathbf{x}, t)$. In this approach, the variables $(f, \mathbf{V})$ are optimized independently. The reconstruction of tracer concentration is effectively reconstructed but the reconstruction of the velocity field is not recovered accurately. Additionally, the computational time is also very long. This approach was restricted to a simple cylindrical geometry and to a velocity field not depending on time.

Several methods have been analyzed in the literature to include a PDE as a constraint to solve an inverse ill-posed problem. Among them, the sequential programming approach has been investigated in (Burger and Mühlhuber, 2002). During this work, firstly, we concentrate on the proposed adjoint method for solving the tomographic ill-posed inverse problem with a PDE constraint. Subsequently, proper orthogonal decomposition (POD) with the adjoint approach is proposed to accelerate the convergence. Finally, the proper orthogonal decomposition is coupled with deep learning techniques to improve the former methods for blood flow reconstruction. The objectives of this work will be given below.

Thesis objectives and outline

Objectives

The objectives of this work are blood velocity components reconstruction with X-ray CT with accelerated convergence, reduced calculation cost, and reduced radiation dose. To accomplish these objectives, the adjoint method is initially considered for solving the tomographic inverse problem with a constraint based on a partial differential equation. Additionally, to accelerate convergence, the proper orthogonal decomposition (POD) method combined with the adjoint method is proposed in this work. Finally, the new Proper Orthogonal Decomposition-Deep

Learning (POD-DL) approach for solving the considered inverse problem is investigated to reduce effectively the computation costs in our work.

Based on the above objectives and methods, we will present the following topics:

(1) To solve the complex tomographic inverse problem, we formulate it as an optimal control problem with a partial differential transport equation. The Radon transform employed perpendicular to the main flow direction plays a critical role in solving the problem. Initially, the adjoint method is proposed to solve the optimal control problem with a PDE. We study the influence of some simulation parameters on the reconstruction: projection box size, number of slices, and number of projection angles, in order to obtain the better parameters. Subsequently, the effect of a smoothing velocity term, and the effect of white Gaussian noise is analyzed. In addition, we validate the adjoint method by testing both stationary and non-stationary velocity fields.

(2) Based on the adjoint method, the proper orthogonal decomposition method(POD) is used to accelerate the reconstruction with reduced bases for the velocity, tracer concentration, and the adjoint variable. The POD bases are obtained from snapshots of velocity, tracer concentration, and adjoint variables and they are used to reduce the dimensions of the transport equation and adjoint equation effectively. Various numbers of POD basis elements for velocity, tracer concentration, and adjoint variable fields have been studied. To assess their performance, full-order approximation (FOA) simulations are conducted, and their results are compared with the reduced-order approximation approach. Stationary and non-stationary velocities are tested.

(3) The POD method combined with deep learning approaches is then explored to improve the convergence and to reduce the calculation cost of the blood velocity reconstruction. Several network architectures such as Proper orthogonal decomposition-fully connected network(POD-FC), and Proper orthogonal decomposition-3D convolutional neural network(POD-3D CNN) are studied to approximate the inverse operator. We compare the reconstruction results using the deep learning methods with the POD-adjoint method on stationary velocity fields.

Contributions and architecture of the manuscript

Our contributions will be detailed in the following chapters:

In Chapter 1, the contrast-enhanced tomography is presented, the dynamic tomography problem is summarized and formulated as an optimal control problem. Subsequently, the adjoint method is explored for solving the optimal control problem, and the optimization parameters for this method are introduced. Within this first step, we aim to give more details about the inverse problem and the adjoint method for the solution. To demonstrate the effectiveness of the method, we study in detail several examples of the blood flow reconstruction. We optimize the simulation parameters for the Radon projections. The regularization parameter and the noise level corrupting the Radon projections are considered. Both non-stationary velocity fields and stationary velocity fields are well investigated.

In Chapter 2, we apply the proper orthogonal decomposition (POD) or principle components analysis in the adjoint method to reduce the dimensions for achieving high convergence and low computational costs compared with the full-order simulations. The simulation results are obtained by varying the number of basis elements for the POD method. The POD method and the full-order approximation approach (FOA) are compared in terms of reconstruction errors and computational costs. Similarly to Chapter 1, non-stationary velocity fields and stationary velocity fields are considered to evaluate the effectiveness of the proposed POD-adjoint method.

In Chapter 3, a review of physics-informed deep learning methods for solving the inverse problem will be given, and two crucial networks such as a fully connected network and a

convolutional neural network will be presented which are very useful for addressing our inverse problem. We study two networks including a Proper orthogonal decomposition-fully connected network(POD-FC), and a Proper orthogonal decomposition-3D convolutional neural network(POD-3D CNN) to solve the inverse problem of blood flow reconstruction. Realistic simulations are performed to evaluate the proposed networks with a stationary velocity field and compared with the previous POD-adjoint method. In the conclusion, we summarize the results of this work and give some perspectives for future research directions.

Chapter 1

Contrast enhanced computed tomography velocity reconstruction: an inverse problem with a PDE constraint

In this chapter, we will mainly introduce the inverse problem set by contrast enhanced computed tomography velocity reconstruction and one of the typical methods for solving the tomographic inverse problem, the adjoint method. In subsection 1.1, the context of computed tomography will be first presented including the principle of CT and Radon transform. In subsection 1.2, the tomographic inverse problem in our work will be detailed. Additionally, the formulation of the inverse problem with a partial differential transport equation will be given and formulated as an optimal control problem. Subsequently, in subsection 1.3, we will particularly introduce the adjoint method for solving the inverse problem. The optimality system and optimization scheme will be presented in this subsection. After, we will focus on the simulation results. More simulation details are presented in section 1.4. In section 1.5, we will give the reconstruction results with the main tomography reconstruction parameters including the box projection size, number of slices, and number of projection angles. Also, the effect of white Gaussian noise will be investigated in this section and two velocity fields including non-stationary velocities and stationary velocities will be taken into consideration. In the end, the conclusion for this first chapter will be presented.

1.1 Computed tomography

X-rays have been first discovered by Wilhelm Röntgen in 1895. X-ray radiation is an electromagnetic radiation with high energy. Due to its well-known penetrating physical property, X-ray radiation attracted more attention from researchers. X-ray CT is an affordable medical imaging technique, which requires some projections from various measurement angles to provide some tomographic scan, based on attenuations for X-rays passing through the object. Usual CT scanners use a rotating X-ray tube and a row of detectors placed in a gantry to measure X-ray attenuations by different tissues inside the body. The multiple X-ray measurements taken from different angles are then processed on a computer using tomographic reconstruction algorithms to produce tomographic cross-sectional images of a body. By combining these projections, the interior of the object can be reconstructed. This non-destructive and non-invasive technique is broadly used in non-medical applications such as archaeology, soil science, the timber industry, biology, industrial X-ray inspection, and especially in medical clinical applications for the human body and brain (van Kaick and Delorme, 2005; Kalender, 2006; Wang et al., 2008).

X-rays and Computed Tomography have been a breakthrough in the medical field to visualize the tissues and organs of a patient.

In this work, we will study the application of this X-ray CT technology to reconstruct the blood flow in a simulated vessel. This section is divided into two sub-sections. Firstly, we will introduce the principle of X-ray CT. Secondly, tomographic projection with Radon transform will be described.

1.1.1 X-rays and principle of CT

X-rays are electromagnetic waves with a wavelength ranging from picometers to nanometers. For medical purposes, hard X-rays - as opposed to soft X-rays - are commonly used thanks to their ability to penetrate the matter. Radiography is based on the fact that X-rays are more or less absorbed depending on the density of the material. In this work, we will use a contrast agent with more attenuation than the surrounding blood.

CT measurement is based on the absorption of the high-energy electromagnetic X-ray beams passing through the object. This transmission process of X-ray beams is expressed by the Beer-Lambert law. According to the law, for a uniform attenuation, the intensity of the X-ray beam $I(x)$ can be expressed with the attenuation coefficient A as:(Beatty, 2012; Paleo, 2017):

$$I(x) = e^{-Ax} \tag{1.1}$$

when the beam goes through the object with a distance x from the origin. The volume can therefore be described by its linear attenuation coefficient, which varies continuously. The intensity is measured at the outside of the object. This formula can be written for a non-homogeneous material with an attenuation $A(x)$ as:

$$\frac{dI}{dx} = -A(x)I(x) \tag{1.2}$$

The intensity of the beam at the initial position x_0 can be denoted as I_0 and the one at the final position x_1 is denoted as I_1. So, by integrating the former formula, we obtain :

$$-\int_{x_0}^{x_1} \frac{dI}{I(x)} = \int_{x_0}^{x_1} A(x)dx \tag{1.3}$$

The left-hand side of the equation is equal to $ln(\frac{I_0}{I_1})$, so we see that:

$$ln(\frac{I_0}{I_1}) = \int_{x_0}^{x_1} A(x)dx \tag{1.4}$$

In other words, taking the logarithm of the ratio between the initial intensity and the received intensity amounts to measuring the integral of the unknown attenuation for each source-detector pair. Such a model is valid considering a mono-energetic beam. The above equation enables us to describe the relationship between the intensity and its attenuation.

1.1.2 Radon transform

The Radon transform plays a very critical role in estimating the attenuation coefficient A in the above equation 1.4. So we will introduce this effective mathematical tool. Let $\Sigma \in \mathbb{R}^2$ be a bounded regular Lipschitz domain, the Radon transform of the function f can be expressed as:

$$Rf(\theta, s) = \int_{\Sigma \cap L(\theta,s)} f(\mathbf{x})dl(\mathbf{x}) \tag{1.5}$$

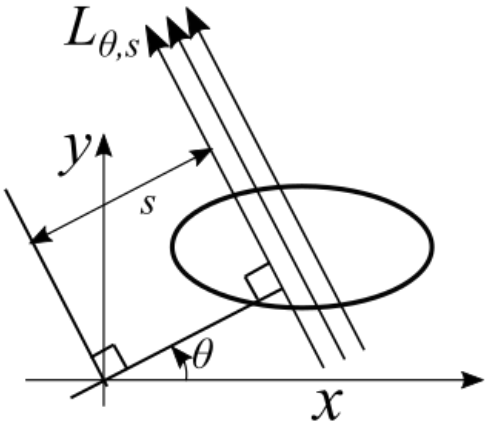

Figure 1.1: Principle of integral Radon transform.

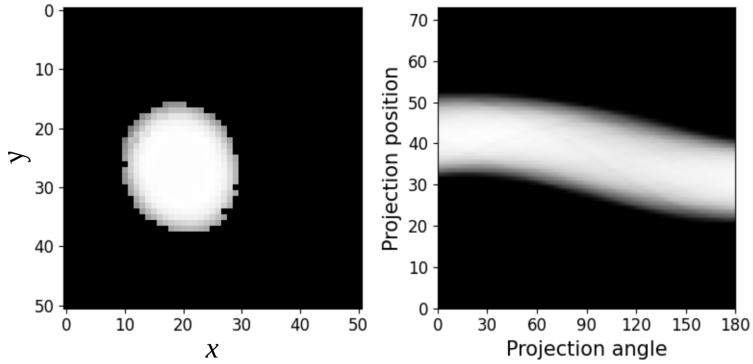

Figure 1.2: Example of Radon transform: the original function f in the left, sinogram Rf in the right.

The line $L(\theta, s)$ is determined by the angle $\theta \in [0, \pi]$ and by the distance $s \in [-a, a]$ from the origin as displayed on Figure 1.1 (Natterer and Natterer, 1986). A finite number of angles θ_i, $1 \leq i \leq N_\theta$ will be selected and referred to as the Radon projection angles. The graphical representation of the Radon transform as a function of the projection angle θ is called a sinogram. In the reconstruction problem considered, the scanner is rotating with time and the Radon projections perpendicular to the main flow direction are acquired for N_θ projection angles regularly distributed in the angular range $\Delta\theta(t)$. For each angle, N_p projections are measured and the 2D Radon projections are obtained for N_z values along the z axis, with $z \in$[0, zmax]. One example of a sinogram with $N_p = 360$ projections in our work is shown in Figure 1.2.

The integral Rf of a function f represents the right-hand side of the equation 1.4. So combined with the above equation 1.4, the Radon transform can be seen as the measured value $ln(\frac{I_0}{I_1})$. In this work, the Radon transform is crucial for solving our inverse problem.

1.2 The tomographic inverse problem with a PDE constraint

An important question is whether we can obtain the density from the Radon measurements. This is an inverse problem that has been much studied. Some analytic reconstruction formulas have been studied for various tomographic projections measurement types. Yet, in the presence

of noise iterative algorithms and regularization techniques are used to reconstruct the attenuation. Our inverse problem is more complex since we want to reconstruct the velocity field from the Radon projections of the tracer concentration. We will thus use the partial differential equation describing the propagation of the tracer as a regularization constraint.

The velocity reconstruction of the blood flow with X-ray CT can be considered an inverse problem with a partial differential equation constraint. Our aim is to reconstruct the tracer concentration of the contrast agent denoted as f together with the velocity field $\mathbf{V}$. In this section, the formulation of the tomographic inverse problem will be given. The associated variational formulation will be presented with a cost function that we need to minimize. The inverse problem is not well posed, it should be considered as an ill-posed inverse problem and we need to use regularization terms. In order to take into account the partial differential equation constraint, we will formulate the inverse problem as an optimal control problem, where the velocity field is considered as a control variable for the state variable f.

1.2.1 Inverse problem of velocity field reconstruction

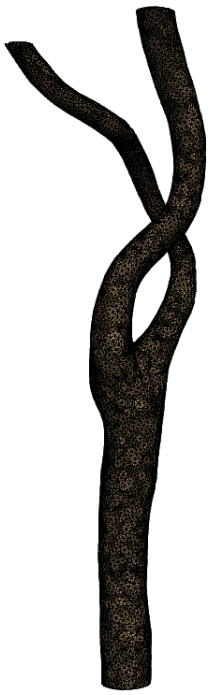

Figure 1.3: The finite element mesh of the vessel used for the simulations.

In this work, the aim is to reconstruct the blood flow in a simulating phantom shown in Figure 1.3. A complex vessel geometry with a bifurcation will be considered. The main flow direction is the z axis and two-dimensional Radon projections are acquired perpendicularly to this axis, in the XY plane. The propagation of the contrast agent with the tracer concentration $f(\mathbf{x}, t)$ is modeled with a partial differential equation based on a realistic velocity field $\mathbf{V}$ obtained with the Navier-Stokes equations Glowinski and Pironneau; Temam; Galdi (1992; 2001; 2011). We will denote Ω the bounded spatial domain, $[0, T]$ the time domain and $Q = \Omega \times [0, T]$. We assume that the tracer is injected in the inlet of the vessel corresponding to $z = 0$. We also assume that the concentrations of the other materials can be neglected and the evolution of the Radon projections with time is related to the propagation of the tracer. We

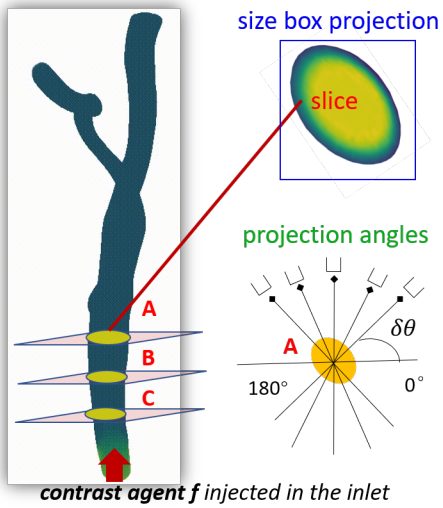

Figure 1.4: The simulation parameters within a vessel for the Radon projection.

will consider some simulation parameters for optimizing the reconstruction from the Radon projections such as size of the box projection, number of slices and number of projection angles shown in the following Figure 1.4. The box projection size is the region containing the tracer concentration used for the Radon projections on a regular grid. Variable number of slices can be selected along the main flow direction for Radon projection, and also variable numbers of projection angles to perform the Radon projection can be considered in each slice. These parameters for the discretization of the problem are difficult to choose because if they are too high the inverse problem and the optimization of the functionals is more difficult. The propagation of the contrast agent in the vessel is modeled by a convection-diffusion equation. We present successively the simple tomographic inverse problem, some variational formulation with a cost function with the tracer concentration and the velocity field, and an optimal control formulation with a PDE constraint.

1.2.2 Generalities on inverse problems

In this section, we present inverse problems and the variational formulation. It is usual to associate a function to minimize the inverse problem. The choice of methods to minimize this function depends on its characteristics, whether it is smooth, convex or not. We will first consider the general formulation of an inverse problem as

$$p^\delta = A(f) \tag{1.6}$$

where p^δ are the noisy observed measurements, A is some operator that transforms the quantity of interest f that we aim to reconstruct. In the sense of Hadamard, the problem is said to be well-posed if it satisfies the three following conditions:
- a solution exists
- the solution is unique
- the solution depends continuously on the data

When at least one of the three mentioned conditions is not fulfilled, the problem is said to be ill-posed. It appears to be the case for most of the real inverse problems. The inverse problems are very often ill-posed (Kabanikhin, 2008, 2011; Adler and Öktem, 2017).

Variational methods consist in finding f^* that minimizes an energy functional J written as:

$$J(f) = \varphi(A(f), p^\delta) + \lambda R(f) \tag{1.7}$$

where φ is a data-consistency term, R is a regularization term that allows to give a priori information on the solution and λ is a weighting parameter.

1.2.3 General formulation of the dynamic tomographic inverse problem

The general formulation of the tomographic problem can be expressed as:

$$Rf(\theta, s, z, t) = p^{\delta}(\theta, s, z, t) \quad \forall\ \theta, s, z, t \tag{1.8}$$

where Rf is the Radon transform of the tracer concentration f based on blood velocity $\mathbf{V}$, p^{δ} are the noisy measured projections that take into account the noise level. The coordinates s and z are the detector coordinates, θ is the projection angle and t the time. Our aim is to find $f : [0, T] \rightarrow L_2(\Omega)$ from the above linear equations 1.8. From the tracer concentration f, our aim is then to estimate the blood velocity field $\mathbf{V}$ and we will add a partial differential equation to describe the propagation of the tracer.

This tomographic inverse problem is ill-posed and very sensible to the noise in the measurements. The solution to the problem is not directly accessible by explicit formulas. We will consider a variational formulation and iterative solutions for solving this problem.

1.2.4 Variational formulation

A variational method is studied based on a cost functional written as:

$$J(f, \mathbf{V}, \boldsymbol{\mu}) = \frac{1}{2}\int_0^T \|Rf(\theta, s, z, t) - p^{\delta}(t)\|_2^2 dt + \frac{\alpha_s}{2}\||\nabla \mathbf{V}|\|_2^2 dt \tag{1.9}$$

This function depends on the tracer concentration f, on the velocity field $\mathbf{V}$, and on some parameters $\boldsymbol{\mu}$ describing the forward model. The first term is a data term to measure the discrepancy between the measured projections and the projections obtained with the tracer concentration. The second term is a regularization term for the velocity. The first term in the right-hand side of the above equation is based on a L_2 norm defined on $[0, \pi] \times [-a, a] \times [0, z_{\max}]$. The second term is widely used as a spatial regularization term. In the regularization part, $\||\nabla \mathbf{V}|\|_2$ is dependent on the Frobenius norm of the Jacobian matrix of the blood velocity $\mathbf{V} = (u, v, w) : [0, T] \times \Omega \rightarrow \mathbb{R}^3$ combined with the $L_2(\Omega)$ norm of the square of each entry of this matrix. The parameter α_s is a regularization parameter. For the sake of simplicity, we have not considered in this work temporal regularizations.

The set of model parameters $\boldsymbol{\mu} = (\mu_1, \mu_2)$ will be separated into two subsets μ_1 and μ_2. The first subset of parameters μ_1 corresponds to the parameters including inlet velocity and outlet pressure in the Navier-Stokes equation related to the velocity, μ_2 is defined as the set of parameters containing the initial tracer concentration on the inlet, the diffusion coefficient in the PDE transport equation presented below. These parameters will be very useful in Chapter 2 which details the Proper Orthogonal Decomposition method. Our aim is to minimize the cost function with a PDE constraint that will be given in the next subsection.

1.2.5 Optimal control formulation with a PDE

As we mentioned, the velocity reconstruction of the blood flow can be written as an inverse problem with a PDE constraint and formulated as an optimal control problem. The propagation of the contrast agent in the simulating vessel is simulated by a convection-diffusion equation, with a diffusion parameter D and the velocity $\mathbf{V} = (u, v, w) : [0, T] \times \Omega \rightarrow \mathbb{R}^3$. In this work, stationary and non-stationary velocity fields are considered, obtained with the stationary and non-stationary Navier-equations detailed in Chapter 3. The velocity field $\mathbf{V}$ is parametrized

with the first component μ_1 of $\boldsymbol{\mu}$ related to the boundary/initial conditions. The parameter μ_1 will be specified in the following. For the sake of simplicity, we assume that the contrast agent enters the vessel through a disk ($\mathcal{D}$) in the plane $z = 0$. We assume that the value of the function f on the disk ($\mathcal{D}$) is associated with the second component μ_2. The convection-diffusion equation with initial and boundary conditions can be written as Huang et al. (2021):

$$\begin{cases} e(f, \mathbf{V}, \boldsymbol{\mu}) = \frac{\partial f(\mathbf{x},t)}{\partial t} + u\frac{\partial f(\mathbf{x},t)}{\partial x} + v\frac{\partial f(\mathbf{x},t)}{\partial y} + w\frac{\partial f(\mathbf{x},t)}{\partial z} - D\triangle f(\mathbf{x},t) = 0 \\ f(\mathbf{x},t) = \mu_2 \quad \forall x \in (\mathcal{D}) \;\; \forall t \in [0,T] \\ f(\mathbf{x},0) = 0 \quad \forall x \in \Omega - (\mathcal{D}) \end{cases} \tag{1.10}$$

We assume that there is zero total flux on the lateral boundary. This boundary condition can be written as:

$$(-D\nabla f + f\boldsymbol{V}).\mathbf{n} = 0 \;\; \forall t \in [0,T] \tag{1.11}$$

where $\mathbf{n}$ is the outward normal. We want the tracer to be able to leave the domain on the outlet, and we allow it to advect freely through this part of the boundary. This is modeled by imposing a homogeneous Neumann condition on the outlet:

$$-D\nabla f.\mathbf{n} = 0 \;\; \forall t \in [0,T] \tag{1.12}$$

This transport equation will be used as a regularization constraint to obtain stable solutions for the reconstruction problem. The unicity of the solution f is guaranteed for a smooth velocity field $\boldsymbol{V}$ by the diffusion term in the transport equation (Ol'ga Aleksandrovna Ladyzhenskaja, 1968). The constraint $e(f(\mathbf{V}), \mathbf{V}, \boldsymbol{\mu})$ is replaced by an operator $f(\mathbf{V}, \boldsymbol{\mu})$ mapping the velocity field to the tracer concentration. The inverse problem can be rewritten with a reduced cost functional $\hat{J}$ depending on the velocity $\mathbf{V}$ and formulated as an optimal control problem:

$$\min_{\mathbf{V}, f \in U \times Y} J(f, \mathbf{V}, \boldsymbol{\mu}) = \min_{\mathbf{V} \in U} J(f(\mathbf{V}), \mathbf{V}, \boldsymbol{\mu}) = \min_{\mathbf{V} \in U} \hat{J}(\mathbf{V}, \boldsymbol{\mu}) \tag{1.13}$$

where $\hat{J}$ is a reduced cost function where only the control variable $\boldsymbol{V}$ appears and U, Y are the set of admissible velocity fields and tracer concentration fields respectively.

Additionally, the inverse problem is also depending on some model parameters $\boldsymbol{\mu}$ when considering the Proper Orthogonal Decomposition method combined with the adjoint method. It is not depending on $\boldsymbol{\mu}$ when only considering the classical adjoint method. It will be discussed in the relevant Chapters 2 and 3.

1.3 Adjoint method for the inverse problem

In order to calculate the gradient of the reduced functional $\hat{J}$ and to derive the optimality conditions, we consider a dual variable $p : [0,T] \rightarrow L_2(\Omega)$, and the Lagrangian L of the constrained problem, combining the data term and the PDE which is given by;

$$L(f, \boldsymbol{V}, p, \boldsymbol{\mu}) = J(f, \boldsymbol{V}, \boldsymbol{\mu}) + \beta \int_0^T < e(f, \boldsymbol{V}, \boldsymbol{\mu}), p(t) > dt \tag{1.14}$$

where β is a Lagrangian parameter and $< ., . >$ denotes the $L_2(\Omega)$ scalar product.

To minimize the functional, we have to derive the first-order optimality conditions with the Euler-Lagrange equations, from which the optimal state f, the optimal speed $\boldsymbol{V}$, and the adjoint variable p can be determined. The optimality system has been detailed in (Sixou et al., 2016). We summarize here the main results.

1.3.1 Optimality system

1.3.1.1 Optimality system for the tracer concentration and adjoint equation

The adjoint equation specifies the first-order necessary condition with respect to the state variable f. The first variation of the Lagrangian L at $f \in L_2(Q)$ in the direction of $h \in L_2(Q)$ is defined by (Courant, 1956):

$$\delta L(f, \boldsymbol{V}, p, \boldsymbol{\mu})(h) = \frac{\partial L(f + \epsilon h, \boldsymbol{V}, p, \boldsymbol{\mu})(h)}{\partial \epsilon}|_{\epsilon=0} \tag{1.15}$$

If a minimizer of L exists, then the equation $\delta L(f, \boldsymbol{V}, p, \boldsymbol{\mu})(h) = 0$ must hold for every $h \in L_2(Q)$ vanishing on the boundary and at $t = 0$.

As a necessary condition, we obtain the following equation for the adjoint variable p:

$$\beta(\frac{dp}{dt} + \boldsymbol{V}.\nabla p + D\nabla.\nabla p) = R^t(Rf - g) \;\; with \;\; p(.,T) = 0 \tag{1.16}$$

This adjoint equation is a backward equation and R^t is the transpose of the Radon operator.

1.3.1.2 Optimality system for the velocity

With the variation with respect to the velocity, we obtain:

$$-\alpha_s \triangle \boldsymbol{V} = \beta p \nabla f \;\; in \;\; \Omega \times [0, T] \tag{1.17}$$

The optimality system is given by the system of coupled partial differential equations Eq.1.10, Eq. 1.16, Eq.1.17.

By the chain rule, the gradient of the reduced functional is written as:

$$\nabla \hat{J}(\boldsymbol{V}) = J_{f,V}(\boldsymbol{V}) - e^*_{\boldsymbol{V}}(f, \boldsymbol{V}, \mu_1) e_f^{-*}(f, \boldsymbol{V}, \boldsymbol{\mu}) J_f(f, \boldsymbol{V}) = J_V(\boldsymbol{V}) + e^*_{\boldsymbol{V}} p \tag{1.18}$$

where $e^*_{\boldsymbol{V}}$ and e^*_f denote the adjoints of the derivative of the constraint e with respect to $\boldsymbol{V}$ or f respectively.

The gradient of the reduced functional is thus given by:

$$\nabla \hat{J} = \int_0^T (\beta p \nabla f - \alpha_s \triangle \boldsymbol{V}) dt \tag{1.19}$$

1.3.2 Optimization scheme and adjoint method implementation

After the initialization with a velocity field $\boldsymbol{V}_0$ and a tracer concentration field f_0, applying the proposed framework requires a few simple steps for each iteration k which are the following:
(1) the tracer concentration at iteration k, $f_k(\mathbf{x}, t)$, is estimated with the transport equation Eq.1.10 using the approximated velocity $\boldsymbol{V}_k$. The discretization method with finite elements is described in the part related to the simulation details in the following subsection.
(2) Solve the backward adjoint equation to obtain the adjoint variable p_k with Eq.1.16. The numerical scheme is the same as the one used for the forward equation by reversing time.
(3) The evaluation of the gradient of the reduced functional $\nabla \hat{J}(\boldsymbol{V}_k)$ can then be obtained. The flow field $\boldsymbol{V}_k$ is updated with a gradient descent using Eq.1.19 with a steepest descent method and a line search strategy (Nocedal and Wright, 1999).

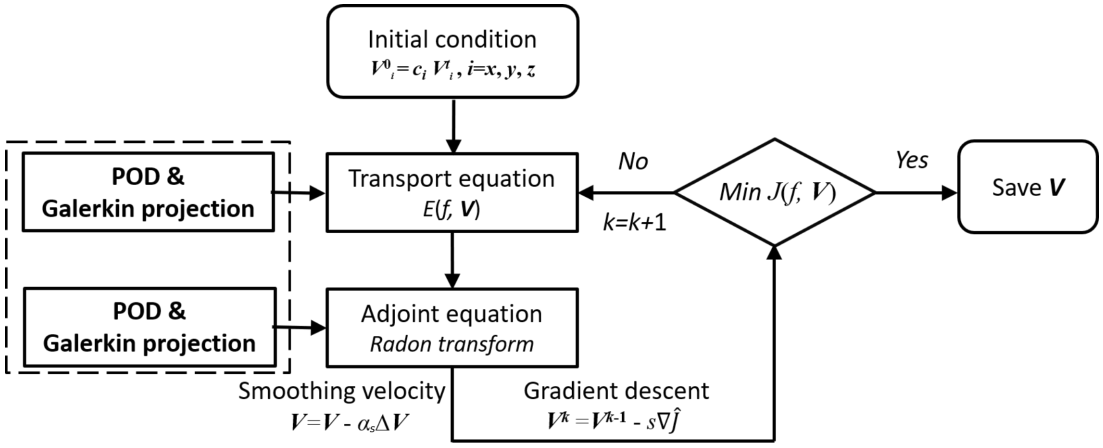

Figure 1.5: The flow chart of the iterative adjoint method.

The flow chart of the iterative adjoint method is presented in Figure 1.5. The parameter α_s is a smoothing velocity parameter and s is here the gradient step or learning rate in the gradient descent. The Proper Orthogonal Decomposition basis and Galerkin projection are considered in the transport equation and in the adjoint equation when the Proper Orthogonal Decomposition method is used for blood velocity reconstruction.

Gradient descent In the iterative method, the gradient descent can be expressed as:

$$\boldsymbol{V}^k = \boldsymbol{V}^{k+1} - s\nabla\hat{J} \tag{1.20}$$

For each component, we have

$$V_i^k = V_i^{k+1} - s\nabla\hat{J}_i, \quad i = x, y, z \tag{1.21}$$

where the initial condition for the velocity field is given. Second-order adjoint method could improve the convergence properties of the first-order method. They are not considered in this work.

1.4 Simulation details

We use a non-structured tetrahedral mesh to implement the simulation experiments shown in Figure 1.6. This numerical phantom is a blood vessel with a bifurcation. The geometry used in this chapter is the geometry 1. The blood vessel is 10 cm long and the mean transverse diameter is around 10 millimeters. The numerical simulations based on the finite element have been performed by using the Fenics software which is a useful tool for the implementation of various schemes related to finite element methods (Goda, 1979; Logg et al., 2012). We discretize the values of the various fields on a grid of size $N_t = 50$ for the time domain $[0, T]$ = [0s, 0.5s] with a small time interval dt = 0.01s based on the Courant-Friedrich-Lax condition. Firstly, a ground truth velocity field is obtained by solving the Navier-Stokes equations and then this velocity field is applied to simulate the forward transport equation detailed above for the tracer concentration. These velocity and tracer concentration fields are used as the ground truth fields to be reconstructed. The inverse problem is then solved with the classical adjoint method starting from an approximation of the ground truth velocity field. We solve the transport equation with finite elements in space and finite differences in time with the Euler explicit method similar to the algorithms presented in (Smith et al., 1985; Morton and Mayers, 1998).

(a) Geometry 1 (b) Geometry 2

Figure 1.6: The non-structured tetrahedral mesh.

For this inverse problem, the spatial discretization grid consists of 64000 nodes with $P1$ finite elements and piecewise linear approximation. The discretizations of space and time domain are selected such that the stability condition $Ddt/dx^2 < 1$ is verified (Morton and Mayers, 1998). In the numerical simulations, the diffusion coefficient is set as $D = 0.001\text{cm}^2/\text{s}$. The simulation results are obtained in the following with the kinematic viscosity $\nu = 0.01\ \text{cm}^2/\text{s}$. We can obtain similar results in the range $\nu \in [0.1, 0.01]$ which corresponds to the laminar state.

We test the adjoint method with two kinds of velocity fields obtained with the stationary and non-stationary Navier-Stokes equations. It is notable that numerical algorithms for computing fluid flows have been studied for several decades and still remain in investigation. Thus, there is a large amount of literature on discretization schemes for the incompressible Navier–Stokes equations such as (Pironneau and Pironneau, 1989; Glowinski and Pironneau, 1992; Girault and Raviart, 2012). Finite element subspaces must be selected carefully to ensure the stability of the solution for finite element problems. In terms of the spatial discretization, the Taylor-Hood ($P2 - P1$) finite element with piecewise linear pressure and piecewise quadratic velocity approximations are used to ensure a stable discretization detailed in (Taylor and Hood, 1973). The non-stationary Navier-Stokes equation to obtain the velocity field $\mathbf{V}$ was simulated with the Incremental Pressure Correction scheme and performed with Fenics (Goda, 1979; Logg et al., 2012). The time interval is used to satisfy the approximate CFL condition. In the numerical simulations, we apply the no-slip boundary conditions to the velocity field on the lateral border of the blood vessels. At the outlet side, a zero Dirichlet boundary condition is employed for the pressure. The non-stationary Navier-Stokes equation is solved with an inflow velocity field given as:

$$\begin{cases} 0.4 + 0.4sin(\pi t) \quad for \ \ t \leq 0.5 \\ 0.4 + 0.4(3/2 - 0.5cos(2\pi(t - 0.5)) \quad for \ \ t \leq 0.5 \end{cases} \tag{1.22}$$

For the stationary velocity field, the velocity along the z-axis was chosen 0.4 m/s in the middle of the inlet boundary with a parabolic profile. Based on these stationary or non-stationary velocity fields that are denoted as $\mathbf{V}^*(\mathbf{x})$ or $\mathbf{V}^*(\mathbf{x}, t)$, the ground truth solution f^* is evaluated using the convection-diffusion equation. The initial tracer concentration of the contrast agent is $f^*(\mathbf{x}, z = 0) = 1$ for all the inflow boundary points and all flow time.

To obtain the Radon projections, for N_z values of the z axis, we project the tracer concen-

tration values obtained on the initial mesh onto a fine rectangular grid. The Radon operator and its adjoint are estimated with the Scipy python library (Virtanen et al., 2020). The values of $R^t(Rf - p)$ are then interpolated on the initial mesh. For the numerical simulations, $N_z = 20$ or $N_z = 40$ slices have been chosen. For each time $t_p = pT/N_t$ in the time domain, $0 \leq t_p \leq T$, different projections angles N_θ in the angular range $\Delta\theta(t)$ and varying numbers of projections N_p have been considered for the discretization of the Radon operator.

We also chose the angular range $\Delta\theta(t) = [p\delta\theta, (p+1)\delta\theta]$ corresponding to the measurement angles for a gantry rotation during a computed tomography scan with a measurement interval $\delta\theta$. The interval $\delta\theta$ has been chosen as 36, 45, 90 or 180°. Furthermore, a Gaussian white noise with a peak-to-peak signal-to-noise ratio (PPSNR) between 0 and 40 dB is added to the Radon projections to test the effect of the noise level. The peak-to-peak signal-to-noise ratio can be determined as:

$$PPSNR = 20log(\frac{S_{max}}{n_{max}}) \tag{1.23}$$

where S_{max} is the maximum signal amplitude and n_{max} represents the maximum noise amplitude.

A global optimum of the velocity field can not be reached by this algorithm and the initializations for the tracer concentration f_0 and for the velocity field $\mathbf{V}_0$ are crucial. Different initializations have been tested for the velocity field obtained with the stationary and non-stationary Navier-Stokes equations. In the simulation results displayed below, we use an initial velocity such that $V_{0,x} = 0.75V_x^*$, $V_{0,y} = 0.75V_y^*$, $V_{0,z} = 0.75V_z^*$ where $\mathbf{V}^*$ is the ground truth velocity. This a priori evaluation of the solution guarantees the convergence of the algorithms. The regularization parameter α_s, and the Lagrangian parameter β are chosen to have the best decrease of the discrepancy term and of the Lagrangian. The values α_s, β used in this work are 1×10^{-6}, and 1×10^{-1} respectively for a PPSNR of 20 dB. The iterations are stopped at the minimum of the data term.

Finite element method

In this subsection, we give a few details about the finite element method. The finite element solution can be obtained by restricting an infinite-dimensional variational problem to a finite-dimensional problem and solving a linear system. A linear variational problem can often be written in the form: find $u \in U$ such that:

$$a(u, \hat{v}) = L(\hat{v}) \tag{1.24}$$

for all $\hat{v} \in V$. U is called the trial space and V the test space. For classical linear problems, a is a bilinear form and L is a linear form. The former variational problem is discretized with discrete test and trial spaces, U_h and V_h. With discrete trial and test bases, the discretized problem can be rewritten as a linear system $A\mathcal{U} = b$, where $\mathcal{U} \in \mathbb{R}^N$ are the degrees of freedom of the finite element solution u_h, A and b are obtained with the finite element bases.N is defined as the dimension of the discrete trial and test spaces. For nonlinear problems, we have to solve nonlinear systems of equations and it may be done with variants of Newton's method.

A crucial aspect of the method is the construction of discrete subspaces $V_h \subset V$ with local function spaces defined by the finite elements. We will not detail here the finite element spaces. We have used the widely used $P1$ and $P2$ Lagrange elements based on tetrahedra. This formulation is useful for linear variational problems, and it is used for the transport equation for the tracer concentration denoted as f. In order to obtain the velocity field, with have to solve more complex mixed problems with the velocity and the pressure as detailed in the following.

There are some key features that characterize physiological flows like the blood flow. Blood flows are highly unsteady and are often pulsatile. They take place in very complex geometries. Not only the geometry of the flow domain might be complex but it also often varies in time.

To a good approximation, the blood is incompressible and it can be described by the Navier-Stokes equation. In this work, for the sake of simplicity, we have also considered stationary Navier-Stokes equations.

Steady Navier-Stokes equation and finite element variational form

It is necessary to emphasize that the snapshots or samples of stationary velocity fields are obtained by the Navier-Stokes equation. The theory of the Navier-Stokes equation and its finite element variation formulation is presented by the Fenics book (Brenner, 2008; Logg et al., 2012). There are some assumptions in this work regarding the fluid properties. The flow is governed by dimensionless parameters. The Reynolds number is the non-dimensional number useful to know whether a flow belongs to a laminar or turbulent flow. It represents the ratio between the magnitude of convective terms and viscous terms.

It is defined as:

$$Re = \frac{\rho V_m d}{\mu} = \frac{V_m d}{\nu} \tag{1.25}$$

where ρ is the tracer concentration of the fluid, V_m is the mean velocity, μ is the dynamic viscosity, ν is the kinematic viscosity, and d is a charateristic length of the flow pattern. Here we consider that it is the the diameter of the vessel. The classical Reynolds number in a medium-sized artery vessel is in the range of 100 to 1000 (Ku, 1997). For our simulations, the mean velocity is around 0.6m/s. The viscosity of blood ν is constant and equal to $10^{-6} m^2 s^{-1}$ and the mean diameter of the vessel is around $d = 10^{-2}$m. The calculated average Reynolds number is around 600. So here we assume that the classic laminar blood flow condition can be used in the vessel. The blood is assumed to be an incompressible and Newtonian fluid. For a region Ω, the stationary Navier-stokes equations are a set of equations for the velocity V and pressure fields P in the incompressible blood fluid:

$$\begin{cases} -\nabla \cdot (\nabla V + P) = 0 & in\ \Omega, \\ \nabla \cdot V = 0 & in\ \Omega, \\ V = V_{\partial\Omega} & in\ \partial\Omega \end{cases} \tag{1.26}$$

where $V_{\partial\Omega}$ is the velocity field on the boundary $\partial\Omega = \Gamma_{in} \cup \Gamma_{out} \cup \Gamma_s$. The spatial domain Ω consists of an inflow part Γ_{in} on the plane $z = 0$, of an outflow boundary Γ_{out} on the output plane and of the lateral side of the vessel Γ_s. A parabolic profile is used in the inlet boundary with a maximum value in the middle of this region denoted as $V_{\Gamma_{in},max}$. The stationary velocity fields will be parametrized with $\mu_1 = (V_{\Gamma_{in},max}, P_{\Gamma_{out}})$,where $P_{\Gamma_{out}}$ is the pressure on the outflow part. This parameter will be sampled regularly for inlet velocities between 0 and 0.6 m/s and for output pressures between 0 and 1000 Pa to obtain a dataset of velocity snapshots. The largest branch of the vessel outlet is 1.5 times larger in diameter than the smaller one, and the same outlet pressure is applied to both branches of the vessel. The Dirichlet boundary condition is employed at the inlet, and no-slip lateral boundaries conditions are used to model the interaction between the fluid and solid surfaces for the velocity field. For the pressure field, we adopt the boundary conditions $\nu \partial_{\mathbf{N}} V + P\mathbf{N} = 0$ at the outlet (Heywood et al., 1996). Where $\mathbf{N}$ represents the outward unit normal vector to the boundary and $\partial_{\mathbf{N}} V = \mathbf{N} \cdot \nabla$ is the normal derivative.

To solve the Navier-stokes equations in Fenics, we have to formulate them in a variational form based on the finite element method for discretization within the spatial domain. The way to write the problem into a variational problem is to multiply the Navier-Stokes equation by a test function u for the velocity, and to multiply the continuous equation by a test function q for the pressure. To explain the variational form, firstly we need to define a mixed-function space

$\hat{W} = (U, \Pi)$ for the velocity and the pressure respectively. Let $U = H_0^1(\Omega)^d$ and $\Pi = \{q \in L^2(\Omega) : \int_\Omega q\, dx = 0\}$. The variational problem turns to find $V \in U$ and $P \in \Pi$ such that:

$$\begin{cases} a(V,u) - b(u,P) = 0, & \forall u \in U \\ b(V,q) = 0, & \forall q \in \Pi, \end{cases} \tag{1.27}$$

where the above first equation of the variational form is expressed with an integral form as:

$$a(V,u) := \int_\Omega \nabla V \cdot \nabla u dx \tag{1.28}$$

$$b(u,P) := \int_\Omega (\nabla \cdot u) P dx \tag{1.29}$$

Additionally, we denote U_h, Π_h the discrete spaces for velocity and pressure. The continuous variational formulation can be transformed into a discrete variational problem, and the aim is to find $V_h \in U_h$ such that:

$$\begin{cases} a(V,u_h) - b(u_h,P) = 0, & \forall u \in U_h \subset U \\ b(V,q_h) = 0, & \forall q \in \Pi_h \subset \Pi, \end{cases} \tag{1.30}$$

In our implementation, the trial and test spaces are considered to be the same. This variational formulation is solved by the Fenics platform. Some implementation details are elaborated in the Fenics book (Logg et al., 2012). The former finite element formulation has been studied extensively in the literature. We can mention that the finite element spaces have to be chosen carefully to ensure the stability of the finite element problem. We have chosen the widely used Taylor-Hood elements with a $P2$ Lagrange element for the velocity components and $P1$ element for the pressure component. They correspond to the space of vector-valued continuous piecewise quadratic polynomials and to the space of scalar continuous piecewise linear polynomials. Increasing the time step length usually speeds up the calculation of the solution but it may be unstable. As long as the Courant–Friedrichs–Lewis(CFL) number with the maximum velocity v_{max}, time step length dt, and minimal length interval h_{min} is smaller than one, the solver should converge. The CFL number is defined as, CFL = $v_{max}\ dt/h_{min}$. Too small time steps, however, can lead to an increasing number of iterations.

Non-steady Navier-Stokes equation and finite element variational form The classical adjoint method used in this work involves both velocity fields obtained with the stationary Navier-Stokes equation and the non-stationary Navier-Stokes equation. Here, the non-stationary Navier-Stokes equation depending on time and its variational form will be introduced similarly to the steady N-S equation.

It is given by:

$$\begin{cases} \frac{\partial V}{\partial t} + \nabla V \cdot V - \nu \Delta V + \nabla P = 0 & in\ \Omega, \\ \nabla \cdot V = 0 & in\ \Omega, \\ V = V_{\partial\Omega} & in\ \partial\Omega \end{cases} \tag{1.31}$$

In this work, we will employ Chorin's method referred to as a non-incremental pressure correction scheme for discretization (Chorin, 1968). The main idea of this method is to calculate a first approximation of the velocity with a neglected pressure in the momentum equation which is the first equation in equation 1.31 and subsequently to project the velocity onto the domain of divergence-free vector fields. To summarize, there are three steps in implementing this method for the non-steady NS equations. In the framework of the Incremental Pressure Correction Scheme, we can first achieve a tentative velocity V_h^* with:

$$\langle D_t^n V_h^*, u\rangle + \langle V_h^{n-1}\cdot\nabla V_h^{n-1}, u\rangle + \langle \nu\nabla V_h^*, \nabla u\rangle = \langle F^n, u\rangle \ \ \forall u \in U_h \tag{1.32}$$

In this equation, $D_t^n V_h$ is defined as a discretized time derivative $(V_h^n - V_h^{n-1})/(t_n - t_{n-1})$. The pressure field will be corrected by:

$$\langle \nabla P_h^n, \nabla q\rangle = -\langle \nabla\cdot V_h^*, q\rangle/(t_n - t_{n-1}) \ \ \forall q \in \Pi_h \tag{1.33}$$

Eventually, the velocity including the boundary conditions will be calculated by:

$$\langle V_h^n, u\rangle = \langle u_h^*, u\rangle - (t_n - t_{n-1})\langle \nabla p_h^n, u\rangle \ \ u \in U_h \tag{1.34}$$

The above variational problem is addressed by employing the python programs with Fenics. Several schemes are presented and compared in the Fenics book.

1.5 Simulation results for blood flow reconstruction

In this section, we first present a study of the influence of the simulation parameters for the inverse problem considered. A higher discretization level may give more information on the tracer or velocity fields. Yet, the optimization problem becomes more complex and the iteration may stagnate in local minima.

1.5.1 Simulation parameters optimization for tomography projection

Based on the classical adjoint method presented above, we explore numerical studies for blood flow reconstruction with the simulation phantom of geometry 1 already displayed. For the purpose of the investigation, we optimize the simulation parameters including the size of the box projection in the range [0.027m×0.027m, 0.067m×0.067m], the number of slices [20, 50], and the number of projection angles [90, 1000] within the angular range [0,180°] while keeping the regularization parameters $\alpha_s = 0$ and with no noise added. After implementing the simulations, we have calculated the evolution of the relative root mean square errors (RMSE) as a function of the iteration number k for several quantities of interest using the $L2$ norm. These quantities include the velocity field V_k, its components, and the reconstructed tracer concentration f_k. The error for the tracer concentration is given as:

$$RMSE(f_k) = (\sum_{p=1}^{N_t} \|f_k(\mathbf{x}, t_p) - f^*(\mathbf{x}, t_p)\|^2_{L_2(\Omega)})^{1/2}/(\sum_{p=1}^{N_t} \|f^*(\mathbf{x}, t_p)\|^2_{L_2(\Omega)})^{1/2} \tag{1.35}$$

The error for the velocity at iteration k is written as:

$$\begin{aligned} RMSE(\mathbf{V}_k) = (\textstyle\sum_{p=1}^{N_t} \|u(\mathbf{x}, t_p) - u_k(\mathbf{x}, t_p)\|^2_{L_2(\Omega)} + \|v(\mathbf{x}, t_p) - v_k(\mathbf{x}, t_p)\|^2_{L_2(\Omega)} \\ + \ \|w(\mathbf{x}, t_p) - w_k(\mathbf{x}, t_p)\|^2_{L_2(\Omega)})^{1/2}/(\textstyle\sum_{p=1}^{N_t} \|u(\mathbf{x}, t_p)\|^2_{L_2(\Omega)} + \|v(\mathbf{x}, t_p)\|^2_{L_2(\Omega)} + \|w(\mathbf{x}, t_p)\|^2_{L_2(\Omega)})^{1/2} \end{aligned} \tag{1.36}$$

where the sum is extended to all the timesteps of the simulations. For the component w for the z-axis, the error is defined as:

$$RMSE(w_k) = \ (\textstyle\sum_{p=1}^{N_t} \|w(\mathbf{x}, t_p) - w_k(\mathbf{x}, t_p)\|^2_{L_2(\Omega)})^{1/2}/(\sum_{p=1}^{N_t} \|w(\mathbf{x}, t_p)\|^2_{L_2(\Omega)})^{1/2} \tag{1.37}$$

Similar definitions for u, and v will be used for the components of the velocity along the x-axis and y-axis. In this part, we will give the results for the unsteady ground truth velocity obtained by solving the non-stationary Navier-Stokes equations.

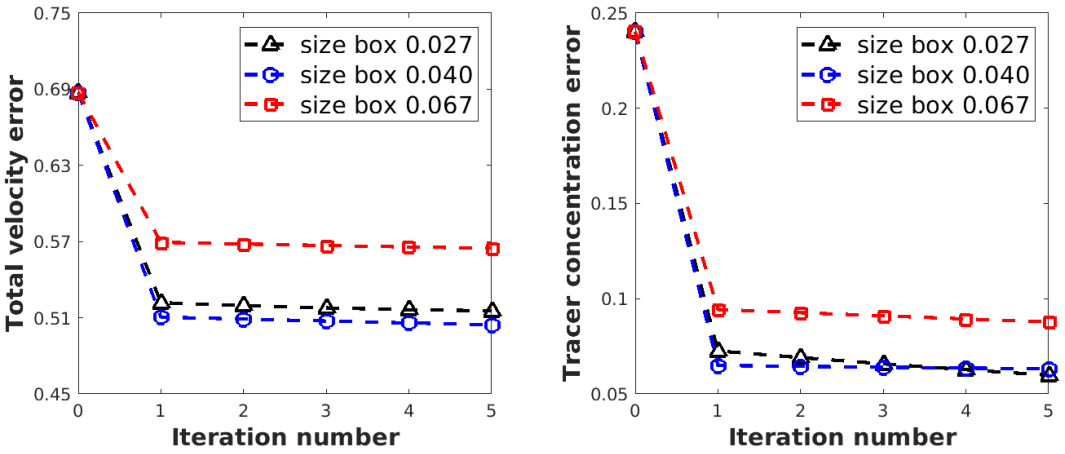

(a) Velocity error (b) Tracer concentration error

Figure 1.7: The average reconstruction error curves for various size of the projection box.

1.5.1.1 Optimization of size box projection

We vary the size of the projection box from 0.027m×0.027m to 0.067m×0.067m. In order to modify a single parameter, the numbers of slices and number of projection angles remain constant with values of 40 and 180 respectively. As we can see in Figure 1.7, the reconstruction errors of velocity and tracer concentration display a decrease, and the decrease behaviors tend to be fast at the first iteration and slow after the first iteration. Moreover, the results show that using the box projection size 0.04m×0.04m can lead to a lower velocity reconstruction error. A small tracer concentration reconstruction error is obtained with the size box 0.04m×0.04m and 0.027m×0.027m. In short, we can make a summary that a middle-size box projection can lead to a lower velocity reconstruction error and a relatively small tracer concentration reconstruction error. In this work, the box projection size 0.04m×0.04m is chosen to obtain the Radon projections. For lower projection box size, more pixels are used to describe some slice of the tracer, the resolution is improved but this is not an optimal choice for the problem considered and the computational burden is higher.

1.5.1.2 Optimization of the number of slices along the z axis

In this part, we will explore the effect of the number of slices selected from 20 to 50 for the optimization of the Radon projections, with an optimized size box projection 0.04m×0.04m and a given number 180 of projection angles.

Figure 1.8 shows again that the velocity reconstruction error and the tracer concentration reconstruction error exhibit a substantial decrease with the first iteration and a small decrease after the first iteration. As the number of z slices decreases in the studied, the reconstruction errors for velocity and tracer concentration display a decrease. So it can be concluded that a small number 20 of slices can improve the velocity reconstruction error and tracer concentration reconstruction error for the simulations. This optimized number of slices will be chosen in the subsequent sections. A larger number of z slices leads to a more complex optimization problem and it is not optimal.

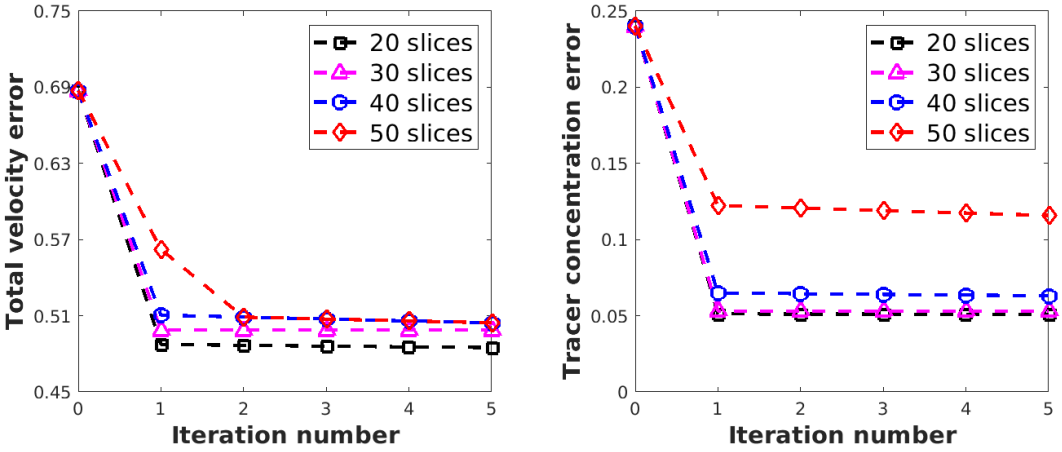

(a) Velocity error (b) Tracer concentration error

Figure 1.8: The average reconstruction error curves for different numbers of slices.

1.5.1.3 Optimization of the number of projection angles

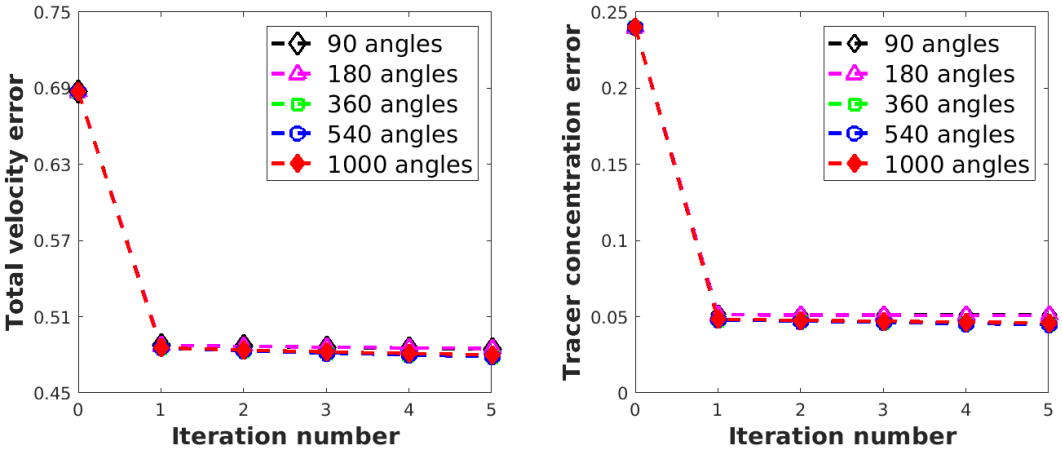

(a) Velocity error (b) Tracer concentration error

Figure 1.9: The average reconstruction error curves for varying numbers of projection angles.

We have already obtained the optimized projection box size 0.04m×0.04m and the optimized number of slices 20 for the Radon projections. With these optimized simulation parameters, the number of projection angles is varied from 90 to 1000 in the interval [0, 180°] in order to find an optimal number. Here we give the results with 90, 180, 360, 540, and 1000 projection angles. The average reconstruction errors for velocity and tracer concentration in Figure 1.9 show again a clear decrease at the first iteration and a slight decrease in the next four iterations. Moreover, a small difference using more projection angles can be observed in the figure. In addition, the reconstruction errors for velocity and tracer concentration corresponding to these error curves are displayed in the table 1.1.

With a number of projection angles larger than 360, the reconstruction errors can be very

Projection angles	E(**V**)	E(f)
90	0.4848	0.0512
180	0.4848	0.0510
360	0.4788	0.0450
540	0.4785	0.0448
1000	0.4800	0.0460

Table 1.1: The reconstruction errors at the end of the iterations for the velocity and tracer concentration fields.

slightly improved. But taking the calculation time into consideration, we prefer to use 180 projection angles for our simulations.

1.5.1.4 Summary

In this part, we have studied the optimization of the simulation parameters: box projection size, number of slices for the Radon projection, and number of projection angles with a range of [0.027m×0.027m, 0.067m×0.067m], [20, 50], [90, 1000]. We have maintained the regularization parameter to the value of 0 and considered no additional noise. The optimized simulation parameters are obtained with the values 0.04m×0.04m for the size of the box projection, 20 for the number of slices, and 360 for the number of projection angles. Considering the calculation cost, we use fewer projection angles and 180 projection angles. The optimized parameters will be used for the following parts to study the effects of the regularization parameter and of the level of white Gaussian noise.

1.5.2 Effect of the regularization parameter

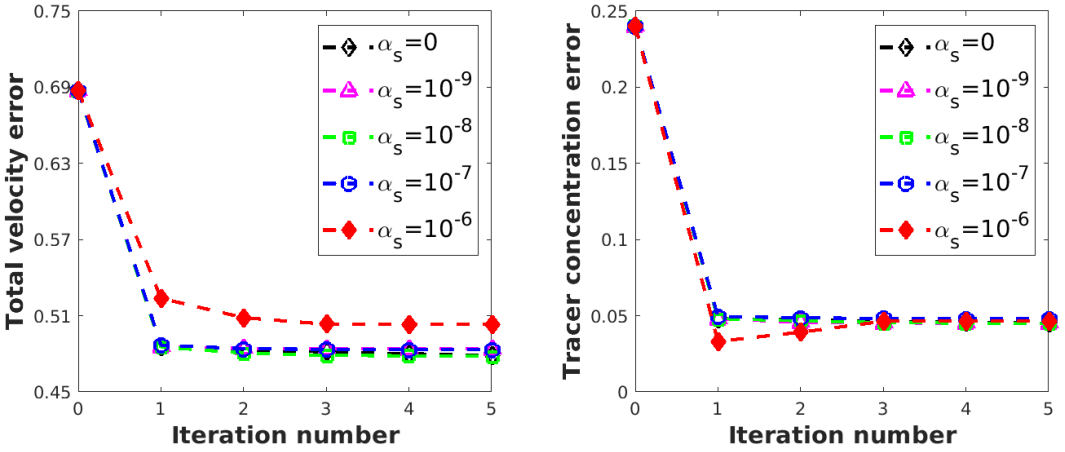

(a) Velocity error (b) Tracer concentration error

Figure 1.10: The average reconstruction error curves for various regularization parameters, PPSNR=40 dB.

.

The regularization parameter α_s included in the cost function is presented above. The

regularization term tends to smooth the reconstructed velocity field and avoid the noise amplification for the inverse problem. In this subsection, we will focus on the range of regularization parameters $[0, 10^{-6}]$ for a PPSNR of 40 dB. The simulation parameters like the size of the projection box, the number of slices, and the number of projection angles are chosen as 0.04m×0.04m, 20, and 360 respectively. From Figure 1.10 a, we see that as the iteration number increases, the velocity error exhibits a sharp decrease after one iteration and a low decrease after this iteration. It is obvious that using a small regularization parameter under 10^{-7} we can obtain a small velocity error. As we can see in Figure 1.10 b, we obtain a decrease in tracer concentration with a regularization parameter below 10^{-7}. It can be concluded that a small regularization can lead to a good reconstruction result for this noise. So we will choose the regularization parameter 10^{-8} for the following investigation for this noise level. Subsequently, we will study the influence of white Gaussian noise on the tracer concentration. The regularization parameter has to be adapted depending on the noise level as explained above and we have used heuristic rules to choose this parameter.

1.5.3 Effect of white Gaussian noise on the Radon projections

Generally speaking, the inverse problem considered is ill-posed and very sensible to the noise on the measured Radon projections. We assume the photons counts on the detectors are high and we consider gaussian noise. As we noted before, some corrupting white Gaussian noise is added to the projection of the tracer concentration for the simulation study with a standard deviation σ and corresponding to some PPSNR. In this study, we consider the noise level within the range of [0 dB, 40 dB] and maintain the box projection size value to 0.04m×0.04m, use 20 slices and 180 projection angles, to study non-stationary velocity fields and stationary velocity fields.

1.5.3.1 Non-stationary velocity field

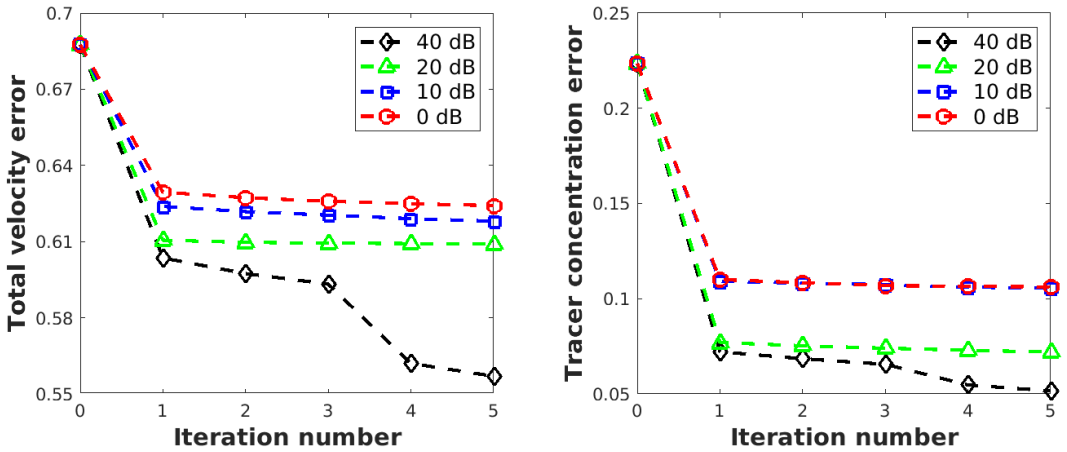

(a) Velocity error (b) Tracer concentration error

Figure 1.11: The average reconstruction error curves with non-stationary velocity field.

Figure 1.11 describes the average reconstruction error curves for various Gaussian noise levels. It shows a decrease in the errors for velocity and tracer concentration fields for the various added Gaussian noise levels. For the velocity magnitude error, we used the sum of

the velocity components errors. Moreover, as the noise level increases from 40 dB to 0 dB, the error for the reconstruction of velocity and tracer concentration fields tends to increase. The reconstructed velocity component error curves are shown in Figure 1.12 to have a better understanding of the effect of the noise level.

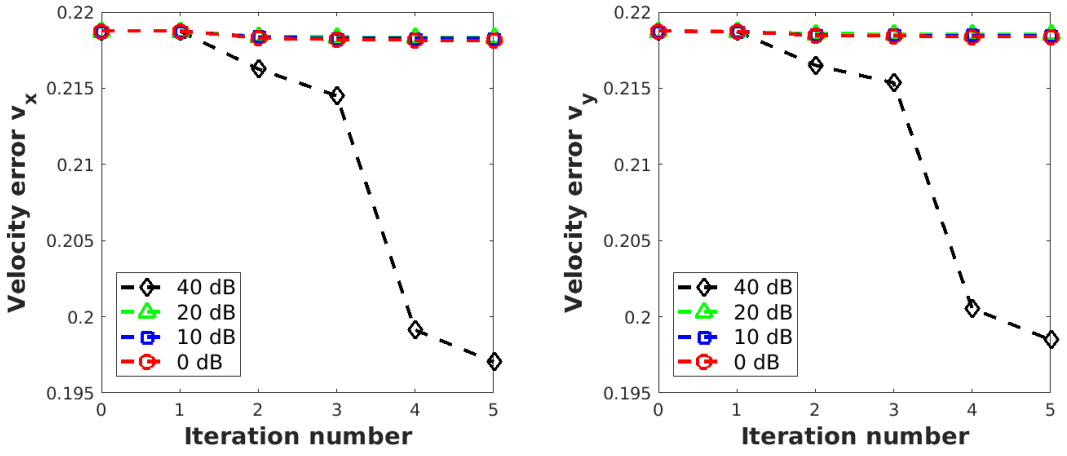

(a) Velocity error along x

(b) Velocity error along y

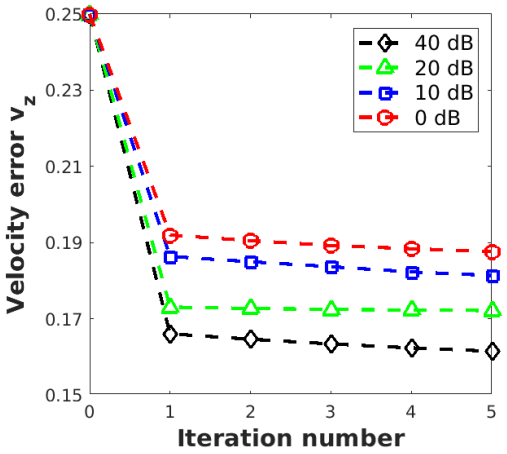

(c) Velocity error along z

Figure 1.12: The average reconstructed velocity components error with non-stationary velocity.

In this figure, the reconstructed velocity error along x and y components displays a small decrease with some noise corrupting the tracer concentration Radon projections, while the velocity error along the z axis exhibits the same regular decrease as the velocity magnitude error. This component decrease is the main cause of the total velocity error decrease as the noise level decreases.

To estimate the efficiency of the method to solve the inverse problem and the accuracy of the numerical approximation, we have used the approach for various values of the angular range $\delta\theta$ and different noise levels. The results are summarized in Table 1.2. The errors for the transverse components along the x axis and y axis of the velocity field display small variations for various $\delta\theta$.

Thus, we can conclude that the noise level plays an important role in blood flow reconstruc-

$\delta\theta$	Noise level (dB)	RMSE (f)	RMSE (u)	RMSE (v)	RMSE (w)
36	20	0.086	0.219	0.219	0.176
36	40	0.092	0.219	0.219	0.177
90	20	0.080	0.219	0.219	0.174
90	40	0.093	0.219	0.219	0.178
180	20	0.072	0.218	0.219	0.172
180	40	0.052	0.197	0.199	0.162

Table 1.2: Evolution of the reconstruction errors for the tracer concentration and the velocity components for various projection angles range $\delta\theta$ and noise levels.

tion and a small noise level in the tracer concentration projections leads to a better blood flow reconstruction for the non-stationary velocity field.

1.5.3.2 Stationary velocity field

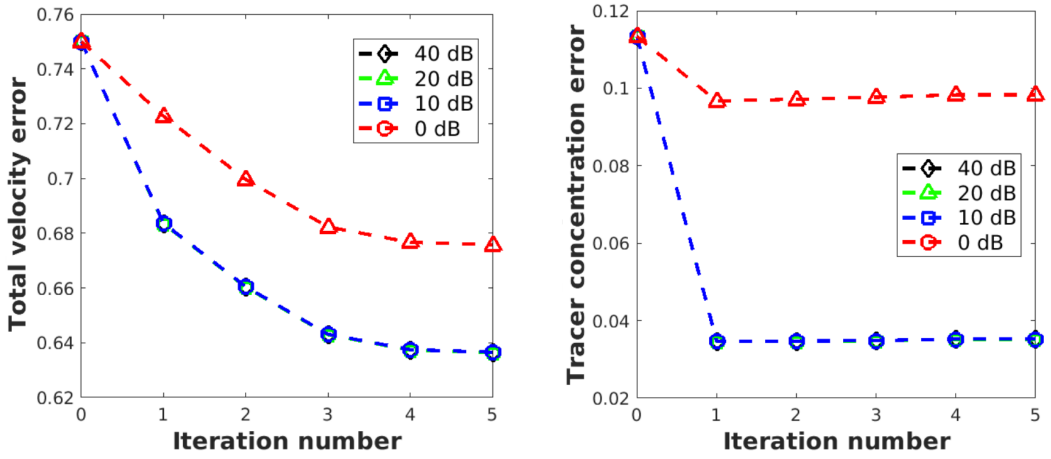

(a) Velocity error

(b) Tracer concentration error

Figure 1.13: The average reconstruction velocity error with stationary velocity field.

We have done the same type of study, with the same simulation parameters and regularization parameters for the stationary velocity field. From Figure 1.13 a, it can be observed that the velocity error continuously decreases as the iteration number increases, and the curves are extremely closed when the PPSNR is larger than 10 dB while a large noise level with a PPSNR below 10 dB exhibits a large velocity error. The corresponding tracer concentration error displays a different trend shown in Figure 1.13 b. It can be seen that a large decrease of the error is obtained after the first iteration and then the error stagnates. The influence of the noise on the error is similar to the one obtained for the velocity. For the velocity components, the velocity error along the x axis and y axis exhibits a relatively small decrease at the first iteration, followed by a continuous decrease as displayed in Figure 1.14.

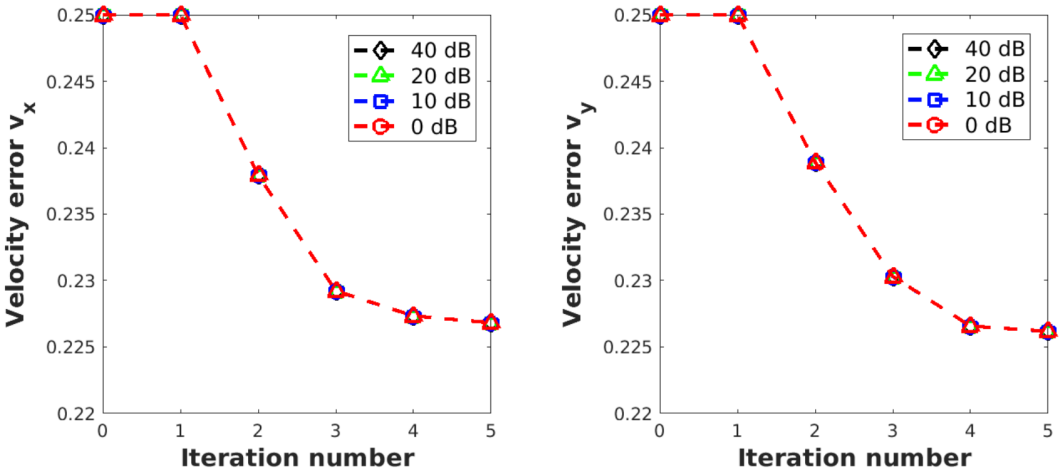

(a) Velocity error along x

(b) Velocity error along y

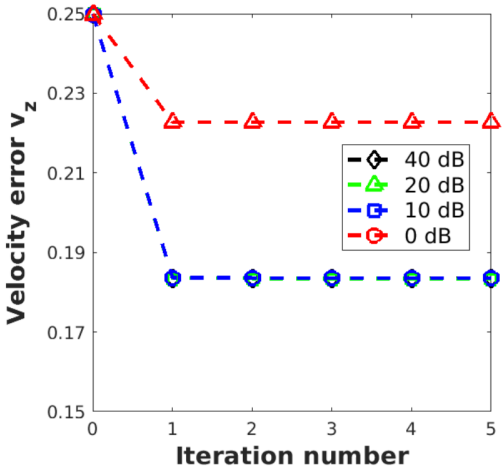

(c) Velocity error along z

Figure 1.14: The average reconstruction velocity component errors with a stationary velocity field.

$\delta\theta$	Noise level (dB)	RMSE (f)	RMSE (w)
36	20	0.045	0.190
36	40	0.040	0.190
90	20	0.045	0.185
90	40	0.040	0.185
180	20	0.033	0.182
180	40	0.033	0.182

Table 1.3: Evolution of the reconstruction errors for the tracer concentration and the velocity along z for various angles range $\delta\theta$ and noise levels for stationary velocity field.

In contrast, a large decrease followed by a smaller change is shown in the velocity error

along z. Moreover, the noise level with a PPSNR above 10 dB present almost similar curves while the high noise level of 0 dB shows a large velocity error associated with the total velocity error. Therefore, it seems that the noise levels with a PPSNR above 10 dB have a small effect on reconstructed velocity error but a large noise level of 0 dB impacts the velocity error a lot.

We have considered the same approach for various values of the angular range $\delta\theta$ and different noise levels with the stationary velocity conditions. The results are summarized in Table 1.3. The errors for the transverse components of the velocity field are not obviously changed by the value of $\delta\theta$ and they have not been presented here as well as for the non-stationary velocity field. The reconstruction errors increase slightly with the decrease of the angular range $\delta\theta$. In the next section, we will display two cases for the velocity and tracer concentration fields with a non-stationary velocity field and a stationary velocity field.

1.5.4 Velocity reconstruction and tracer concentration fields reconstruction

This subsection aims to detail the blood flow field reconstruction. Two different flow states have been considered in this study including a non-steady velocity field and a steady velocity field. The ground truth velocity field and tracer concentration, and the corresponding reconstructed fields will be displayed. The boundary conditions, the optimized parameters, and the regularization parameter are given in the former subsections.

1.5.4.1 Non-stationary velocity field

Velocity field First, we study the reconstructed velocity components fields including the x axis, y axis, and z axis components to give the reconstruction information for the blood flow. Here, the results for the location at z=0.155m are presented for the velocity and also the tracer concentration reconstruction. The time $t = 0.05s$ is chosen to display the reconstruction results.

From Figures 1.15, 1.16, 1.17, it can be observed that the reconstructed velocity is similar to the ground truth.

Tracer concentration field For the tracer concentration field shown in Figure 1.18, it can be seen that the reconstructed tracer concentration is similar to the ground truth with a slightly lower value. Next, the case with the stationary velocity field condition will be presented.

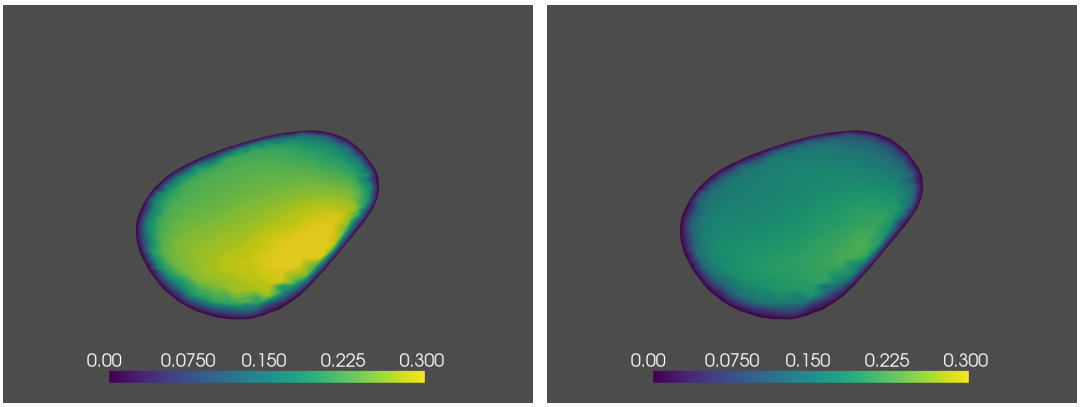

(a) Ground truth velocity along x (b) Reconstructed velocity along x

Figure 1.15: The non-stationary velocity field along x for $z = 0.155$ and $t = 0.05$s, for a PPSNR = 40 dB.

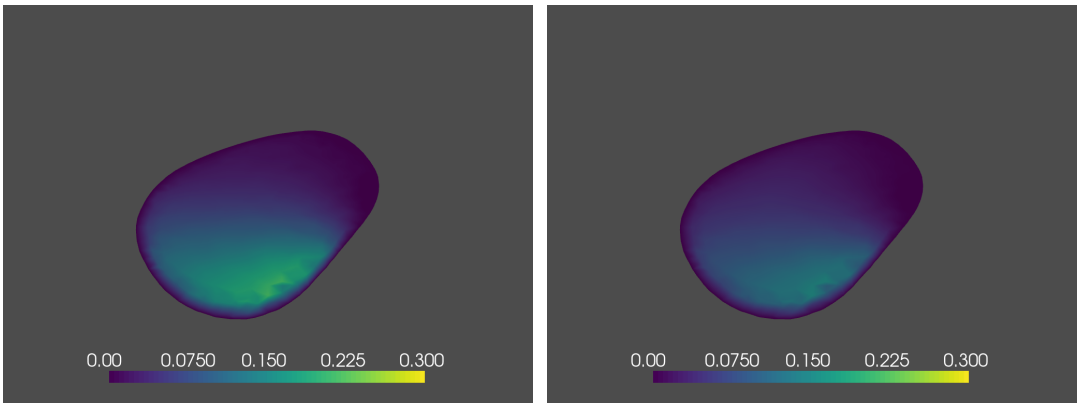

(a) Ground truth velocity along y (b) Reconstructed velocity along y

Figure 1.16: The non-stationary velocity field along y for $z = 0.155$ and $t = 0.05$s, for a PPSNR = 40 dB.

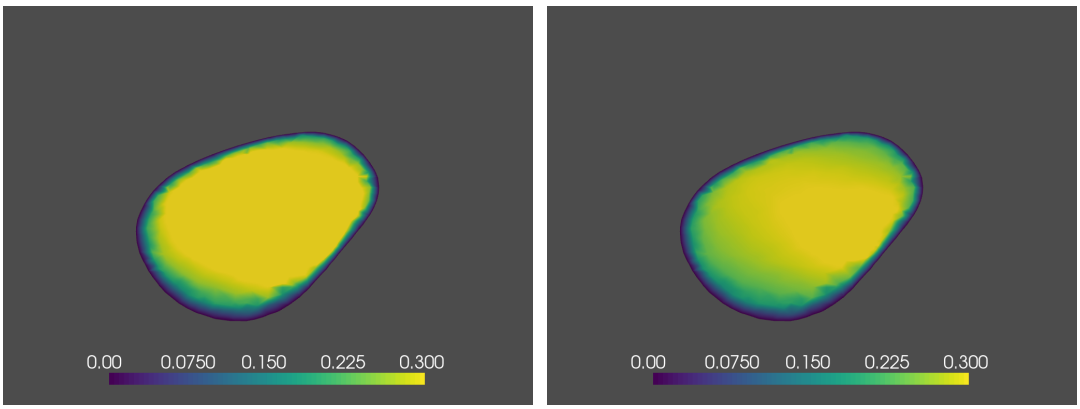

(a) Ground truth velocity along z (b) Reconstructed velocity along z

Figure 1.17: The non-stationary velocity field along z for $z = 0.155$ and $t = 0.05$s, for a PPSNR = 40 dB.

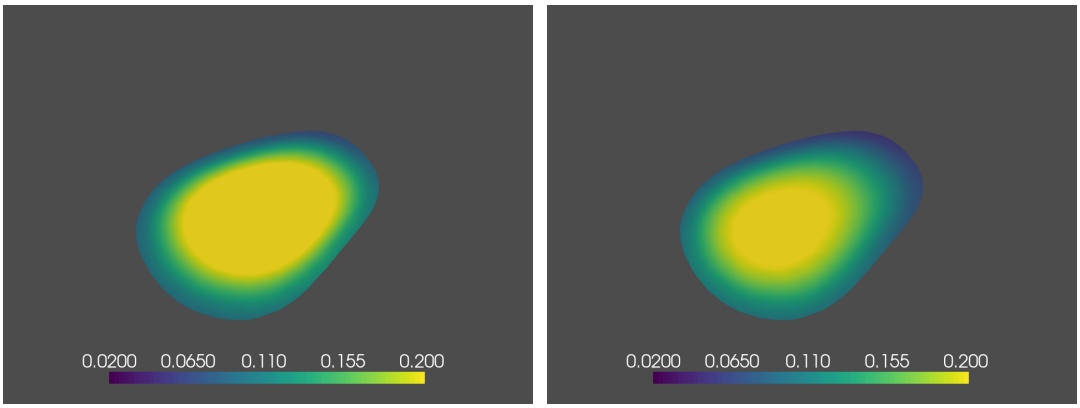

(a) Ground truth tracer concentration (b) Reconstructed tracer concentration

Figure 1.18: The tracer concentration field for non-stationary velocity for $z = 0.155$ and $t = 0.05$s, for a PPSNR = 40 dB.

1.5.4.2 Stationary velocity field condition

Velocity field The same parameter conditions are used in this case while the velocity considered is a stationary one. In this case, the location z=0.125 is used to display the reconstructed velocity and tracer concentration fields.

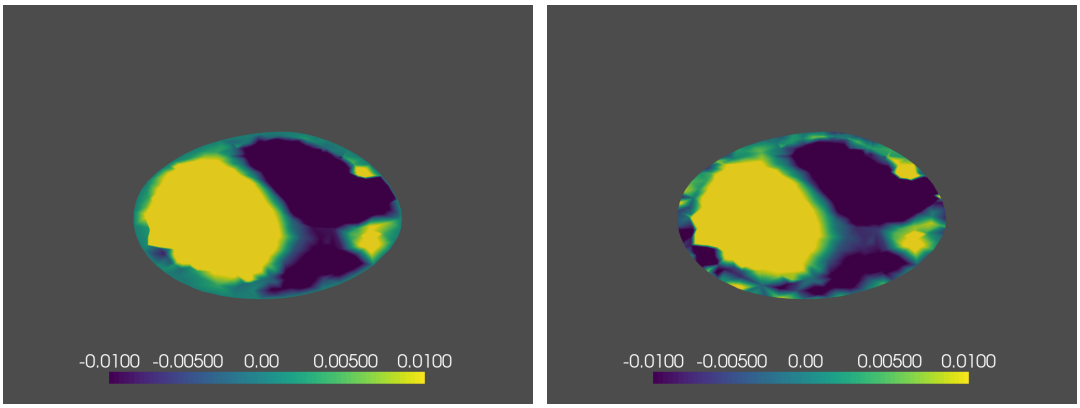

(a) Ground truth velocity along x (b) Reconstructed velocity along x

Figure 1.19: The stationary velocity field along x for z = 0.125, for a PPSNR = 40 dB.

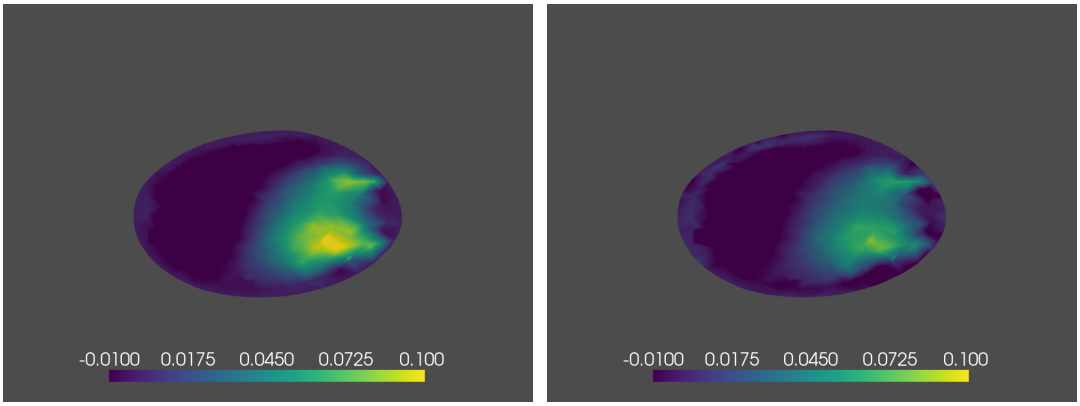

(a) Ground truth velocity along y (b) Reconstructed velocity along y

Figure 1.20: The stationary velocity field along y for z = 0.125, for a PPSNR = 40 dB.

From Figure 1.19, the reconstructed velocity along x is extremely close to the ground truth especially in the higher positive regions and in the lower negative regions.

The same behavior is presented for the reconstructed velocity along y in Figure 1.20 and some reconstruction error can be noticed on the region of higher positive value. Good reconstruction results are also obtained for the z component of the velocity, with higher positive values, as displayed in Figure 1.21.

Tracer concentration field The tracer concentration field for the ground truth and reconstructed field using the adjoint method are shown in Figure 1.22. It can be observed that the reconstructed tracer concentration is similar to the ground truth tracer concentration but the higher value region is not very well reconstructed.

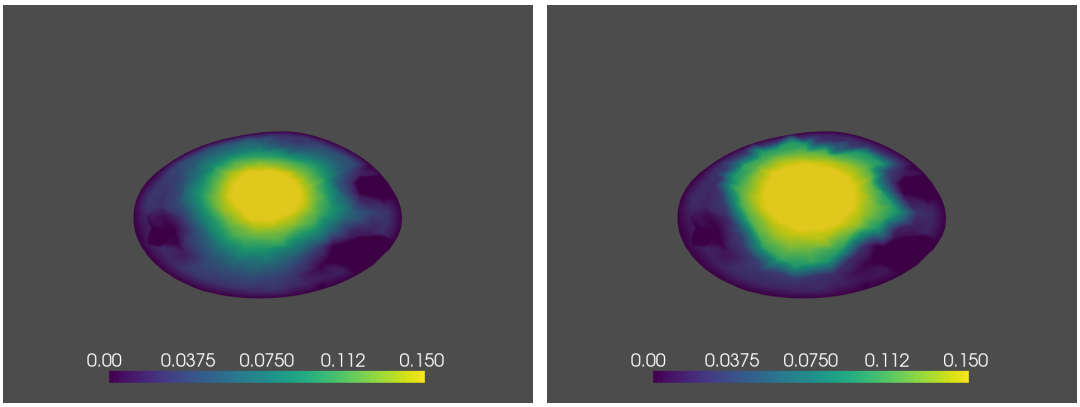

(a) Ground truth velocity along z (b) Reconstructed velocity along z

Figure 1.21: The stationary velocity field along z for $z = 0.125$, for a PPSNR = 40 dB.

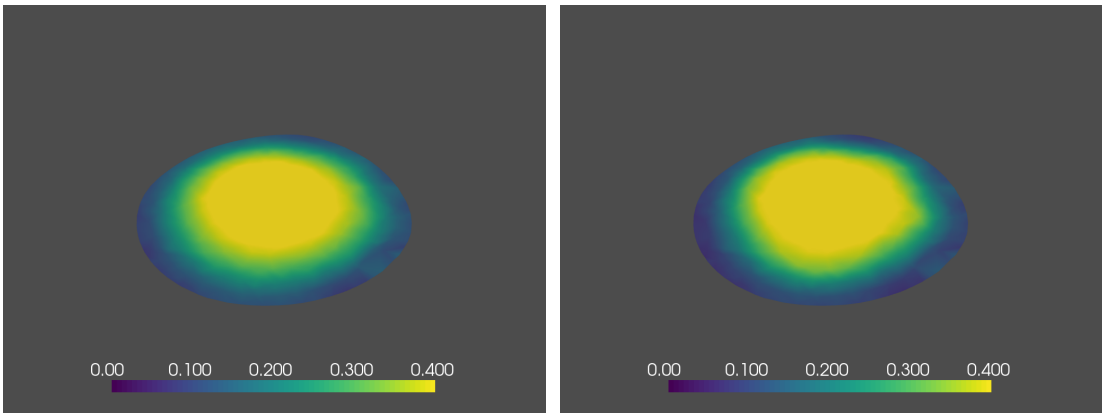

(a) Ground truth tracer concentration (b) Reconstructed tracer concentration

Figure 1.22: The tracer concentration field for stationary velocity for $z = 0.125$ and $t = 0.05$s, for a PPSNR = 40 dB.

1.6 Conclusion

In this section, we have used a novel approach for the velocity field reconstruction of the blood flow within a simulation vessel. The methodology is based on the propagation of a contrast agent and on the acquisition of Radon projections perpendicularly to the main propagation direction. The PDE constraint describing the transport of the contrast agent into the vessel phantom is considered to evaluate the tracer concentration in the optimization problem. Then, the optimal control problem is tackled with the classic adjoint method. We have proved the feasibility of this new approach in a vessel phantom with a bifurcation for stationary and nonstationary velocity flows based on the Navier–Stokes equations.

We have mainly studied the simulation parameters optimization, the effect of the regularization parameter, and the effect of white Gaussian noise corrupting the projections of the tracer concentration fields. The reconstructed velocity and tracer concentration error curves are provided and two velocity fields including a non-stationary velocity field and a stationary velocity field are tested to investigate the reconstructed blood flow.

Optimized simulation parameters are obtained: 0.04m×0.04m for the size of the projection box, 20 slices, and 360 projection angles from a range of studied values [0.027m×0.027m, 0.067m×0.067m], [20, 50], [90, 1000] respectively. After that, various Gaussian noise levels with PPSNR from 0 dB to 40 dB are investigated for the non-stationary velocity field and stationary velocity field. For the non-stationary velocity field, the noise shows an important effect in blood flow reconstruction. For a small noise level, the blood flow can be well reconstructed. We also study various angles range $\delta\theta$: $\delta\theta$=180 is the optimal choice to have a good reconstruction of velocity and tracer concentration for both non-stationary velocity and stationary velocity conditions. Additionally, the ground truth velocity, tracer concentration, and the corresponding reconstructed quantities are presented to deeply understand the blood flow reconstruction. For the non-stationary field, the location of z=0.155m is considered. The reconstructed velocity components and reconstructed tracer concentration are similar to the ground truth velocity components and tracer concentration respectively.

Satisfactory reconstruction results are achieved for the velocity and the tracer concentration. The proposed algorithms result in better results for the axial component of the velocity than for the transverse components. The reconstruction of the axial component is robust with respect to the noise disturbing the Radon projections.

The same reconstructed results are shown in the case of the stationary velocity field condition with a location of z=0.125m. So in the following work, we aim to improve these results and reduce the calculation cost by employing Proper Orthogonal Decomposition and deep learning approaches.

Chapter 2

Proper orthogonal decomposition for accelerating blood flow reconstruction

2.1 Introduction

We have already emphasized that the blood velocity reconstruction in a simulation phantom with contrast-enhanced X-ray computed tomography projections is a difficult inverse problem. In the previous chapter, the classical adjoint method has already been considered as a solution for the tomographic inverse problem under study. We have studied the inversion method that relies on the typical adjoint approach with a transport equation as a constraint. Nevertheless, the calculation cost remains very high. From the time cost point of view, the challenge persists in attaining high-resolution velocity component fields with a reasonable cost.

We need to frequently evaluate the outcomes of forward and adjoint partial differential equations(PDEs) to tackle the tomographic inverse problem and it is significant to decrease the computational costs. Within the reduced-order modeling, we can incorporate the physical problem's structure and the governing equations as well. The reduced model method is based on basis functions that encode information about the solution structure as discussed in (Quarteroni et al., 2015). Model reduction is attained by coupling Proper Orthogonal Decomposition (POD) with Galerkin projection for problems depending on time and parameters (Volkwein, 2013; Ghattas and Willcox, 2021). This method effectively reduces the computational cost while accounting for the behavior described by full-order computations. The fundamental view based on this reduced method is to achieve a low-dimensional approximation by projecting the high-dimensional problem onto a reduced-dimensional subspace. The reduced order POD methods are among the most remarkable techniques for investigating fluid flows (Arian et al., 2000; Rowley, 2005; Daly and Leahy, 2013; Lu et al., 2019). This reduced model can be considered with a set of physical or geometric parameter values and plays an essential role in solving inverse problems and also for the uncertainty quantification, as emphasized by (Volkwein, 2013; Ghattas and Willcox, 2021). This approximation modality based on the reduced method has been proposed for addressing parameterized optimal control problems and inverse problems with parameterized PDEs that are widely used in various applications, like biomedical applications (Ballarin et al., 2017; Ravindran, 2000).

To handle the challenge noted before, inspired by the above methods and to accelerate the convergence using the previous adjoint method to solve the inverse problem of blood flow velocity reconstruction, we turn our attention to coupling the Proper Orthogonal Decomposition method approximation with the adjoint method. The variables of interest are the velocity, tracer concentration, and adjoint variables. They are represented with suitable sets of basis functions obtained from samples or snapshots. To take into account the uncertainty of this for-

ward model with several parameters, we have taken the varying parameters into consideration. The effectiveness of this framework can be illustrated through numerical simulations employing both stationary and non-stationary velocity fields in a realistic phantom. Furthermore, the comparison with the full-order approximation presented in this work can demonstrate the effectiveness of the reduced method for blood flow velocity reconstruction.

The outline of this Chapter will be detailed below. After the introduction, in subsection 2.2, we detail the mathematical concepts of the Proper Orthogonal Decomposition method. We will elaborate on the fundamentals of the POD-adjoint method for tackling the inverse problem of blood velocity reconstruction involving the transport equation and the adjoint equation in subsection 2.3. Subsequently, in subsection 2.4, the simulation details including the finite elements and POD basis construction will be introduced. In subsection 2.5, the results of various simulation cases for the flow pattern in a simulation phantom addressed by this approach will be presented. We will present the POD basis elements analysis and the simulation results using the POD-adjoint approach will be compared with the full-order approximation strategy in terms of the reconstruction errors and computational cost. At the end, we will make a conclusion for this chapter.

2.2 Proper orthogonal decomposition principle

In this work, Proper Orthogonal Decomposition is also called Principal Component Analysis (PCA). Here, we will give insights into the fundamental mathematical formalism.

The discrete version of Proper Orthogonal Decomposition (POD) is equivalent to the Singular Value Decomposition (SVD) of matrices. Here, the construction of the POD basis will be detailed for the tracer concentration as an example. Similar methods to compute the POD basis can be also used for the velocity components and the adjoint variable. The POD basis $\{\psi_{f,j}\}_{1\leq j\leq N_f}$ of rank N_f is obtained with the snapshots $\{y_j\}_{1\leq j\leq N_s} = \{f(\mu_j)\}_{1\leq j\leq N_s} \in \mathbb{R}^m$ obtained with the parameters $\{\mu_j\}_{1\leq j\leq N_s}$, where N_s is the number of snapshots. Some first-order necessary optimality conditions are associated with the SVD decomposition of the matrix $Y = [y_1, ...y_{Ns}] \in \mathbb{R}^{m\times N_s}$. The columns of this matrix are the snapshots y_j (Volkwein, 2013). The SVD of the matrix Y can be expressed as:

$$\Psi_f^t Y \Phi_f = \begin{pmatrix} D & 0 \\ 0 & 0 \end{pmatrix} = \Sigma \in \mathbb{R}^{m\times N_s} \tag{2.1}$$

where we have $D = \mathsf{diag}(\sigma_1, ..., \sigma_d) \in \mathbb{R}^{d\times d}$ with eigenvalues in a decreasing order such that $\sigma_j \geq \sigma_{j+1} \geq 0$. The matrix Σ is a matrix of rank d. The matrices $\Phi_f \in \mathbb{R}^{N_s\times N_s}$ and $\Psi_f \in \mathbb{R}^{m\times m}$ are orthogonal matrices with columns $\{\varphi_{f,j}\}_{1\leq j\leq N_s}$ and $\{\psi_{f,j}\}_{1\leq j\leq m}$ respectively. The vectors $\psi_{f,j}$ and $\varphi_{f,j}$ represent eigenvectors of the empirical non centered covariance matrices YY^t and Y^tY respectively with corresponding eigenvalues $\lambda_j = \sigma_j^2$ for $j = 1, ...d$ and they satisfy the relations:

$$Y\varphi_{f,j} = \sigma_j\psi_{f,j} \qquad Y^t\psi_{f,j} = \sigma_j\varphi_{f,j} \quad for \quad j = 1, ...d \tag{2.2}$$

The POD basis of rank N_f can be obtained with the eigenvalue problem

$$Y^tY\varphi_{f,i} = \lambda_i\varphi_{f,i} \quad for \quad i = 1, ...N_f \tag{2.3}$$

The N_f eigenvectors $\varphi_{f,1}$ ... $\varphi_{f,N_f} \in \mathbb{R}^{N_s}$ are calculated and then we have:

$$\psi_{f,i} = \frac{1}{\sqrt{\lambda_i}} Y\varphi_{f,i} \quad for \quad i = 1, ...N_f \tag{2.4}$$

Figure 2.1: The finite element mesh of the vessel used for the simulations.

We have calculated several reduced basis of rank N_f, N_V, and N_p for the tracer concentration f, the velocity components V_x, V_y, V_z, and the adjoint variable p. These bases will be denoted Ψ_f, Ψ_{V_x}, Ψ_{V_y}, Ψ_{V_z} and Ψ_p respectively in the following. The estimation of these POD bases will be presented in the following.

2.3 POD-adjoint method for the inverse problem

In this part, we highlight the setup of the inverse problem again and the adjoint method used in the preceding studies. Additionally, the derived version of this adjoint method is combined with a POD methodology based on various parametric conditions.

The simulation phantom is the same as before which was used for numerical studies with the adjoint method and shown in Figure 2.1. We study the inverse problem associated with the blood flow reconstruction by employing a parametrized problem by a parameter μ belonging to some parameter space $\mathcal{M}$. This leads us to reformulate the inverse problem setup and solution modalities with this novel parameter.

We can reformulate the inverse problem of the blood flow reconstruction as an optimal control problem including a cost function with a partial differential equation as constraint. The main flow direction is the z axis and two-dimensional Radon projections are obtained perpendicularly to this z axis, in the xy plane. The space-time box considered is denoted $Q = \Omega \times [0,T]$ where Ω is a bounded spatial domain and $[0,T]$ is the time interval. We will consider the Hilbert space $\mathcal{L} = L_2([0,T], L_2(\Omega))$ of square integrable functions, $t \to f(\mathbf{x},t)$, $t \in [0,T]$, with values in the Hilbert space $L_2(\Omega)$ of square integrable functions on Ω, embedded

using the norm:

$$\|f\|_{\mathcal{L}} = (\int_0^T \|f\|^2_{L_2(\Omega)} dt)^{1/2}. \tag{2.5}$$

The propagation of the contrast agent with the tracer concentration $f(\mathbf{x}, t)$ is described by a partial differential equation relying on a realistic velocity field obtained by solving the Navier-Stokes equation (Glowinski and Pironneau, 1992; Galdi, 1994; Temam, 2001). It is assumed that the concentration of the other materials can be ignored and the evolution of the Radon projections as time changes is related to its propagation of the tracer. We model the propagation of the contrast agent in the vessel through a convection-diffusion equation with a diffusion parameter D and the velocity $\mathbf{V} = (u, v, w) : [0, T] \times \Omega \to \mathbb{R}^3$. In our work, stationary and non-stationary velocity fields are both considered, obtained by addressing the stationary and non-stationary Navier-equations. The velocity field $\mathbf{V}$ is parametrized by the first component μ_1 of μ related to the boundary or initial conditions. We will detail the parameter μ_1 in the following. The contrast agent is injected into the vessel passing through a disk ($\mathcal{D}$) in the boundary plane $z = 0$. It is also assumed that the value of the function f on the disk ($\mathcal{D}$) is associated with the parameter μ_2 of the parametrized inverse problem. The convection-diffusion equation with its initial and boundary conditions has been detailed in equation 1.10 in Chapter 1.

The algorithmic scheme and the numerical implementation of the adjoint method are detailed in Chapter 1. It has been shown that the inverse problem is well-posed for any value of μ. The proof is based on the implicit function theorem, on the fact that J and e are Fréchet differentiable and that for every value $\mu \in \mathcal{M}$ and for every control variable $\mathbf{V}$, and there exists a unique solution $f(\mathbf{V}, \mu)$. The reduced order method proposed in this work is based on the assumption that the solution manifold

$$\mathcal{M} = \{f(\mu), \mathbf{V}(\mu), p(\mu); \mu \in \mathcal{M}\} \tag{2.6}$$

can be approximated by a low dimensional subspace in an offline phase that may be computationally expensive. The set $\mathcal{M}$ is sampled with a discrete subset of parameters $\mathcal{M}_s \subset \mathcal{M}$. This finite-dimensional parametric set has cardinality $N_s = |\mathcal{M}_s|$. A solution manifold can be defined for the snapshots, $\{f(\mu), \mathbf{V}(\mu), p(\mu); \mu \in \mathcal{M}_s\}$. If the finite parameter space $\mathcal{M}_s$ is large enough, this manifold is a good representation of the manifold $\{f(\mu), \mathbf{V}(\mu), p(\mu); \mu \in \mathcal{M}\}$. The full-order discretized finite element solutions will be denoted as $\{f_{\mathcal{F}}(\mu), \mathbf{V}_{\mathcal{F}}(\mu), p_{\mathcal{F}}(\mu), \mu \in \mathcal{M}_s\}$. After finite element discretization, they are vectors of $\mathbb{R}^m$ or $\mathbb{R}^{3m}$ for the tracer concentration, adjoint, and velocity fields respectively, where m is the number of coefficients in the full order finite element approximation. They will be projected on low dimensional spaces to obtain the reduced basis $(\Psi_{f,i})_{1\le i\le N_f}$, $(\mathbf{\Psi}_{V,j})_{1\le j\le N_v}$, $(\Psi_{p,k})_{1\le k\le N_p}$ with dimensions N_f, N_V^3 and N_p.

In subsection 2.3.1, we give a description of the POD method with the construction of the basis functions from the collection of evaluations of the velocity, tracer concentration, and adjoint variables. In subsection 2.3.2, we then present the methodology to solve the inverse problem.

2.3.1 The offline step: building POD basis of tracer concentration, velocity, and adjoint variables

In this work, separate PODs are employed on each of the solution manifolds $\{f_{\mathcal{F}}(\mu_1), ...f_{\mathcal{F}}(\mu_{N_s})\}$, $\{\mathbf{V}_{\mathcal{F}}(\mu_1), ...\mathbf{V}_{\mathcal{F}}(\mu_{N_s})\}$, $\{p_{\mathcal{F}}(\mu_1), ...p_{\mathcal{F}}(\mu_{N_s})\}$ to obtain the low dimensional spaces Y_{N_f}, U_{N_V} and P_{N_p} of dimension N_f, N_V^3 and N_p respectively (Strazzullo et al., 2018). For any finite-dimensional space $\mathcal{V}$, we denote $\Pi_{\mathcal{V}}$ the orthogonal projection onto this subspace. The aim of

the POD method is to extract a few basis vectors capturing the critical information from some data and the algorithm gives finite-dimensional spaces that minimize the empirical projection errors for the tracer concentration, velocity field, and adjoint variable respectively:

$$\frac{1}{N_s}\sum_{\mu\in\mathcal{M}_s}\|f_{\mathcal{F}}(\mu)-\Pi_{Y_{N_f}}f_{\mathcal{F}}(\mu)\|^2_{\mathcal{L}} \tag{2.7}$$

$$\frac{1}{N_s}\sum_{\mu\in\mathcal{M}_s}\|\mathbf{V}_{\mathcal{F}}(\mu)-\Pi_{U_{N_V}}\mathbf{V}_{\mathcal{F}}(\mu)\|^2_{\mathcal{L}} \tag{2.8}$$

$$\frac{1}{N_s}\sum_{\mu\in\mathcal{M}_s}\|p_{\mathcal{F}}(\mu)-\Pi_{P_{N_p}}p_{\mathcal{F}}(\mu)\|^2_{\mathcal{L}} \tag{2.9}$$

The optimality conditions for the minimization of these errors lead to the Proper Orthogonal Decomposition presented in the section 2.2.

2.3.2 The online step: POD reduced model for the inverse problem

During the online phase, a Galerkin projection of $f(\mu), \mathbf{V}(\mu), p(\mu)$ is performed onto Y_{N_f}, U_{N_V} and P_{N_p} respectively. We will obtain the reduced order model with the reduced operators when the basis for the tracer concentration, the velocity, and the adjoint variable are defined. The goal of the model reduction is to project a high-dimensional space onto a low-dimensional approximation space and subsequently derive a system of ordinary differential equations in this low-dimensional space. To rewrite the model with a reduced form, here the tracer concentration f is approximated in the POD basis

$$f = \Psi_f \hat{f} \tag{2.10}$$

where $\Psi_f \in \mathbb{R}^{m\times N_f}$ is the basis matrix for the tracer concentration. The reduced tracer concentration $\hat{f}$ denotes the expansion coefficients in the basis. After the Galerkin projection, a linear operator is associated with the differential equations. The reduced model can be obtained as:

$$\frac{d\hat{f}}{dt} = \hat{A}\hat{f} \tag{2.11}$$

with $\hat{f}(0) = \Psi_f^t f(0)$.

The reduced-order operator is related to the full-order operator with $\hat{A} = \Psi_f^t A \Psi_f$. We will solve this equation in time with the finite difference discretization method. After implementing finite difference discretization in time, the PDE $e(f, \mathbf{V}, \mu) = 0$ can be rewritten as

$$A^n f = f^n \tag{2.12}$$

with

$$A^n f = f + (u^n\frac{\partial f}{\partial x} + v^n\frac{\partial f}{\partial y} + w^n\frac{\partial f}{\partial z} - D\triangle f)\delta t \tag{2.13}$$

where δt is the time step of the discretization and f^n, u^n, v^n, and w^n refer to the tracer concentration and velocity components at time step n. With the projection onto the tracer concentration

space, the N_f coefficients of the expansion of the tracer concentration at time step $n+1$ are computed as the solution of a linear system with a matrix in $\mathbb{R}^{N_f \times N_f}$.

We will also implement model reductions for the adjoint equation and the gradient of the function J. For the adjoint equation, we can obtain the reduced ordinary differential equation with the matrix Ψ_p generated with the adjoint snapshots. The velocity gradient is projected on the velocity basis. For example, we can denote $\nabla \hat{J}_x$ the component along x of the gradient obtained with equation 1.19 in Chapter 1, then the component along x of the projected gradient is computed as follows:

$$\nabla \tilde{J}_x = \Psi_{V_x} \Psi_{V_x}^t \nabla \hat{J}_x \tag{2.14}$$

We can obtain similar components along y and z of the reduced gradient with the basis matrices Ψ_{V_y} and Ψ_{V_z}. The online step also follows an iteration scheme for optimizing the best blood flow velocity as the classical adjoint method shown in Figure 1.5 and presented in Chapter 1. The difference from the adjoint method is the POD and projection implementation for the transport equation and also the adjoint equation.

2.4 Numerical simulation details

In this section, we present some numerical experiments to validate the former methodology on a realistic phantom with complex blood flows described by the Navier-Stokes equations.

2.4.1 Finite elements

We will perform the numerical studies with a realistic blood vessel phantom shown in Figure 2.1. The geometry involves a 10 cm long blood vessel with a bifurcation. The mean transverse diameter is around 10 millimeters. Simulations with finite elements have been performed by using the Fenics software (Goda, 1979; Logg et al., 2012). For the discretization of the time interval $[0,T] = [0s, 0.5s]$, a regular grid of size $N_t = 50$ with a small time step $dt = 0.01s$ in agreement with the Courant-Friedrich-Lax (CFL) condition is considered in this work. The realistic velocity fields to be reconstructed $\mathbf{V}^*(\mathbf{x})$ or $\mathbf{V}^*(\mathbf{x},t)$ are obtained by solving the Navier-Stokes equations. These ground truth velocity fields are used with the transport equation mentioned before to calculate the ground truth tracer concentration of the contrast agent, f^*. The method introduced above coupling the adjoint method and POD is then used for reconstructing the velocity field with an initialization with a first guess solution. The transport equation 1.10 in Chapter 1 is solved with finite elements for the space dimension and with the Euler explicit discretization for the time domain (Morton and Mayers, 1998). We discretize the simulation region with $P1$ finite elements and 56845 nodes. Stability conditions $Ddt/dx^2 < 1$ and CFL conditions are both satisfied with the selected space and time discretizations (Morton and Mayers, 1998). The constant values for the diffusion coefficient and the kinematic viscosity are set as D=0.001cm^2/s and ν= 0.01 cm^2/s respectively. We also validate the proposed method with POD on velocity fields obtained with the stationary and non-stationary Navier-Stokes equations detailed in (Huang et al., 2021). It is well-known that stable spatial discretizations are needed for these types of numerical simulations. In this work, the Taylor-Hood ($P2-P1$) finite elements are used (Taylor and Hood, 1973). We consider the algorithm for the non-stationary Navier-Stokes velocity field which is the Incremental Pressure Correction scheme in Fenics (Goda, 1979; Logg et al., 2012). The Radon projections of tracer concentration perpendicular to the major flow direction are implemented with the Scipy python library (Virtanen et al., 2020) for $N_z = 40$ values regularly spaced. The Radon projections of tracer concentration are obtained for $N_p = 100$ values, for $N_\theta = 180$ projection angles in the angular range $\Delta\theta(t) = [p\delta\theta, (p+1)\delta\theta]$, with a measurement interval $\delta\theta$= 180° and for each time step $t_p = pT/N_t$ in the time domain,

$0 \leq t_p \leq T$. Gaussian white noises with a peak-to-peak signal-to-noise ratio (PPSNR) between 0 and 20 dB are applied to corrupt the Radon projections. The peak-to-peak signal-to-noise ratio is expressed as:

$$PPSNR = 20log(\frac{S_{max}}{n_{max}}) \tag{2.15}$$

where S_{max} is the maximum signal amplitude and n_{max} is the maximum noise amplitude. We will present the simulation results which are obtained with the initial velocity field $\mathbf{V}_0$ such that $V_{0,x} = 0.75V_x^*$, $V_{0,y} = 0.75V_y^*$, $V_{0,z} = 0.75V_z^*$ where $\mathbf{V}^*$ is the ground truth velocity. The optimal decrease of the discrepancy term or of the Lagrangian function is applied for the selection of the regularization parameter α_s and of the Lagrangian parameter β.

To evaluate the blood flow velocity reconstruction and the convergence characteristics of the POD method, the evolution of the relative root mean square errors (RMSE) is used as a function of the iteration number k for various quantities of interest using L_2 norms. These quantities contain the velocity field $\mathbf{V}_k$, its components, and the reconstructed tracer concentration f_k for the iteration k. These error metrics can be described as follows:

$$RMSE(f_k) = (\sum_{p=1}^{N_t} \|f_k(\mathbf{x}, t_p) - f^*(\mathbf{x}, t_p)\|^2_{L_2(\Omega)})^{1/2} / (\sum_{p=1}^{N_t} \|f^*(\mathbf{x}, t_p)\|^2_{L_2(\Omega)})^{1/2} \tag{2.16}$$

$$\begin{aligned} RMSE(\mathbf{V}_k) = (\textstyle\sum_{p=1}^{N_t} \|u(\mathbf{x}, t_p) - u_k(\mathbf{x}, t_p)\|^2_{L_2(\Omega)} + \|v(\mathbf{x}, t_p) - v_k(\mathbf{x}, t_p)\|^2_{L_2(\Omega)} \\ + \|w(\mathbf{x}, t_p) - w_k(\mathbf{x}, t_p)\|^2_{L_2(\Omega)})^{1/2} / (\textstyle\sum_{p=1}^{N_t} \|u(\mathbf{x}, t_p)\|^2_{L_2(\Omega)} + \|v(\mathbf{x}, t_p)\|^2_{L_2(\Omega)} + \|w(\mathbf{x}, t_p)\|^2_{L_2(\Omega)})^{1/2} \end{aligned} \tag{2.17}$$

where the sum of the error metrics is extended to all time steps of the numerical simulations. For one of the components w, the error can be written as:

$$RMSE(w_k) = (\textstyle\sum_{p=1}^{N_t} \|w(\mathbf{x}, t_p) - w_k(\mathbf{x}, t_p)\|^2_{L_2(\Omega)})^{1/2} / (\sum_{p=1}^{N_t} \|w(\mathbf{x}, t_p)\|^2_{L_2(\Omega)})^{1/2} \tag{2.18}$$

We will apply similar definitions for the velocity components along the x-axis and y-axis.

2.4.2 POD basis construction

In this subsection, we will give more information on the POD basis construction. The inverse problem of blood flow reconstruction relies on a set of parameters μ. The snapshots or samples are obtained both in time and parameter space. The POD method has been used for time-dependent and parametrically varying states and with a regular grid sampling over the specified range of conditions. The parameter μ_1 is related to the initial or boundary conditions for the velocity field. As we noted before, in order to obtain the snapshots of the velocity fields, we consider the stationary and non-stationary Navier-Stokes equations (Glowinski and Pironneau, 1992; Temam, 2001). The non-stationary Navier-Stokes equation in an incompressible viscous flow condition is written as:

$$\begin{cases} \frac{\partial \mathbf{V}}{\partial t} + \mathbf{V}.\nabla\mathbf{V} + \nabla p - \nu\triangle\mathbf{V} = 0 \\ \nabla.\mathbf{V} = 0 \\ \mathbf{V} = \mathbf{V}_{\partial\Omega} \ \ on \ \ \partial\Omega \end{cases} \tag{2.19}$$

and the stationary equation is expressed as:

$$\begin{cases} \mathbf{V}.\nabla\mathbf{V} + \nabla p - \nu\triangle\mathbf{V} = 0 \\ \nabla.\mathbf{V} = 0 \\ \mathbf{V} = \mathbf{V}_{\partial\Omega} \ \ on \ \ \partial\Omega \end{cases} \tag{2.20}$$

where we denotes the kinematic viscosity as ν, the pressure field $p(\mathbf{x})$ and the velocity field $\mathbf{V}_{\partial\Omega}$ on the boundary $\partial\Omega$. The boundary $\partial\Omega = \Gamma_{in} \cup \Gamma_{out} \cup \Gamma_s$ of the spatial domain Ω includes an inflow part Γ_{in} on the plane $z = 0$, an outflow boundary Γ_{out} on the output plane and the lateral side of the blood vessel Γ_s.The velocity $\mathbf{V}_{\Gamma_{in}}$ on the inflow region Γ_{in} and the pressure $p_{\Gamma_{out}}$ on the outflow region Γ_{out} are used as control variables. The Dirichlet boundary condition at the inlet is thus $\mathbf{V} = \mathbf{V}_{\Gamma_{in}}$ on the domain Γ_{in}. For the outlet, we consider $\nu\partial_{\mathbf{N}}\mathbf{V} + p\mathbf{N} = \mathbf{0}$ where $\mathbf{N}$ is the unit normal vector and $\partial_{\mathbf{N}} = \mathbf{N}.\nabla$ denotes the normal derivative. We select a parabolic profile with a maximum value $\mathbf{V}_{\Gamma_{in},max}$ in the center of the inlet boundary. The steady-state velocity fields will thus be parametrized with $\mu_1 = (\mathbf{V}_{\Gamma_{in},max}, p_{\Gamma_{out}})$. The snapshots of the velocity field have been obtained with regular grid sampling of the inlet velocity and the outlet pressure. For the inlet velocity, we select a total of 10 values between 0.2 and 0.6 m/s, and for the outlet pressure 10 values between 0 and 1000Pa. For the non-stationary velocity field, the inlet velocity is as follows:

$$\begin{cases} \mathbf{V}_{\Gamma_{in},max} + \mathbf{V}_{\Gamma_{in},max} sin(\pi t) \quad for \;\; t \leq 0.5 \\ \mathbf{V}_{\Gamma_{in},max} + \mathbf{V}_{\Gamma_{in},max}(3/2 - 0.5cos(2\pi(t-0.5)) \quad for \;\; t \leq 0.5 \end{cases} \tag{2.21}$$

Therefore, the non-stationary velocity fields will be parametrized with $\mu_1 = (\mathbf{V}_{\Gamma_{in},max}, p_{\Gamma_{out}}, t_i)$, where $(t_i)_{1\leq i\leq 50}$ are the time steps of the time interval in the simulation process. To obtain the POD basis for tracer concentration we use snapshots with state solution computed with the transport equation at different times or for different velocity fields and inlet tracer concentration. The parameter μ_2 depends on the inlet boundary condition for the tracer concentration. Three various inlet tracer concentrations between 0.5 and 1.5 kg/m^3 have been considered. A similar approach has been applied for the adjoint variable snapshots. The reduced states for the tracer concentration, the velocity, and the adjoint variable are obtained from these snapshots in the offline step as explained above.

The POD basis is obtained with the minimization of the projection errors given by equations 2.7, 2.8, and 2.9 above over the set of N_f, N_v^3 or N_p, finite-dimensional subspaces. It is well-known that the empirical projection error is the sum of squares of the singular values for the singular values not contained in the POD basis. For instance, the projection error of the tracer concentration is calculated by $\sum_{i=N_f+1}^{N_s} \sigma_i^2$. We estimate the quality of the POD with this projection error. For the tracer concentration, a basis vector number with a tolerance κ is considered for the singular values such that:

$$\frac{\sum_{i=1}^{N_f} \sigma_i^2}{\sum_{i=1}^{N_s} \sigma_i^2} > \kappa \tag{2.22}$$

We have chosen $\kappa = 1\%$. We consider the same selection criteria for the velocity fields, adjoint variables, and tracer concentration.

To confirm the former results, the mean relative errors for the tracer concentration, velocity, and adjoint variable are calculated for several values of μ from the obtained POD basis. For example, for a given value of μ, and a time step t_k, the relative error for the tracer concentration f is defined as follows:

$$e_f(t_k) = \| \sum_{i=1}^{N_f} \langle f(t_k), \psi_i^f \rangle_{\mathbb{R}^m} \psi_i^f - f(t_k) \| / \| f(t_k) \| \tag{2.23}$$

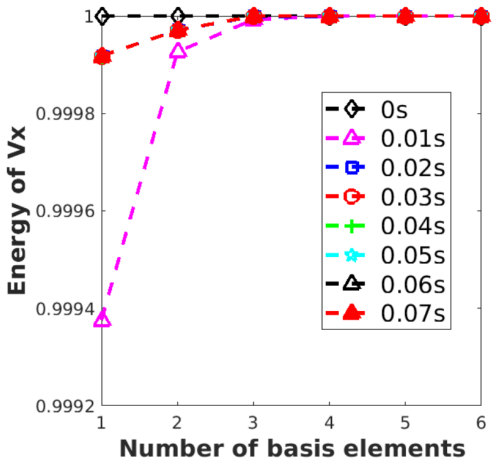

(a) Energy of velocity POD basis along x

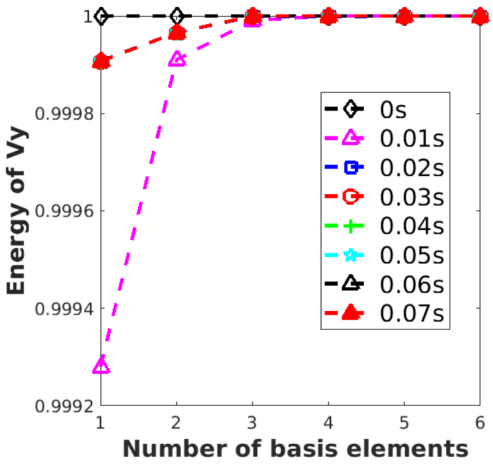

(b) Energy of velocity POD basis along y

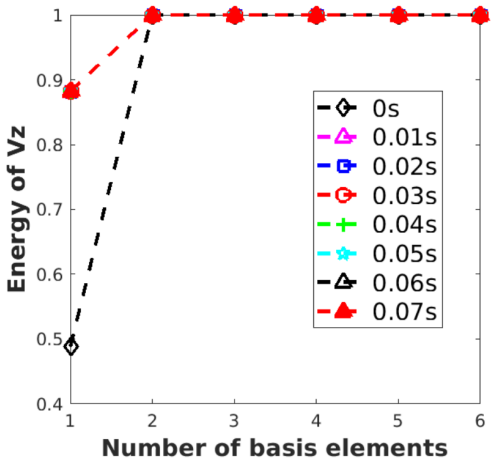

(c) Energy of velocity POD basis along z

Figure 2.2: The energy of the POD basis of velocity components for non-stationary velocity condition.

where N_f is the number of basis functions used for the tracer concentration. We obtain Monte-carlo estimates of the relative errors with 100 testing samples with a uniform sampling of the μ parameter.

In general, few basis elements can achieve a high energy or a small relative error for our simulations. The energy curves of the POD basis of velocity components are shown in Figure 2.2 and it can be observed that the energy of these bases can achieve a high level with few basis elements. In our simulations, for the non stationary velocity fields $N_v = 6$, $N_f = 40$, and $N_p = 2$ have been chosen. With these values, the relative POD projection errors are below 1%, and with these truncations, the POD bases achieve a high accuracy. For the stationary velocity field, some of the energy curves as a function of the POD basis number are shown in Figure 2.3. High energy is obtained using few POD basis vectors for both velocity fields, tracer concentrations, and adjoint variable fields. For the stationary velocity fields, the basis functions for the velocity, the tracer concentration, and the adjoint variables are obtained by selecting the first 2, 75, or 6 eigenvectors of the snapshots matrix respectively. Thus, the total

reduced dimension is $2^3 * 75 * 6$.

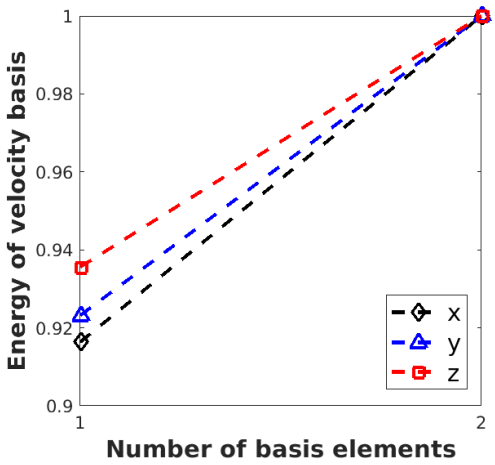

(a) Energy of velocity POD basis

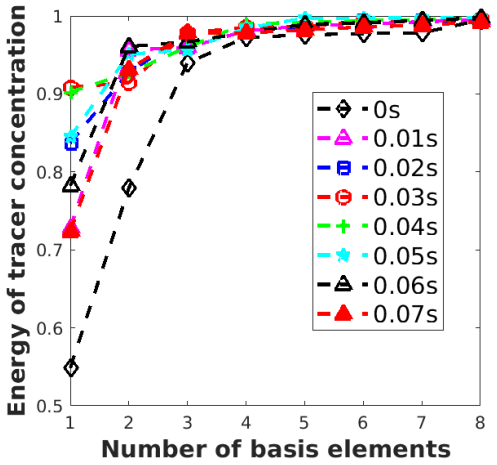

(b) Energy of tracer concentration POD basis

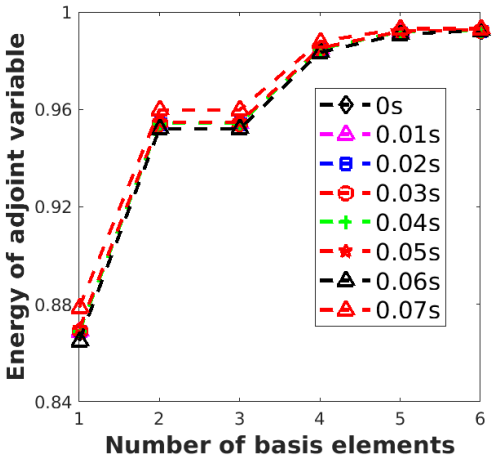

(c) Energy of adjoint variable POD basis

Figure 2.3: The energy of the POD basis for stationary velocity condition.

Finally, we have successfully obtained a highly efficient low-dimensional subspace that still maintains a high level of accuracy. In the following section, we demonstrate that leveraging these bases is an effective way of addressing the inverse problem.

2.5 Blood flow reconstruction results discussion

In this section, the effect of the number of POD basis elements for the velocity, tracer concentration, and adjoint variable is investigated to have a deep understanding of its impact in this reconstruction method. The bases are obtained from the snapshots with a set of parameters μ as discussed above. Based on the POD bases, some cases are considered to demonstrate the effectiveness of this POD-based method. Here, we will give an example with an inlet velocity of 0.45m/s and outlet pressure of 500Pa for solving the Navier-Stokes equation, the inlet injected tracer concentration of is 0.5kg/m^3 for the transport equation and adjoint equation.

We will study both the non-stationary velocity setup and the stationary velocity regime in our numerical studies.

2.5.1 Velocity and tracer concentration errors depending on the number of POD basis elements

2.5.1.1 POD basis elements analysis of velocity

Non-stationary velocity condition Here, we consider the noise level 10 dB with a standard deviation σ =0.1$max(Rf)$ corrupting the tracer concentration Radon projections for the non-stationary velocity field reconstruction. In this condition, the number of velocity basis elements studied is varied in the range from 2 to 6, and 40 tracer concentration basis elements with 2 adjoint variable basis elements are simultaneously considered.

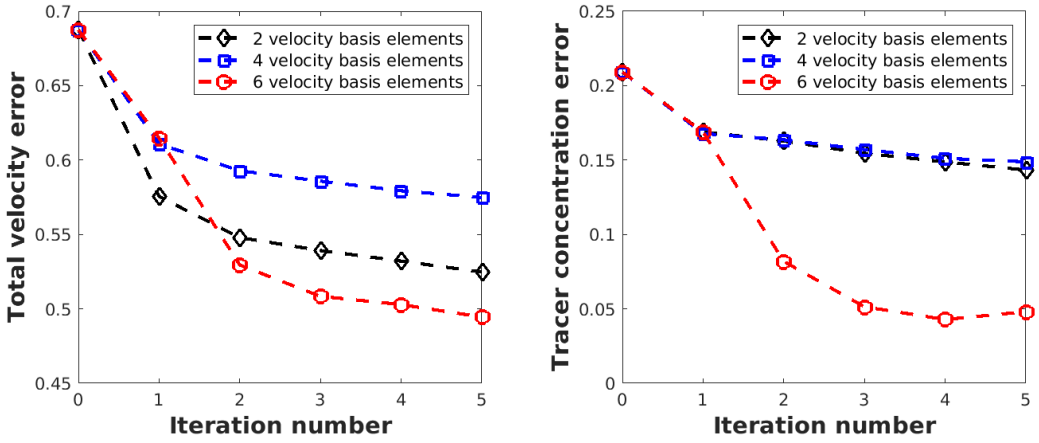

(a) Velocity error (b) Tracer concentration error

Figure 2.4: The average reconstruction error curves of different velocity basis elements numbers with non-stationary velocity field using POD.

In Figure 2.4, the velocity and tracer concentration reconstruction error curves show a decrease as the iteration number increases. Using 6 velocity basis elements, we can achieve a faster decline of the velocity error than with a small number of elements 2 or 4 after the first iteration. The same results are found for the tracer concentration error. Additionally, the reconstructed velocity component errors are displayed in the following Figure 2.5. From these velocity component error curves in Figure 2.5 a and b, we see that the error on the transverse components is lower with fewer basis elements. Yet, with 6 velocity basis elements, we can achieve a smaller velocity error along the main flow direction z-axis and the smaller total velocity error obtained with 6 velocity basis elements.

Therefore, it can be concluded that using 6 velocity basis elements we can obtain a small velocity error in comparison with other number of basis elements for non-stationary states.

Stationary velocity condition For the stationary velocity reconstruction, the case with a noise level of 0 dB is used to study the effect of the number of POD basis elements. The same study was performed with the stationary velocity field. One or two basis elements for each component of the velocity can lead to the lowest reconstruction errors.

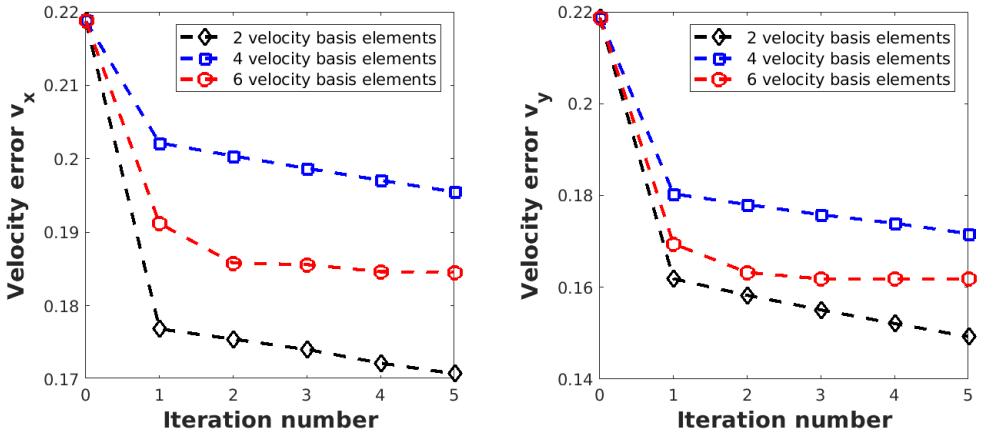

(a) Velocity error along x

(b) Velocity error along y

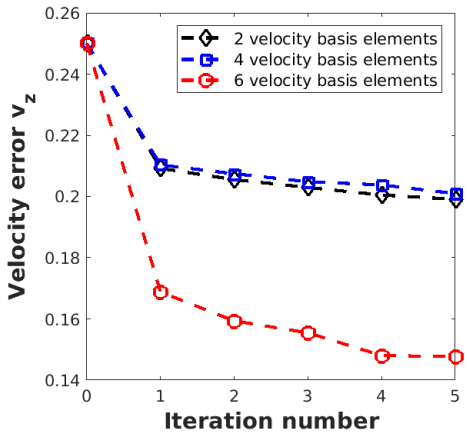

(c) Velocity error along z

Figure 2.5: The average reconstruction velocity component error curves of different velocity basis elements numbers with non-stationary velocity field using POD.

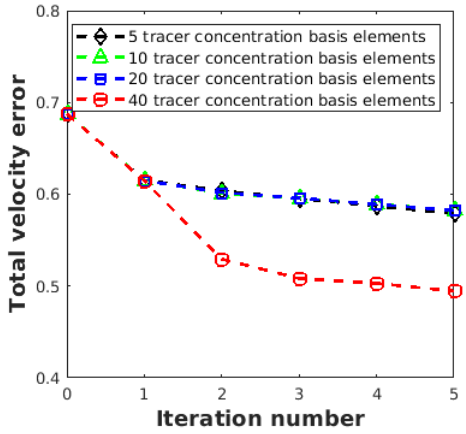

(a) Velocity error

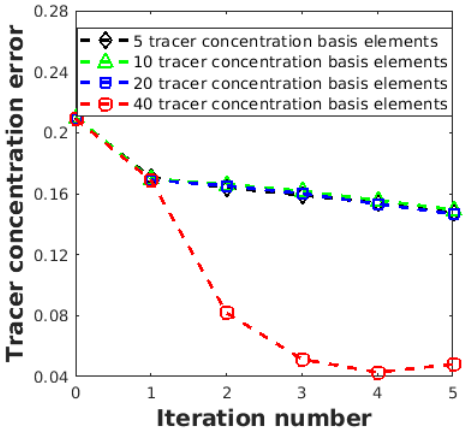

(b) Tracer concentration error

Figure 2.6: The average reconstruction error curves of different tracer concentration basis elements with non-stationary velocity field using POD.

2.5.1.2 POD basis elements analysis of tracer concentration

Non-stationary velocity condition Keeping 6 velocity basis elements and 2 adjoint variable basis elements, the number of POD basis elements of tracer concentration is explored in this work with a non-stationary velocity state, as shown in Figure 2.6.

Generally speaking, as the iteration number increases, the velocity error and tracer concentration error tend to decrease. In particular, the significant finding is that the large number of basis elements 40 can decrease the reconstruction error for both velocity and tracer concentration fields. The impact on the error is small for few basis elements, less than 20. Meanwhile, in order to better understand the trend of velocity error, the velocity component errors are shown in Figure 2.7. The trends are evidently similar when examining the errors for various velocity components. The figures show decreasing velocity error curves for each component and the optimal number of basis elements for the tracer concentration is 40.

Thus, it can be concluded that using more tracer concentration basis elements yields a favorable performance for blood flow reconstruction in non-stationary velocity situations. Additionally, employing a relatively small number of basis elements, particularly less than 20, has a small impact on the blood flow reconstruction in non-stationary velocity situations.

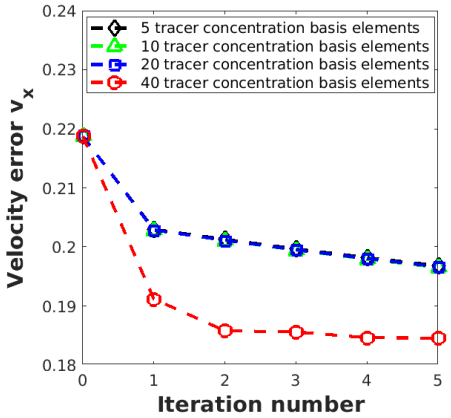

(a) Velocity error along x

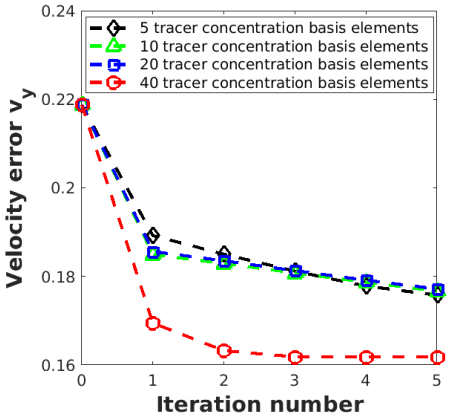

(b) Velocity error along y

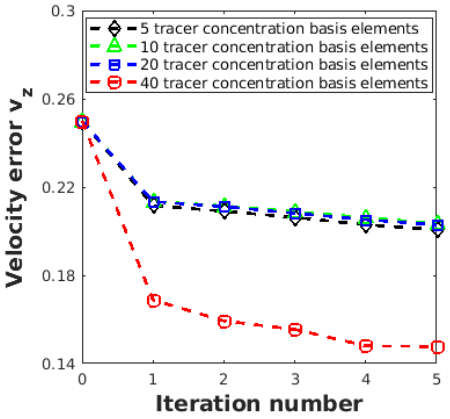

(c) Velocity error along z

Figure 2.7: The average reconstruction velocity component error curves of different tracer concentration basis elements with non-stationary velocity field using POD.

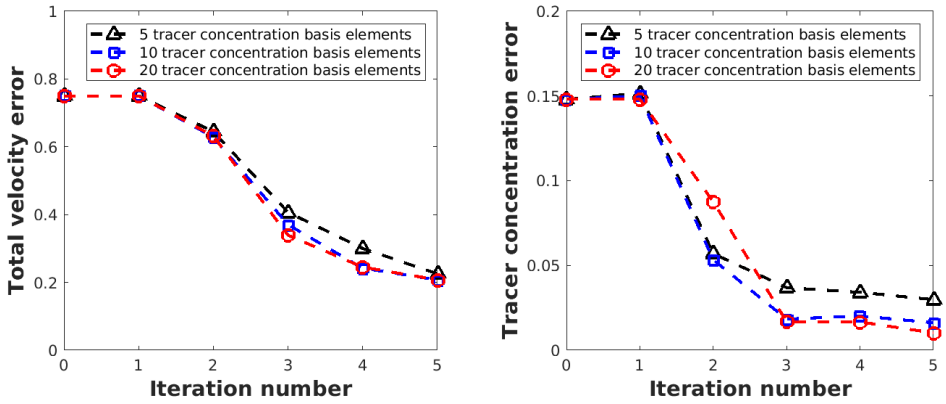

(a) Velocity error (b) Tracer concentration error

Figure 2.8: The average reconstruction error curves of different tracer concentration basis elements with stationary velocity field using POD.

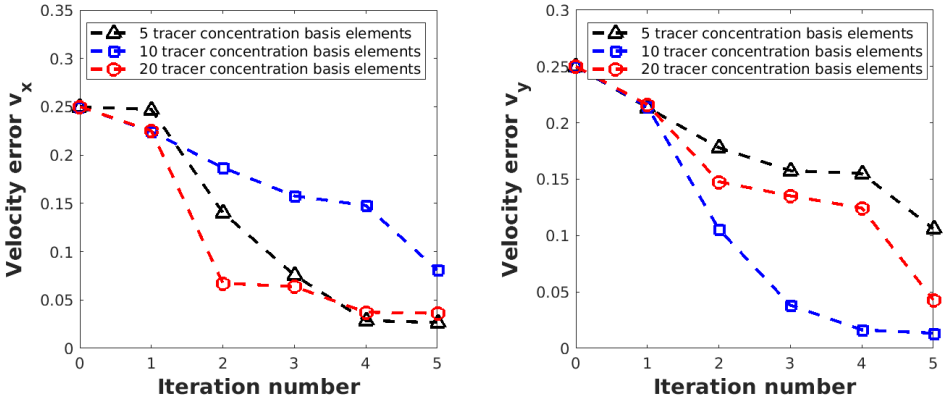

(a) Velocity error along x (b) Velocity error along y

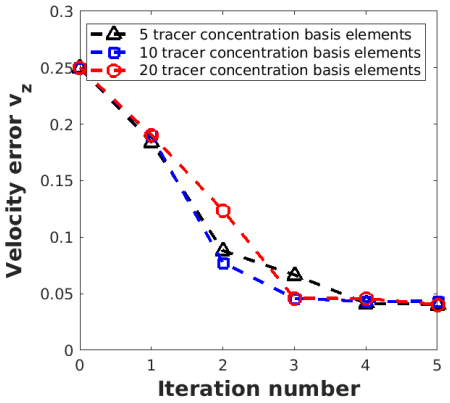

(c) Velocity error along z

Figure 2.9: The average reconstruction velocity component error curves of different tracer concentration basis elements with stationary velocity field using POD.

Stationary velocity condition For the stationary velocity condition, we have also studied the effect of the number of tracer concentration basis elements, with the 2 velocity basis elements with 4 adjoint variable basis elements fixed. The reconstruction error curves are presented in the following Figure 2.8. A continuous decrease is found in the reconstructed velocity error and a decreasing trend is generally found for the tracer concentration error.

The utilization of more basis elements can result in a small velocity error and a low tracer concentration error as well. Additionally, the velocity component error curves are given with 5 iterations and the decrease of the velocity component error can be seen in Figure 2.9.

In conclusion, using 20 tracer concentration basis elements can result in small reconstruction errors for blood flow reconstruction for stationary velocity conditions.

2.5.1.3 POD basis elements analysis of adjoint variables

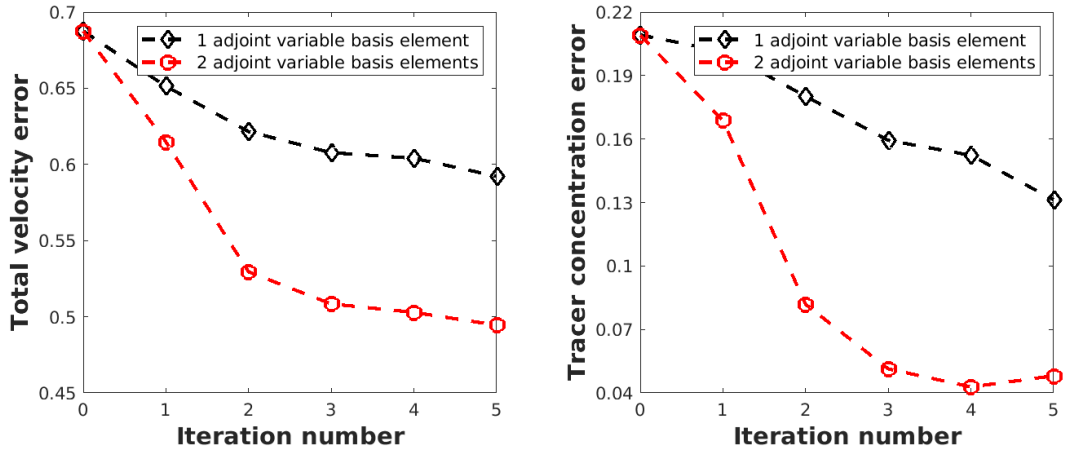

(a) Velocity error (b) Tracer concentration error

Figure 2.10: The average reconstruction error curves of different adjoint variable basis elements with non-stationary velocity field using POD.

Non-stationary velocity condition In this context, retaining the 6 velocity basis elements and 40 tracer concentration basis elements, the impact of the number of adjoint variable basis elements is investigated to study the blood flow reconstruction. The reconstruction error curves of different numbers of adjoint variable basis elements will be shown to explore the impact of the number of POD basis elements.

As we can see in Figure 2.10, we find a decrease in velocity error and tracer concentration error when the iteration number increases. Moreover, using two adjoint variable basis elements for projection into the transport equation and adjoint equation can lead to a remarkable reduction in reconstruction errors compared with a single adjoint variable basis element.

Additionally, the velocity component errors display a similar trend as the total velocity error shown in Figure 2.11.

So, we can make a short conclusion that using two adjoint variable basis elements, we can obtain lower reconstruction errors for achieving better blood flow reconstruction results in non-stationary velocity conditions. It turns out that the number of adjoint variable basis elements plays an important role in blood flow reconstruction in non-stationary velocity states.

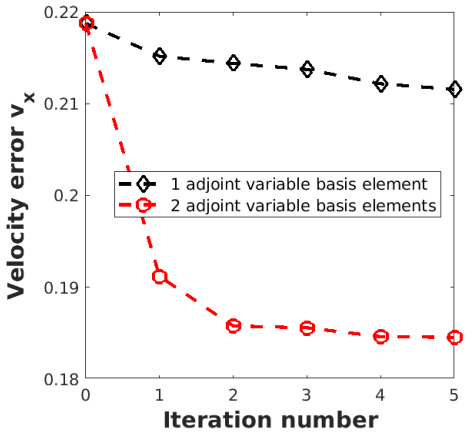

(a) Velocity error along x

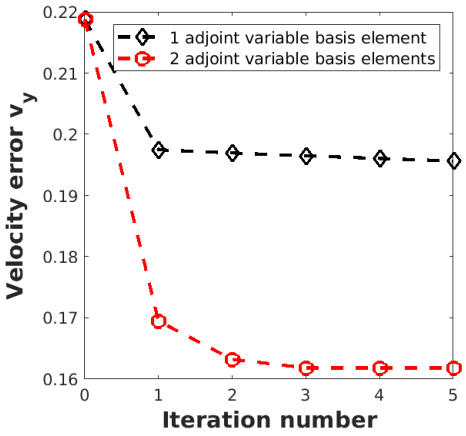

(b) Velocity error along y

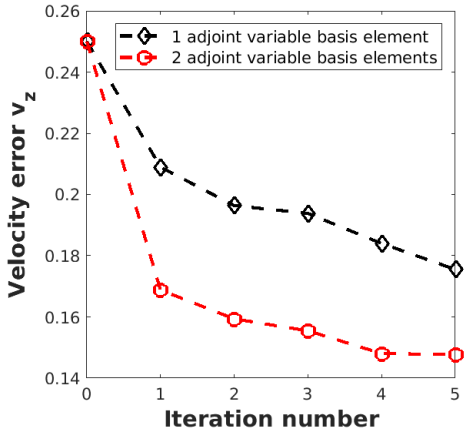

(c) Velocity error along z

Figure 2.11: The average reconstruction velocity component error curves of different adjoint variable basis elements with non-stationary velocity field using POD.

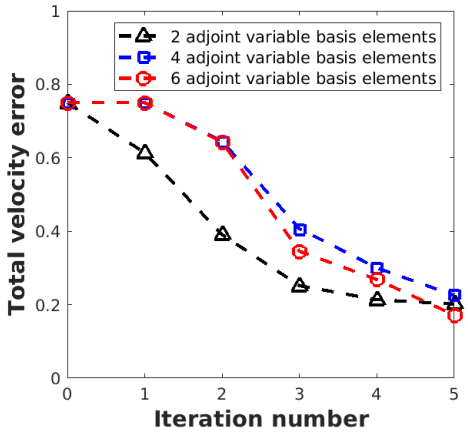

(a) Velocity error

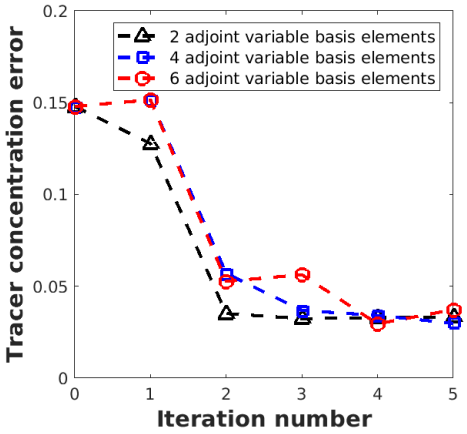

(b) Tracer concentration error

Figure 2.12: The average reconstruction error curves of different adjoint variable basis elements with stationary velocity field using POD.

Stationary velocity condition Keeping 2 velocity basis elements and 5 tracer concentration basis elements, we study the impact of adjoint variable basis elements for stationary velocity condition. In Figure 2.12, it can be found that the reconstructed velocity error shows a decrease when increasing the number of adjoint variable basis elements. Using 6 adjoint variable basis elements and 4 adjoint variable basis elements can result in a relatively small velocity error and a lower tracer concentration error. The velocity error in each component is presented and a decrease in the velocity error for each component can be observed in Figure 2.13. Furthermore, using 4 adjoint variable basis elements and 6 adjoint variable basis elements, we can obtain a lower velocity error along the x component and y component respectively. However, a small impact of the adjoint variable basis elements along the z-axis is observed.

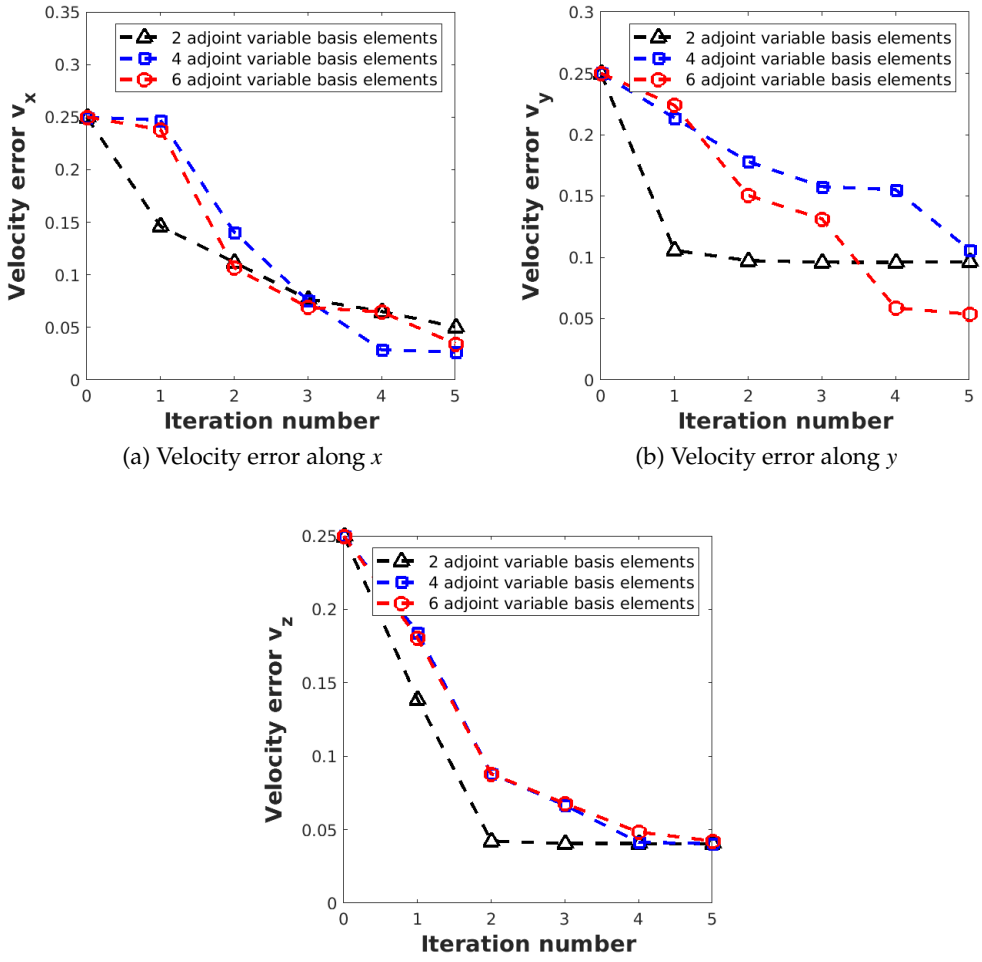

(a) Velocity error along x

(b) Velocity error along y

(c) Velocity error along z

Figure 2.13: The average reconstruction velocity component error curves of different adjoint variable basis elements with stationary velocity field using POD.

We come to the conclusion that using 6 adjoint variable basis elements, we can achieve a small velocity error, and using 4 adjoint variable basis elements, we can obtain a lower tracer concentration error for blood flow reconstruction in stationary velocity conditions.

2.5.1.4 Summary

In this subsection, we explore the impact of the number of POD basis elements for the velocity field, tracer concentration field, and adjoint variable for blood flow reconstruction. Non-stationary velocity and stationary velocity fields are especially investigated to find the impact of the number of POD basis elements.

In the non-stationary velocity state, the test case remains the inlet velocity of 0.45m/s, outlet pressure of 500Pa for solving the Navier-Stokes equation, and the inlet injected tracer concentration of 0.5kg/m3 for the transport equation and adjoint equation, with a noise level of 10 dB is considered in this work. The number of velocity basis elements studied falls within the range of [2, 6], while the range for tracer concentration basis elements is between 5 and 40, and for adjoint variable basis elements, it is within the range of [1, 2]. Generally speaking, the number of POD basis elements plays a significant role in decreasing the velocity error. It can be found that using 6 velocity basis elements can result in a small velocity error. Moreover, the large value of tracer concentration basis elements of 40 exhibits good performance to reduce the reconstruction errors for blood flow reconstruction. Additionally, using 2 adjoint variable basis elements, we obtain low reconstruction errors.

The stationary velocity state is also considered in this work and the test cases investigated share the same initial and boundary conditions as the non-stationary velocity situation except for a different noise level of 0 dB. In this work, to evaluate the impact of the POD basis elements, the number of velocity basis elements, tracer concentration basis elements, and adjoint variable basis elements are studied within the ranges of [1, 2], [5, 20], [2, 6] respectively. It can turn out that using one or two velocity basis elements can yield a lower velocity error for this steady simulation condition, as long as the full basis elements of tracer concentration and adjoint variable are maintained. In addition, another finding indicates that using 20 tracer concentration basis elements, along with 2 velocity basis elements and 4 adjoint variable basis elements, can lead to small reconstruction errors for blood flow reconstruction. Furthermore, retaining 2 velocity basis elements and 5 tracer concentration basis vectors, and 6 adjoint variable basis elements can achieve a small velocity error. However, in stationary velocity conditions, using 4 adjoint variable basis elements can lead to a lower tracer concentration error for blood flow reconstruction.

Thus, we can conclude that the number of POD basis elements plays an important role in blood flow reconstruction for both unsteady velocity states and steady velocity conditions. To estimate the effectiveness of the POD-adjoint method, the comparison with the full-order adjoint method will be considered.

2.5.2 POD-adjoint method compared with full order approximation

In this section, to evaluate the effectiveness of the POD-adjoint method, we use the same cases to compare the two methods: the model reduction POD-adjoint approach and the classical adjoint method with the non-stationary velocity conditions and the stationary velocity states. The boundary and initial conditions are chosen as follows: inlet velocity of 0.55m/s, outlet pressure of 750Pa for solving the Navier-Stokes equation, and inlet injected tracer concentration of 1.1kg/m3 for the transport equation.

2.5.2.1 Non-stationary velocity condition

In this section, we summarize the results obtained with a non-stationary velocity field. It must be noted that we are not considering the regimes where the blood flow states become chaotic and turbulent. We show the reconstruction results for the velocity and tracer concentration

corresponding to $\mu_1 = (0.55m/s, 500Pa)$ and an inlet tracer concentration of $\mu_2 = 1.1kg/m^3$. The velocity field is calculated with the non-stationary Navier-Stokes equation. The evolution with the iterations of the relevant quantitative metrics, root mean square error (RMSE) for the velocity, and tracer concentration are presented in Figure 2.14 for different noise levels and the two reconstruction approaches. The reconstruction errors for velocity fields and tracer concentration are remarkably reduced with the proposed POD-adjoint approach and it clearly outperforms the full order approximation (FOA) method.

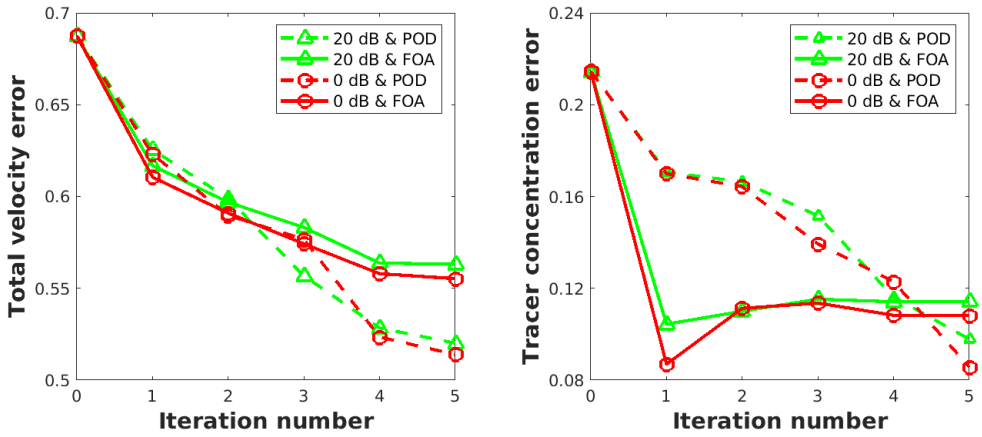

(a) Velocity error (b) Tracer concentration error

Figure 2.14: The average reconstruction error curves of POD and FOA in the non-stationary velocity condition. Initial test velocity 0.55 m/s, outlet pressure 500 Pa.

Noise level (dB)	POD	FOA
0	0.086	0.108
20 dB	0.098	0.114

Table 2.1: Comparison of tracer concentration reconstruction errors for POD and FOA for two noise levels within non-stationary velocity conditions. Initial test velocity 0.55 m/s, outlet pressure 500 Pa.

Noise level (dB)	POD	FOA
0	0.514	0.555
20 dB	0.520	0.563

Table 2.2: Comparison of velocity reconstruction errors for POD and FOA for two noise levels within non stationary velocity conditions. Initial test velocity 0.55 m/s, outlet pressure 500 Pa.

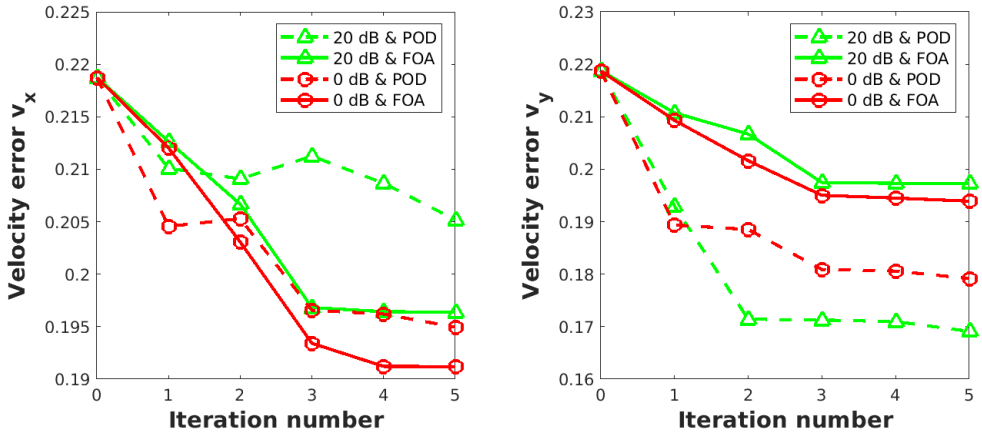

(a) Velocity error along x

(b) Velocity error along y

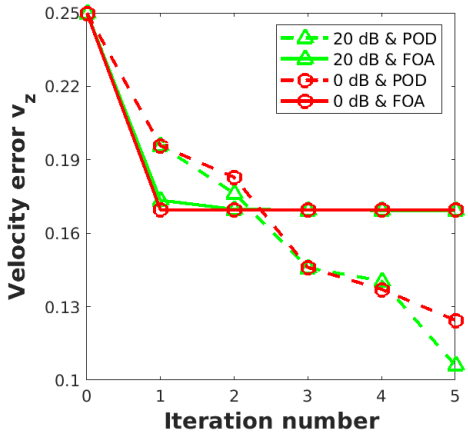

(c) Velocity error along z

Figure 2.15: The average reconstructed velocity component error curves of POD and FOA in the non-stationary velocity condition.

Direction	Noise level (dB)	POD	FOA
X	0	0.195	0.191
X	20	0.205	0.196
Y	0	0.179	0.194
Y	20	0.169	0.197
Z	0	0.1215	0.170
Z	20	0.106	0.169

Table 2.3: Comparison of velocity components reconstruction errors for POD and FOA for two noise levels within non-stationary velocity conditions. Initial test velocity 0.55 m/s, outlet pressure 500 Pa.

In Figure 2.15 a, a slightly lower reconstruction velocity error along x axis can be obtained by using the full-order approximation method. Figure 2.15 b displays that using the POD

method we can decrease the velocity error along the y component. The largest decrease is obtained for the z component of the velocity in Figure 2.15 c. The reconstruction errors are summarized in Tables 2.1, 2.2, and 2.3. The accuracy of the reconstruction of the z component of the velocity and of the tracer concentration is weakly dependent on the noise level, for the noise levels investigated. The POD methodology introduced can be used for more challenging inverse problems such as those arising with time-dependent velocity fields.

2.5.2.2 Stationary velocity condition

In order to describe the results with a steady velocity field, we detail the reconstruction results for the velocity and tracer concentration fields obtained with $\mu_1 = (0.55m/s, 500Pa)$ and an inlet tracer concentration of $\mu_2 = 1.1kg/m^3$.

Figures 2.16 and 2.17 display the evolution with the iterations of the RMSE for the tracer concentration, for the velocity components along different directions and for the velocity norm, for various noise levels. These figures compare the errors as a function of the iterations for POD approximation and full order approximation simulations.

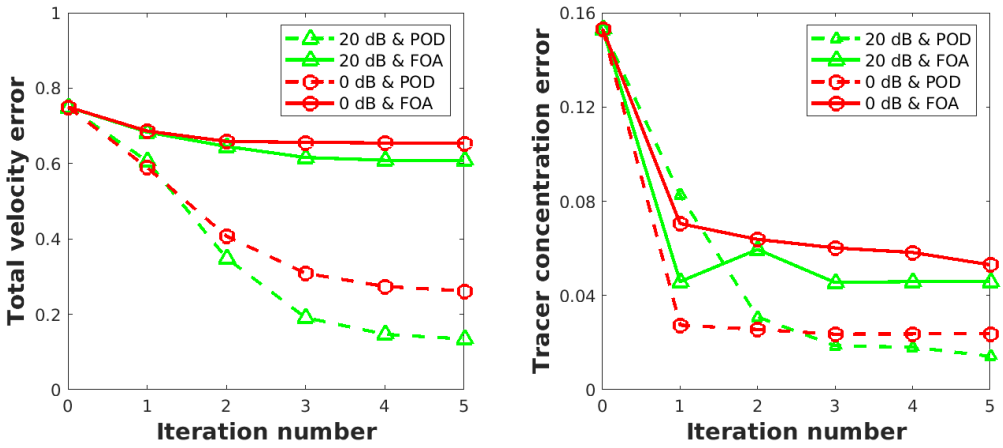

(a) Velocity error (b) Tracer concentration error

Figure 2.16: The average reconstruction error curves of POD and FOA in the stationary velocity condition.

Noise level (dB)	POD	FOA
0	0.024	0.053
20	0.014	0.046

Table 2.4: Comparison of tracer concentration reconstruction errors for POD and FOA for two noise levels within stationary velocity conditions. Initial test velocity 0.55 m/s, outlet pressure 500 Pa.

We summarize the reconstruction errors in Tables 2.4, 2.5, and 2.6 for the tracer concentration, the velocity components, and the velocity norm for the two noise levels considered and the two reconstruction methodologies. It should be noted that similar reconstruction errors are obtained for the range of parameters μ investigated.

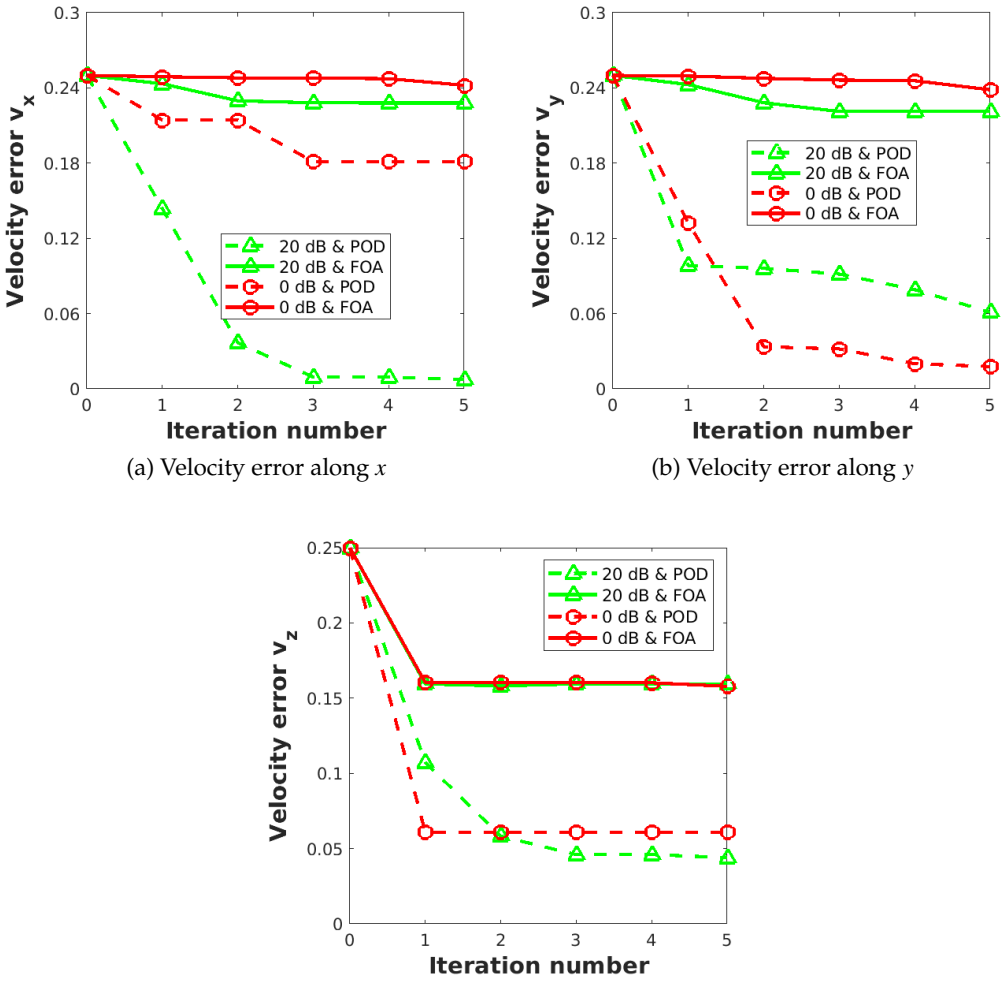

(a) Velocity error along x

(b) Velocity error along y

(c) Velocity error along z

Figure 2.17: The average reconstructed velocity component error curves of POD and FOA in the stationary velocity condition.

Noise level (dB)	POD	FOA
0	0.262	0.653
20	0.135	0.609

Table 2.5: Comparison of velocity reconstruction errors for POD and FOA for two noise levels within stationary velocity conditions. Initial test velocity 0.55 m/s, outlet pressure 500 Pa.

With the POD method, the reconstruction errors for the tracer concentration and the velocity display large and fast reductions and the method is able to offer a good approximation of these unknown fields. The reconstruction accuracy for the tracer concentration and the z axis component of the velocity decreases when the noise level on the Radon projections increases. Good reconstruction results for the transverse components of the velocity can be obtained. It can be found that these components are less sensitive to the noise corrupting the Radon projections. With the proposed POD approach and the partial differential equation constraint,

Direction	Noise level (dB)	POD	FOA
X	0	0.181	0.242
X	20	0.008	0.228
Y	0	0.018	0.239
Y	20	0.061	0.221
Z	0	0.061	0.158
Z	20	0.044	0.159

Table 2.6: Comparison of velocity components reconstruction errors for POD and FOA for two noise levels within stationary velocity conditions. Initial test velocity 0.55 m/s, outlet pressure 500 Pa.

we can obtain the simultaneous reconstruction of the axial and transverse components of the velocity. When more basis functions are contained in the POD method, the errors stagnate and the basis can be considered optimal for the inversion for the range of μ values investigated.

The proposed POD approach outperforms the full order approximation method. The errors for the tracer concentration and velocity field are much decreased with respect to the ones obtained with the classical finite element simulations.

Using the POD-based method can lead to a high offline cost. The offline cost for a reduced order model consists of obtaining the model snapshot solutions and of the calculation cost for the POD bases from the snapshots. To allow large-scale simulations, the offline basis construction for the model reduction could be performed with parallel computation on distributed-memory clusters. Without this parallel implementation, the repeated solution of the full-scale system of equations requires 20 h on a modern HPC cluster with 10 processors, and each of the snapshots is around 5 M.

Information	POD	FOA
Mesh size	-	56845
Degrees of freedom	3600	56845^5
Simulation time for transport equation (s)	10^{-2} (online)	0.9
Simulation time for adjoint method (s)	35	450

Table 2.7: Comparison of the number of degrees of freedom, average simulation time for the transport equation, and for one iteration of the online step of the whole adjoint method implemented with POD and FOA and a stationary velocity field.

Yet, it costs much less for online time than the full-order simulation. The number of degrees of freedom and the average simulation times required for the transport equation and a single iteration of the entire adjoint method are summarized in Table 2.7. The speed-up index is defined as the ratio of the computation time of the FOA solution divided by the computation time of the reduced basis approximation. It can be evaluated to 90 for the forward step and 15 for the inversion method with a remarkable decrease in the number of degrees of freedom. With the basis numbers considered and our implementation, the computational time is obviously reduced with the POD approach. It is the most suitable approach for applications where the velocity field has to be estimated multiple times and for real-time applications. The results of this section thus clearly demonstrate the effectiveness of the proposed POD methodology to address the inverse problem.

2.5.3 Blood flow reconstruction for non-stationary velocity condition

In this section, the non-stationary velocity field and stationary velocity field are both studied to demonstrate the effectiveness of blood flow reconstruction for each velocity component field and for the tracer concentration field. In addition, the reconstruction error of the tracer concentration and the z component of the reconstructed velocity have been considered to compare with the full-order approximation method.

2.5.3.1 Velocity field reconstruction

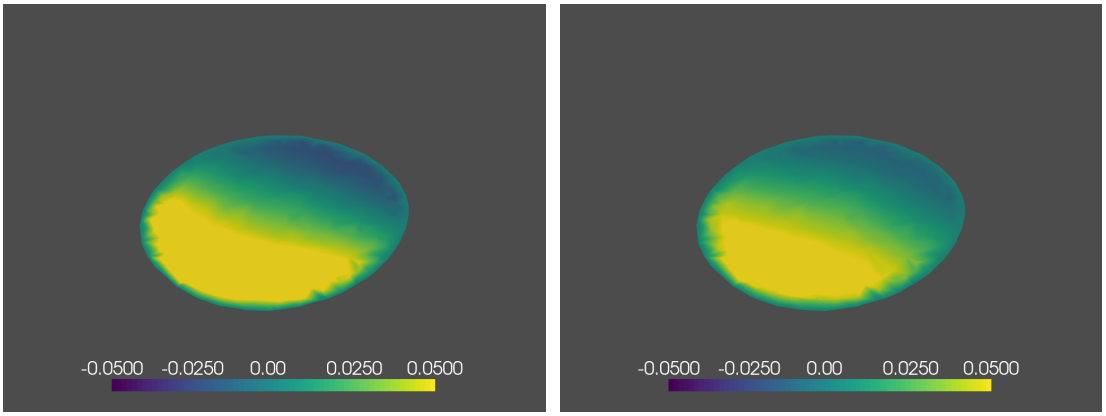

(a) Ground truth velocity field along x component (b) Reconstructed velocity field along x component

Figure 2.18: The velocity field along x component using the POD method for non-stationary velocity for $z = 0.155$ and $t = 0.05$s, for a PPSNR = 20 dB.

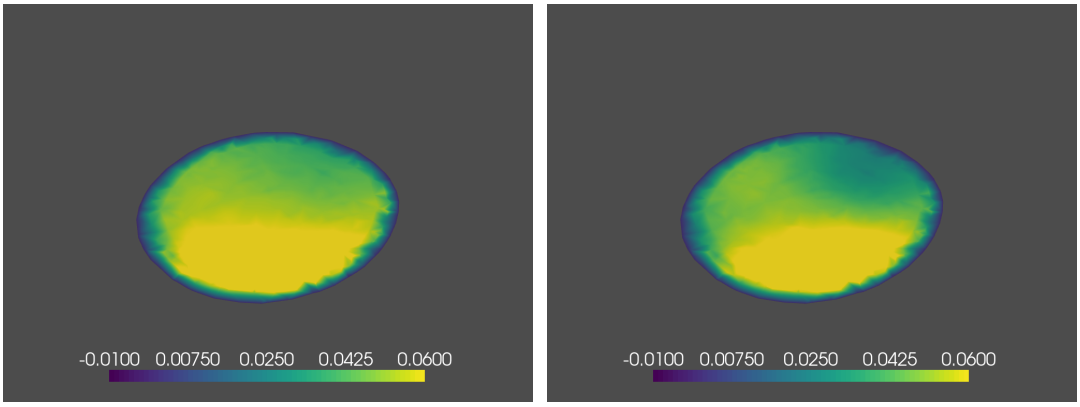

(a) Ground truth velocity field along y component (b) Reconstructed velocity field along y component

Figure 2.19: The velocity field along y component using the POD method for non-stationary velocity for $z = 0.155$ and $t = 0.05$s, for a PPSNR = 20 dB.

Here, the velocity field components distributions are shown in Figures 2.18, 2.19, 2.20. The reconstructed velocity component fields are similar to the ground truth velocity component fields, especially the reconstructed higher positive domain with highlighted yellow colors. The error maps of reconstructed velocity along z using the POD method and FOA approach are also

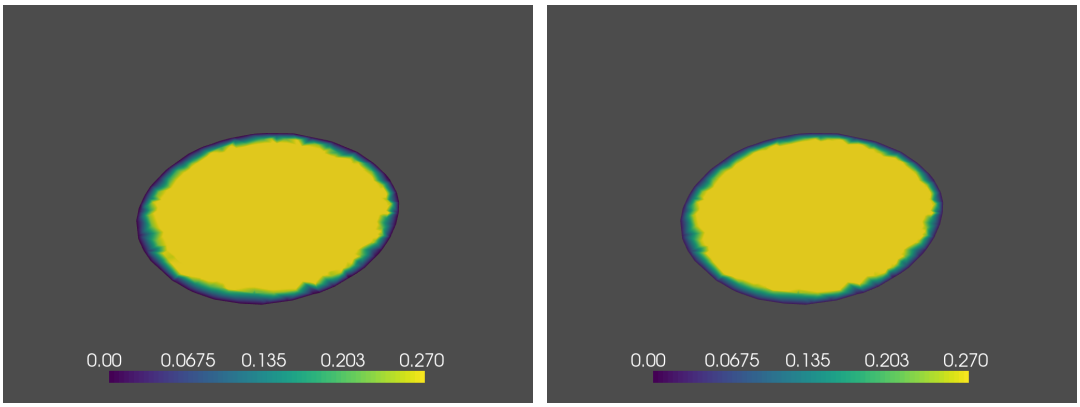

(a) Ground truth velocity field along z component (b) Reconstructed velocity field along z component

Figure 2.20: The velocity field along z component using the POD method for non-stationary velocity for $z = 0.155$ and $t = 0.05$s, for a PPSNR = 20 dB.

displayed for comparison of the reconstruction methodologies in Figure 2.21. It is obvious that there are fewer negative values in the center region when using the POD method compared to the full-order approximation method and a good reconstruction on the border with the POD method. Thus, these figures confirm that good reconstruction results are obtained by employing the POD method and this result corresponds to the reconstruction error curves shown before. Next, we will display the tracer concentration field reconstruction.

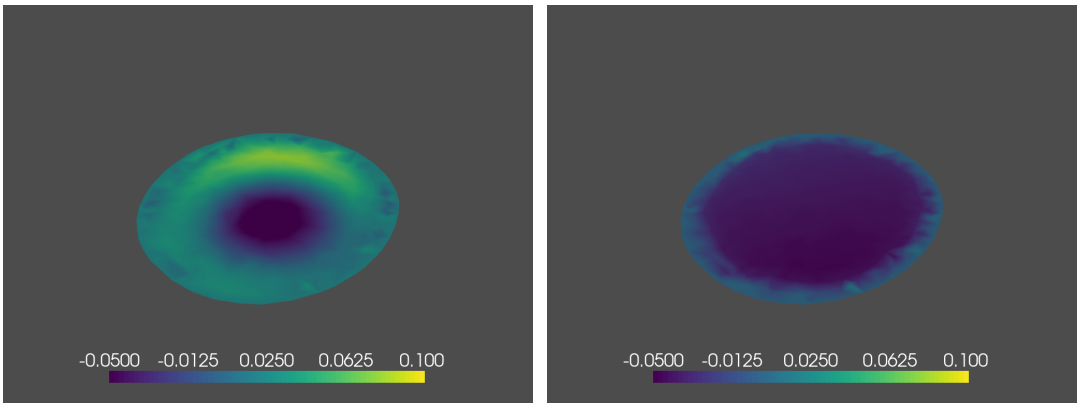

(a) POD method (b) Full order approximation

Figure 2.21: Error map of reconstructed velocity along z with POD or full order approximation for non-stationary velocity for $z = 0.155$ and $t = 0.05$s, for a PPSNR = 20 dB.

2.5.3.2 Tracer concentration field reconstruction

The reconstructed tracer concentration field distributions related to the velocity field closely resemble the ground truth displayed in Figure 2.22. Furthermore, the error maps of the tracer concentration field are displayed to highlight the differences between the POD method and the FOA approach in Figure 2.23. It is noticeable that we obtain a uniform error map distribution for the POD method while there is a region with large negative values for the FOA method. Hence,

it becomes obvious that the POD scheme produces a well-reconstructed tracer concentration field, improving the performance of the FOA strategy.

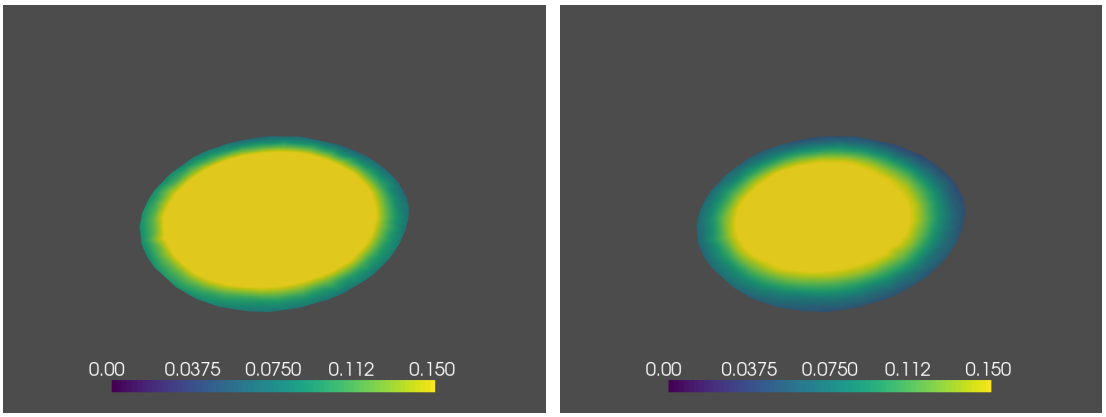

(a) Ground truth tracer concentration (b) Reconstructed tracer concentration

Figure 2.22: The tracer concentration field using the POD method for non-stationary velocity for $z = 0.155$ and $t = 0.05$s, for a PPSNR = 20 dB.

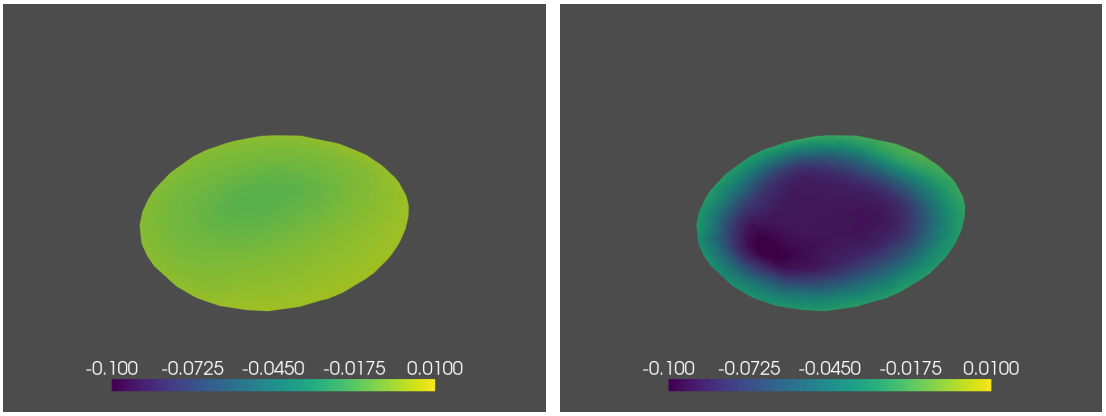

(a) POD method (b) Full order approximation

Figure 2.23: Error map of tracer concentrations reconstructed with POD and full order approximation for non-stationary velocity for $z = 0.155$ and $t = 0.05$s, for a PPSNR = 20 dB.

2.5.4 Blood flow reconstruction for stationary velocity condition

2.5.4.1 Velocity field reconstruction

Some examples of reconstructed velocity fields w along the z-axis obtained with the POD-based approach are displayed in Figure 2.26 together with the ground truth velocity for a low noise level, for selected simulation times and cross-sections. Similar figures are displayed for the component along the y and x components in Figure 2.24 and Figure 2.25 respectively. These figures show that good reconstruction results are obtained with the proposed approach. Figure 2.27 compares the error maps for the velocity for the POD and the full-order approximation methods.

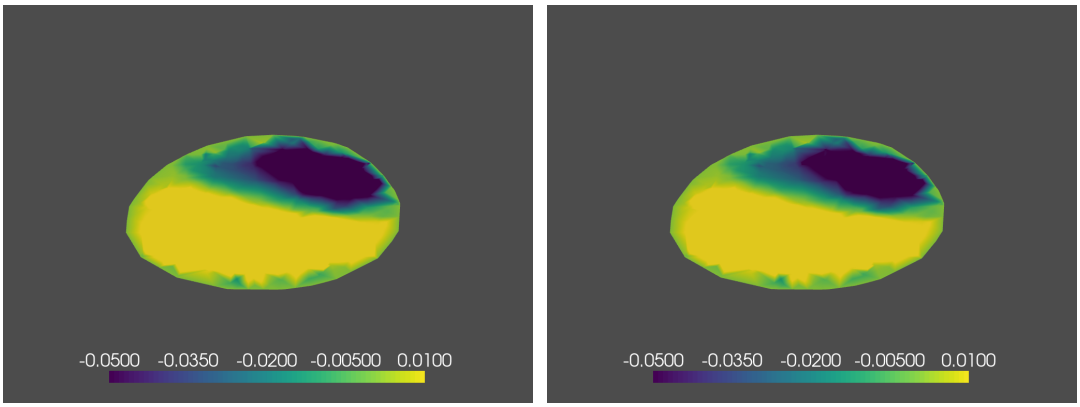

(a) Ground truth velocity field along x component (b) Reconstructed velocity field along x component

Figure 2.24: The velocity field along x component using the POD method for stationary velocity for $z = 0.125$, for a PPSNR = 20 dB.

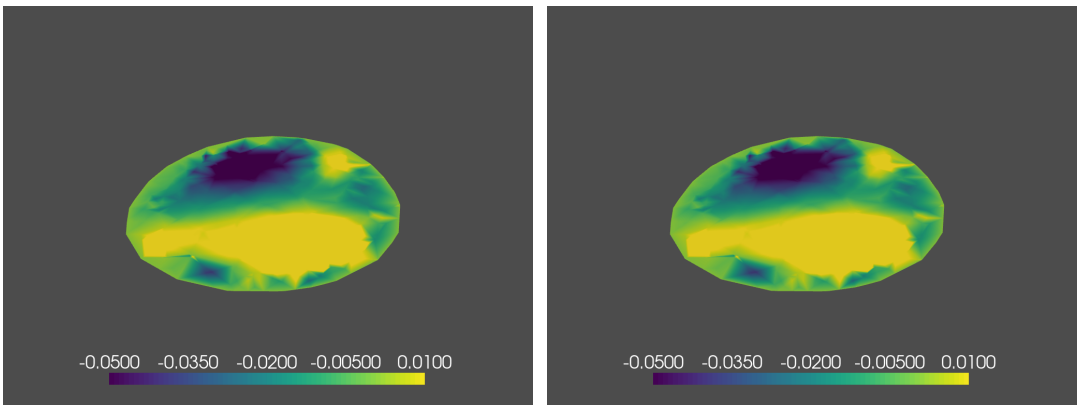

(a) Ground truth velocity field along y component (b) Reconstructed velocity field along y component

Figure 2.25: The velocity field along y component using the POD method for stationary velocity for $z = 0.125$, for a PPSNR = 20 dB.

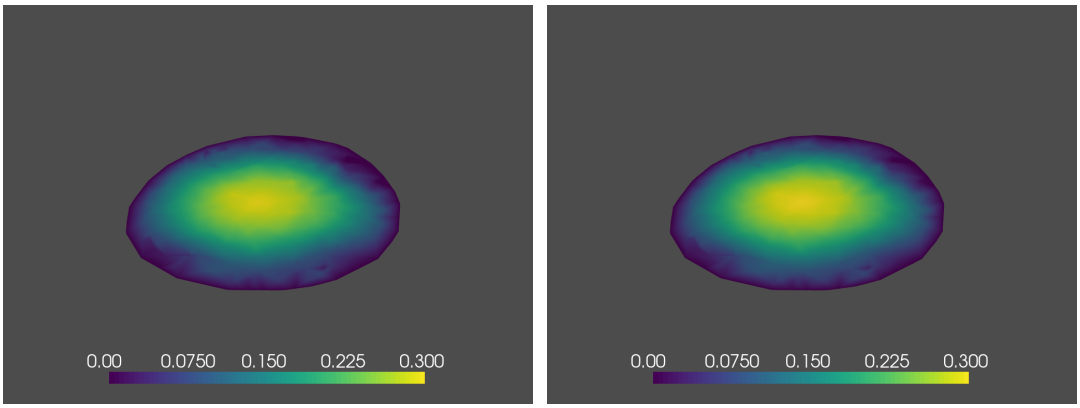

(a) Ground truth velocity field along z component (b) Reconstructed velocity field along z component

Figure 2.26: The velocity field along z component using the POD method for stationary velocity for $z = 0.125$, for a PPSNR = 20 dB.

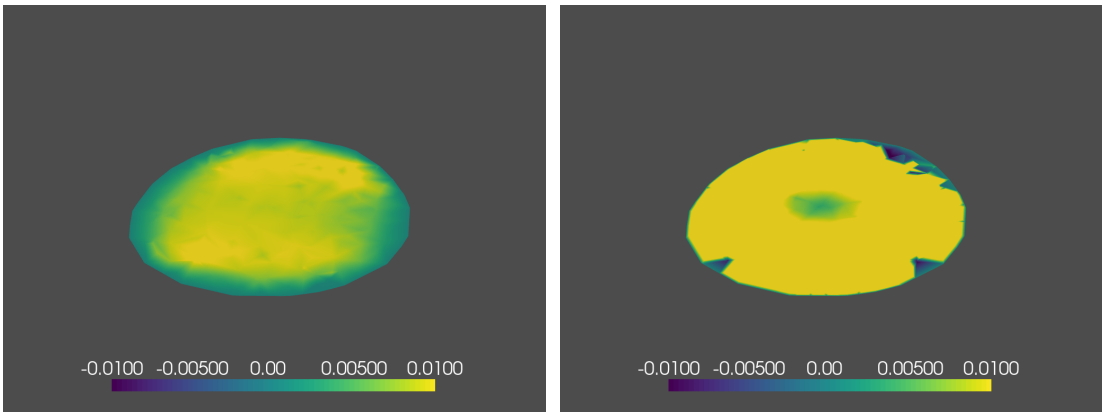

(a) POD method (b) Full order approximation

Figure 2.27: Error map of reconstructed velocity along z with POD or full order approximation for stationary velocity for $z = 0.125$, for a PPSNR = 20 dB.

2.5.4.2 Tracer concentration field reconstruction

Cross-sections of the ground truth tracer concentration and the similar reconstructed tracer concentration are displayed below in Figure 2.28. Moreover, the error maps of tracer concentration fields are provided for understanding the difference between the POD method and the FOA approach shown in Figure 2.29. It can be seen in Figures 2.21 and 2.29 that the POD-based inversion method effectively reduces reconstruction errors on the boundaries of the vessel. As illustrated in these figures, the full-order approximation simulations have a non-optimal behavior, and the optimization problem is trapped in local minima away from the optimal solution. Increasing the number of parameters for the unknown field does not improve the error. This result is related to the increased complexity of the optimization problem. Therefore, it is advantageous to use reduced bases to simplify the complexity of the optimization and to achieve a better approximation of the solution in such scenarios.

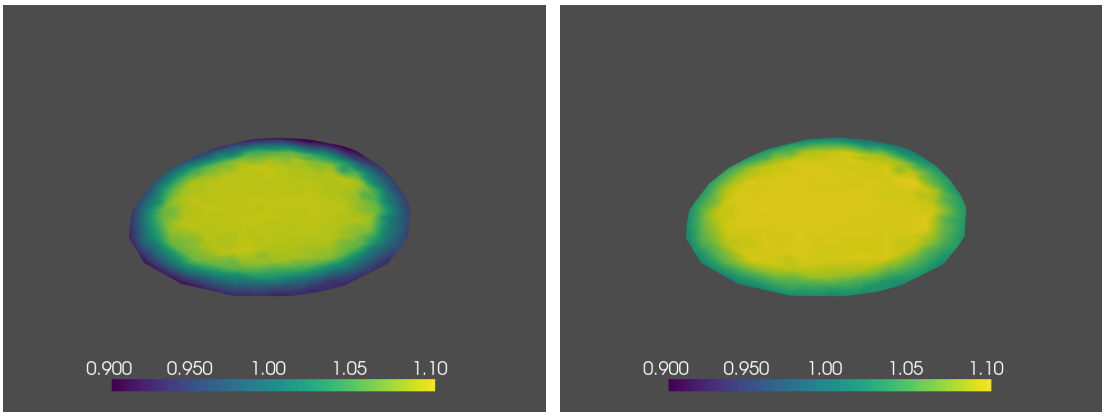

(a) Ground truth tracer concentration (b) Reconstructed tracer concentration

Figure 2.28: The tracer concentration field using the POD method for stationary velocity for $z = 0.125$ and $t = 0.05$s, for a PPSNR = 20 dB.

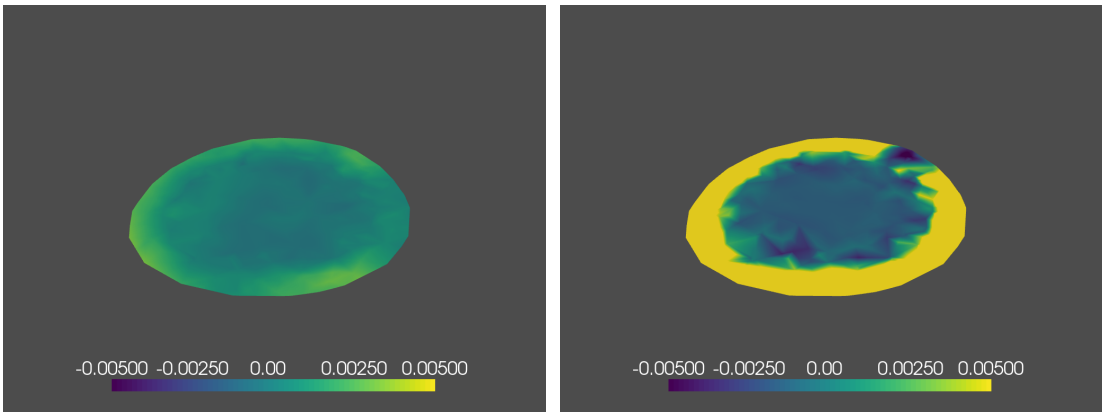

(a) POD method (b) Full order approximation

Figure 2.29: Error map of tracer concentrations reconstructed with POD and full order approximation for stationary velocity for $z = 0.125$ and $t = 0.05$s, for a PPSNR = 20 dB.

2.5.5 Discussion

The highlight of this study was to demonstrate by implementing several realistic cases, the performance of the algorithm to infer the velocity field from the Radon projections by leveraging the known underlying PDE. Through the application of the POD approach, it enables us to make highly accurate predictions for stationary or non-stationary velocity flows. We have also dealt with the inverse problem with relatively high noise levels but the dominant blood flow features can be extracted by dimensional reduction. We have shown that the POD methodology exhibits good numerical performance for stationary and non-stationary velocity fields. The inversion method obtained with the POD decompositions combined with Galerkin projection is computationally efficient and it leads to lower reconstruction errors compared to methods based on full-order approximation. It is also a suitable approach to be used in order to reduce the computational costs. When using the conventional full-order approximation, one needs to tackle significantly more costly and high-dimensional optimization problems. In such cases, the information on the tracer concentration and its gradients in the simulation domain and near its boundaries is not sufficient to yield a satisfactory solution for the velocity field. In contrast, the POD approach is capable of accurately reconstructing the velocity fields even without having access to full observations of the tracer concentration fields and without prior knowledge of initial and boundary conditions. Furthermore, the boundary conditions for the velocity are more accurately recovered.

The presented approach is promising for any application addressing incompressible transient or turbulent fluid dynamic problems that demand real-time computing and visualization. It can be useful in fluid mechanics and hydrology where the spatially and temporally underlying physical processes are heterogeneous. We primarily aim to characterize blood flow in vessels for clinical applications. Evaluating the hemodynamics of the blood inside the cardiovascular system has the potential application for patients with cardiovascular diseases. Yet, some applications can be found in the realm of engineering physical problems involving industrial viscous flows.

We can note several shortcomings of the proposed POD approach. The transformation applied to obtain the POD coefficients is an orthogonal linear transformation. Linear projection-based reduced order methods may not be efficient for dimension reduction for complex flow patterns because the number of required modes increases significantly. It is an assumption that

the blood is a Newtonian fluid. Whereas the blood can be assumed to be a Newtonian fluid in large vessels, its viscosity varies with the blood flow rate in smaller arteries and capillaries. For medical conditions such as stenosis, a non-Newtonian model may be outperformed over a Newtonian model. More complex physics should be contained in models to account for realistic states, such as non-Newtonian blood behavior and visco-elastic properties of the arterial wall. In addition, a variation of the domain/structure and fluid–structure interaction problems are not considered in this study. More generally, we have assumed that the partial differential equation and operators governing the fluid dynamics and tracer propagation are known during the projection process. Another possible drawback of the investigation is the utilization of synthetically generated data.

A simple generalization of the approach can be obtained by replacing the Navier–Stokes equation with a nonlinear non-Newtonian equation. The proposed approach based on the POD can be applied for higher Reynolds numbers but with more POD basis elements. We could also extend the approach to encompass an efficient geometrical parametrization for dynamic domains since our method exploits a parametrized formulation of the problem. Therefore, the approach could be generalized to varying domains with fluid–structure interactions. This work leaves many interesting research perspectives open in the ongoing work. Many concepts from deep learning can be widely used with classical approaches to address complex inverse problems involving dynamical systems. It is available to couple model order reduction and deep learning neural networks for parametric PDEs (Bhattacharya et al., 2021). The reduced bases adopted in this work are sufficiently abundant and the projected model can provide the accurate solution of the inverse problem. Yet, it should be mentioned that the POD method may not be the optimal selection for dimension reduction. The fast development of deep learning technologies and autoencoders on function spaces may outperform the principal component analysis (PCA) type methodology proposed here. Neural network-based autoencoders have been studied as an alternative to nonlinear approximation because they can tackle a lot of limitations of linear projection techniques introduced by (Gonzalez and Balajewicz, 2018). They offer significant flexibility for the dimensionality reduction.

Generally, our geometry is precisely defined but the challenge we face is that the initial and boundary conditions for both the tracer concentration and the velocity field are not known accurately. Yet, there is an assumption that the tracer concentration field is known, follows a special physical law such as the transport equation described by a partial differential equation. The prior knowledge of the underlying physical law presents a prior that effectively regularizes the minimization procedure and allows us to address the inverse problem and reconstruct accurate velocity fields. In future works, we will study non-intrusive and purely data-driven methods.

2.6 Conclusion

In this work, we have considered a novel POD method for the velocity field reconstruction of the blood inside a vessel. The method is based on the propagation of a contrast agent and on the acquisition of Radon projections perpendicularly to the primary propagation direction. The PDE constraint modeling the transport of the contrast agent is applied to estimate the tracer concentration in the optimization problem. We leverage our previous solution of the inverse problem with the adjoint method. The full-order approximation is replaced by reduced-order approximations with POD for the tracer concentration, the velocity, and the adjoint variable fields. We demonstrate the effectiveness of this new methodology and its numerical performance on a simulation vessel phantom with a bifurcation for both stationary and non-stationary velocity flows based on the Navier–Stokes equations.

In this chapter, to demonstrate the effectiveness of these simulations using the POD method and we consider POD basis elements for the velocity field, tracer concentration field, and adjoint variable field for blood flow reconstruction. Non-stationary velocity and stationary velocity fields of blood flow are studied to find the impact of the number of POD basis elements.

With the non-stationary velocity condition, it is found that employing 6 velocity basis elements can suppress a large part of the velocity reconstruction error. The optimal number of basis elements for the tracer concentration is 40. Additionally, by employing 2 adjoint variable basis elements we can achieve lower reconstruction errors.

For the stationary velocity, the optimal number of basis elements is 2 for the velocity, 20 for the tracer concentration, and 6 for the adjoint variable to obtain small reconstruction errors.

To prove the efficiency of the POD method, the full-order approximation approach is also considered to reconstruct blood flow for comparison. With the non-stationary velocity field, it can be found that the accuracy of the reconstruction of the z component of the velocity and of the tracer concentration weakly depends on the noise level corrupting the Radon projections. The POD methodology can be considered for more complex inverse problems such as those arising from time-dependent velocity fields. On the other hand, for the stationary velocity field, the errors for the tracer concentration and velocity field are largely decreased with respect to the ones achieved by the classical finite element simulations. These differences are reflected in the velocity and tracer concentration field reconstructions. Using the POD method we can obtain a similar reconstructed velocity and tracer concentration field. From the error map, it can be seen the boundaries are well reconstructed. Additionally, computational online time is much decreased using the POD method in comparison with the FOA approach.

In short, good reconstruction results are achieved for the velocity and the tracer concentration by applying the proposed POD method. The proposed POD algorithms yield better results than the full-order approximation scheme. The computational cost is remarkably reduced and the accuracy is improved.

Chapter 3

Deep learning methods for blood flow reconstruction

In Chapter 1, we have already introduced the conventional adjoint method for solving the inverse problem with a partial differential equation as a constraint. Deep learning methods addressing inverse problems often exhibit notable improvements over traditional variational approaches, including rapid convergence and reduced calculation time. In this chapter, we will give some generalities about deep-learning methods.

Deep learning is a of part the machine learning field. A neural network can be seen as a set of layers and parameters as detailed below. In the past decade, the deep learning techniques has received widespread attention in some fields such as computer vision, semantic analysis, natural language processing, information retrieval, and customer relationship management. New fields have field have been explored in medical imaging with clinical applications reviewed by (Shinde and Shah, 2018; Mathew et al., 2021; Hazra et al., 2021). Especially, plenty of deep learning-based methods for solving inverse problems with medical imaging were reviewed by (McCann et al., 2017; Lundervold and Lundervold, 2019; Zhang and Dong, 2020; Ahishakiye et al., 2021; Li et al., 2021a; Yaqub et al., 2022). However, there are no studies of inverse problems for reconstructing blood flow velocity using the CT technique and deep learning approaches.

In the context of deep learning for inverse problems in medical imaging reconstruction, we consider deep learning methods to address the inverse problem with a PDE which is used to reconstruct blood flow velocity using the CT technique. Thus, the aim of this Chapter is to review some deep learning methods useful for blood flow reconstruction using the CT technique. We will cover deep learning methods including basic fully connected networks and Convolutional Neural Networks (CNN).

The structure of this Chapter will be given below. In subsection 3.1, we present the widely adopted deep learning technique will be presented. In subsection 3.2, we will present the deep learning methods for addressing the challenges of the tomographic inverse problem. In sub-section 3.3 will be given the problem statement first. In sub-section 3.4, the dataset generation methodology will be introduced including the generation of snapshots of the ground truth velocity, density, and Radon projections. We will focus on presenting the architectures of the networks with the POD-FC (POD-Fully connected) and POD-3D CNN in sub-section 3.5 and we will give the network details to explain how we implement the network training. In sub-section 3.6, we will test different time intervals, different noise levels, and various network training parameters such as the learning rate, the batch size, and the dropout rate in order to analyze the behavior of the various networks. Additionally, two cases with a low inlet velocity and higher inlet velocity will be given with 3D distributions displayed in various planes XY, XZ, and YZ to show the velocity reconstruction and the reconstruction errors. We also compare the

POD-DL method with the POD-adjoint method more quantitatively with the reconstruction errors and then discuss the clinical application and the limitations of the methods. At the end of this Chapter, we will give some concluding remarks in sub-section 3.7.

3.1 Deep learning techniques

In this section, the advantage of using deep learning techniques is summarized. Subsequently, fundamental concepts and components in deep learning will be detailed for a deeper understanding of deep learning. Moreover, two classic neural networks such as the fully connected networks and the Convolutional Neural Networks are presented.

3.1.1 Advances in deep learning

Deep learning is one subset of machine learning. Deep learning is part of the broader family of machine learning methods, that aim at solving problems by learning on data. It is an effective tool for automatizing tasks, and finding regular patterns in some data that humans could not find. Deep learning techniques can process large data sets and drastically reduce the computational time with the computational resources GPUs. In practice, the implementation of deep learning techniques with Tensorflow is widely used for scientific research. It achieved plenty of scientific results, especially in medical imaging. Typical deep learning algorithms based on fully connected networks and classic Convolutional Neural Networks are widely used in the field of medical imaging (Miller et al., 1992; Lee et al., 2017; Anwar et al., 2018; Kim et al., 2019; Wang et al., 2019; Sheikhjafari et al., 2022; Singh et al., 2020).

There is a large application of this technique for scientific research. It is not easy to have a whole review summarizing all of the fields. We will just explain the notions that will be used. So, in this work, to satisfy the objective of the tomographic inverse problem and the requirement of solving physics-informed partial differential equations, our main focus will be on deep learning techniques with fully connected networks and Convolutional Neural Networks. In our project, the deep learning method is a supervised method, so we will detail the supervised method in the following.

3.1.2 Fundamental concepts and components in deep learning

In this part, we explain how to employ the deep learning algorithm and how to create a model. It is critical to understand the fundamental elements and the main concepts of some complex deep learning algorithms.

3.1.2.1 Supervised and unsupervised learning

Based on the information available during the learning and testing, we can distinguish between supervised and unsupervised learning. In supervised learning, the training data includes the desired output, often called labels. The training data consists of pairs (x_i, y_i) of inputs and desired outputs as explained below. The aim is to find a model with parameters θ that generalizes well on new data. During the training step, the optimal parameters are obtained. Models are often dependent on hyper-parameters, which are parameters of a learning algorithm and not parameters of the model.The validation phase consists of testing the model on data that has not been used for training, in order to adjust the hyper-parameters. This phase prevents the model from over-fitting. The model is evaluated on new data during the testing phase. In unsupervised learning, the algorithm is trained on a dataset without supervision with labeled targets. The aim is to learn classes with common characteristics.

3.1.2.2 General formalism for supervised learning

Most deep learning techniques rely on supervised learning. A classic deep learning setup encompasses the following four parts. First, there is a dataset $\mathcal{D} = (I, O) \subset (X, Y)$ consisting of a set of input data $I \in X$ and its corresponding output data $O \in Y$. Second, the nonlinear predictor function or operator $\Psi_\theta(.)$ with parameters $\theta \in R^D$. This operator is represented by a neural network that needs to be defined. This operator has to be trained. This is done by giving paired data (x_i, y_i) where y_i is the true output corresponding to the input x_i. These input and output data are samples within batches I_i and O_i. The samples (x_i, y_i) can be regarded as the realizations of a joint probability distribution. Our aim is to find the optimal parameters θ^* that minimize some error between the predicted outputs $\Psi_\theta(x_i)$ and the ground-truths y_i. This distance between the input and the output is measured by a loss function $\mathcal{L}$. The loss function is specific to the problem under consideration. In this work, we will only consider the L_2 distance. Therefore, the real objective is to find the best parameter with the minimization of the empirical error function $\mathcal{L}_N$. It can be written as:

$$\arg\min_{\theta \in R^D} \mathcal{L}_N(\theta) = \sum_{I_i \in X, O_i \in Y} \mathcal{L}(\Psi_\theta(I_i), O_i, \theta) \tag{3.1}$$

The problem could be ill-posed, so a regularization term is usually considered. The problem will be written as:

$$\arg\min_{\theta \in R^D} \frac{1}{2} \sum_{I_i \in X, O_i \in Y} ||\Psi^*(I_i) - O_i||_2^2 + \beta \mathcal{R}(\theta) \tag{3.2}$$

where $\mathcal{R}$ is a regularization function and β denotes the regularization parameter. The L_1 norm can be used or the L_2 norm to accelerate learning.

Other distances between the input and the output can be considered depending on the problem considered. The efficiency of a machine learning model can be assessed by evaluating the accuracy of the predictions on data that have never been seen by the model. This is the test step. There is another category of deep methods which is based on unsupervised learning. In this case, the training dataset does not contain the ground-truth y_i.

The major thing that makes a machine learning algorithm a deep learning one is the form taken by the predictor operator: it corresponds to an Artificial Neural Network. Deep learning models consist of a neural network comprising numerous layers and parameters, activation functions, and associated with optimization algorithms. It means that neural networks are the fundamental building blocks of deep learning.

A typical artificial neuron takes some numbers x as input, computes a weighted sum, $z = x^t w$ and the output of the neuron is $a(z)$ where a is called an activation function. The neurons are organized in different layers. These layers contain nonlinear activation functions for capturing the main features and implementing feature transformation. Deep learning algorithms can transform the data from lower layers to higher layers. The lower layers extract simple features, while higher layers catch the complex features transformed from the lower layers. In the next subsection, we detail the backpropagation and the stochastic operator Adam which is the mathematical optimization tool to achieve the minimization of the loss function and to obtain the best parameters.

3.1.2.3 Gradient backpropagation: unraveling the learning process

The optimization problems in deep learning are high-dimensional problems. The gradient of the cost function with respect to parameters can not be calculated with finite differences. The

alternative is the back-propagation algorithm. Gradient backpropagation plays a fundamental role in driving the learning process in neural networks. There are some articles that studied backpropagation and the chain rule in neural networks (Rumelhart et al., 1985; Kun, 2012; Cilimkovic, 2015; Géron, 2019). There are two parts for backpropagation: forward pass and backward pass. Firstly, the inputs pass the network layer by layer from the input layer to the output layer and can produce some outputs in the forward pass. Then, the loss function associated with the predicted output and the real label can be calculated with the chain rule. Secondly, during the backward propagation phase, the gradient of the loss with respect to the parameters θ including the weights and biases are obtained transforming layer by layer from the output layer to the input layer with the chain rule again. Eventually, the obtained gradient will be used to update the parameters θ with the gradient descent method or other optimization algorithms.

Gradient computation and its propagation backward through the layers can be a simple problem if we understand the chain rule. The chain rule can allow us to calculate the gradients of the objective with the parameters θ for intricate networks. For simplicity, we consider a fully-connected network with L fully connected layers. The idea of the back-propagation can be adapted to other types of architectures. We denote W^l the matrix that contains the weights of the l^{th} layer and b^l the vector with the biases. We introduce the activation a^l of the l^{th} layer as $a^l = \gamma(W^l a^{l-1} + b^l)$, with γ the activation function, a^0 the input of the network, and a^L the output of the network. We also introduce the weighted input of every layer l as $z^l = W^l a^{l-1} + b^l$. We define the error of neuron j in layer l as $\delta_j^l = \frac{\partial C}{\partial z_j^l}$ where C is the cost function. The back-propagation algorithm is based on the following equations:

$$\delta^L = \nabla_{a^L} C \odot \gamma'(z^L) \tag{3.3}$$

$$\delta^l = (W^{l+1})^t \delta^{l+1} \odot \gamma'(z^L) \tag{3.4}$$

$$\frac{\partial C}{\partial b_j^l} = \delta_j^l \tag{3.5}$$

$$\frac{\partial C}{\partial w_{j,k}^l} = a_k^{l-1} \delta_j^l \tag{3.6}$$

Once the first equation has been used, the values of δ across the different layers can be computed iteratively with the second equation. The gradient of the cost function with respect to $(W_l)_{0 \leq l \leq L}$ and $(b_l)_{0 \leq l \leq L}$ can then be obtained. In terms of complexity, the back-propagation takes about the same number of operations as two forward passes through the neural network.

The rule for updating the weights or biases of the network is given by the optimizer. Simple gradient descent can be a relevant choice; in this thesis, we will mostly use the Adam optimizer which is an optimized version of the gradient descent that has proven to be generally efficient to train neural networks.

The activation functions enable the network to capture intricate patterns and relationships in data. We will consider it below.

3.1.2.4 Activation Functions

An important aspect of deep learning is the use of nonlinearities in order to create highly non-linear functions. These nonlinearities are called activation functions. Most of them are defined pointwise, and are applied independently to all the coordinates of the input. There are

many classic activation functions such as sigmoid, tanh, ReLU and LeakyRelu embedded in the neural networks reviewed by (Apicella et al., 2021; Lederer, 2021; Dubey et al., 2022). The activation functions play an important role in introducing non-linearities in the network. We will concisely present three activation functions.

Sigmoid The sigmoid function can be written as:

$$\sigma(\theta') = 1/(1 + e^{-\theta'}) \tag{3.7}$$

If a negative value is provided as the input θ', the sigmoid function will output a value of approximately 0. On the contrary, if a positive value is given as an input, the function will map it to approximately 1 as output.

tanh The tanh function can be defined by the following:

$$\sigma(\theta') = tanh(\theta') = sinh(\theta')/cosh(\theta') = (e^{\theta'} - e^{-\theta'}/(e^{\theta'} + e^{-\theta'}) \tag{3.8}$$

For the tanh function, when a positive value is used as the input θ', it will output a value close to 1. Conversely, if a negative value is obtained as the input, the function will map it to a value near -1.

Relu The Relu function can be described as:

$$\sigma(\theta') = max(0, \theta') \tag{3.9}$$

When a negative value is used as input, the ReLU function will produce an output close to 0. The ReLU is not perfect and may lead to vanishing gradients. The LeakyReLu may outperform the classical ReLU. It is defined as $\max(\alpha\theta, \theta)$ for an input θ and a parameter α.

In this work, we mainly consider the Relu function. After the activation function into the neural network, we will consider the effective optimizer used in the reconstruction scheme.

3.1.2.5 Optimization Algorithms

When using a large database, it becomes impractical to use classical optimization algorithms whose complexity increases with the size of the data set. To address this challenge, stochastic optimization methods are employed. The most used algorithm in this category is the Mini Batch Gradient Descent. The training set is divided into batches and the optimization is repeated for each batch until the entire database has been processed. This constitutes what is known as an epoch. We repeat epochs as needed until the network converges.

Training a very large deep neural network can be very difficult. The gradient of the loss function will be calculated by the classic Adam optimizer using the ideas of AdaGrad and RMSProp algorithms (Kingma and Ba, 2014). We will only explain some principles of this algorithm and will not present all the technical details. Like momentum optimization, it keeps track of an exponentially decaying average of the past gradients that have been calculated. It depends on a momentum decay hyperparameter β_1 typically initialized to 0.9, and a scaling decay hyperparameter β_2 often initialized to 0.999. Adam is an adaptive learning rate algorithm (like AdaGrad and RMSProp), and it requires less tuning of the learning rate. The ADAM algorithm relies on the first-order partial derivatives (Jacobians). It is summarized below:

1) $m_t \leftarrow \beta_1 m_{t-1} - (1 - \beta_1)\nabla_\theta J(\theta)$
2) $s_t \leftarrow \beta_2 s_{t-1} + (1 - \beta_2)\nabla_\theta J(\theta) \otimes \nabla_\theta J(\theta)$
3) $\hat{m}_t \leftarrow \frac{m_t}{(1-\beta_1)^t}$
4) $\hat{s}_t \leftarrow \frac{s_t}{(1-\beta_2)^t}$
5) $\theta_t \leftarrow \theta_{t-1} + \eta \frac{\hat{m}_t}{\sqrt{\hat{s}_t + \varepsilon}}$

The goal of the first and second steps is to update the biased first-moment estimate m_t and

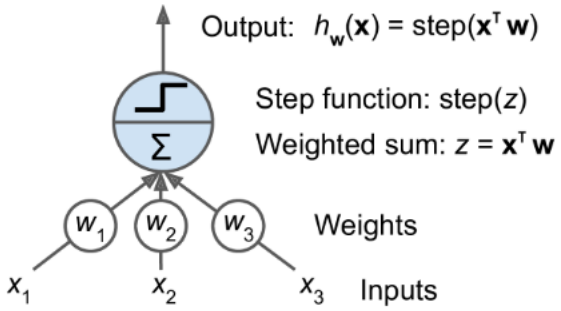

Figure 3.1: Threshold logic unit or linear threshold unit (Géron, 2019).

the second raw-moment estimate s_t respectively, which is related to the previous time step. Moving forward, the biases with respect to the first-moment estimate and second-raw-moment estimate are corrected through step 3 and step 4. Finally, the model parameter can be updated with a learning rate hyperparameter η.

Algorithms with Hessians and second-order derivatives are very hard to apply to deep neural networks because a neural network has many parameters. With a gradient descent algorithm, the parameter θ is updated with $\theta - \eta \nabla J(\theta)$ where η is the gradient step and J is the loss function. It does not take into account the earlier gradients and it can be very slow. Momentum optimization takes into the former gradients and defines a momentum vector m. A hyperparameter is also used to add more or less 'friction'. With adaptive gradient descent, the algorithm corrects its direction earlier to point more toward the global optimum. It is done with a scaling vector s and a new hyperparameter. The method exhibits an exceptional performance for stochastic optimization and a little memory required for first-order gradients. It also exhibits remarkable stability for a varying scale of the gradient. (Kingma and Ba, 2014). The stochastic Adam algorithm allows us to solve the problem with a high speed and efficiency, its effectiveness will be demonstrated in the following. Having provided a concise presentation of the fundamental concepts of deep learning in the preceding parts, we will move our attention to two typical deep learning architectures for addressing the inverse problem: the fully connected network and the Convolutional Neural Network (CNN).

3.1.3 Deep learning with fully connected network

In this subsection, we will introduce the basic concept of the fully connected network from the aspect of perceptron and MultiLayer perceptron.

3.1.3.1 Perceptron

The Perceptron architecture is the most widely used Artificial Neural Network first proposed by Frank Rosenblatt (Rosenblatt, 1958). It is based on a threshold logic unit (TLU) shown in Figure 3.1. It computes the weighted sum $z = \mathbf{x}^T \mathbf{w}$ and applies a step function. The step function can be replaced by a sigmoid function, the ReLU function mentioned before in the activation function subsection. Additionally, the bias term plays a crucial role in the neural network with its high capability for correcting offsets. An example of a Perceptron with a bias neuron shown in Figure 3.2. More details can be found in (Géron, 2019).

More generally, the perceptron applied on an input signal $x \in \mathbb{R}^N$ can be defined as:

$$f(x) = \sigma(W^t x + b) \tag{3.10}$$

where W is a weight matrix and b a bias vector.

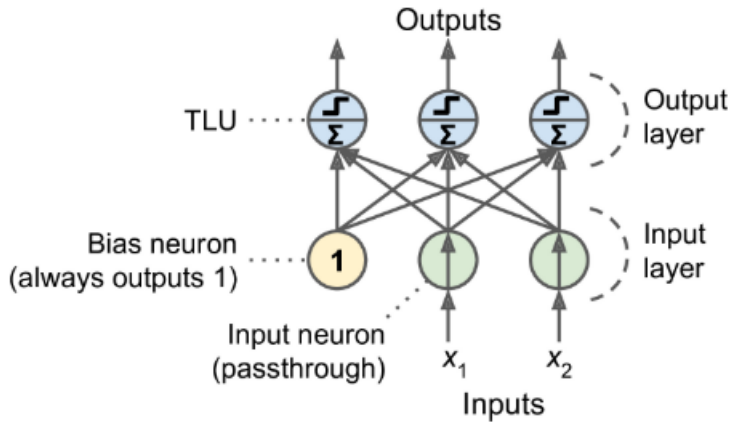

Figure 3.2: A perception with a bias neuron (Géron, 2019).

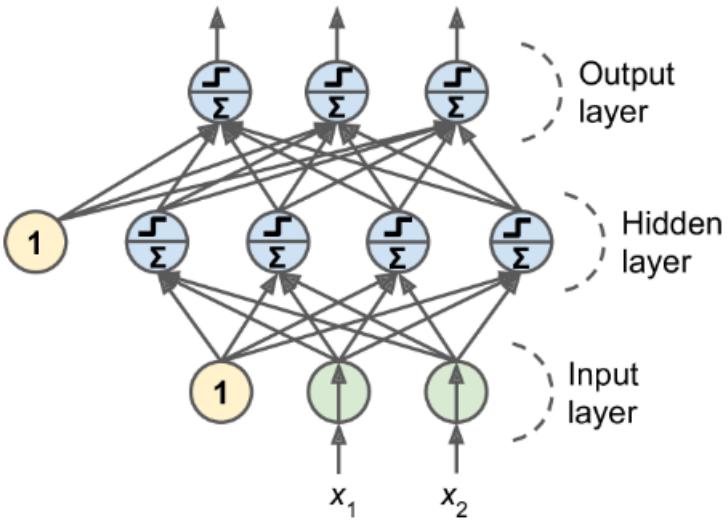

Figure 3.3: A simple fully connected network (Géron, 2019).

3.1.3.2 MultiLayer perceptron or fully connected network

A MultiLayer Perceptron is the composition of several perceptron layers, with varying dimensions and is also referred to fully connected network(FC). It can be observed that the outputs of the perceptron serve as the inputs of the next successive perceptrons as shown in Figure 3.3. The neurons are arranged in several layers while each neuron is linked to others to allow it to receive an input and give an output. The typical neural network can be constructed by a series of neurons distributed in multiple layers, where each layer takes the input from the output of the preceding layer. We are interested only in feed forward neural networks where a neuron takes the input from the output of the previous layer. In the structure of MLP displayed, all the neurons in a layer are connected to all neurons in the previous layer, this layer is well-known as a fully connected or dense layer. A simple example of a fully connected network including the input layer, one hidden layer, and the output layer shown in Figure 3.3.

The mathematical concept of the MLP with l layers and the learned parameters $\theta_k = (W_k, b_k)$ can be written as:

$$\begin{aligned} f_\theta : \mathbb{R}^{N_0} &\to \mathbb{R}^{N_l} \\ x &\mapsto x_l \end{aligned} \tag{3.11}$$

And its general operator form can be expressed as:

$$f_\theta = \Psi_{\theta_l} \circ \Psi_{\theta_{l-1}} \circ ... \Psi_{\theta_2} \circ \Psi_{\theta_1} \tag{3.12}$$

For a given $k <= l$, the operator for the k-th layer can be written as:

$$\begin{aligned} \Psi_{\theta_k} : \mathbb{R}^{N_{k-1}} &\rightarrow \mathbb{R}^{N_k} \\ x &\mapsto \sigma_k(W_k x + b_k) \end{aligned} \tag{3.13}$$

where the nonlinear activation operator is denoted as $\sigma_k : \mathbb{R}^{N_{k-1}} \rightarrow \mathbb{R}^{N_k}$, linear weight operator $W_k : \mathbb{R}^{N_{k-1}} \rightarrow \mathbb{R}^{N_k}$ and the bias vector is $b_k \in \mathbb{R}^k$. For every step, the weight operator W_k can be seen as a matrix where its rows are associated with N_k neurons in the k-th layer, while each column represents the number N_{k-1} neurons in the $k-1$ th layer. The aim of this MLP is to learn the parameters θ_k including the weights and biases.

3.1.4 Deep learning with Convolutional Neural Network

The Convolutional Neural Network(CNN) is a classical artificial neural network exhibiting outstanding outperformance in computer vision. It is successfully applied in several areas such as time series prediction, signal identification, image classification, object detection, image segmentation, face recognition, human action recognition, and Object Recognition/Detection surveyed by (Li et al., 2021b). In this work, we also apply this typical CNN for the blood flow velocity reconstruction in a realistic phantom. Subsequently, we present successively the various parts involved in a CNN for a deeper understanding.

3.1.4.1 Convolutional layer

A Convolutional layer serves as a block that is the fundamental construction of the Convolutional Neural Network. As opposed to the fully connected layer whose neuron is fully connected to every neuron within the previous layer, their neurons only connect to the input neurons or pixels for images in their receptive field. It is worth noting that neurons in a given convolutional layer are exclusively connected to a rectangular field with a limited number of neurons in the previous layer. The architecture of CNN can capture the low-level features of the layer at the initial layer and learn the high-level features at the deeper layer. The hierarchical structure of Convolutional Neural Networks (CNNs) explains the remarkable performances in computer vision because it mirrors the organization of features in real-world images.

Subsequently, we will introduce the fundamental elements for bridging two layers including the convolutional filter, stride, and padding.

Convolutional filter A convolution filter also called a convolution kernel, can be represented by a matrix K. We can define this matrix with height and width which are associated with the size of the receptive field. The matrix can be added a bias term as well and the optimized weights are the matrix elements and the biases. If the image I with a size of $a \times b$, and the filter K a size $p \times q$, the discrete convolution operation can be described as:

$$O(i,j) = \sum_s \sum_t I(s,t), K(s+i, t+j) \tag{3.14}$$

Where $O(i,j)$ is the pixel value at the position (i,j) in the output, $I(s,t)$ denotes the value at (s,t) in the input. The size of the output of the image will be $(a-p+1) \times (b-q+1)$. A convolution layer consists of neurons employing the same filter to obtain a feature map, that highlights these regions in the image with the highest response for that filter.

Stride The stride is used to control the spatial step size for moving the filter from one

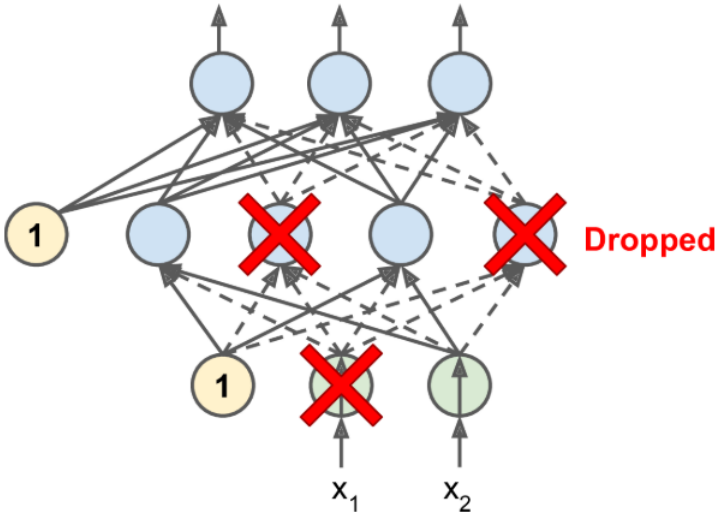

Figure 3.4: Dropout regularization (Géron, 2019).

receptive field to another field. It is worth noting that the stride is useful for reducing the image size while increasing the quantity of information captured from the original image. In short, it plays an important role in enhancing the efficiency of the convolutional layers by minimizing redundant computations.

Padding The padding is based on an increase in the image size. It can be used to keep the image size after implementing the convolution and also to maintain the dimension of the image. Padding can be useful to reduce aliasing effects. With zero padding, pixels are added with a zero value. One can also add pixels with mirror values.

3.1.4.2 Pooling layer

The pooling layer after the convolution layer can reduce the dimension of the signal with some operations on neighbor pixels like an average. When working with signals, it is sometimes useful to consider multiple scales. This can be done using pooling operations, which reduce the dimension of the signal. The neurons in the pooling layer are only connected to a limited receptive field in the preceding layer. There are two common operations such as max pooling and average pooling. In this study, we have not used it in the CNN. After introducing convolutional layers and pooling layers, dropout layers will be taken into consideration.

3.1.4.3 Dropout layers

Dropout is one of the well-known regularization techniques for neural networks. To achieve the goal of regularization, the dropout layer can drop the connections with a random dropout rate between layers to be more independent. When the model shows an overfitting trend, we can use dropout layers with a higher dropout rate to effectively avoid these phenomena. Here is an example of dropout regularization in Figure 3.4. More details are presented in the handbook (Géron, 2019).

The hyperparameters setting in the networks will then be presented.

3.1.4.4 Hyperparameters in networks

Hyperparameters in neural networks, include learning rate, batch size, and number of epochs, which play a significant role in training a network model effectively.

Learning rate The learning rates are significant for the computation time and the convergence. Therefore, a proper rate has a direct impact on the training results. It should be not too high or too low. A good strategy starts with a high learning rate and subsequently shifts to a small rate during the training procedure.
Batch Batch refers to a subset of the data that is processed together during a single iteration of the training process. During the training procedure, the mini-batches are used to train the network.
Batch size The number of data sets in one batch is defined as the batch size. The selection of batch size plays a crucial role in influencing both the performance of the model training and the computation time needed for training. Nowadays, lots of researchers consider a large batch size with GPU hardware devices. In practice, the better batch size is chosen depending on the cases.
Epoch The process of passing all mini-batches through the model to train the network one time is called an epoch.

We have already introduced the deep-learning techniques above. Following that, we will present state-of-the-art deep learning techniques for addressing the inverse problem.

3.2 Deep learning methods for inverse problems

Novel methodologies based on deep learning have been proposed recently to solve complex inverse problems (Arridge et al., 2019). There are many situations in which data are abundant but governing laws are uncertain or do not exist. The use of deep learning models is particularly promising in scientific problems involving processes that are not completely understood, or where it is computationally infeasible to run models at high resolutions in space and time. Deep learning structures are often used as a surrogate model where the goal is to accurately reproduce the behavior of the model at substantially reduced computational cost. For complex scientific and engineering applications, deep learning alone can not be considered sufficient. Many hybrid physics-deep learning frameworks have been studied, that integrate traditional physics-based modeling approaches with state-of-the-art machine learning or deep learning technique (Rai and Sahu, 2020; Karpatne et al., 2017). Several methods incorporate physical knowledge into loss functions to help deep learning models capture patterns consistent with physical laws. They thus considered physics-guided loss functions where the governing equations are used as regularizers to reduce the search space of parameters (Jia et al., 2021; Raissi et al., 2019; Zhu et al., 2019; Geneva and Zabaras, 2020; de Hoop et al., 2022). In several works, a neural network is used to approximate the solution operator mapping elements of the space of the parameters of a PDE and the space of the solutions of this PDE by minimizing a loss function using the discretized values of the solution and of the parameter. These approaches may be successful but are not robust to mesh refinement. In order to overcome some limitations of these works, there has been some work about operator approximations with deep learning techniques that have the property of discretization invariance. These neural networks are defined to act between infinite-dimensional function spaces. PCA-Net uses neural networks to map between PCA coefficients representing input and output functions (Bhattacharya et al., 2021; Lu et al., 2021). Recently, DeepONet has been investigated for operator approximation comprising two sub-networks, the branch and trunk network (Lu et al., 2022). In (Tenderini et al., 2022), the authors couple a POD with a convolutional network to solve the cardiac electrophysiology inverse problem.

In this work, inspired by these approaches and in order to improve the reconstruction results obtained for blood velocity reconstruction with our Proper Orthogonal Decomposition-adjoint approach detailed above, we investigate the coupling of POD model reduction with deep learn-

Figure 3.5: Simulation phantom.

ing techniques. We compare several neural network architectures to approximate the inverse operator. The quantities of interest, the velocity field, and Radon projections, corresponding to the inputs and the outputs of our inverse problem are expanded in terms of appropriate sets of basis functions obtained from snapshots. Various neural network architectures are used to map the coefficients associated with the representations of these functions. The efficiency of the framework is demonstrated with numerical examples with stationary velocity fields with realistic simulations.

3.3 Problem statement

As we mentioned, it is a complex inverse problem to reconstruct the blood flow velocity in a simulation phantom with a bifurcation as shown in Figure 3.5. In this work, we combine model reduction with deep neural networks to learn the mapping between two Hilbert spaces, $\mathcal{L}_V = L_2(\Omega \to \mathbb{R}^3)$ for the velocity field V and $\mathcal{L}_p = L_2([0,T] \times [-a,a] \times [0,z_{max}] \to \mathbb{R})$ for the Radon projections p. We consider only stationary velocity fields but we have to include the time domain to describe the evolution of the tracer concentration and of the Radon projections. In the following, the POD for the Radon projections includes the time domain.

The velocity space $\mathcal{L}_V$ is considered as the product of three spaces $\mathcal{L}_V^x \times \mathcal{L}_V^y \times \mathcal{L}_V^z$ corresponding to the components of the velocity field. We have $\mathcal{L}_V^x = \{V_x : \Omega \to \mathbb{R}\}$ for the velocity component along x and similar definitions for the other directions. We aim to determine a nonlinear inverse operator $\Psi = \Psi^x \times \Psi^y \times \Psi^z : \mathcal{L}_p \to \mathcal{L}_V$ from samples corresponding to the two probability measures on these spaces, the probability measures ν on $\mathcal{L}_p$ and its push forward measures $\Psi^*\nu$ on $\mathcal{L}_V$. With these notations, for given Radon projections p, the velocity compo-

nents are given by $V_x = \Psi^x(p)$, $V_y = \Psi^y(p)$ and $V_z = \Psi^z(p)$. This operator is approximated with a class of parametric operators $\Psi_\theta = \Psi^x_\theta \times \Psi^y_\theta \times \Psi^z_\theta : \mathcal{L}_p \to \mathcal{L}_V$ with different neural network architectures, where $\theta \in \mathbb{R}^D$ represents the set of parameters D of the neural network. This corresponds to an inverse nonlinear operator learning. The direct learning of solution operators of inverse problems is currently a popular research area, and many deep neural network architectures have been considered (Arridge et al., 2019). One of the limitations is the interplay between the ill-posedness of learning and the ill-posedness of the inverse problem itself. In practical terms, a finite number N of samples for the Radon projections and velocity measures are available $\{p_n\}_{1\leq n\leq N}$ and $\{V_n = \Psi(p_n)\}_{1\leq n\leq N}$ defining empirical measures. So this inverse problem is to determine the optimal parameter θ^*, with the cost function $\mathcal{L}$ written as:

$$\mathcal{L} = \frac{1}{N}\sum_{n=1}^{N} \frac{E_n^x + E_n^y + E_n^z}{\|\Psi^x(p_n)\|_2 + \|\Psi^y(p_n)\|_2 + \|\Psi^z(p_n)\|_2} \tag{3.15}$$

where $E_n^x = \left\|\Psi^x(p_n) - \Psi^x_\theta(p_n,\theta)\right\|^2_{L_2}$ is the reconstruction error along x and similar definitions can be used for the other axes. In practice, in view of the non-convex nature of the optimization over θ, we obtain an approximation of θ^* for the solution.

In this work, we have used approaches similar to the ones presented in (Bhattacharya et al., 2021; Tenderini et al., 2022). In order to learn a data-driven mapping between the two Hilbert spaces, we first estimate finite dimensional approximations on these spaces with POD. We approximate the identity mappings $I_{\mathcal{L}_p}$ and $I_{\mathcal{L}_V}$ by the composition of two maps, a linear encoder and a linear decoder, with finite-dimensional range and domain respectively. The finite-dimensional outputs of the encoders are called latent codes corresponding to the POD coefficients and a mapping α between these latent codes will be built. In the following, we will denote $F_{\mathcal{L}_p}\colon \mathcal{L}_p \to \mathbb{R}^{N_R}$ and $G_{\mathcal{L}_p}\colon \mathbb{R}^{N_R} \to \mathcal{L}_p$ the encoder and the decoder of the space $\mathcal{L}_p$, and N_R the dimension of the reduced space for the Radon projections. Similarly, $F_{\mathcal{L}_V}$ and $G_{\mathcal{L}_V}$ the encoder and the decoder of the space $\mathcal{L}_V$ will be defined, with a reduced dimension N_V for each direction. To summarize, we have the following approximations, $I_{\mathcal{L}_p} \simeq G_{\mathcal{L}_p} \circ F_{\mathcal{L}_p}$, $I_{\mathcal{L}_V} \simeq G_{\mathcal{L}_V} \circ F_{\mathcal{L}_V}$; $\Psi_\theta \simeq G_{\mathcal{L}_V} \circ \alpha \circ F_{\mathcal{L}_p}$. The combination of POD with a neural network is the basis of the computational methodology. A diagram with the different mappings is displayed in Figure 3.6.

In the framework of the deep learning approaches, the dimension reduction is not performed on the density, the adjoint variable, and the velocity field as in the adjoint method, but on the Radon projections and the velocity field. We denote the reduced dimensions of Radon projections and velocity fields as N_R and N_V^3 corresponding to the number of basis elements. It should be noted that the POD could be replaced by encoding/decoding with nonlinear autoencoders. The first step of the methods thus consists in obtaining finite dimensional approximations on the velocity and Radon projection spaces. The POD presented above lead to orthonormal bases $\{\psi_{Rf,i}\}_{1\leq i\leq N_R}$ for $\mathcal{L}_p$ and $\{\psi_{V,i}\}_{1\leq i\leq N_V} = \{\psi^x_{V,i}\}_{1\leq i\leq N_V} \times \{\psi^y_{V,i}\}_{1\leq i\leq N_V} \times \{\psi^z_{V,i}\}_{1\leq i\leq N_V}$ for $\mathcal{L}_V$ which are truncated to the first N_R and N_V first modes before the training of the network. We proposed two different architectures of networks, POD-FC and POD-3D CNN.

a)POD-FC:

The first method presented in this section is similar to the work introduced in (Bhattacharya et al., 2021; de Hoop et al., 2022), to obtain the modeling of nonlinear operators. The method is based on a fully connected network (FC) and it will be named POD-FC in the following. Given Radon projections $p \in \mathcal{L}_p$, the operator Ψ_θ is defined along the x component by:

$$\Psi^x_\theta(p,\theta)(\boldsymbol{M}) = \sum_{j=1}^{N_v} \alpha^x_j(F_{\mathcal{L}p}(p),\theta)\psi^x_{V,j}(\boldsymbol{M}) \tag{3.16}$$

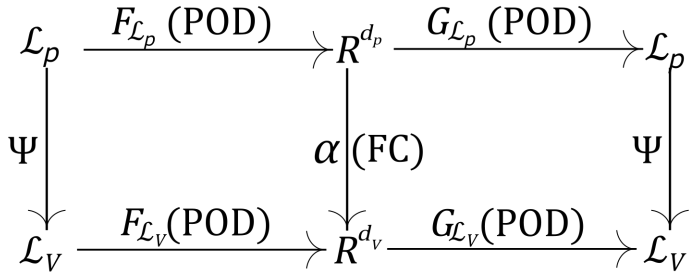

Figure 3.6: The input-output map of the autoencoder structure of POD-FC.

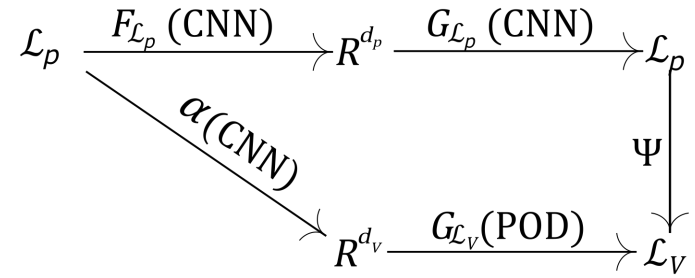

Figure 3.7: The input-output map of the autoencoder structure of POD-CNN.

where $M \in \Omega$ for stationary velocity fields. The function $\alpha_j^x : \mathbb{R}^{N_R} \times \mathbb{R}^D \to \mathbb{R}$ for $1 \leq j \leq N_V$, is mapping the coefficients obtained for the POD of p, $F_{\mathcal{L}_p}(p) = \{(\psi_{Rf,i}, p)\}_{1 \leq i \leq N_R}$ and the coefficients corresponding to the velocity field along x, $F^x_{\mathcal{L}_V}(V)$. The other definitions are similar for the other axes. Additionally, the input-output map with the autoencoder structure of this network can be displayed in Figure 3.6.

b)POD-3D CNN:

We propose the second neural network architecture that is based on a Convolutional Neural Network (CNN) that will be called POD-CNN. It uses some ideas presented in (Tenderini et al., 2022). For our inverse problem, we will write the corresponding approximate inverse operator along the x component as:

$$\Psi^x_\theta(p, \theta)(\boldsymbol{M}) = \sum_{j=1}^{N_v} \alpha_j^x(p, \theta)\psi^x_{V,j}(\boldsymbol{M}) \tag{3.17}$$

with similar definitions for y and z. It is worth noting that the operator $F_{\mathcal{L}_p}$ and the Proper Orthogonal Decomposition in the input space is not used. Additionally, the input-output map and the autoencoder structure of the 3DCNN network are displayed in Figure 3.7. The two networks will be tested in the next section with many numerical simulations.

In order to study the two networks, we have generated datasets and considered the velocity reconstruction error and its standard deviation. To investigate the behaviours of the networks, we have studied successively the impact of time intervals and of the noise level on the blood flow velocity reconstruction. We have implemented the optimization of the network parameters including learning rate, batch size, and dropout rate with an Adam optimizer for blood flow velocity reconstruction. The main parameters range is detailed below: time steps [8, 50], noise level [0 dB, 20 dB], learning rate [10^{-4}, 10^{-3}], batch size [50, 200], and dropout rate value [0, 0.2]. To evaluate the effectiveness of the velocity reconstruction with POD-DL methods, we will present the 3D velocity reconstruction, and 2D slices velocity reconstruction with two cases, one case involves a low inlet velocity condition, and another involves a higher inlet velocity condition. The dataset generation, network architecture details, and the results will be

discussed in the following sections.

3.4 Dataset generation

The vessel used for the simulations with a fine mesh is displayed in Figure 3.5. In order to test the performance of the proposed deep learning methods, it is necessary to calculate the POD bases on which the dimension reduction is based for the velocity field and the Radon projections. We concentrate here on stationary velocity fields. The ground truth velocity, density, and Radon projections will be generated by solving the Navier-Stokes equation, and the transport equation, and by employing the Radon transform, step by step during the offline step. More details will be given below.

3.4.1 Ground truth blood velocity generation

In our work, we generate stationary velocity fields by solving the stationary Navier-Stokes equation and then we estimate the synthetic Radon projections of the tracer concentration obtained through the transport equation on a realistic phantom displayed in Figure 3.5. The Fenics finite element library is used for these simulations (Logg et al., 2012). To establish the computational model, we use two function spaces, one for velocity and the other for pressure. For the transport equation, the spatial discretization is considered using finite elements of type $P1$ with a total of 56845 nodes. For simulating the Navier-Stokes equations, we use the Taylor-Hood finite element formulation ($P2 - P1$). Additionally, we use the Incremental Pressure Correction method in Fenics for efficiently solving the Navier-Stokes equations.

Velocity fields are achieved by sampling with variable boundary conditions: inlet velocities range between 0 and 0.6 m/s, and outlet pressures vary from 0 to 1000 Pa. These parameters correspond to the parameter μ_1. After simulating the Navier-Stokes equations, we obtain 1000 snapshots of the velocity field. For each velocity component along the x,y, or z axes, we retain $N_v = 2$ POD basis elements. As explained below, this low number of basis elements is sufficient to capture the main features of the flow pattern.

3.4.2 Ground truth blood tracer concentration generation

The partial differential transport equation is solved for achieving the tracer concentration fields with the given velocity field solved by the Navier-Stokes equation. The tracer concentration on the inlet surface is varied between 0.5 and 1.5 kg/m^3 and the diffusion coefficients D between 0.001cm^2/s and 0.00001cm^2/s. These parameters correspond to the parameter μ_2. The transport equation is presented in Chapter 1.

3.4.3 Ground truth Radon projection generation

From the obtained velocity fields, Radon projections are calculated by using the Radon transform of the tracer concentration fields achieved by solving the transport equation. Radon projections are perpendicular to the main flow direction z. They are implemented using the Scipy python library with $N_z = 100$ for the number of slices along z and with $N_p = 285$ projections, $N_\theta = 30$ projection angles in the interval $[0, 180°]$ for each time step. Gaussian noise of PPSNR between 0 and 20 dB is added to the Radon projections. The POD bases for the Radon projections are obtained after the implementation of POD. Here, we consider $N_R = 60$ basis elements for the Radon projections.

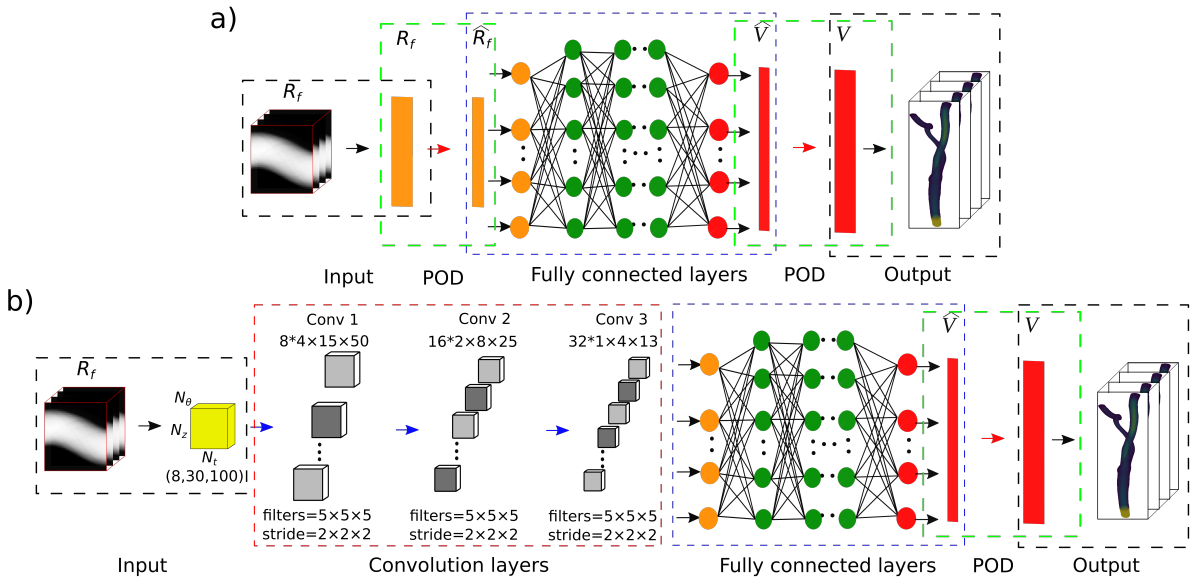

Figure 3.8: Architecture of the networks.

3.5 Deep learning methods

After the data generation, in this section, the network architectures and the training method will be detailed. The training was performed by using the open-source library Keras 2.2.5 with Tensorflow backbone and implemented on a modern high-performance computing cluster in Creatis with 10 processors.

3.5.1 Architecture of networks

We consider two networks including the POD-Fully connected network(POD-FC) and POD-3D Convolutional Neural Network(POD-3D CNN). Their architectures are displayed in the schematic Figure 3.8.

3.5.1.1 POD-Fully connected network

The POD-Fully connected network is considered to reconstruct the blood velocity. The architecture of the POD-Fully connected network is shown in Figure 3.8 a. This network consists of five parts: the input, POD, fully connected layers, reverse POD, and the output. The Radon projections and velocity fields correspond to the input and output respectively. The POD decomposition step connects the input and the inlet of the fully connected layers while the reverse POD connects the output and the outlet of fully connected layers. We call reverse POD the calculation of a function given its POD coefficients. After implementing this network, we have been inspired by some research taking the Convolutional Neural Network into consideration.

3.5.1.2 POD-3D Convolutional Neural Network

In this second network shown in Figure 3.8 b, the Convolutional layers are used instead of the POD for reducing the high dimension of the Radon projections. In this drawing, N_t, N_θ, and N_z are corresponding to the number of time intervals, number of projection angles, and number of slices respectively. The 3D input data correspond to the evolution in time of the Radon projections, which are transformed with convolutional layers to obtain latent coefficients that

are similar to the POD coefficients of the Radon projections. Yet, the Radon POD basis is not used in this network and the transformation is learned. The other parts of the networks are similar to the ones of the first network.

3.5.2 Network details

To train these networks, we generated 800 snapshots for the velocity field and their corresponding Radon projections, and we estimated first their Proper Orthogonal Decomposition (POD) coefficients. The POD coefficients of the velocity field and of the Radon projections are effectively evaluated by our work as shown in Figure 3.9 where the relative energy or L_2 norm of the basis is plotted as a function of the number of basis elements. These plots are used to choose the number of basis elements. For the test dataset, we used 200 snapshots for each noise level to obtain Monte-Carlo estimates of the errors and standard deviations. To compare with the POD-adjoint method, we considered 50 samples to estimate the errors using this approach.

For the POD-FC network, we obtain the best results with a fully connected neural network with 4 internal layers of width (500, 1000, 1000, 1000) between the input and the output with the ReLU activation function, except in the last layer. For this network architecture, the results have been considered with a dropout layer with a rate of 0 to 0.2 to avoid overfitting after the first layer. In the end, the network model consists of 3,550,506 trainable parameters, with weights ranging from -0.1017 to 0.1017 and there are 0 bias parameters in the model.

For the POD-CNN network, we adopt a 3D convolutional architecture to extract the Proper Orthogonal Decomposition (POD) coefficients, which represent the reduced dynamics of the input dataset of Radon projection. The 3D CNN operations, filter lengths, and strides considered in this network are summarized in Figure 3.8. The input to each convolutional layer is a 4D tensor, except for the input layer of the network which is of shape (N_t, N_θ, N_z). The average of the projections along the s direction shown in Figure 1.3 in Chapter 1 is obtained for each angle θ. The L^{th} layer takes each 3D slice of the tensor of the layer $L-1$ and convolves it with all the kernels to create a 4D tensor. For any convolutional layer L, we denote k_L as the number of feature channels. These kernels of size $f_x \times f_y \times f_z$ can be grouped into a 4D tensor $K_L \in R^{f_x \times f_y \times f_z \times k_L}$. A schematic drawing associated with the shapes (f_x, f_y, f_z, k_L) is given in Figure 3.8. Three convolutional layers with shapes (f_x, f_y, f_z) = (5, 5, 5) and strides (2,2,2) are adopted in our study. The 3D convolutional layers are followed by a feed-forward network with 300 neurons to return a vectorized feature map $(\alpha_j^x)_{1\leq j\leq Nv} \times (\alpha_j^y)_{1\leq j\leq Nv} \times (\alpha_j^z)_{1\leq j\leq Nv}$. We represent nonlinearities in these networks by choosing the ReLU activation function. The number of hidden layers, the number of weights per hidden layer, the nonlinear activation functions, the batch size for mini-batch gradient descent, and the number of epochs to employ model training have been optimized in this work. We train the network with 100 epochs, with a common Adam optimizer, and a varied learning rate between 10^{-3} and 10^{-4}. Finally, 92,762 trainable parameters with a weight range from -0.1394 to 0.1397 together with 0 bias are used in the model.

3.5.3 Model evaluation

To accurately and quantitatively assess the performance of the coupled POD-DL approach, the normalized root mean square error (NMSE) metric is used on the reconstructed velocity fields on 200 test snapshots. This metric enables us to evaluate the accuracy of the reconstructed velocity fields compared with the ground truth. It is defined as follows:

$$E(\mathbf{V}) = \frac{\|\mathbf{V} - \mathbf{V}_{\text{true}}\|_2}{\|\mathbf{V}_{\text{true}}\|} \tag{3.18}$$

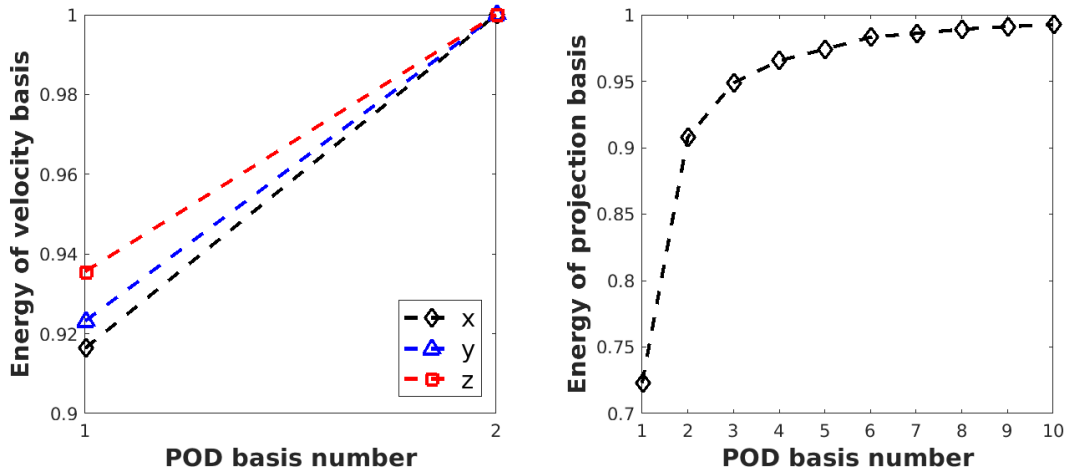

(a) Velocity (b) Radon projection

Figure 3.9: The energy of velocity and Radon projection basis.

where $\mathbf{V}$ is the reconstructed velocity and $\mathbf{V}_{true}$ is the ground truth velocity. We can estimate the same normalized error for the x, y, and z components of the velocity field. Additionally, the mean and the standard deviation for these different velocity errors can be obtained with the classical formula.

3.6 Blood flow velocity reconstruction results discussion and applications

In this section, we will first analyze the reconstructed velocity error and its standard deviation for different time intervals and noise levels. With simulations on a small time interval, the comparison with the adjoint method will be easier. We optimize the network training parameters including the learning rate, batch size, and dropout rate. Then, we will move our focus to two cases of velocity reconstruction. We will display three-dimensional reconstruction and two-dimensional reconstruction with slices. One case is considered with a low inlet velocity and another is presented with a high inlet velocity. Afterward, the reconstruction errors in comparison with the POD-adjoint method are given to validate the improvement given by this work. Eventually, we will discuss the clinical application and the limitations of this work.

3.6.1 Velocity error and standard deviation depending on the time interval, noise level, and network training parameters

3.6.1.1 Time interval analysis

First, we consider the POD-Fully connected network. To evaluate the network model, the loss function curve is presented in Figure 3.10 for the train and test samples for 8 or 50 time intervals. The loss shows a decrease with the increase of the epoch number and the training loss curve is below the test loss curve for different time intervals. The loss function displays a clear decrease, so the network can be considered useful for predicting the blood velocity field.

Subsequently, the Table 3.1 presents the velocity error and its standard deviation for this network with various time intervals. In this table, E($\mathbf{V}_{tr}$) denotes the average training error

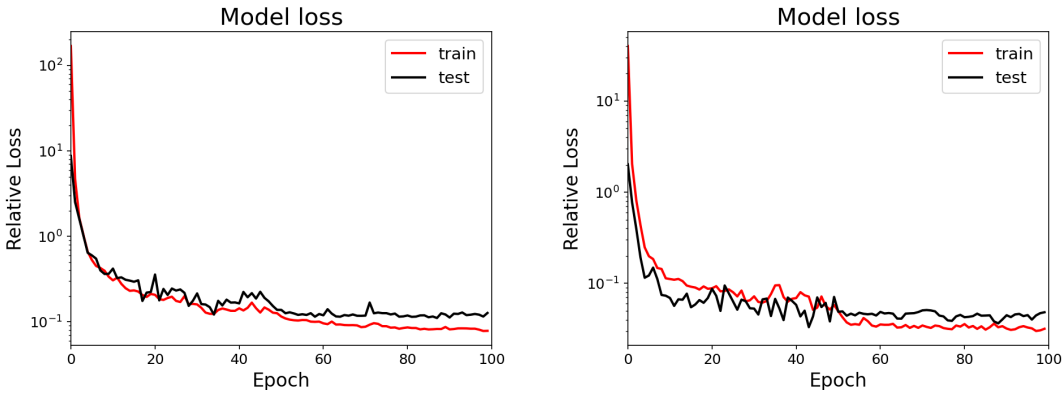

(a) 50 time intervals (b) 8 time intervals

Figure 3.10: The loss function curve for different time intervals for POD-FC.

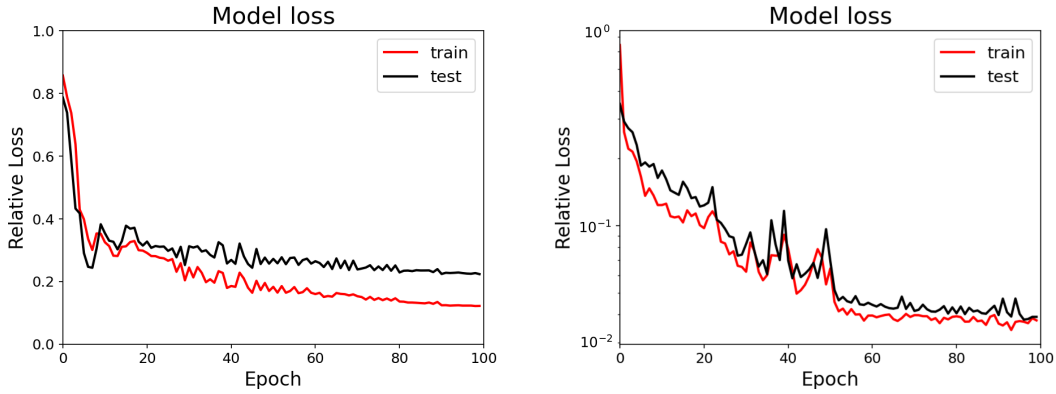

(a) 50 time intervals (b) 8 time intervals

Figure 3.11: The loss function curve for different time intervals for POD-3D CNN.

in the training set of 800 snapshots of the model, E($\mathbf{V}_{te}$) is the average testing error in the 200 snapshots to validate the model and D(V_{te}) is the standard deviation of the velocity error. As expected, the errors for the components of the velocity and their corresponding standard deviations are smaller when 8 time intervals are selected in the network. This small time interval will be useful for the comparison with the adjoint method.

For POD-3D CNN, the training and testing loss functions show a decreasing trend as the epoch number increases as displayed in Figure 3.11. The corresponding velocity error and its standard deviation value are summarized in the Table 3.2. A small testing velocity error and small standard deviation are obtained with a smaller time interval.

time interval	E($\mathbf{V}_{tr}$)	E($\mathbf{V}_{te}$)	E(Vx_{te})	E(Vy_{te})	E(Vz_{te})	D($\mathbf{V}_{te}$)	D(Vx_{te})	D(Vy_{te})	D(Vz_{te})
50	0.094	0.127	0.122	0.123	0.128	0.508	0.402	0.488	0.523
8	0.025	0.049	0.050	0.057	0.049	0.039	0.039	0.057	0.038

Table 3.1: Velocity error and its standard deviation for POD-FC: 8 time intervals compared with 50 time intervals corresponding to a noise level of 20 dB, batch size 50, dropout rate 0.05, variable learning rate from 10^{-3} to 10^{-4}.

time interval	E($\mathbf{V}_{tr}$)	E($\mathbf{V}_{te}$)	E(Vx_{te})	E(Vy_{te})	E(Vz_{te})	D($\mathbf{V}_{te}$)	D(Vx_{te})	D(Vy_{te})	D(Vz_{te})
50	0.122	0.224	0.229	0.220	0.223	0.239	0.243	0.226	0.239
8	0.038	0.039	0.035	0.036	0.040	0.089	0.069	0.063	0.093

Table 3.2: Velocity error and its standard deviation of POD-3D CNN: 8-time intervals compared with 50-time intervals corresponding to 20 dB noise level, batch size 50, dropout rate 0.05, variable learning rate from 10^{-3} to 10^{-4}.

3.6.1.2 Noise level analysis

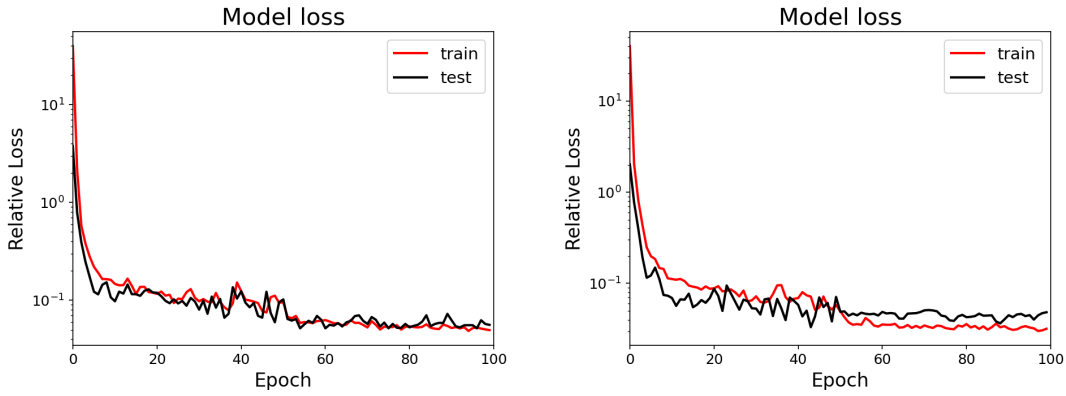

(a) 0 dB (b) 20 dB

Figure 3.12: The loss function curve for different noise levels of POD-FC.

In this study, we consider two Gaussian noise levels corrupting the Radon projections with the POD-Fully connected network architecture. Generally speaking, from the loss function curve displayed in Figure 3.12, we can see that the loss decreases as the epoch number increases for training and testing for both noise levels.

Furthermore, the velocity error and its standard deviation are shown in the Table 3.3. With a lower noise level of 20 dB, we can obtain a smaller velocity error and standard deviation.

For POD-3D CNN, the training loss curve and testing loss curves show a decrease as the epoch number increases for different noise levels as displayed in Figure 3.13. The noise of 0 dB shows a large testing error. Furthermore, the standard deviation is also larger as displayed in the Table 3.4.

It turns out that with a lower noise level, we can achieve a more precise velocity reconstruction and a smaller standard deviation together with more accurate components reconstruction.

Noise level	E($\mathbf{V}_{tr}$)	E($\mathbf{V}_{te}$)	E(Vx_{te})	E(Vy_{te})	E(Vz_{te})	D($\mathbf{V}_{te}$)	D(Vx_{te})	D(Vy_{te})	D(Vz_{te})
0dB	0.050	0.056	0.060	0.061	0.055	0.067	0.102	0.066	0.064
20dB	0.032	0.048	0.051	0.052	0.047	0.017	0.022	0.038	0.015

Table 3.3: Velocity error and its standard deviation for POD-FC: 8 time intervals considered with two noise levels 0 dB and 20 dB, batch size 100, dropout rate 0.05, variable learning rate from 10^{-3} to 10^{-4}.

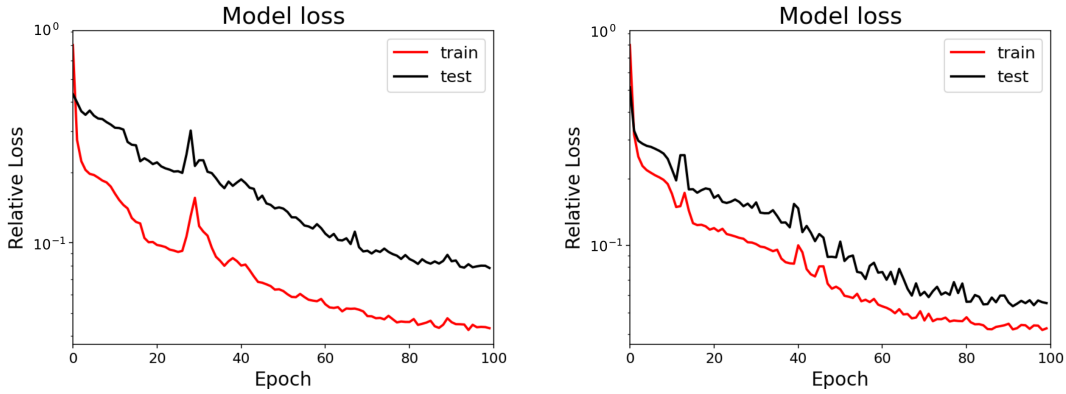

(a) 0 dB (b) 20 dB

Figure 3.13: The loss function curve for different noise levels for POD-3D CNN.

In addition, using the POD-FC method, we can achieve a small standard deviation compared with the POD-CNN method.

3.6.1.3 Network training parameters analysis

After the investigation of time intervals and noise level, in this sub-section, we will present successively the effect of the network training parameters: learning rate, batch size, and dropout rate. For each parameter, for the tuning process, we consider three different values of these parameters at least, to explore its effect on blood velocity reconstruction. And we will also discuss the two different architectures of the network.

Learning rate analysis

For this study, we investigate the range of learning rates from 10^{-3} to 10^{-4} to implement the parameter optimization. The learning rate range is selected between 10^{-3} and 10^{-4}, the batch size 100 for POD-FC and POD-3D CNN, and the dropout rate of 0.05 will be maintained for this investigation. First, we consider the POD-FC network. Generally speaking, the loss function curve shows a decrease following the epoch number increase as displayed in Figure 3.14. This curve shows a small oscillation when choosing a varying learning rate from 10^{-3} to 10^{-4}. After that, we can see in the Table 3.5 that with a varying learning rate from 10^{-3} to 10^{-4} can achieve a small velocity error and a small standard deviation. Therefore, we can conclude that a varying learning rate from 10^{-3} to 10^{-4} can allow us to obtain a small reconstructed velocity error and a small standard deviation for the POD-FC network.

Noise level	E($\mathbf{V}_{tr}$)	E($\mathbf{V}_{te}$)	E(Vx_{te})	E(Vy_{te})	E(Vz_{te})	D($\mathbf{V}_{te}$)	D(Vx_{te})	D(Vy_{te})	D(Vz_{te})
0dB	0.043	0.078	0.082	0.075	0.078	0.447	0.432	0.394	0.455
20dB	0.042	0.055	0.062	0.059	0.054	0.335	0.370	0.325	0.331

Table 3.4: Velocity error and its standard deviation of POD-3D CNN: 8 time intervals considered with two noise levels 0 dB and 20 dB, batch size 100, dropout rate 0.05, variable learning rate from 10^{-3} to 10^{-4}.

Learning rate	E($\mathbf{V}_{tr}$)	E($\mathbf{V}_{te}$)	E(Vx_{te})	E(Vy_{te})	E(Vz_{te})	D($\mathbf{V}_{te}$)	D(Vx_{te})	D(Vy_{te})	D(Vz_{te})
10^{-3}	0.043	0.050	0.087	0.038	0.045	0.054	0.055	0.065	0.054
10^{-3} to 10^{-4}	0.031	0.044	0.054	0.055	0.042	0.023	0.049	0.030	0.020
10^{-4}	0.058	0.078	0.110	0.100	0.069	0.095	0.164	0.192	0.078

Table 3.5: Velocity error and its standard deviation for POD-FC: 8 time intervals, corresponding to a noise level of 20 dB, batch size 100, dropout rate 0.05.

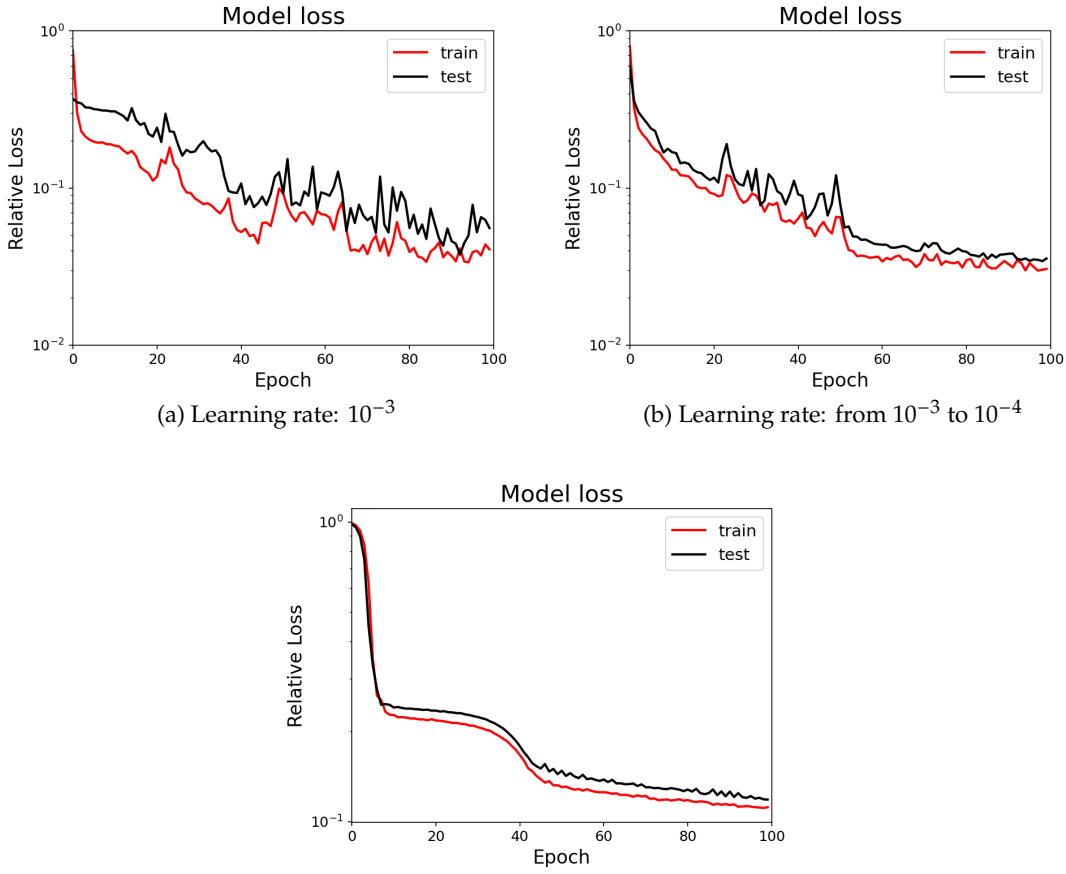

(a) Learning rate: 10^{-3}

(b) Learning rate: from 10^{-3} to 10^{-4}

(c) Learning rate: 10^{-4}

Figure 3.15: The loss function curve of the POD-3D CNN for different learning rate values.

For the POD-3D CNN, the loss function curve is shown in Figure 3.15. It exhibits a big

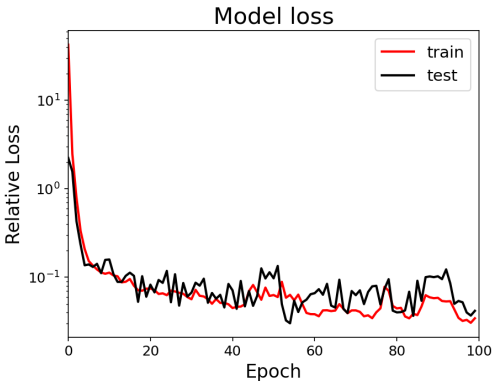

(a) Learning rate: 10^{-3}

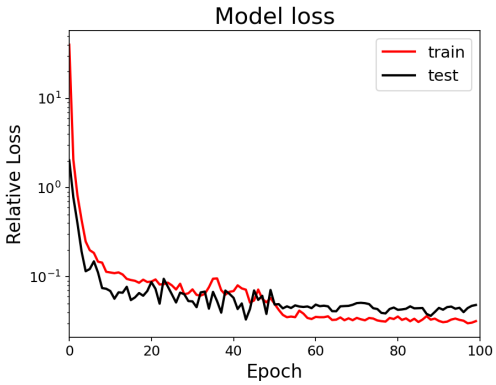

(b) Learning rate: from 10^{-3} to 10^{-4}

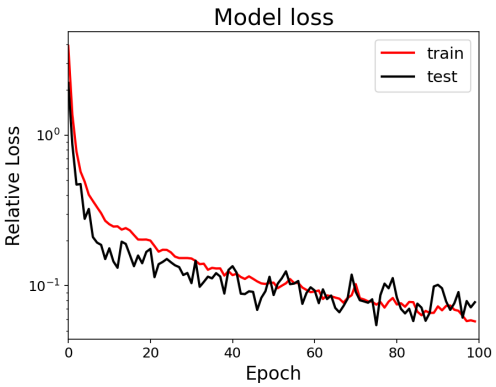

(c) Learning rate: 10^{-4}

Figure 3.14: The loss function curve of the POD-FC for different learning rate values.

oscillation when a higher learning rate of 10^{-3} is selected for the training step as shown in Figure 3.15 a. In contrast, we obtain a small oscillation if a varying learning rate from 10^{-3} to 10^{-4} and a small learning rate 10^{-4} are chosen, as we can see in Figure 3.15 b and c. Moreover, we obtain the same result that a small velocity error and a small standard deviation occur when the variable learning rate decreasing from 10^{-3} to 10^{-4} is considered for training, as we can see in the Table 3.6. We obtain a higher standard deviation using a very small learning rate of 10^{-4}. So, to summarize our results, with the variable learning rate from 10^{-3} to 10^{-4}, we can achieve a small velocity error and a small standard deviation for POD-3D CNN.

Learning rate	E($\mathbf{V}_{tr}$)	E($\mathbf{V}_{te}$)	E(Vx$_{te}$)	E(Vy$_{te}$)	E(Vz$_{te}$)	D($\mathbf{V}_{te}$)	D(Vx$_{te}$)	D(Vy$_{te}$)	D(Vz$_{te}$)
10^{-3}	0.062	0.069	0.071	0.069	0.069	0.091	0.098	0.081	0.091
10^{-3} to 10^{-4}	0.053	0.055	0.060	0.057	0.054	0.118	0.142	0.111	0.117
10^{-4}	0.112	0.118	0.113	0.119	0.119	0.351	0.293	0.332	0.361

Table 3.6: Velocity error and its standard deviation for POD-3D CNN: 8 time intervals, corresponding to a noise level of 20 dB, batch size 100, dropout rate 0.05.

In this work, a variable learning rate from 10^{-3} to 10^{-4} will be used to train the two networks.

Batch size analysis

In this part, we study the batch sizes from 50 to 200 for parameters optimization by keeping the optimized and variable learning rate from 10^{-3} to 10^{-4} and the dropout rate value of 0.05.

For the POD-FC, Figure 3.16 shows that the loss decreases as the epoch number increases. The training error curve is close to the test error curve with a batch size of 200. The corresponding velocity error and its standard deviation are displayed in the Table 3.7. As the batch size increases, the velocity error decreases while the standard deviation shows a decrease. Thus, the batch sizes can play a critical role in affecting the velocity error and its standard deviation.

Batch size	E($\mathbf{V}_{tr}$)	E($\mathbf{V}_{te}$)	E(Vx$_{te}$)	E(Vy$_{te}$)	E(Vz$_{te}$)	D($\mathbf{V}_{te}$)	D(Vx$_{te}$)	D(Vy$_{te}$)	D(Vz$_{te}$)
50	0.025	0.049	0.050	0.057	0.049	0.039	0.039	0.057	0.038
100	0.031	0.044	0.054	0.055	0.042	0.023	0.049	0.030	0.020
200	0.042	0.043	0.044	0.059	0.042	0.018	0.028	0.027	0.017

Table 3.7: Velocity error and its standard deviation for POD-FC network: 8-time intervals, corresponding to a noise level of 20 dB, variable learning rate from 10^{-3} to 10^{-4}, dropout rate 0.05.

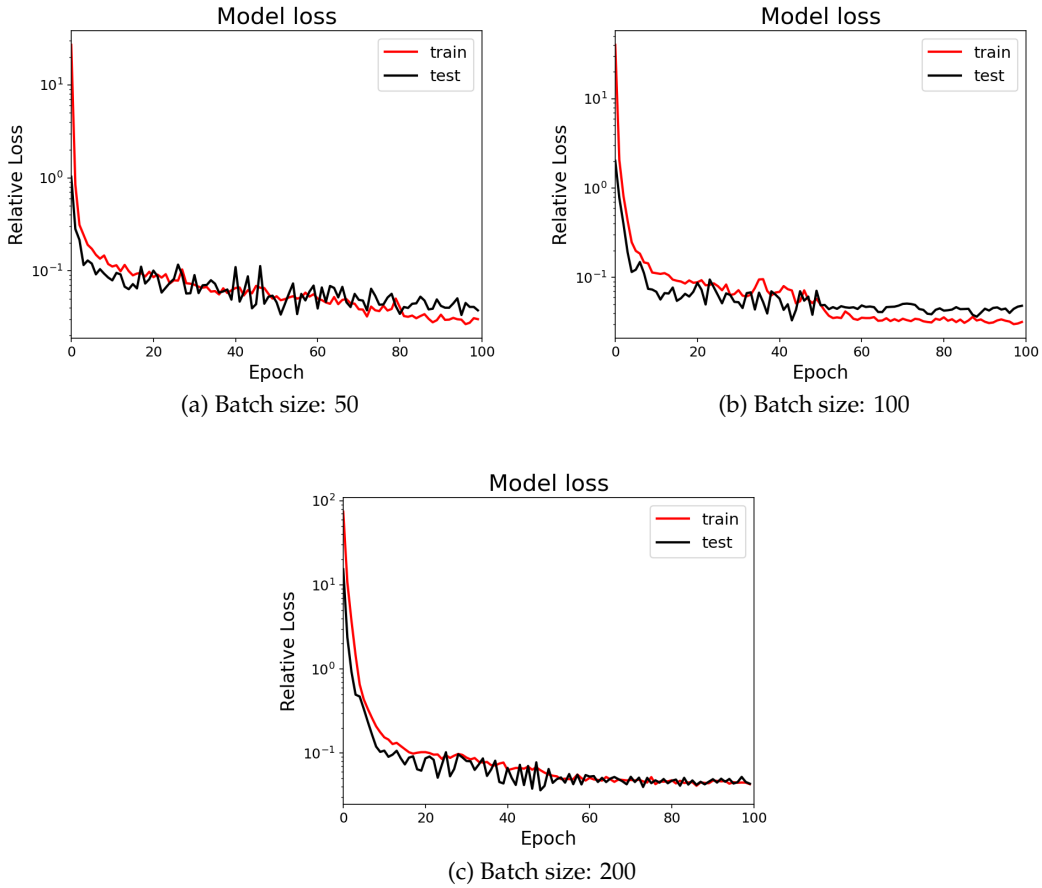

(a) Batch size: 50

(b) Batch size: 100

(c) Batch size: 200

Figure 3.16: The loss function curve of the POD-FC network for different batch sizes.

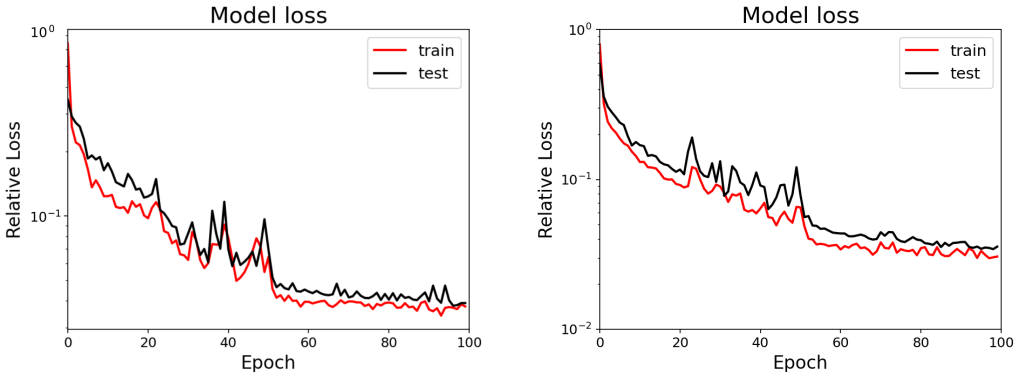

(a) Batch size: 50

(b) Batch size: 100

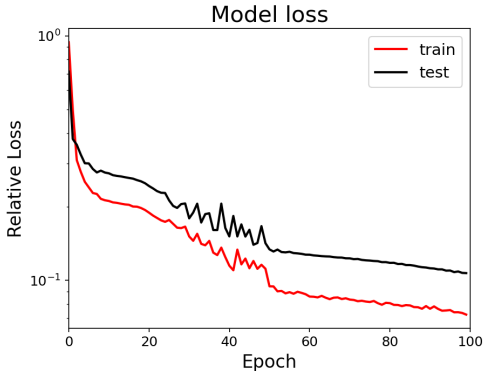

(c) Batch size: 200

Figure 3.17: The loss function curve of the POD-3D CNN for different batch sizes.

For the POD-CNN network, the loss function shows a decrease, and the two curves of training and testing error are not very close in comparison with the POD-FC network in Figure 3.17. Moreover, in the Table 3.8, the predicted velocity error and its standard deviation increase as the batch size increases. So it can be concluded that the batch size has an important effect on the POD-3D CNN model.

Batch size	E($\mathbf{V}_{tr}$)	E($\mathbf{V}_{te}$)	E(Vx$_{te}$)	E(Vy$_{te}$)	E(Vz$_{te}$)	D($\mathbf{V}_{te}$)	D(Vx$_{te}$)	D(Vy$_{te}$)	D(Vz$_{te}$)
50	0.037	0.039	0.035	0.036	0.040	0.241	0.148	0.154	0.258
100	0.053	0.055	0.060	0.057	0.054	0.118	0.142	0.111	0.117
200	0.072	0.107	0.101	0.104	0.108	0.694	0.535	0.628	0.720

Table 3.8: Velocity error and its standard deviation for POD-3D CNN network: 8 time intervals, corresponding to a noise level of 20 dB, variable learning rate from 10^{-3} to 10^{-4}, dropout rate 0.05.

According to the results, a batch size of 200 can achieve a low standard deviation for a POD-Fully connected network. A small batch size of 50 can improve the accuracy of the velocity reconstruction for the POD-3D CNN network. Furthermore, it should be mentioned that the standard deviation is higher compared with POD-FC. So to avoid this possible overfitting, we will try to optimize the dropout rate in the next section. The optimized batch size parameter

will be used in the following sections.

Dropout layer analysis

Based on the optimized variable learning rate from 10^{-3} to 10^{-4}, the optimized batch size value of 200 and 50 for POD-FC, and POD-3D CNN respectively, a dropout rate in the range [0, 0.2] is considered to find the optimal dropout rate.

The loss decreases as the epoch number increases in Figure 3.18 for one dropout layer after the first fully connected layer when using the POD-FC. The training and the testing curves exhibit a similar trend when using a small dropout. Additionally, as the dropout rate increases, the velocity error and its standard deviation increase in Table 3.9.

For the POD-3D CNN, the same phenomenon that the training curve is closed to the testing curve with a small dropout rate is displayed in Figure 3.19. Meanwhile, as the dropout rate increases, the velocity error increases as shown in Table 3.10.

It is worth noticing that the overfitting phenomenon might occur when the velocity error is small while the standard deviation is large with a dropout rate value of 0.05. Thus, to avoid overfitting in the model, a small dropout rate value can be considered for POD-3D CNN. So it turns out that a very small dropout rate value can achieve a small velocity error and a small standard deviation for both POD-FC and POD-3D CNN.

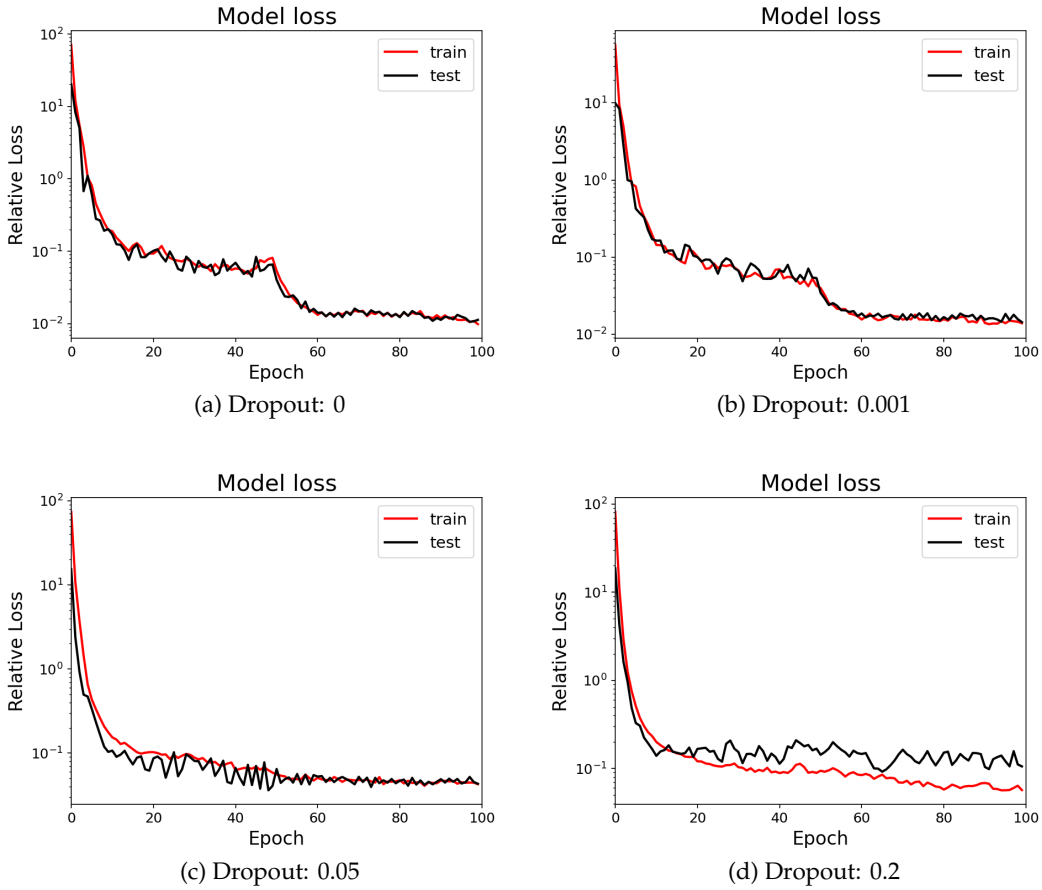

(a) Dropout: 0 (b) Dropout: 0.001

(c) Dropout: 0.05 (d) Dropout: 0.2

Figure 3.18: The loss function curve of the POD-FC for different dropout rate values.

Dropout rate	E($\mathbf{V}_{tr}$)	E($\mathbf{V}_{te}$)	E(Vx$_{te}$)	E(Vy$_{te}$)	E(Vz$_{te}$)	D($\mathbf{V}_{te}$)	D(Vx$_{te}$)	D(Vy$_{te}$)	D(Vz$_{te}$)
0	0.010	0.011	0.014	0.019	0.010	0.015	0.021	0.019	0.014
0.001	0.013	0.014	0.017	0.018	0.013	0.022	0.027	0.017	0.021
0.05	0.042	0.043	0.044	0.059	0.042	0.018	0.028	0.027	0.017
0.2	0.064	0.111	0.107	0.118	0.111	0.067	0.095	0.065	0.065

Table 3.9: Velocity error and its standard deviation for POD-FC network: 8 time intervals, corresponding to a noise level of 20 dB noise level, variable learning rate from 10^{-3} to 10^{-4}, batch size 200.

3.6.1.4 Summary

In this sub-section, we have studied the reconstructed velocity error and its standard deviation. The main investigation is the influence of time interval, noise level and network training parameters such as learning rate, batch size, and dropout rate. The range of the time interval, noise level, and network training parameters investigated are the following: time intervals [8, 50], noise level [0 dB, 20 dB], learning rate [10^{-4}, 10^{-3}], batch size [50, 200], and dropout rate [0, 0.2]. We will make a short summary to recognize the influence of the various parameters and

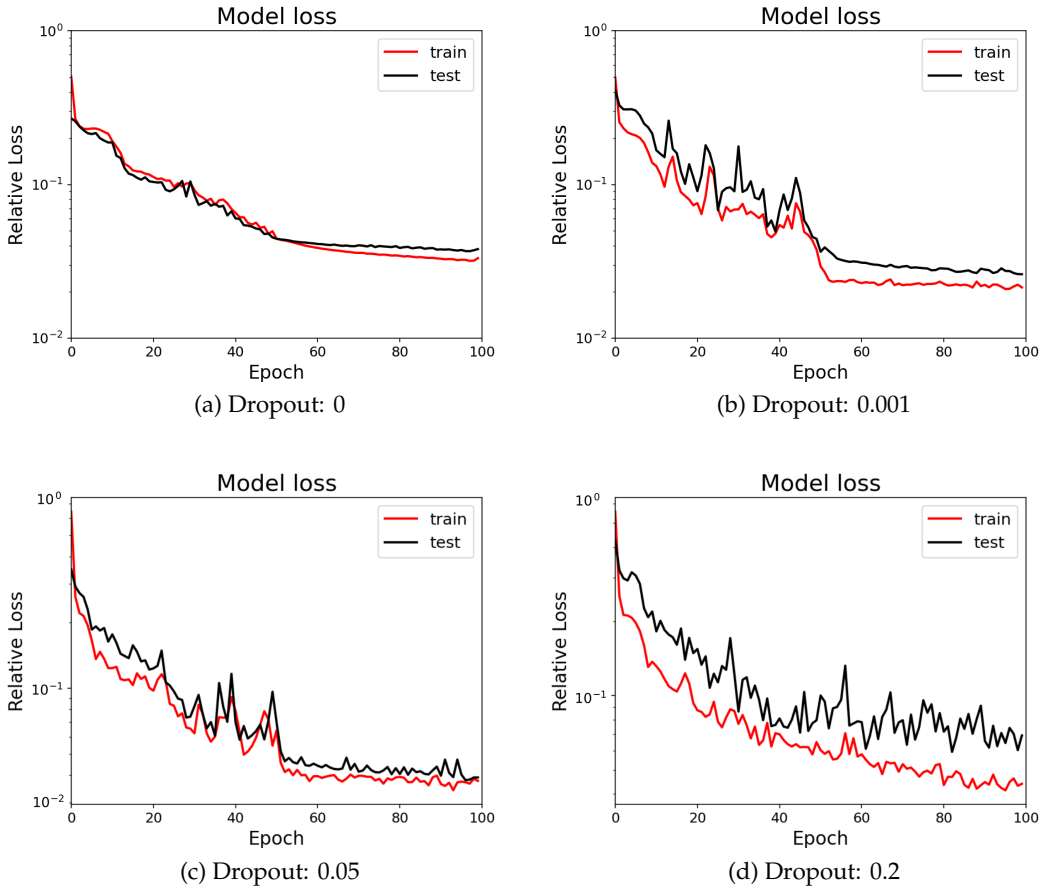

(a) Dropout: 0 (b) Dropout: 0.001

(c) Dropout: 0.05 (d) Dropout: 0.2

Figure 3.19: The loss function curve of the POD-3D CNN for different dropout rate values.

Dropout rate	E($\mathbf{V}_{tr}$)	E($\mathbf{V}_{te}$)	E(Vx$_{te}$)	E(Vy$_{te}$)	E(Vz$_{te}$)	D($\mathbf{V}_{te}$)	D(Vx$_{te}$)	D(Vy$_{te}$)	D(Vz$_{te}$)
0	0.024	0.025	0.028	0.029	0.024	0.039	0.044	0.037	0.039
0.001	0.0214	0.026	0.028	0.032	0.026	0.088	0.087	0.097	0.088
0.05	0.038	0.039	0.035	0.036	0.040	0.241	0.148	0.154	0.258
0.2	0.059	0.065	0.071	0.067	0.065	0.104	0.122	0.089	0.104

Table 3.10: Velocity error and its standard deviation of POD-3D CNN: 8-time intervals, corresponding to a noise level of 20 dB, variable learning rate from 10^{-3} to 10^{-4}, batch size 50.

present the optimized parameters below.

The results indicate that the reconstructed velocity is obviously affected by these parameters with the two network architectures. In this work, choosing a 8 time steps interval, we can achieve a small velocity error and a small standard deviation compared with the 50 time steps intervals. A small noise of 20 dB leads to a more precise velocity reconstruction with a small standard deviation. But a variable learning rate from 10^{-3} to 10^{-4} can effectively decrease the velocity error and improve the network results. On the other hand, as the batch size increases, the velocity error does not display a large change but its standard deviation decreases for POD-FC while the velocity error and its standard deviation increase for POD-3D CNN. In other words, batch sizes of 200 can improve standard deviations for a POD-Fully connected network, and a batch sizes of 50 can improve the accuracy of the velocity reconstruction for the POD-3D CNN network. Furthermore, a small dropout rate value(<0.05) can achieve a small velocity error and then enhance the network performance.

Based on these results, the optimal parameters are a variable learning rate from 10^{-3} to 10^{-4} for both networks, batch size of 200 for POD-FC, batch size of 50 for POD-3D CNN, and small dropout rate 0.05 for both networks. We will use these parameters to reconstruct the blood velocity. To validate the applicability of the network model for different conditions, we will present two cases, one case with a low inlet velocity and another case with a higher inlet velocity below.

3.6.2 Velocity reconstruction with a low inlet velocity

In this section, We will study the reconstructed velocity with a low inlet velocity of 0.025 m/s. The three dimensions of the velocity distribution will be discussed, and we will present the reconstructed velocity distribution in various flow directions: XY plane, XZ plane, and YZ plane, focusing on local views. Especially, the regions close to the bifurcation and the bifurcation region will be considered to estimate reconstruction results in the complex regions. The results displayed are the one obtained with the POD-FC network. Similar results are obtained with the CNN based method.

3.6.2.1 3D velocity distribution

Here, the ground truth ($\mathbf{V}_{true}$), the reconstructed velocity ($\mathbf{V}_r$) and the error map ($\mathbf{V}_r$-$\mathbf{V}_{true}$) for the 3D velocity components are shown in Figure 3.20. It can be seen that the reconstructed velocities in Figure 3.20 b, e, and h are similar to the ground truth in Figure 3.20 a, d, and g, especially the region with a negative velocity value or the region with a high-velocity value. The error map allows us to understand the difference in the velocity fields particularly the regions of positive error or negative error. From the error maps shown in Figure 3.20 c, f, and i, we can find that the error map velocity fields present a positive value along the z-axis, while negative values occur along the x and y-axes, so it can indicate that the reconstructed velocity

is obtained with high values in comparison with the ground truth along the z-axis while lower values are obtained along the x and y-axes.

3.6.2.2 Velocity distribution in the XY plane

After giving the 3D overall velocity field, the slices along different directions will be presented and the XY planes will be presented first. Here, two slices located at z=0.155m, and z=0.165m near the bifurcation or in the bifurcation will be displayed.

Regions z=0.155

In this region with z=0.155m near the inlet, the ground truth, and reconstructed velocity, error map of velocity components are mainly distributed in the center of the vessel as shown in Figure 3.21. There are negative values for the velocity along x. The reason is that the vessel is

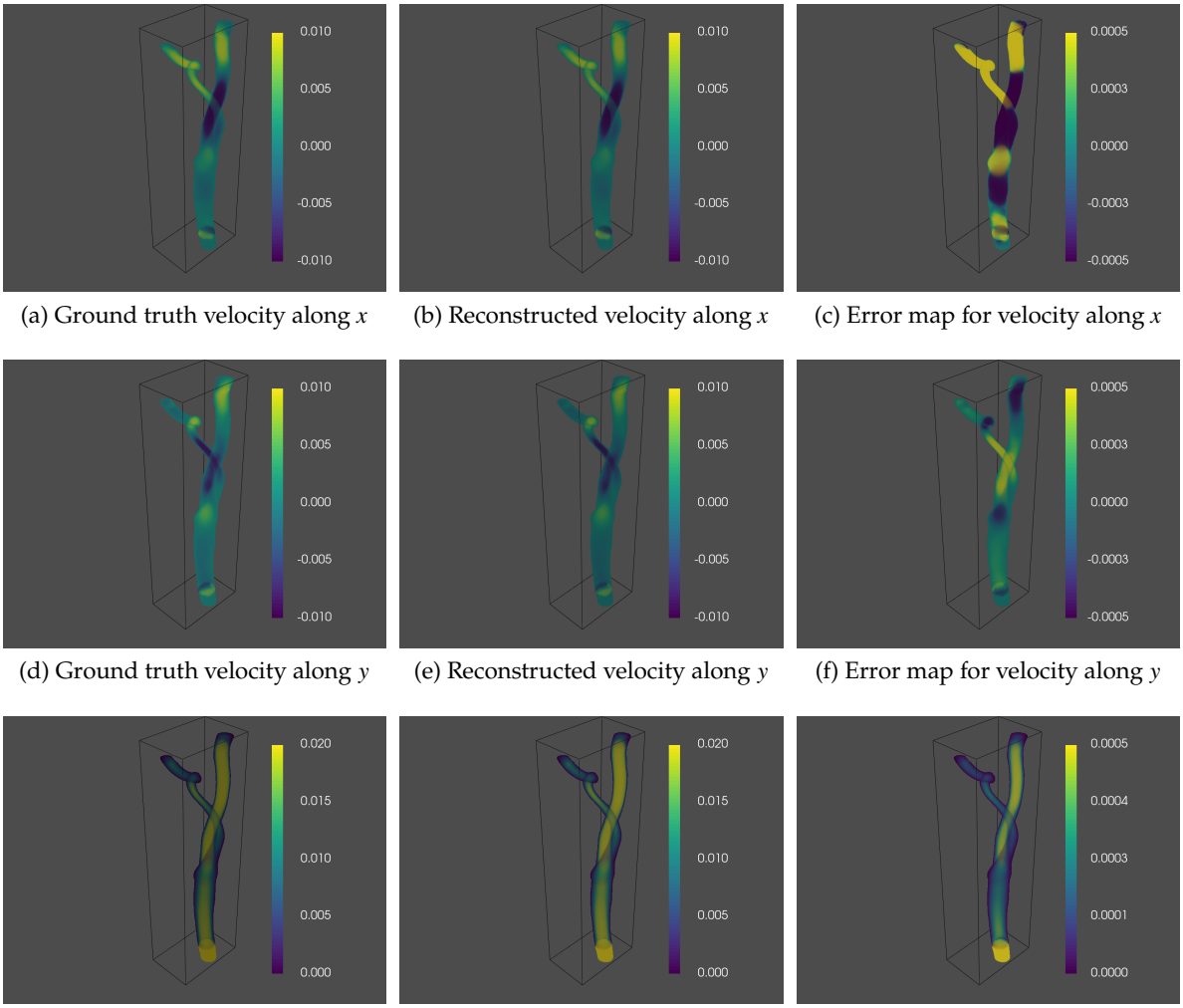

(a) Ground truth velocity along x (b) Reconstructed velocity along x (c) Error map for velocity along x

(d) Ground truth velocity along y (e) Reconstructed velocity along y (f) Error map for velocity along y

(g) Ground truth velocity along z (h) Reconstructed velocity along z (i) Error map for velocity along z

Figure 3.20: Distribution of ground truth velocity, reconstructed velocity with POD-DL methods and its error map: inlet velocity 0.025m/s, inlet tracer concentration 1.0kg/m^3, diffusion coefficient 1e-5, noise level 20 dB

complex and bent which can lead to a complex flow near the border. The corresponding error map allows us to understand that the main error region appears in the center, so we can pay more attention to improving this region in the future. From the error map, we observe the positive velocity error that appears along the z-axis and the negative velocity error along the x and y components in agreement with the 3D velocity fields. Generally, it turns out that the reconstructed velocity closely matches the ground truth at this location.

Region in the bifurcation z=0.165

One position has already been presented above. We will explore another region in the bifurcation z=0.165m. The velocity distributions are displayed in Figure 3.22. As we can see from Figure 3.22, the high velocity is exhibited close to the border of the large vessel branch. Conversely, a relatively small velocity is exhibited in another vessel branch and it shows a negative value along the x, and y components due to the twisted vessel leading to a direction change. The corresponding error maps in Figure 3.22 c, f, and i show that the error is distributed in the region with a high absolute velocity through the bifurcation. Additionally, the same result is obtained that a negative error is observed along the x and y components as in the region studied before.

Towards the z direction, the blood velocity can be reconstructed with a complex bifurcation with a small inlet velocity. The reconstructed velocity is higher than the ground truth along the z-axis as shown in Figure 3.22 i, and could be lower than the ground truth along other axes in Figure 3.22 c and f.

3.6.2.3 Velocity distribution of XZ plane

After studying the XY planes, we will present the XZ planes. It is also interesting to study the blood velocity distribution along these XZ planes. The velocity reconstruction at two positions y=0.014m and y=0.024m will be given in the following figures.

Regions y=0.014

The location y=0.014m is selected in this study because there is a single blood vessel. The ground truth, reconstructed velocity, and error map of velocity components are shown in Figure 3.23. The reconstructed velocities in Figure 3.23 b, e, and h are similar to the ground truth velocities in Figure 3.23 a, d, and g. It can be found that the positive velocity error proves that the value of reconstructed velocity is higher than the ground truth along the z-axis in Figure 3.23 i. In contrast, the lower reconstructed velocity occurs along the x and y components in Figure 3.23 c and f respectively.

Regions y=0.024

The ground truth velocity, reconstructed velocity, and their error map at the position y=0.024m are shown in Figure 3.24. This plane shows how complex the vessel is. Generally speaking, the reconstructed velocity in Figure 3.24 b, e, and h are similar to the ground truth in Figure 3.24 a, d, and g respectively. Along the z-axis, the high-velocity value is more concentrated on the center of the blood vessel. One branch of the blood vessel concentrates the main part of the flow. Additionally, the figures show that the blood velocity is positive and the error map between reconstructed velocity and ground truth is positive in Figure 3.24 i. The error map may exhibit negative values for the x and y axes in Figure 3.24 c and f respectively, indicating that the reconstructed velocity can be lower than the ground truth in some regions.

In these two regions of XZ planes, we find that the reconstructed velocity is similar to the ground truth. The reconstructed velocity error is higher than the ground truth along the z-axis and could be lower than the ground truth along the x and y axes.

3.6.2.4 Velocity distribution of YZ plane

We have already presented the blood velocity reconstruction at XY and the XZ plane. In this part, we will turn our attention to the x-axis or YZ plane with two locations such as x=0.187m and x=0.199m.

Regions x=0.187

The velocity distributions of the ground truth, reconstructed velocity, and their error map at the position x=0.187m are shown in Figure 3.25.

Similarly to what was observed before, the reconstructed velocity in Figure 3.25 b, e, and h are similar to the ground truth a, d, and g respectively. Particularly, the top small region belongs to the small branch of the blood vessel in the bifurcation and its speed value is lower than in the main branch. The reason why it shows a small speed value is that the vessel is a complex phantom and the flow resistance is big. The ground truth and reconstructed velocity show a positive value along the z-axis and they exhibit negative values in some regions along the x and y components. Figures 3.25 c, f, and i are the error maps along the x, y, and z components respectively. The velocity error is positive along the z-axis while could be negative along other axes.

Regions x=0.199

The position x=0.187m has been presented before. Now, the velocity distributions of ground truth velocity, reconstructed velocity, and their error map at another plane x=0.199m will be given in Figure 3.26. The results show that the reconstructed velocity for each component matches the ground truth very well. From the error maps in Figure 3.26 c, f, and i, we can find that the velocity error is positive along the z-axis while could be negative along other axes.

So for the YZ plane, we can have a similar conclusion that the velocity can be reconstructed well and the reconstructed velocity value is higher than the ground truth along the z-axis while it could be lower along other axes.

3.6.2.5 Summary

With a low inlet velocity, we have used the optimized deep-learning network model POD-FC to reconstruct a velocity field similar to the ground truth. Two dimensional sections of the reconstructed velocity fields, including the XY plane, XZ plane, and YZ plane are presented in this part. From the 3D reconstructed velocity, we find that the reconstructed velocity is similar to the ground truth. Additionally, the error map velocity fields exhibit a positive value along the z-axis, while negative values can occur along the x and y-axes. It turns out that the velocity is reconstructed with high values in comparison with ground truth along the z-axis while high values or lower values along the x and y-axes are obtained. Furthermore, the same result is obtained in various 2D planes corresponding to the 3D investigation.

3.6.3 Velocity reconstruction with a higher inlet velocity

The low inlet velocity of 0.025m/s has already been considered in the former subsection. The higher inlet velocity of 0.55m/s will be considered. Similarly to what has been presented for

the lower inlet velocity, the three dimensions of the velocity distribution along the XY plane, XZ plane, and YZ plane will be investigated below.

3.6.3.1 3D velocity distribution

In this part, we will give the 3D velocity distribution with a higher inlet velocity condition. The reconstructed velocity components displayed in Figure 3.27 b, e, and h are similar to the ground truth ones 3.27 a, d, and g respectively, especially the region with a negative velocity value or a high-velocity absolute value. From the error maps shown in Figure 3.27 c, f, and i, we can find that the error map velocity fields display a positive value along the z-axis, while negative values occur along the x and y-axes, so it turns out that the reconstructed velocity can achieve similar values than the ground truth and it shows high values in comparison with ground truth along the z-axis while possible high values or lower values along the x and y-axes.

3.6.3.2 Velocity distribution of XY plane

The 3D overall velocity fields are presented above. Next, we will provide the slice along different directions and present the main flow direction z direction or XY plane first. Here, two slices located at z=0.155m, and z=0.165m near the bifurcation or in the bifurcation will be shown.

Regions z=0.155

In this region near the inlet at z=0.155m, the ground truth velocity, reconstructed velocity, and its error maps of velocity components are concentrated in the central area of the vessel or lower left corner of the figure for the x-axis, as depicted in Figure 3.28. Notably, negative values for the velocity along the x-axis are observed at the upper right corner of Figure 3.28 a and b. This behavior can be attributed to the complexity and bending of the blood vessel, leading to intricate flow patterns near the borders of the blood vessel. By presenting the corresponding error map in Figure 3.28 c, f, and i, we can obtain valuable insights into the predominant error region situated at the center or lower left corner of the figure. As a result, we can focus on the reconstruction performance in this relatively big error area.

The error map reveals the presence of positive velocity errors along the z-axis and negative velocity errors along the x and y components, consistent with the characteristics of the three-dimensional velocity fields. Generally speaking, the reconstructed velocity closely aligns with the ground truth at this XY plane, indicating the reliability and accuracy of the proposed POD-DL method. Meanwhile, the main errors are found in the center for the y and z components and the lower left corner for x components.

Region in the bifurcation z=0.165

We will display the distribution of ground truth velocity, the reconstructed velocity for POD-DL methods, and the error map at the bifurcation z=0.165m in Figure 3.29. Evidently, the reconstructed velocity distributions Figure 3.29 b, e, and h show a similar shape compared with the ground truth Figure 3.29 a, d, and g respectively. From the velocity error maps Figure 3.29 c, f, and i, the error map shows a positive region along y and z components while a negative region can occur along x component.

3.6.3.3 Velocity distribution of XZ plane

After presenting the XY plane, we will give the ground truth velocity, reconstructed velocity, and its error map at two locations y=0.014m and y=0.024m.

Regions y=0.014

Firstly, the location y=0.014m is considered. The ground truth, reconstructed velocity, and error map of velocity components are shown in Figure 3.30. The reconstructed velocities in Figure 3.30 b, e, and h are similar to the ground truth velocities in Figure 3.30 a, d, and g respectively. Additionally, the positive region in the error map is shown in Figure 3.30 c and i correspond to the x and z components while the negative region can occur along the y-axis in Figure 3.30 f.

Regions y=0.024

The ground truth velocity, reconstructed velocity, and its error map at the position y=0.024m are displayed in Figure 3.31. The reconstructed velocities in Figure 3.31 b, e, and h are similar to the ground truth in Figure 3.31 a, d and g respectively. Furthermore, it shows that the blood velocity error is positive along the z component in Figure 3.31 i, and the error map may exhibit negative values for the x and y components in Figure 3.31 c and f respectively.

3.6.3.4 Velocity distribution of YZ plane

In the former subsection, the blood velocity reconstruction at XY and the XZ plane have been presented. Then, we will pay attention to the x-axis or YZ plane with two locations such as x=0.187m and x=0.199m.

Regions x=0.187

The velocity distribution of the ground truth, reconstructed velocity, and its error map at the position x=0.187m are shown in Figure 3.32. In these figures, the small region at the top is related to the small branch of the blood vessel. Similarly to the other planes, the reconstructed velocities in Figure 3.25 b, e and h are similar to the ground truth in Figure 3.32 a, d and g respectively. From the error maps in Figure 3.32 c, f, i, it is obvious that the velocity error is positive along z component and can be negative along x and y components in this region.

Regions x=0.199

we have presented the location x=0.187m before. Next, the velocity distribution of ground truth velocity, reconstructed velocity, and its error map at YZ plane x=0.199m will be given in Figure 3.33. The results show that the reconstructed velocity for each component in Figure 3.33 b, e, and h can match the ground truth in Figure 3.33 a, d and g respectively. Moreover, the error maps in Figure 3.33 c, f, and i, show positive values along the z-axis and could give negative values along the x and y components.

3.6.3.5 Summary

In the previous sub-section, we already demonstrated the application of blood velocity reconstruction with a low inlet velocity. To further assess the effectiveness of our POD-DL network model for blood velocity reconstruction with a higher inlet velocity of 0.55m/s, we presented additional reconstructions. We analyzed the 3D reconstructed velocity field, as well as 2D

velocity fields along the XY, XZ, and YZ planes, and compared them with the corresponding ground truth velocity. Overall, we observed that the reconstructed velocity closely matches the ground truth in the 3D reconstruction. Moreover, when observing the error map of the velocity fields, we noticed positive values along the z-axis, while negative values were observed along the x and y-axis. These findings indicate that the reconstructed velocity shows relatively higher velocity along the z-axis compared to the ground truth, whereas the x and y-axes may exhibit both high and low values of reconstructed velocities. Additionally, this pattern was consistent across the different 2D planes (XY, XZ, and YZ) corresponding to the 3D investigation. The similarity between the 2D and 3D results further validates the accuracy and reliability of our POD-DL network model for blood flow velocity reconstruction under higher inlet velocity conditions.

In summary, this case with a higher inlet velocity condition demonstrates that the POD-DL network model is effective in accurately reconstructing blood velocity, showing that it can be applied in the field of medical imaging and cardiovascular research.

3.6.4 Comparison with the POD-adjoint method

Here, we will compare the POD-DL methods and the POD-adjoint method with respect to the offline CPU time, the online CPU time for blood velocity reconstruction, and the reconstructed velocity error with its standard deviation.

3.6.4.1 Offline step

The offline step includes the calculation of snapshots for the velocity $\mathbf{V}$, the tracer concentration f, the Radon projections Rf, and the training of the POD-DL method. For the POD-adjoint method, we need the snapshots of velocity $\mathbf{V}$, tracer concentration f, and adjoint variable p obtained with the adjoint equation. We will give more detailed information associated with the offline CPU time for these calculations. The Table below gives the CPU time for the different calculations in the context of this investigation. Particularly, it gives the time required for estimating the velocity field in a stationary state, simulating the tracer concentration for a one-time step interval, and performing gradient descent with the adjoint variable for a one-time step interval. For the POD-DL method, the CPU time corresponds to the calculation of the velocity field, of the Radon projections for the one-time interval, to the training of the model for 800 snapshots and with 8-time intervals.

Velocity	Tracer concentration	Adjoint variable	Gradient descent
8377.7s	54.3s	54.6s	5586.6s

Table 3.11: CPU time for offline step using POD-adjoint method

Velocity	Tracer concentration	Radon projection	DL model training
8377.7s	54.3s	2.13s	6042.8s

Table 3.12: CPU time for offline step using POD-DL method

This Table indicate that the POD-DL method can outperform the POD-adjoint approach with a lower offline CPU time. Yet, the offline time for calculating numerous snapshots on a single processor remains very long. And we are currently working on a decrease of the number of nodes in the mesh to accelerate the calculation of these snapshots.

3.6.4.2 Online step

The reconstruction times are 35s and 3.8×10^{-3}s and 9.6×10^{-4}s for the POD-adjoint, POD-CNN, and POD-FC methods respectively for one test sample. Comparing the online CPU time, it shows that the POD-DL method can reconstruct the blood velocity quickly. After giving the online CPU time, We will give the reconstructed velocity error and its standard deviation below.

NMSE	PPSNR(dB)	POD-adjoint	POD-CNN	POD-FC
$\mathbf{V}$	20	0.061 (0.042)	0.025 (0.039)	0.011 (0.015)
$\mathbf{V}$	0	0.082 (0.061)	0.024 (0.035)	0.024 (0.033)
V_x	20	0.081 (0.085)	0.028 (0.044)	0.014 (0.021)
V_x	0	0.096(0.090)	0.025 (0.038)	0.027 (0.038)
V_y	20	0.070 (0.075)	0.029 (0.037)	0.019 (0.015)
V_y	0	0.082 (0.086)	0.026 (0.032)	0.029 (0.032)
V_z	20	0.051 (0.042)	0.024 (0.039)	0.010 (0.014)
V_z	0	0.074 (0.062)	0.022 (0.036)	0.029 (0.033)

Table 3.13: Comparison of the reconstruction errors for the methods POD-adjoint and POD-CNN for two noise levels. The mean and standard deviation are given for each method and noise level.

The reconstruction error and its standard deviation(in brackets) for various methods including POD-adjoint, POD-CNN, and POD-FC are displayed in the Table 3.13. We can observe that with a lower noise level of 20 dB, we can achieve a smaller reconstruction error and a smaller standard deviation using the POD-FC method in comparison with POD-adjoint and POD-CNN methods. The two POD-DL methods lead to a small reconstruction error and a small standard deviation with a higher noise level of 0 dB compared with the conventional and typical POD-adjoint approach.

The relative reduction rate of total velocity error I with the POD-DL method is expressed as:

$$I(E(\mathbf{V})) = |\overline{E(\mathbf{V})}_{DL} - \overline{E(\mathbf{V})}_{adj}|/|\overline{E(\mathbf{V})}_{adj}| \tag{3.19}$$

where $\overline{E(\mathbf{V})}_{DL}$ and $\overline{E(\mathbf{V})}_{adj}$ denote the reconstructed velocity error with POD-DL methods and with POD-adjoint method respectively. And the relative reduction rate of the velocity error along the x component can be written similarly as:

$$I(E(V_x)) = |\overline{E(V_x)}_{DL} - \overline{E(V_x)}_{adj}|/|\overline{E(V_x)}_{adj}| \tag{3.20}$$

The relative error for the other components is similar.

From the Table 3.14, we can observe that the reduction rate is higher than 80 percent using the POD-FC method compared with the POD-adjoint method. Based on these results, it turns out that the POD-DL method can improve blood velocity reconstruction with a small CPU time.

3.6.5 Clinical applications and challenges

A large number of studies have shown the decisive role of blood flow and disturbed shear stress patterns in clinical atherosclerosis. The studied approaches achieve a more detailed flow of information than classical methods like NMR or ultrasound with a better spatial resolution. The accuracy of the reconstruction of the longitudinal component of the velocity field is improved.

Reduction rate I	PPSNR(dB)	POD-CNN	POD-FC
$\mathbf{V}$	20	59.01%	81.96%
$\mathbf{V}$	0	70.73%	70.73%
V_x	20	65.43%	82.71%
V_x	0	73.95%	71.87%
V_y	20	58.57%	72.85%
V_y	0	68.29%	64.63%
V_z	20	52.94%	80.39%
V_z	0	70.27%	60.81%

Table 3.14: Relative reduction rate velocity error of POD-DL method compared with the POD-adjoint method.

In the framework of our simulations, the resolution for the longitudinal component of the velocity can be estimated as the maximum size of the tetrahedra in the mesh. The estimated resolution, 0.1mm, is better than the typical resolution for phase contrast MRI (Pelc et al., 1994). The developed inversion methods can also estimate accurately the transverse components of the velocity field. This study displayed the accuracy and effectiveness of blood velocity reconstruction with deep learning, but there are some limitations in clinical application such as the measurement of ground truth velocity in the blood vessel. We could use segmented vessels to perform simulations to obtain a large dataset.

3.7 Conclusion

In this Chapter, we have studied two POD-DL methods including POD-FC and POD-3D CNN to reconstruct blood flow velocity in a vessel with a bifurcation. The dataset generation and the architectures of the networks are introduced. To validate the behavior of the network, a large range of network parameters has been considered including the time interval [8, 50], noise level [0 dB, 20 dB], and network training parameters such as learning rate [10^{-4}, 10^{-3}], batch size [50, 200], and dropout rate [0, 0.2].

We have explored the impact of time intervals and noise levels on our results. We find that a small testing velocity error and a small standard deviation are obtained with a smaller 8-time interval. Furthermore, it turns out that we can achieve a more precise velocity reconstruction and a smaller standard deviation together with more accurate components reconstruction with a lower noise level of 20 dB. Additionally, the results show that a variable learning rate from 10^{-3} to 10^{-4} for both networks, batch size of 200 for POD-FC, batch size, of 50 for POD-3D CNN, and a dropout rate of 0 for the two networks are optimized parameters. These parameters can achieve a small reconstructed velocity error and standard deviation.

This work also studies the reconstruction of flow velocity based on the optimized parameters. We study two cases with different inlet velocity conditions, one with a lower inlet velocity condition and another with a higher inlet velocity condition. In these two cases, we have presented the distribution of the blood flow velocity with a 3D view, XY planes, YZ planes, and XZ planes to display the effectiveness of the method for the reconstructed velocity. Obviously, the results show that the 3D reconstructed velocity fields are similar to the ground truth fields, especially in the velocity concentration regions. The 2D velocity fields along the XY, XZ, and YZ planes lead to the same conclusion for both networks with a small reconstruction error.

Furthermore, we compare the POD-DL methods with the POD-adjoint approach with

respect to the offline CPU time and online CPU time, reconstruction error, and its standard deviation. The POD-DL methods improve blood velocity reconstruction with a smaller offline CPU time, smaller CPU time for reconstruction, smaller reconstruction errors, and smaller standard deviations. The relative reduction rate of velocity error using the POD-FC method is estimated to be 80%.

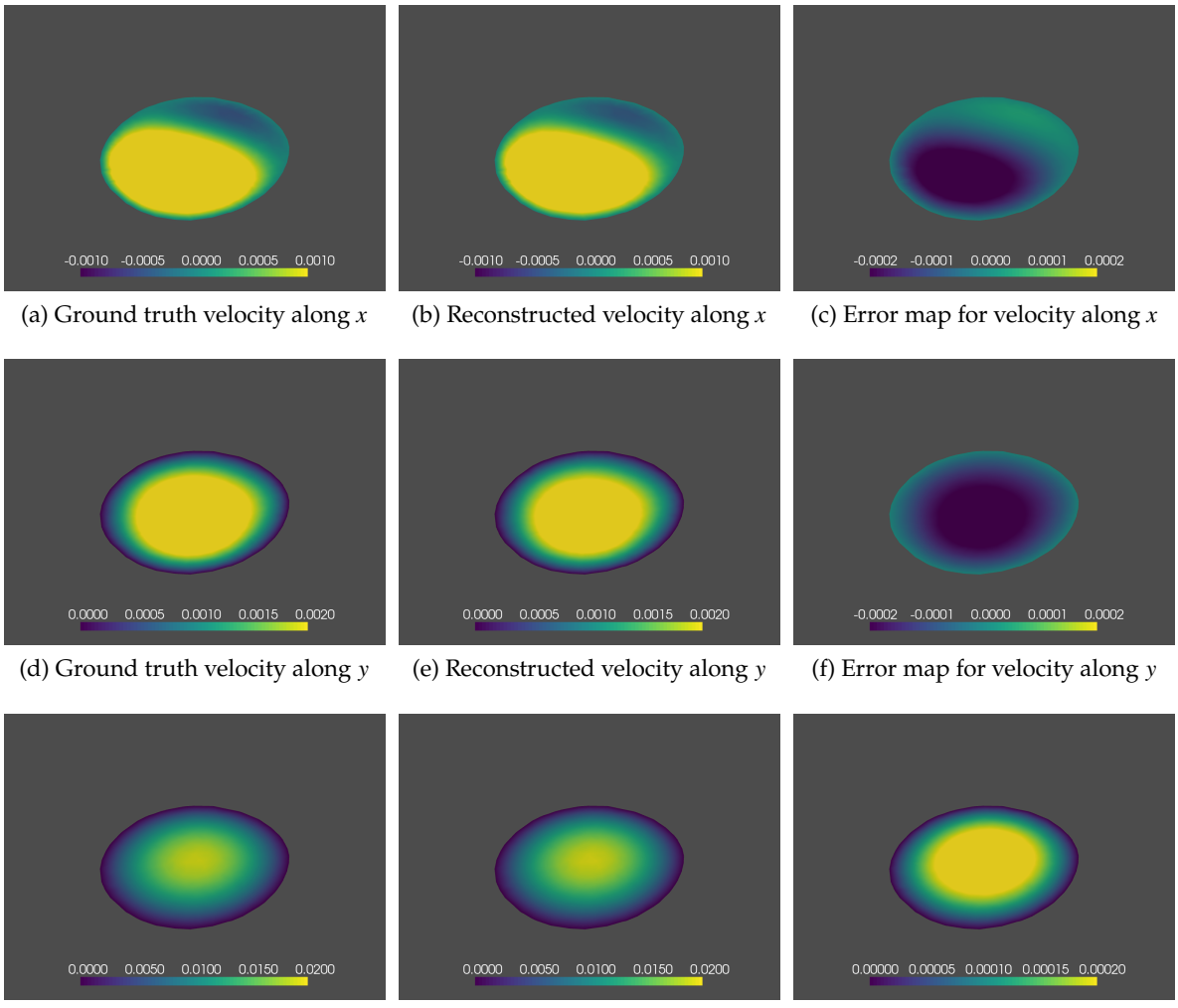

(a) Ground truth velocity along x (b) Reconstructed velocity along x (c) Error map for velocity along x

(d) Ground truth velocity along y (e) Reconstructed velocity along y (f) Error map for velocity along y

(g) Ground truth velocity along z (h) Reconstructed velocity along z (i) Error map for velocity along z

Figure 3.21: Distribution of ground truth velocity, reconstructed velocity of POD-DL methods and its error map: slice location z=0.155m, inlet velocity 0.025m/s, inlet tracer concentration 1.0kg/m^3, diffusion coefficient 1e-5, noise level 20 dB

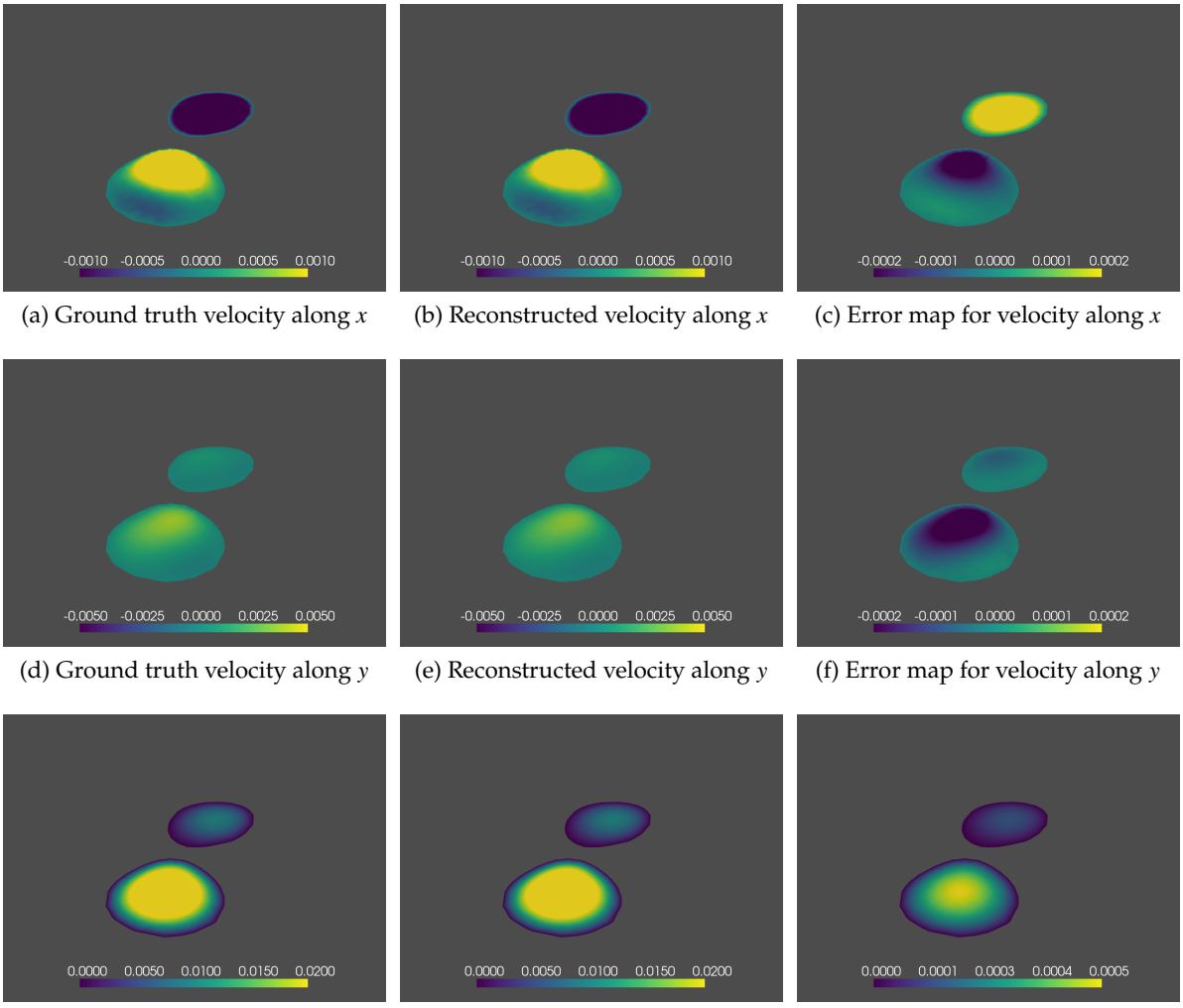

(a) Ground truth velocity along x (b) Reconstructed velocity along x (c) Error map for velocity along x

(d) Ground truth velocity along y (e) Reconstructed velocity along y (f) Error map for velocity along y

(g) Ground truth velocity along z (h) Reconstructed velocity along z (i) Error map for velocity along z

Figure 3.22: Distribution of ground truth velocity, reconstructed velocity with POD-DL methods and its error map: slice location z=0.165m, inlet velocity 0.025m/s, inlet tracer concentration 1.0kg/m^3, diffusion coefficient 1e-5, noise level 20 dB

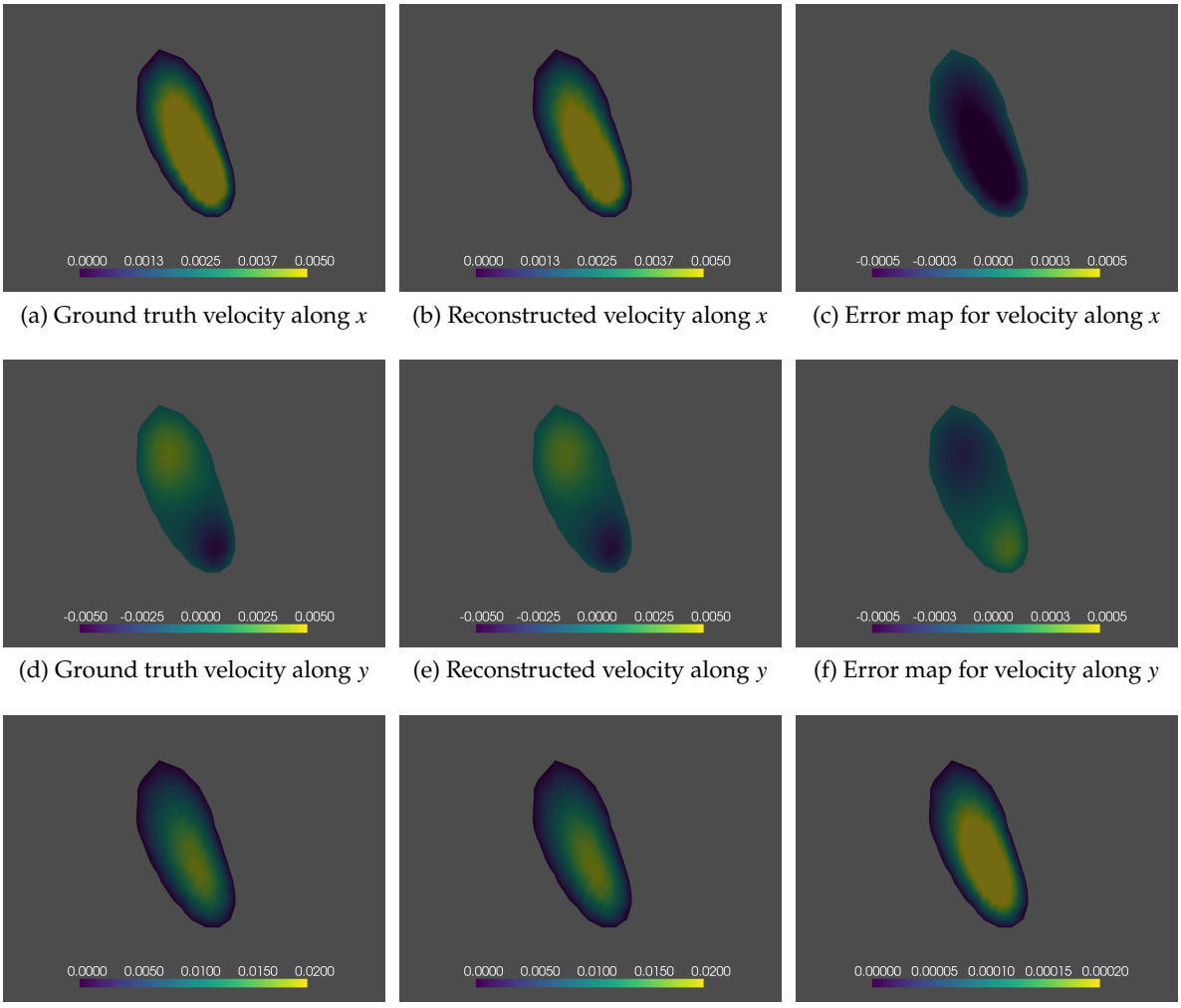

(a) Ground truth velocity along x (b) Reconstructed velocity along x (c) Error map for velocity along x

(d) Ground truth velocity along y (e) Reconstructed velocity along y (f) Error map for velocity along y

(g) Ground truth velocity along z (h) Reconstructed velocity along z (i) Error map for velocity along z

Figure 3.23: Distribution of ground truth velocity, reconstructed velocity with POD-DL methods and its error map: slice location y=0.014m, inlet velocity 0.025m/s, inlet tracer concentration 1.0kg/m^3, diffusion coefficient 1e-5, noise level 20 dB

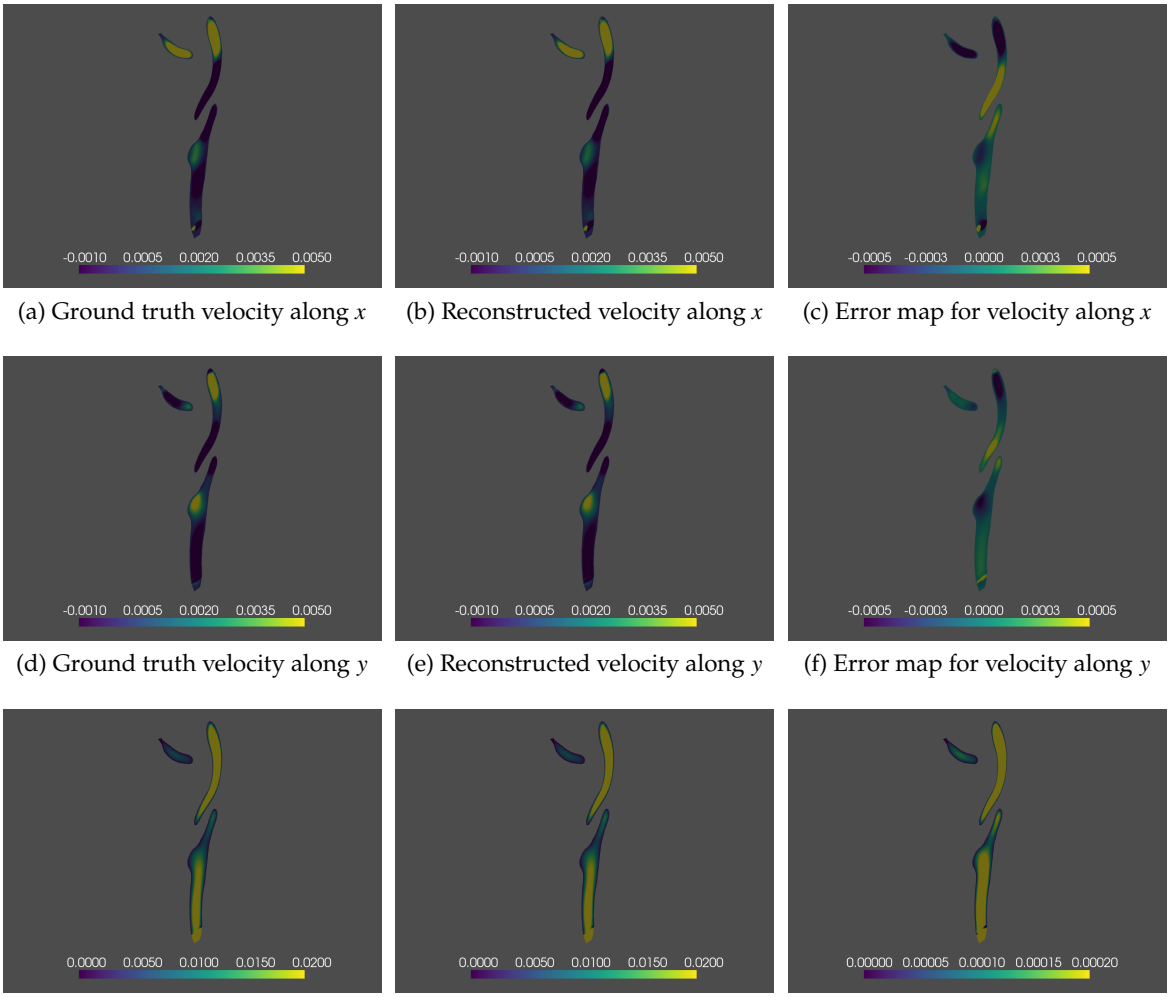

(a) Ground truth velocity along x (b) Reconstructed velocity along x (c) Error map for velocity along x

(d) Ground truth velocity along y (e) Reconstructed velocity along y (f) Error map for velocity along y

(g) Ground truth velocity along z (h) Reconstructed velocity along z (i) Error map for velocity along z

Figure 3.24: Distribution of ground truth velocity, reconstructed velocity with POD-DL methods and its error map: slice location y=0.024m, inlet velocity 0.025m/s, inlet tracer concentration 1.0kg/m^3, diffusion coefficient 1e-5, noise level 20 dB

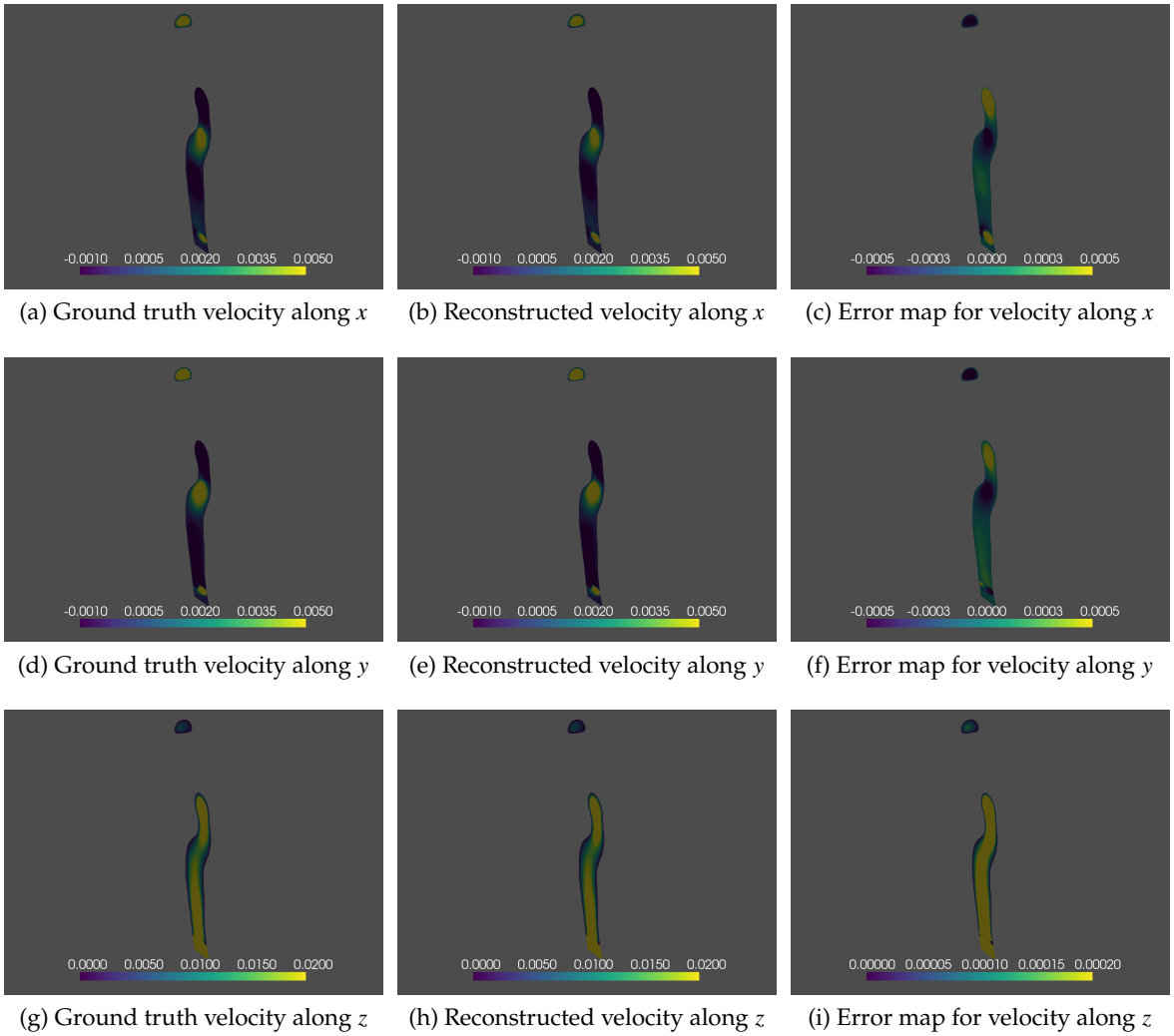

(a) Ground truth velocity along x (b) Reconstructed velocity along x (c) Error map for velocity along x

(d) Ground truth velocity along y (e) Reconstructed velocity along y (f) Error map for velocity along y

(g) Ground truth velocity along z (h) Reconstructed velocity along z (i) Error map for velocity along z

Figure 3.25: Distribution of ground truth velocity, reconstructed velocity of POD-DL methods and its error map: slice location x=0.187m, inlet velocity 0.025m/s, inlet tracer concentration 1.0kg/m^3, diffusion coefficient 1e-5, noise level 20 dB

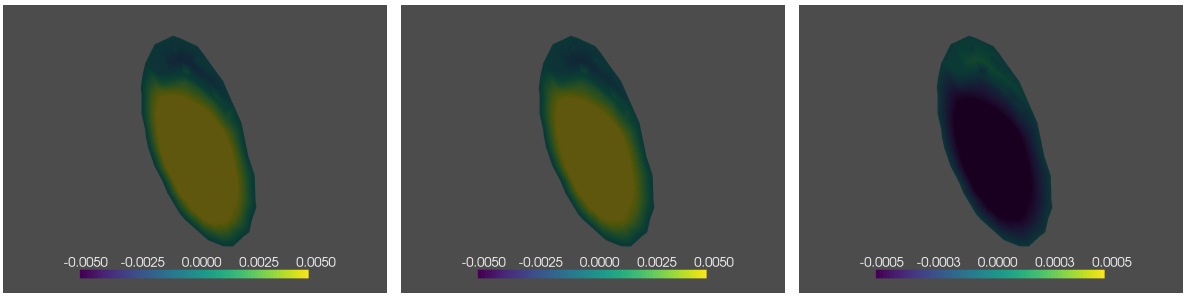

(a) Ground truth velocity along x (b) Reconstructed velocity along x (c) Error map for velocity along x

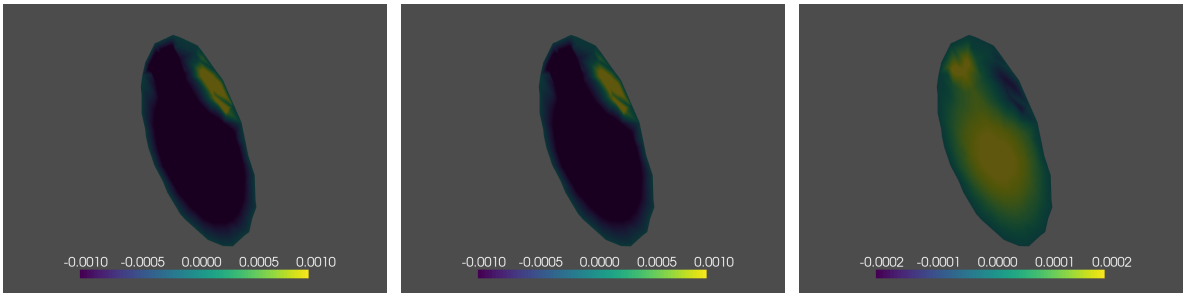

(d) Ground truth velocity along y (e) Reconstructed velocity along y (f) Error map for velocity along y

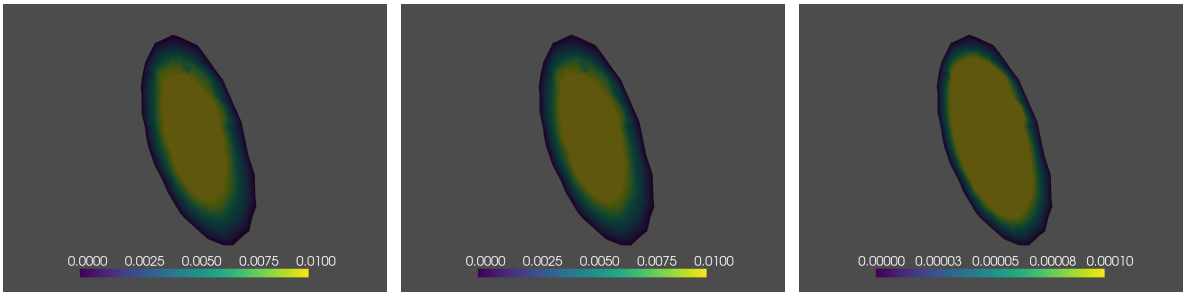

(g) Ground truth velocity along z (h) Reconstructed velocity along z (i) Error map for velocity along z

Figure 3.26: Distribution of ground truth velocity, reconstructed velocity of POD-DL methods and its error map: slice location x=0.199m, inlet velocity 0.025m/s, inlet tracer concentration 1.0kg/m^3, diffusion coefficient 1e-5, noise level 20 dB

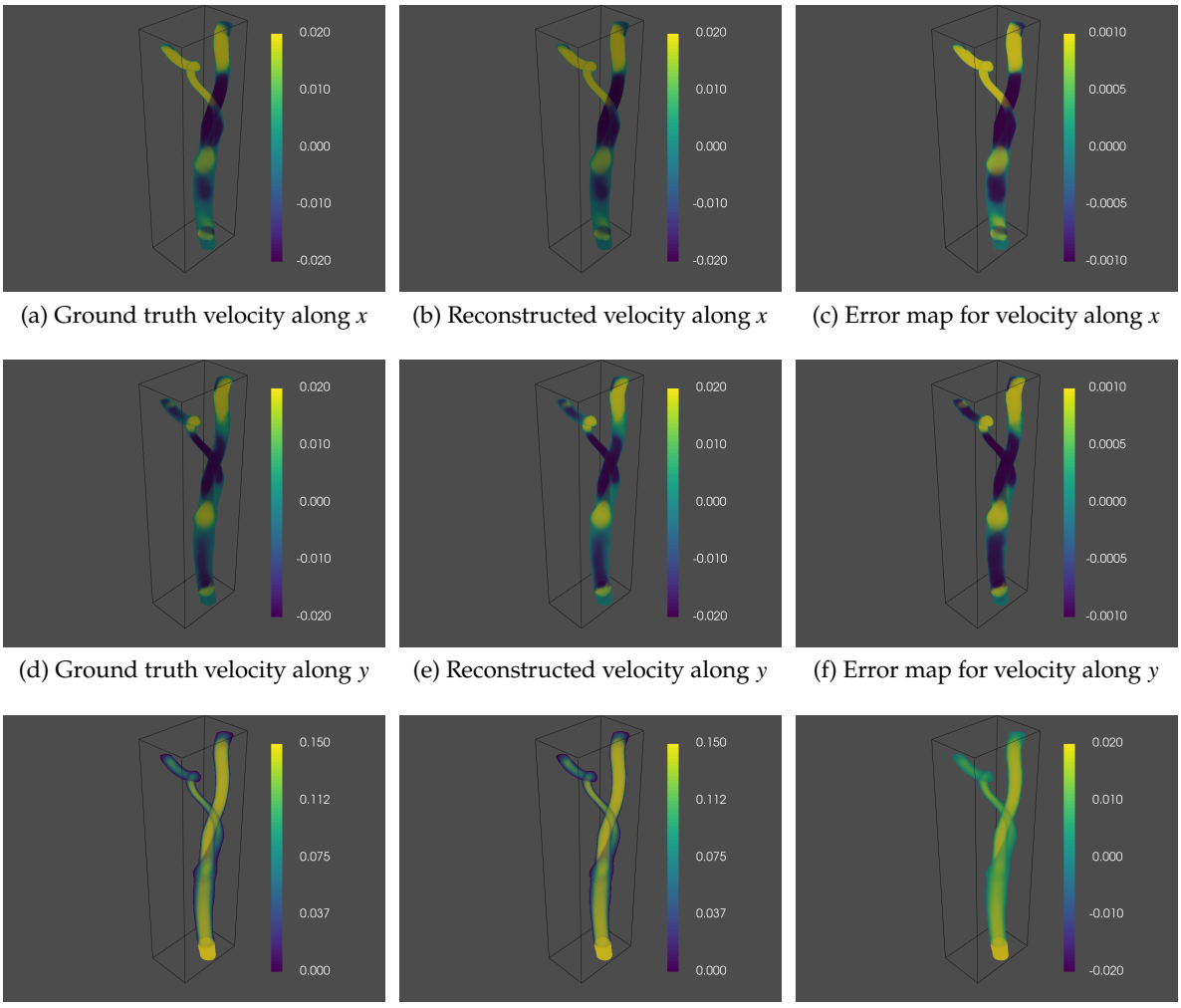

(a) Ground truth velocity along x (b) Reconstructed velocity along x (c) Error map for velocity along x

(d) Ground truth velocity along y (e) Reconstructed velocity along y (f) Error map for velocity along y

(g) Ground truth velocity along z (h) Reconstructed velocity along z (i) Error map for velocity along z

Figure 3.27: Distribution of ground truth velocity, reconstructed velocity of POD-DL methods and its error map in a full vessel: inlet velocity 0.55m/s, outlet pressure 500Pa, inlet tracer concentration 1.0kg/m^3, diffusion coefficient 1e-5, noise level 0 dB

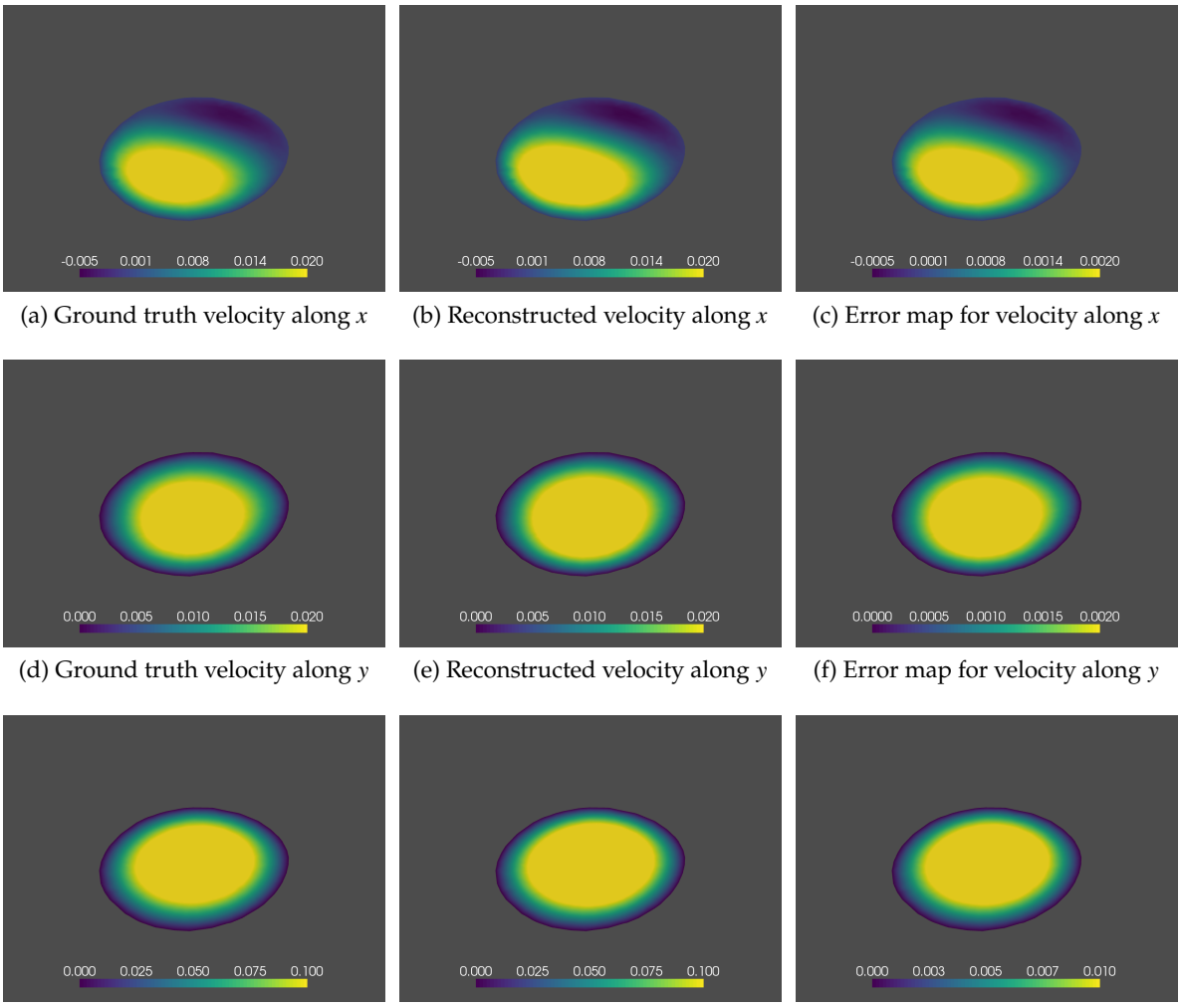

(a) Ground truth velocity along x (b) Reconstructed velocity along x (c) Error map for velocity along x

(d) Ground truth velocity along y (e) Reconstructed velocity along y (f) Error map for velocity along y

(g) Ground truth velocity along z (h) Reconstructed velocity along z (i) Error map for velocity along z

Figure 3.28: Distribution of ground truth velocity, reconstructed velocity for POD-DL methods and its error map: slice location z=0.155m, inlet velocity 0.55m/s, outlet pressure 500Pa, inlet tracer concentration 1.0kg/m^3, diffusion coefficient 1e-5, noise level 0 dB

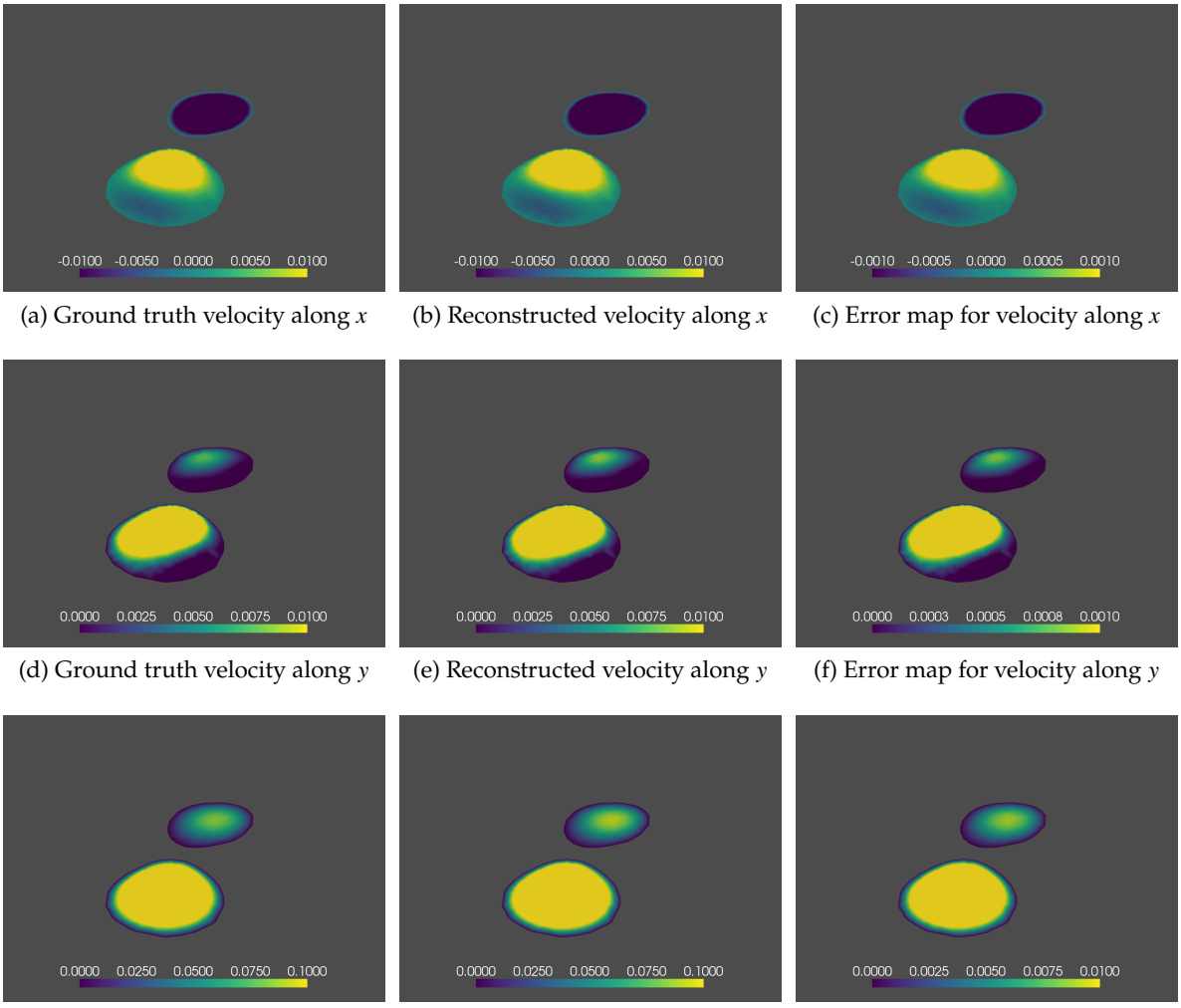

(a) Ground truth velocity along x (b) Reconstructed velocity along x (c) Error map for velocity along x

(d) Ground truth velocity along y (e) Reconstructed velocity along y (f) Error map for velocity along y

(g) Ground truth velocity along z (h) Reconstructed velocity along z (i) Error map for velocity along z

Figure 3.29: Distribution of ground truth velocity, reconstructed velocity of POD-DL methods and its error map: slice location z=0.165m, inlet velocity 0.55m/s, outlet pressure 500Pa, inlet tracer concentration 1.0kg/m^3, diffusion coefficient 1e-5, noise level 0 dB

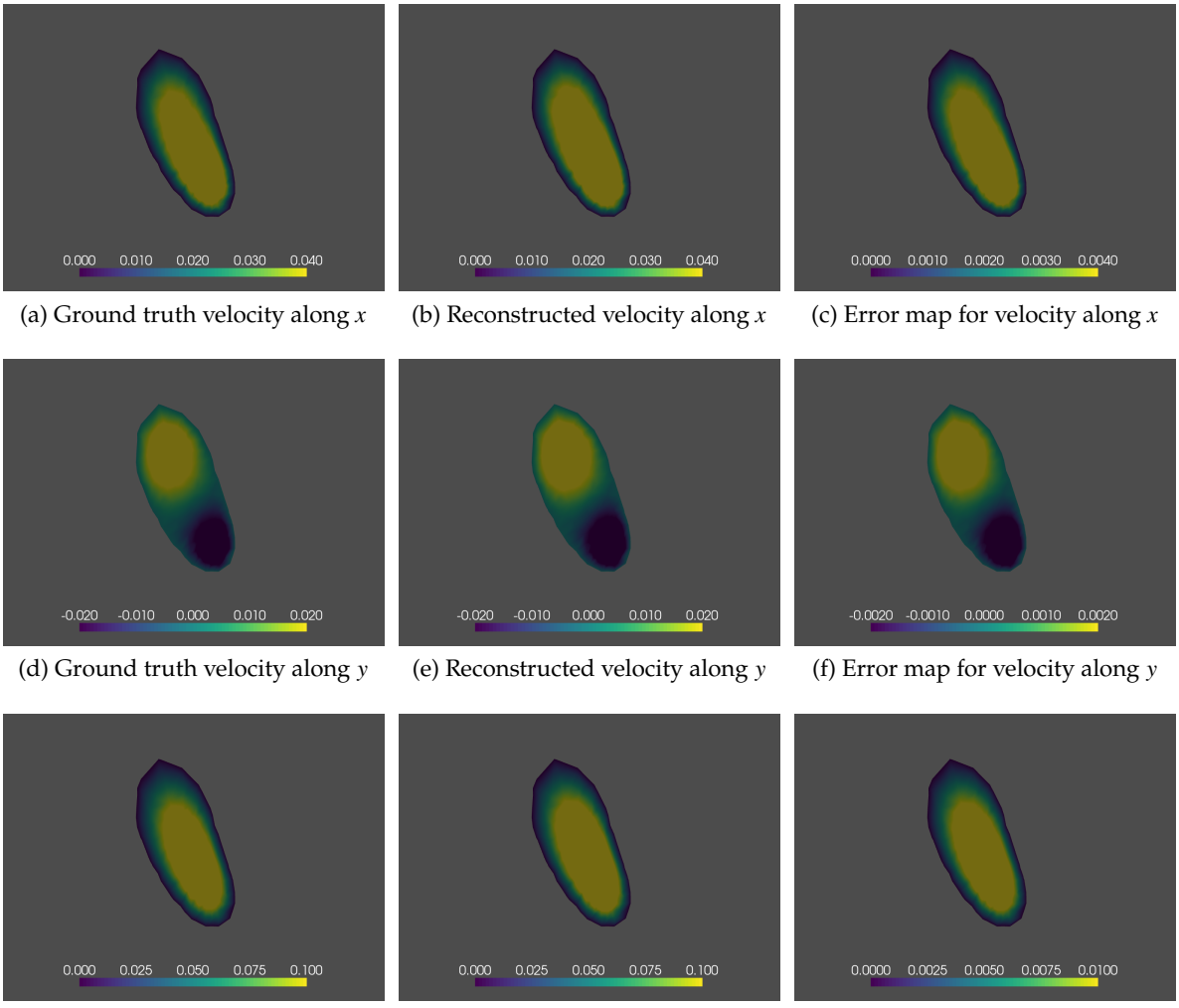

(a) Ground truth velocity along x (b) Reconstructed velocity along x (c) Error map for velocity along x

(d) Ground truth velocity along y (e) Reconstructed velocity along y (f) Error map for velocity along y

(g) Ground truth velocity along z (h) Reconstructed velocity along z (i) Error map for velocity along z

Figure 3.30: Distribution of ground truth velocity, reconstructed velocity of POD-DL methods and its error map: slice location y=0.014m, inlet velocity 0.55m/s, outlet pressure 500Pa, inlet tracer concentration 1.0kg/m^3, diffusion coefficient 1e-5, noise level 0 dB

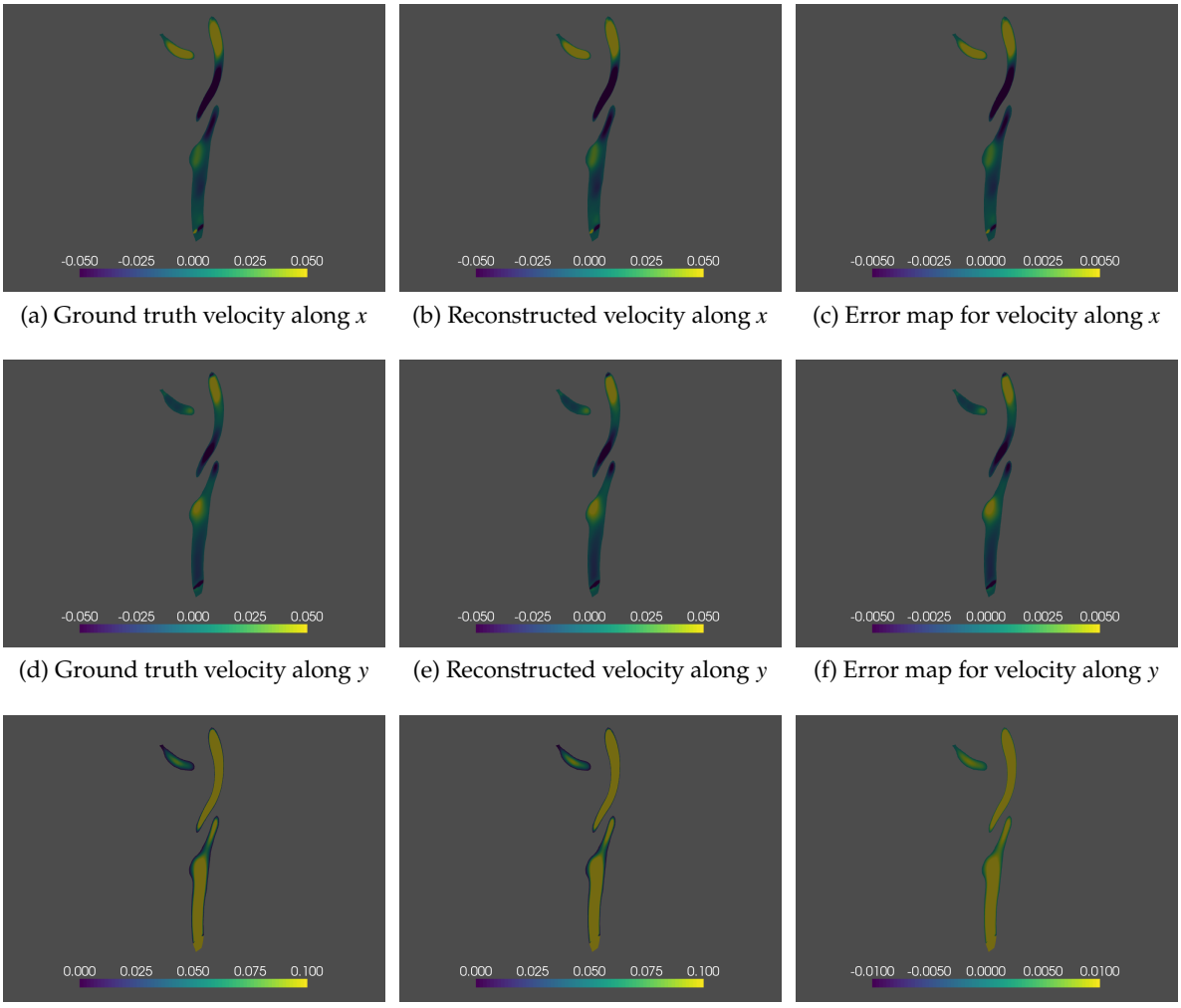

(a) Ground truth velocity along x (b) Reconstructed velocity along x (c) Error map for velocity along x

(d) Ground truth velocity along y (e) Reconstructed velocity along y (f) Error map for velocity along y

(g) Ground truth velocity along z (h) Reconstructed velocity along z (i) Error map for velocity along z

Figure 3.31: Distribution of ground truth velocity, reconstructed velocity of POD-DL methods and its error map: slice location y=0.024m, inlet velocity 0.55m/s, outlet pressure 500Pa, inlet tracer concentration 1.0kg/m^3, diffusion coefficient 1e-5, noise level 0 dB

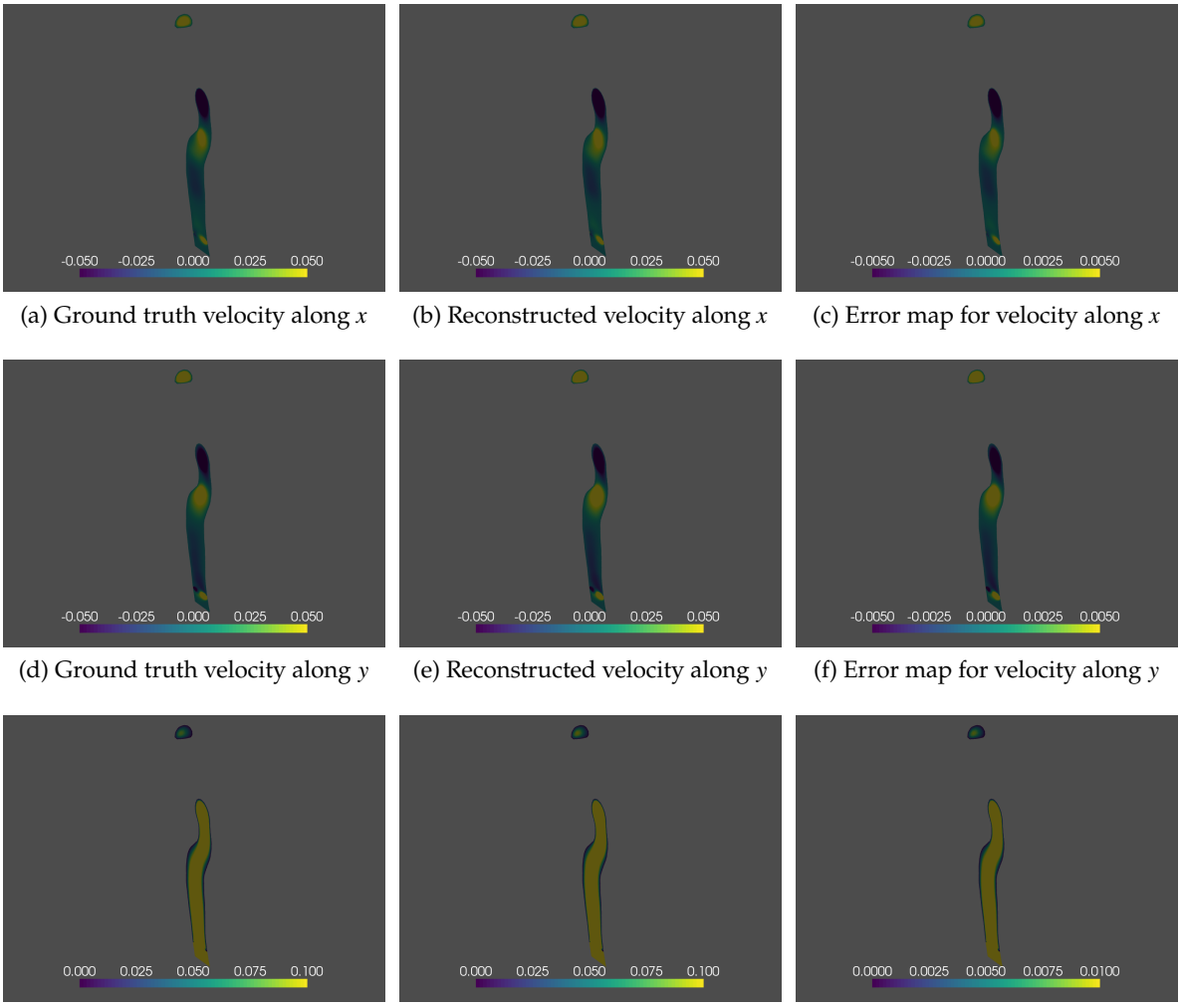

(a) Ground truth velocity along x (b) Reconstructed velocity along x (c) Error map for velocity along x

(d) Ground truth velocity along y (e) Reconstructed velocity along y (f) Error map for velocity along y

(g) Ground truth velocity along z (h) Reconstructed velocity along z (i) Error map for velocity along z

Figure 3.32: Distribution of ground truth velocity, reconstructed velocity for POD-DL methods and its error map: slice location x=0.187m, inlet velocity 0.55m/s, outlet pressure 500Pa, inlet tracer concentration 1.0kg/m^3, diffusion coefficient 1e-5, noise level 0 dB

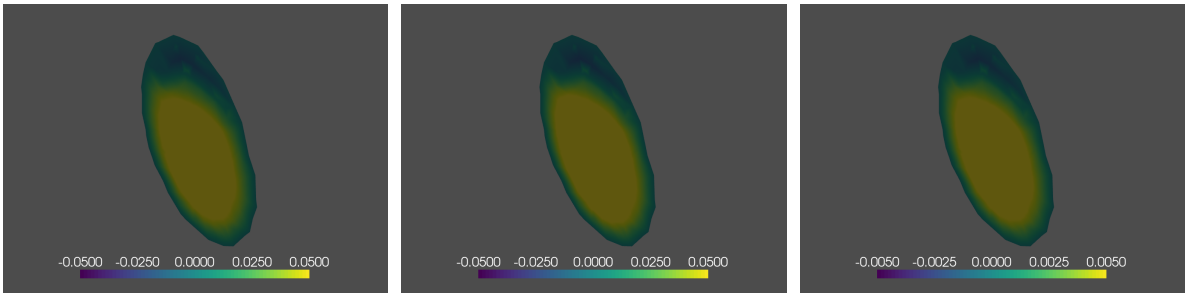

(a) Ground truth velocity along x (b) Reconstructed velocity along x (c) Error map for velocity along x

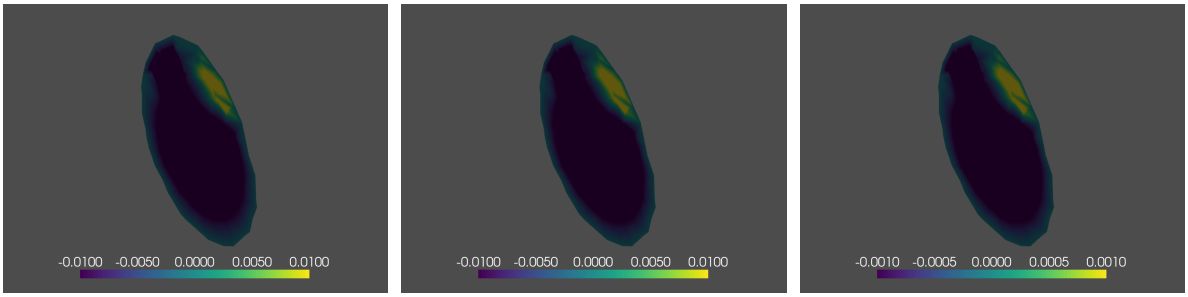

(d) Ground truth velocity along y (e) Reconstructed velocity along y (f) Error map for velocity along y

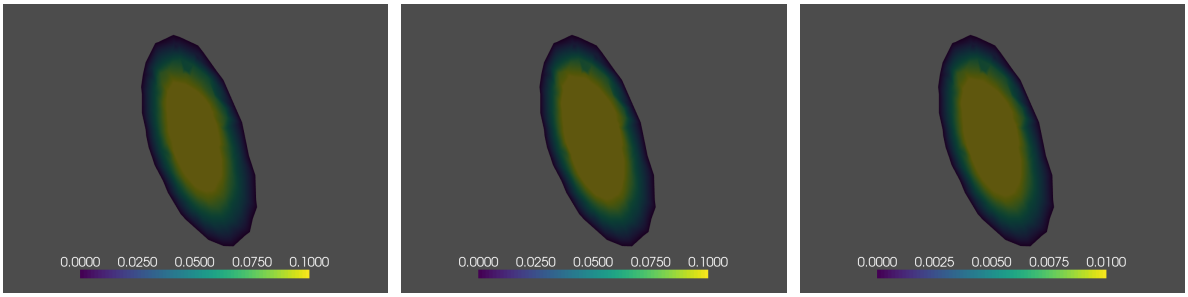

(g) Ground truth velocity along z (h) Reconstructed velocity along z (i) Error map for velocity along z

Figure 3.33: Distribution of ground truth velocity, reconstructed velocity for POD-DL methods and its error map: slice location x=0.199m, inlet velocity 0.55m/s, outlet pressure 500Pa, inlet tracer concentration 1.0kg/m^3, diffusion coefficient 1e-5, noise level 0 dB

Conclusion

In this thesis, we have introduced the study of blood flow hemodynamics for cardiovascular diseases and reviewed the in-vivo blood flow measurement methods. In this work, we primarily focus on the reconstruction of blood flow using X-ray CT techniques involving Radon projections perpendicular to the main flow direction of vessels. There are limited research studies dedicated to in vivo blood velocity measurement with X-ray CT and shortcomings of the computational costs. Regarding this challenge, we study the blood flow velocity reconstruction with X-ray CT with accelerated convergence, reduced computational cost, and reduced radiation dose. On the one hand, the classic adjoint method has been used to solve the inverse problem of blood flow reconstruction. On the other hand, the POD-adjoint approach based on the dimensionality reduction of the model has been applied to explore the acceleration of the convergence and to reduce the computation time. Finally, we investigate deep learning techniques combined with model reduction POD for the blood flow velocity reconstruction. The main research results are presented below.

In the first chapter, the classic adjoint method has been considered to reconstruct the blood flow within a complex vessel phantom. We have implemented the parameters optimization for the simulations, and have studied the impact of the regularization parameters and the impact of noise level corrupting the Radon projections. The results show that using the optimized simulation parameters 0.04m×0.04m for the size of the projection box, 20 slices, and 360 projection angles, we can reduce significantly the reconstruction errors for the blood flow velocity and the tracer concentration. Furthermore, a proper regularization parameter is chosen for the numerical simulations. With the presented approach, we can achieve small reconstruction errors, for small noise levels for both non-stationary velocity and stationary velocity fields. Additionally, an angle range of 180° for Radon projections can effectively improve the reconstruction. Thus, the simulations presented in this chapter show that the adjoint-based model can be used to reconstruct the blood flow.

In the second chapter, to accelerate the convergence and reduce the computational time, the POD reduction coupled with the adjoint method is used to study the blood flow reconstruction. We consider various numbers of POD basis elements for the velocity field, tracer concentration field, and adjoint variable field to investigate the blood flow reconstruction. With the non-stationary velocity, it is found that employing 6 velocity basis elements is the optimal choice. The optimal number of basis elements for the tracer concentration is estimated to 40. Additionally, by using 2 adjoint variable basis vectors, the lower reconstruction errors can be obtained. For the steady velocity, the optimal number of basis elements is 2 for the velocity, 20 for the tracer concentration, and 6 for the adjoint variable to achieve small reconstruction errors. We have also compared the POD-adjoint methodology to the full-order approximation (FOA) approach to reconstruct blood flow to demonstrate its high efficiency. The above results are confirmed by the calculation of the reconstruction errors and by the visualization of the various fields. The error map for the three velocity components has been used to show better reconstruction in the boundary region using the POD method rather than the FOA method. Therefore, with

the proposed POD-adjoint method we can achieve a significant computational cost reduction and better accuracy compared to the FOA strategy.

To obtain a substantial cost decrease for blood flow velocity reconstruction, in the third Chapter, we have investigated two POD-DL approaches based on two special architectures the POD-FC and POD-3D CNN. To deeply understand the behavior of the networks, we have also investigated the impact of the network parameters containing the time interval [8, 50], noise level [0 dB, 20 dB], and network training parameters such as learning rate [10^{-4}, 10^{-3}], batch size [50, 200], and dropout rate [0, 0.2]. Moreover, we can obtain a more accurate velocity reconstruction, a small standard deviation, and an enhanced velocity component reconstruction with a lower noise level of 20 dB. Additionally, we have found optimized parameters to obtain a small reconstructed velocity error: a variable learning rate from 10^{-3} to 10^{-4} for both networks, batch size of 200 for POD-FC, batch size of 50 for POD-3D CNN. We have explored two cases involving a low inlet velocity condition and a high inlet velocity condition for a stationary velocity field to reconstruct the blood flow velocity. In these cases, the 3D view and the XY planes, YZ planes, and XZ planes are displayed to show the effectiveness of the velocity field reconstruction. We have observed reconstructed velocity fields similar to the ground truth velocity fields. Finally, we have compared the POD-DL methods with the POD-adjoint approaches. The POD-DL methods show a good performance for blood velocity reconstruction with a lower offline CPU time, lower CPU time for velocity reconstruction, smaller velocity reconstruction errors, and smaller standard deviations.

In general, the above studies demonstrate the effectiveness of blood flow reconstruction. Particularly, the POD-DL methods enable us to accelerate the blood flow velocity reconstruction and reduce significantly the computational cost. The proposed approach is an interesting research direction to apply deep learning methods in clinical settings. This work leaves many interesting research directions open. We can generalize the approach with more POD coefficients to describe more complex fluid structures. It can also be extended to geometrical parametrizations for moving domains in order to take into account the fluid-structure interactions. As already mentioned, we could leverage new deep learning auto-encoders structures for dimension reduction. We have to take into account the real geometry of scanners and we may study the effect of Poisson noise corrupting the Radon projections.

We intend to leverage deep learning techniques with real cardiovascular data to achieve a better quantification of the hemodynamics in the vessels for diagnosing vascular diseases in clinical practice. To use the deep learning method in a real clinical context, the vessel model of patients should be extracted using CT imaging techniques. An abundant database of high-quality solutions has to be computed with the vessel model based on a set of physical and geometric flow parameters for training the network model.

Bibliography

Adler, J. and Öktem, O. (2017). Solving ill-posed inverse problems using iterative deep neural networks. *Inverse Problems*, 33(12):124007. 11

Ahishakiye, E., Bastiaan Van Gijzen, M., Tumwiine, J., Wario, R., and Obungoloch, J. (2021). A survey on deep learning in medical image reconstruction. *Intelligent Medicine*, 1(03):118–127. 65

Anwar, S. M., Majid, M., Qayyum, A., Awais, M., Alnowami, M., and Khan, M. K. (2018). Medical image analysis using convolutional neural networks: a review. *Journal of medical systems*, 42:1–13. 66

Apicella, A., Donnarumma, F., Isgrò, F., and Prevete, R. (2021). A survey on modern trainable activation functions. *Neural Networks*, 138:14–32. 69

Arian, E., Fahl, M., and Sachs, E. W. (2000). Trust-region proper orthogonal decomposition for flow control. Technical report, INSTITUTE FOR COMPUTER APPLICATIONS IN SCIENCE AND ENGINEERING HAMPTON VA. 33

Arridge, S., Maass, P., Öktem, O., and Schönlieb, C.-B. (2019). Solving inverse problems using data-driven models. *Acta Numerica*, 28:1–174. 74, 76

Axel, L., Shimakawa, B. A., and MacFall, J. (1986). A time-of-flight method of measuring flow velocity by magnetic resonance imaging. *Magnetic resonance imaging*, 4(3):199–205. 2

Azarine, A., Garçon, P., Stansal, A., Canepa, N., Angelopoulos, G., Silvera, S., Sidi, D., Marteau, V., and Zins, M. (2019). Four-dimensional flow mri: principles and cardiovascular applications. *Radiographics*, 39(3):632–648. 2

Ballarin, F., Faggiano, E., Manzoni, A., Quarteroni, A., Rozza, G., Ippolito, S., Antona, C., and Scrofani, R. (2017). Numerical modeling of hemodynamics scenarios of patient-specific coronary artery bypass grafts. *Biomechanics and modeling in mechanobiology*, 16:1373–1399. 33

Barfett, J. J., Fierstra, J., Mikulis, D. J., and Krings, T. (2010). Blood velocity calculated from volumetric dynamic computed tomography angiography. *Investigative radiology*, 45(12):778–781. 3

Barfett, J. J., Velauthapillai, N., Fierstra, J., Crawley, A., Coolens, C., Crean, A., Jaskolka, J., Dufort, P., Krings, T., and Mikulis, D. (2014). Intra-vascular blood velocity and volumetric flow rate calculated from dynamic 4d ct angiography using a time of flight technique. *The international journal of cardiovascular imaging*, 30:1383–1392. 3

Beatty, J. (2012). The radon transform and the mathematics of medical imaging. 8

Bhattacharya, K., Hosseini, B., Kovachki, N. B., and Stuart, A. M. (2021). Model reduction and neural networks for parametric pdes. *The SMAI journal of computational mathematics*, 7:121–157. 62, 74, 76

Boonen, P. T., Buls, N., Van Gompel, G., De Brucker, Y., Aerden, D., De Mey, J., and Vandemeulebroucke, J. (2018). Automated quantification of blood flow velocity from time-resolved ct angiography. In *Intravascular Imaging and Computer Assisted Stenting and Large-Scale Annotation of Biomedical Data and Expert Label Synthesis: 7th Joint International Workshop, CVII-STENT 2018 and Third International Workshop, LABELS 2018, Held in Conjunction with MICCAI 2018, Granada, Spain, September 16, 2018, Proceedings 3*, pages 11–18. Springer. 3

Boonen, P. T., Buls, N., Van Gompel, G., De Brucker, Y., Aerden, D., Leiner, T., De Mey, J., and Vandemeulebroucke, J. (2020). Contrast flow velocity quantification from time-resolved ct angiography: a phantom study. In *Medical Imaging 2020: Physics of Medical Imaging*, volume 11312, pages 281–286. SPIE. 3

Bouillot, P., Brina, O., Chnafa, C., Cancelliere, N. M., Vargas, M. I., Radovanovic, I., Krings, T., Steinman, D. A., and Pereira, V. M. (2019). Robust cerebrovascular blood velocity and flow rate estimation from 4d-cta. *Medical physics*, 46(5):2126–2136. 1, 4

Brenner, S. C. (2008). *The mathematical theory of finite element methods*. Springer. 18

Briers, J. D. (2001). Laser doppler, speckle and related techniques for blood perfusion mapping and imaging. *Physiological measurement*, 22(4):R35. 1

Burger, M. and Mühlhuber, W. (2002). Iterative regularization of parameter identification problems by sequential quadratic programming methods. *Inverse Problems*, 18(4):943. 4

Calamante, F., Gadian, D., and Connelly, A. (2002). Quantification of perfusion using bolus tracking magnetic resonance imaging in stroke: assumptions, limitations, and potential implications for clinical use. *Stroke*, 33(4):1146–1151. 3

Calamante, F., Thomas, D. L., Pell, G. S., Wiersma, J., and Turner, R. (1999). Measuring cerebral blood flow using magnetic resonance imaging techniques. *Journal of cerebral blood flow & metabolism*, 19(7):701–735. 2

Chorin, A. J. (1968). Numerical solution of the navier-stokes equations. *Mathematics of computation*, 22(104):745–762. 19

Cilimkovic, M. (2015). Neural networks and back propagation algorithm. *Institute of Technology Blanchardstown, Blanchardstown Road North Dublin*, 15(1). 68

Cnudde, V. and Boone, M. N. (2013). High-resolution x-ray computed tomography in geosciences: A review of the current technology and applications. *Earth-Science Reviews*, 123:1–17. 3

Courant, R. (1956). *Calculus of Variations 1945-1946*. New York University. 14

Crosetto, P., Reymond, P., Deparis, S., Kontaxakis, D., Stergiopulos, N., and Quarteroni, A. (2011). Fluid–structure interaction simulation of aortic blood flow. *Computers & Fluids*, 43(1):46–57. 1

Daly, S. M. and Leahy, M. J. (2013). 'go with the flow': a review of methods and advancements in blood flow imaging. *Journal of biophotonics*, 6(3):217–255. 1, 33

de Hoop, M. V., Huang, D. Z., Qian, E., and Stuart, A. M. (2022). The cost-accuracy trade-off in operator learning with neural networks. *arXiv preprint arXiv:2203.13181*. 74, 76

Dubey, S. R., Singh, S. K., and Chaudhuri, B. B. (2022). Activation functions in deep learning: A comprehensive survey and benchmark. *Neurocomputing*. 69

Dubsky, S., Jamison, R., Higgins, S., Siu, K., Hourigan, K., and Fouras, A. (2012). Computed tomographic x-ray velocimetry for simultaneous 3d measurement of velocity and geometry in opaque vessels. *Experiments in fluids*, 52:543–554. 3

Engelhard, S., Voorneveld, J., Vos, H. J., Westenberg, J. J., Gijsen, F. J., Taimr, P., Versluis, M., De Jong, N., Bosch, J. G., Reijnen, M. M., et al. (2018). High-frame-rate contrast-enhanced us particle image velocimetry in the abdominal aorta: first human results. *Radiology*, 289(1):119–125. 1

Fan, A. P., Jahanian, H., Holdsworth, S. J., and Zaharchuk, G. (2016). Comparison of cerebral blood flow measurement with [15o]-water positron emission tomography and arterial spin labeling magnetic resonance imaging: a systematic review. *Journal of Cerebral Blood Flow & Metabolism*, 36(5):842–861. 3

Galdi, G. (2011). *An introduction to the mathematical theory of the Navier-Stokes equations: Steady-state problems*. Springer Science & Business Media. 10

Galdi, G. P. (1994). An introduction to the mathematical theory of the navier-stokes equations. vol. i, volume 38 of springer tracts in natural philosophy. 36

Geneva, N. and Zabaras, N. (2020). Modeling the dynamics of pde systems with physics-constrained deep auto-regressive networks. *Journal of Computational Physics*, 403:109056. 74

Géron, A. (2019). Hands-on machine learning with scikit-learn, keras & tensorflow farnham. *Canada: O'Reilly*. xiv, 68, 70, 71, 73

Ghattas, O. and Willcox, K. (2021). Learning physics-based models from data: perspectives from inverse problems and model reduction. *Acta Numerica*, 30:445–554. 33

Girault, V. and Raviart, P.-A. (2012). *Finite element methods for Navier-Stokes equations: theory and algorithms*, volume 5. Springer Science & Business Media. 16

Glowinski, R. and Pironneau, O. (1992). Finite element methods for navier-stokes equations. *Annual review of fluid mechanics*, 24(1):167–204. 10, 16, 36, 39

Goda, K. (1979). A multistep technique with implicit difference schemes for calculating two-or three-dimensional cavity flows. *Journal of computational physics*, 30(1):76–95. 15, 16, 38

Gonzalez, F. J. and Balajewicz, M. (2018). Deep convolutional recurrent autoencoders for learning low-dimensional feature dynamics of fluid systems. *arXiv preprint arXiv:1808.01346*. 62

Hazra, A., Choudhary, P., and Sheetal Singh, M. (2021). Recent advances in deep learning techniques and its applications: an overview. *Advances in Biomedical Engineering and Technology: Select Proceedings of ICBEST 2018*, pages 103–122. 65

Heywood, J. G., Rannacher, R., and Turek, S. (1996). Artificial boundaries and flux and pressure conditions for the incompressible navier–stokes equations. *International Journal for numerical methods in fluids*, 22(5):325–352. 18

Hoskins, P. (1999). A review of the measurement of blood velocity and related quantities using doppler ultrasound. *Proceedings of the Institution of Mechanical Engineers, Part H: Journal of Engineering in Medicine*, 213(5):391–400. 2

Huang, S., Sigovan, M., and Sixou, B. (2021). Reconstruction of vascular blood flow in a vessel from tomographic projections. *Biomedical Physics & Engineering Express*, 7(6):065032. 13, 38

Jahng, G.-H., Li, K.-L., Ostergaard, L., and Calamante, F. (2014). Perfusion magnetic resonance imaging: a comprehensive update on principles and techniques. *Korean journal of radiology*, 15(5):554–577. 2, 3

Jia, X., Willard, J., Karpatne, A., Read, J. S., Zwart, J. A., Steinbach, M., and Kumar, V. (2021). Physics-guided machine learning for scientific discovery: An application in simulating lake temperature profiles. *ACM/IMS Transactions on Data Science*, 2(3):1–26. 74

Jong, S. (2015). Quantifying cerebral blood flow of both the micro-and macrovascular system using perfusion computed tomography. Master's thesis, University of Twente. 3

Kabanikhin, S. I. (2008). Definitions and examples of inverse and ill-posed problems. 11

Kabanikhin, S. I. (2011). Inverse and ill-posed problems. In *Inverse and Ill-posed Problems*. de Gruyter. 11

Kalender, W. A. (2006). X-ray computed tomography. *Physics in Medicine & Biology*, 51(13):R29. 7

Kamada, H., Nakamura, M., Ota, H., Higuchi, S., and Takase, K. (2022). Blood flow analysis with computational fluid dynamics and 4d-flow mri for vascular diseases. *Journal of cardiology*. 2

Karpatne, A., Atluri, G., Faghmous, J. H., Steinbach, M., Banerjee, A., Ganguly, A., Shekhar, S., Samatova, N., and Kumar, V. (2017). Theory-guided data science: A new paradigm for scientific discovery from data. *IEEE Transactions on knowledge and data engineering*, 29(10):2318–2331. 74

Kato, T., Indo, T., Yoshida, E., Iwasaki, Y., Sone, M., and Sobue, G. (2002). Contrast-enhanced 2d cine phase mr angiography for measurement of basilar artery blood flow in posterior circulation ischemia. *American journal of neuroradiology*, 23(8):1346–1351. 3

Kim, M., Yun, J., Cho, Y., Shin, K., Jang, R., Bae, H.-j., and Kim, N. (2019). Deep learning in medical imaging. *Neurospine*, 16(4):657. 66

Kingma, D. P. and Ba, J. (2014). Adam: A method for stochastic optimization. *arXiv preprint arXiv:1412.6980*. 69, 70

Korporaal, J. G., Benz, M. R., Schindera, S. T., Flohr, T. G., and Schmidt, B. (2016). Contrast gradient-based blood velocimetry with computed tomography: theory, simulations, and proof of principle in a dynamic flow phantom. *Investigative radiology*, 51(1):41–49. 3

Ku, D. N. (1997). Blood flow in arteries. *Annual review of fluid mechanics*, 29(1):399–434. 18

Kun, J. (2012). Backpropagation algorithm. 68

Lederer, J. (2021). Activation functions in artificial neural networks: A systematic overview. *arXiv preprint arXiv:2101.09957*. 69

Lee, J.-G., Jun, S., Cho, Y.-W., Lee, H., Kim, G. B., Seo, J. B., and Kim, N. (2017). Deep learning in medical imaging: general overview. *Korean journal of radiology*, 18(4):570–584. 66

Li, Y., Sixou, B., and Peyrin, F. (2021a). A review of the deep learning methods for medical images super resolution problems. *Irbm*, 42(2):120–133. 65

Li, Z., Liu, F., Yang, W., Peng, S., and Zhou, J. (2021b). A survey of convolutional neural networks: analysis, applications, and prospects. *IEEE transactions on neural networks and learning systems*. 72

Lia, T.-Q., Chen, Z. G., Østergaard, L., Hindmarsh, T., and Moseley, M. E. (2000). Quantification of cerebral blood flow by bolus tracking and artery spin tagging methods. *Magnetic resonance imaging*, 18(5):503–512. 3

Logg, A., Mardal, K.-A., and Wells, G. (2012). *Automated solution of differential equations by the finite element method: The FEniCS book*, volume 84. Springer Science & Business Media. 15, 16, 18, 19, 38, 78

Lotz, J., Meier, C., Leppert, A., and Galanski, M. (2002). Cardiovascular flow measurement with phase-contrast mr imaging: basic facts and implementation. *Radiographics*, 22(3):651–671. 1, 2, 3

Lu, J. and Lu, W.-Q. (2010). Blood flow velocity and ultra-filtration velocity measured by ct imaging system inside a densely bundled hollow fiber dialyzer. *International journal of heat and mass transfer*, 53(9-10):1844–1850. 3

Lu, K., Jin, Y., Chen, Y., Yang, Y., Hou, L., Zhang, Z., Li, Z., and Fu, C. (2019). Review for order reduction based on proper orthogonal decomposition and outlooks of applications in mechanical systems. *Mechanical Systems and Signal Processing*, 123:264–297. 33

Lu, L., Jin, P., Pang, G., Zhang, Z., and Karniadakis, G. E. (2021). Learning nonlinear operators via deeponet based on the universal approximation theorem of operators. *Nature machine intelligence*, 3(3):218–229. 74

Lu, L., Meng, X., Cai, S., Mao, Z., Goswami, S., Zhang, Z., and Karniadakis, G. E. (2022). A comprehensive and fair comparison of two neural operators (with practical extensions) based on fair data. *Computer Methods in Applied Mechanics and Engineering*, 393:114778. 74

Lundervold, A. S. and Lundervold, A. (2019). An overview of deep learning in medical imaging focusing on mri. *Zeitschrift für Medizinische Physik*, 29(2):102–127. 65

Lusby, R., Machleder, H., Jeans, W., Skidmore, R., Woodcock, J., Clifford, P., and Baird, R. (1981). Vessel wall and blood flow dynamics in arterial disease. *Philosophical Transactions of the Royal Society of London. B, Biological Sciences*, 294(1072):231–239. 1

MacDonald, M. E. and Frayne, R. (2015). Cerebrovascular mri: a review of state-of-the-art approaches, methods and techniques. *NMR in Biomedicine*, 28(7):767–791. 2, 3

Mathew, A., Amudha, P., and Sivakumari, S. (2021). Deep learning techniques: an overview. *Advanced Machine Learning Technologies and Applications: Proceedings of AMLTA 2020*, pages 599–608. 65

McCann, M. T., Jin, K. H., and Unser, M. (2017). Convolutional neural networks for inverse problems in imaging: A review. *IEEE Signal Processing Magazine*, 34(6):85–95. 65

Meunier, J. and Bertrand, M. (1995). Ultrasonic texture motion analysis: theory and simulation. *IEEE transactions on medical imaging*, 14(2):293–300. 2

Miller, A., Blott, B., and Hames, T. (1992). Review of neural network applications in medical imaging and signal processing. *Medical and Biological Engineering and Computing*, 30:449–464. 66

Morgan, A. G., Thrippleton, M. J., Wardlaw, J. M., and Marshall, I. (2021). 4d flow mri for non-invasive measurement of blood flow in the brain: a systematic review. *Journal of Cerebral Blood Flow & Metabolism*, 41(2):206–218. 2

Morton, K. and Mayers, D. (1998). Numerical solution of partial differential equations. *Journal of Fluid Mechanics*, 363:349–349. 15, 16, 38

Natterer, F. and Natterer, F. (1986). Computerized tomography. *The Mathematics of Computerized Tomography*, pages 1–8. 9

Nocedal, J. and Wright, S. J. (1999). *Numerical optimization*. Springer. 14

Ol'ga Aleksandrovna Ladyzhenskaja, V. A. (1968). Solonnikov, and nina n. ural'ceva. linear and quasi-linear equations of parabolic type, volume 23 of translations of mathematical monographs. *American Mathematical Society*. 13

Østergaard, L. (2005). Principles of cerebral perfusion imaging by bolus tracking. *Journal of Magnetic Resonance Imaging: An official journal of the international society for magnetic resonance in medicine*, 22(6):710–717. 3

Paleo, P. (2017). *Iterative methods in regularized tomographic reconstruction*. PhD thesis, Université Grenoble Alpes. 8

Pates, J. A., Hatab, M. R., McIntire, D. D., Cunningham, F. G., and Twickler, D. M. (2010). Determining uterine blood flow in pregnancy with magnetic resonance imaging. *Magnetic Resonance Imaging*, 28(4):507–510. 2

Pelc, N. J., Sommer, F. G., Li, K. C., Brosnan, T. J., Herfkens, R. J., and Enzmann, D. R. (1994). Quantitative magnetic resonance flow imaging. *Magnetic resonance quarterly*, 10(3):125–147. 99

Pipe, J. G. (2001). Limits of time-of-flight magnetic resonance angiography. *Topics in Magnetic Resonance Imaging*, 12(3):163–174. 3

Pironneau, O. and Pironneau, O. (1989). *Finite element methods for fluids*. Wiley Chichester. 16

Poelma, C. (2017). Ultrasound imaging velocimetry: a review. *Experiments in Fluids*, 58:1–28. 1, 2

Prevrhal, S., Forsythe, C. H., Harnish, R. J., Saeed, M., and Yeh, B. M. (2011). Ct angiographic measurement of vascular blood flow velocity by using projection data. *Radiology*, 261(3):923–929. 3

Quarteroni, A., Manzoni, A., and Negri, F. (2015). *Reduced basis methods for partial differential equations: an introduction*, volume 92. Springer. 33

Quarteroni, A., Manzoni, A., and Vergara, C. (2017). The cardiovascular system: mathematical modelling, numerical algorithms and clinical applications. *Acta Numerica*, 26:365–590. 1

Rai, R. and Sahu, C. K. (2020). Driven by data or derived through physics? a review of hybrid physics guided machine learning techniques with cyber-physical system (cps) focus. *IEEE Access*, 8:71050–71073. 74

Raissi, M., Perdikaris, P., and Karniadakis, G. (2019). A deep learning framework for solving forward and inverse problems involving nonlinear partial differential equations. *J. Comput. Phys*, 378:686–707. 74

Ravindran, S. S. (2000). A reduced-order approach for optimal control of fluids using proper orthogonal decomposition. *International journal for numerical methods in fluids*, 34(5):425–448. 33

Rosenblatt, F. (1958). The perceptron: a probabilistic model for information storage and organization in the brain. *Psychological review*, 65(6):386. 70

Rowley, C. W. (2005). Model reduction for fluids, using balanced proper orthogonal decomposition. *International Journal of Bifurcation and Chaos*, 15(03):997–1013. 33

Rumelhart, D. E., Hinton, G. E., Williams, R. J., et al. (1985). Learning internal representations by error propagation. 68

Sakuma, H., Kawada, N., Takeda, K., and Higgins, C. B. (1999). Mr measurement of coronary blood flow. *Journal of Magnetic Resonance Imaging: An Official Journal of the International Society for Magnetic Resonance in Medicine*, 10(5):728–733. 2

Sheikhjafari, A., Noga, M., Punithakumar, K., and Ray, N. (2022). Unsupervised deformable image registration with fully connected generative neural network. In *Medical imaging with deep learning*. 66

Shi, Y., Lawford, P., and Hose, R. (2011). Review of zero-d and 1-d models of blood flow in the cardiovascular system. *Biomedical engineering online*, 10(1):1–38. 1

Shinde, P. P. and Shah, S. (2018). A review of machine learning and deep learning applications. In *2018 Fourth international conference on computing communication control and automation (ICCUBEA)*, pages 1–6. IEEE. 65

Singh, S. P., Wang, L., Gupta, S., Goli, H., Padmanabhan, P., and Gulyás, B. (2020). 3d deep learning on medical images: a review. *Sensors*, 20(18):5097. 66

Sixou, B. (2019). Contrast enhanced tomographic reconstruction of vascular blood flow with first order and second order adjoint methods. *Journal of Inverse and Ill-posed Problems*, 27(1):87–102. 4

Sixou, B., Boissel, L., and Sigovan, M. (2016). Contrast enhanced computerized tomography measurement of vascular blood flow. In *Journal of Physics: Conference Series*, volume 756, page 012003. IOP Publishing. 4, 13

Sixou, B., Boussel, L., and Sigovan, M. (2018). Vascular blood flow reconstruction with contrast-enhanced computerized tomography. *Inverse Problems in Science and Engineering*, 26(6):855–876. 4

Smith, G. D., Smith, G. D., and Smith, G. D. S. (1985). *Numerical solution of partial differential equations: finite difference methods*. Oxford university press. 15

Soulat, G., McCarthy, P., and Markl, M. (2020). 4d flow with mri. *Annual review of biomedical engineering*, 22:103–126. 2

Sourbron, S. P. and Buckley, D. L. (2013). Classic models for dynamic contrast-enhanced mri. *NMR in Biomedicine*, 26(8):1004–1027. 3

Srichai, M. B., Lim, R. P., Wong, S., and Lee, V. S. (2009). Cardiovascular applications of phase-contrast mri. *American Journal of Roentgenology*, 192(3):662–675. 2

Strazzullo, M., Ballarin, F., Mosetti, R., and Rozza, G. (2018). Model reduction for parametrized optimal control problems in environmental marine sciences and engineering. *SIAM Journal on Scientific Computing*, 40(4):B1055–B1079. 36

Suñol, F., Ochoa, D. A., and Garcia, J. E. (2018). High-precision time-of-flight determination algorithm for ultrasonic flow measurement. *IEEE Transactions on Instrumentation and Measurement*, 68(8):2724–2732. 2

Tarbell, J. M., Shi, Z.-D., Dunn, J., and Jo, H. (2014). Fluid mechanics, arterial disease, and gene expression. *Annual review of fluid mechanics*, 46:591–614. 1

Taylor, C. and Hood, P. (1973). A numerical solution of the navier-stokes equations using the finite element technique. *Computers & Fluids*, 1(1):73–100. 16, 38

Temam, R. (2001). *Navier-Stokes equations: theory and numerical analysis*, volume 343. American Mathematical Soc. 10, 36, 39

Tenderini, R., Pagani, S., Quarteroni, A., and Deparis, S. (2022). Pde-aware deep learning for inverse problems in cardiac electrophysiology. *SIAM Journal on Scientific Computing*, 44(3):B605–B639. 74, 76, 77

Trahey, G. E., Allison, J. W., and Von Ramm, O. T. (1987). Angle independent ultrasonic detection of blood flow. *IEEE Transactions on Biomedical Engineering*, (12):965–967. 2

van Kaick, G. and Delorme, S. (2005). Computed tomography in various fields outside medicine. *European Radiology Supplements*, 15:d74–d81. 7

Vaz, P. G., Humeau-Heurtier, A., Figueiras, E., Correia, C., and Cardoso, J. (2016). Laser speckle imaging to monitor microvascular blood flow: a review. *IEEE reviews in biomedical engineering*, 9:106–120. 1

Vennemann, P., Lindken, R., and Westerweel, J. (2007). In vivo whole-field blood velocity measurement techniques. *Experiments in fluids*, 42:495–511. 1

Virtanen, P., Gommers, R., Oliphant, T., Haberland, M., Reddy, T., Cournapeau, D., Burovski, E., Peterson, P., Weckesser, W., Bright, J., et al. (2020). Fundamental algorithms for scientific computing in python and scipy 1.0 contributors. scipy 1.0. *Nat. Methods*, 17:261–272. 17, 38

Volkwein, S. (2013). Proper orthogonal decomposition: Theory and reduced-order modelling. *Lecture Notes, University of Konstanz*, 4(4):1–29. 33, 34

Wagner, S., Helisch, A., Bachmann, G., and Schaper, W. (2004). Time-of-flight quantitative measurements of blood flow in mouse hindlimbs. *Journal of Magnetic Resonance Imaging: An Official Journal of the International Society for Magnetic Resonance in Medicine*, 19(4):468–474. 2

Wang, C., Hayashi, Y., Oda, M., Itoh, H., Kitasaka, T., Frangi, A. F., and Mori, K. (2019). Tubular structure segmentation using spatial fully connected network with radial distance loss for 3d medical images. In *Medical Image Computing and Computer Assisted Intervention–MICCAI 2019: 22nd International Conference, Shenzhen, China, October 13–17, 2019, Proceedings, Part VI 22*, pages 348–356. Springer. 66

Wang, G., Yu, H., and De Man, B. (2008). An outlook on x-ray ct research and development. *Medical physics*, 35(3):1051–1064. 7

Wang, L.-M. and Shung, K. K. (1996). Adaptive pattern correlation for two-dimensional blood flow measurements. *IEEE transactions on ultrasonics, ferroelectrics, and frequency control*, 43(5):881–887. 2

Wehrli, F., Shimakawa, A., Gullberg, G., and MacFall, J. (1986). Time-of-flight mr flow imaging: selective saturation recovery with gradient refocusing. *Radiology*, 160(3):781–785. 2

Yaqub, M., Jinchao, F., Arshid, K., Ahmed, S., Zhang, W., Nawaz, M. Z., and Mahmood, T. (2022). Deep learning-based image reconstruction for different medical imaging modalities. *Computational and Mathematical Methods in Medicine*, 2022. 65

Zhang, H.-M. and Dong, B. (2020). A review on deep learning in medical image reconstruction. *Journal of the Operations Research Society of China*, 8:311–340. 65

Zhang, N., Gordon, M. L., and Goldberg, T. E. (2017). Cerebral blood flow measured by arterial spin labeling mri at resting state in normal aging and alzheimer's disease. *Neuroscience & Biobehavioral Reviews*, 72:168–175. 3

Zheng, H., Liu, L., Williams, L., Hertzberg, J. R., Lanning, C., and Shandas, R. (2006). Real time multicomponent echo particle image velocimetry technique for opaque flow imaging. *Applied physics letters*, 88(26):261915. 2

Zhu, Y., Zabaras, N., Koutsourelakis, P.-S., and Perdikaris, P. (2019). Physics-constrained deep learning for high-dimensional surrogate modeling and uncertainty quantification without labeled data. *Journal of Computational Physics*, 394:56–81. 74

Publications

Huang, Shusong, Sigovan, Monica et Sixou, bruno (2023). Deep learning methods for blood flow reconstruction in a vessel with contrast enhanced x-ray computed tomography. *International Journal for Numerical Methods in Biomedical Engineering*, 2023;e3785.

Huang, Shusong, Sigovan, Monica et Sixou bruno (2022). Reconstruction of vascular blood flow in a vessel from tomographic projections. *Biomedical Physics & Engineering Express*, (2022): 1-13.

Huang, Shusong, Sigovan, Monica et Sixou bruno (2021). POD method for acceleration of blood flow reconstruction in a vessel with contrast enhanced X-ray CT. *Computer Methods in Biomechanics and Biomedical Engineering: Imaging & Visualization*, 7.6 (2021): 065032.

Contents

List of Figures

List of Tables

Introduction

Hemodynamique et maladies cardiovasculaires

Les maladies cardiovasculaires sont la principale cause de décès dans le monde et le développement de méthode de diagnostic est un problème crucial. La vitesse du sang et d'autres paramètres hémodynamiques jouent un très grand role pour la compréhension des phénomènes physiologiques dans les maladies cardiovasculaires. La compréhension du flux sanguin est complexe. Au cours du cycle cardiaque, le nombre de Reynolds évolue beaucoup et des phénomènes de turbulence peuvent apparaître. Les variation de la forme des vaisseaux et les intéractions fluide-structure ont un fort impact sur l'écoulement sanguin et les paramètres hémodynamiques.

Mesure in-vivo du flux sanguin

Techniques de mesure Doppler et RMN

Un certain nombre de techniques d'imagerie médicale comme les ultrasons ou l'Imagerie par Résonance Magnétique (IRM) en contraste de phase permettent une mesure non invasive du flux sanguin. Ces techniques ont des avantages mais aussi des limitations. Par exemple, une limitation importante de la technique des ultrasons et qu'elle ne donne accès qu'aux composantes de vitesse orientées selon le faisceau d'ultrasons. La RMN mesure les propriétés de relaxation des moments magnétiques de certains atomes soumis à des champs magnétiques haute fréquence. En RMN 4D de contraste de phase, il existe une relation simple entre la phase du signal mesuré et la vitesse des protons qui est utile pour reconstruire le flux sanguin. Une description spatio-temporelle du champ de vecteurs dans les trois dimensions peut être obtenue ainsi que la morphologie de la région d'intérêt. Certaines quantités comme la pression ou les champ de contraintes peuvent être estimées ce qui est crucial pour le diagnostic et très difficile à réaliser avec d'autres modalités. La RMN est une technique d'imagerie non invasive mais les temps d'acquisition sont longs. La résolution spatio-temporelle est faible pour une description précise du flux sanguin. Les données acquises dépendent des appareils et séquences de mesure.

Tomographie

Il existe peu de travaux de recherche sur les mesures in vivo par rayons X de la vitesse du sang. Les mesures CT ont a priori une résolution temporelle et spatiale plus grande. Dans les travaux publiés, toutes les composantes du champ de vitesse ne sont pas mesurées simultanément. Une vitesse moyenne est souvent obtenue avec le rapport de la distance entre des lignes du détecteur et le temps de propagation, obtenus à partir des changements dans la densité du traceur.

Utilisation des simulations numériques pour améliorer la charactérisation du flux sanguin

Les simulations de dynamiques des fluide ont souvent été utlisées pour la prédiction du flux sanguin dans le système cardiovasculaire. Elles sont souvent couplées à des mesures de RMN et permettent d'améliorer la résolution spatio-temporelle et le calcul des paramètres hémodynamiques. Les conditions aux limites et initiales doivent être bien connues et les interactions fluide-structure sont souvent négligées. Ces simulations peuvent être utiles pour valider des approches de reconstruction.

Récemment, des travaux dans notre équipe ont étudié une nouvelle approche pour reconstruire ce champ de vitesse à partir de mesure de tomographie avec agent de contraste. (Sixou et al., 2016, 2018; Sixou, 2019). Cette méthode a été validée avec des simulations. Des projections de Radon 2D sont acquises perpendiculairement à la direction du vaisseau avec un traceur injecté dans le vaisseau. Afin de résoudre le problème inverse de la reconstruction du flux sanguin, une fonctionelle est minimisée incluant un terme d'attache aux données avec les projections de Radon et une équation aux dérivées partielles décrivant la propagation du traceur de concentration $f(\mathbf{X}, t)$ utilisée comme contrainte. Dans cette première approche, les variables $(f, \mathbf{V})$ sont optimisées indépendamment et les calculs sont très longs.

Dans ce travail, nous nous concentrons sur la méthode de l'état adjoint pour résoudre le problème inverse de la reconstruction du flux sanguin à partir des projections tomographiques avec une équation aux dérivées partielles comme contrainte. Nous proposons ensuite une décomposition en composantes principales couplée (POD) avec la méthode de l'état adjoint pour accélérer la convergence. Cette décompostion POD est finalement couplée avec des techniques de deep learning pour améliorer la reconstruction.

Objectifs de la thèse

Les objectifs de ce travail sont donc la reconstruction des composantes du champ de vitesse sanguin à partir de mesures de projections tomographiques avec une convergence accélérée, un temps de calcul réduit et une dose réduite. Dans la suite, les aspects suivants seront développés: (1) L'équation de transport est donc utilisée comme contrainte et les projections de Radon acquises perpendiculairement au vaisseau. Nous étudions l'influence de certains paramètres de simulation sur la reconstruction: taille de la zone de projection, nombre d'angles de projection, nombre de coupes suivant z, afin d'obtenir les meilleurs paramètres. Nous étudions ensuite l'effet d'un bruit Gaussien et nous validons la méthode sur des champs de vitesses stationnaires ou dépendant du temps.
(2) A partir de la méthode de l'état adjoint, une décomposition en composantes principales est utilisée pour accélérer la reconstruction avec des bases pour la vitesse, la concentration du traceur et la variable adjointe. Ces bases sont obtenues à partir d'échantillons du champ de vitesse, de la concentration du traceur et de la variable adjointe. Ils sont utilisés pour réduire les dimensions de l'équation de transport et de l'équation adjointe. Différents nombres de vecteurs sont étudiés. Les résultats de reconstrution de la méthode adjointe complète ou avec POD sont comparés. Des champs de vitesses stationnaires ou dépendant du temps sont testés.
(3) La méthode POD combinée avec des approches deep learning est ensuite explorée pour améliorer la convergence et réduire les temps de calculs de la reconstruction du flux sanguin. Plusieurs architectures de réseaux de neurones sont étudiées pour approcher l'opérateur inverse: Proper orthogonal decomposition-fully connected network(POD-FC), et Proper orthogonal decomposition-3D convolutional neural network(POD-3D CNN). Nous comparons les résultats de reconstruction obtenus en utilisant les méthodes deep learning ou la méthode

de l'état adjoint avec POD pour des champs de vitesses stationaires.

Chapter 1

Reconstruction de vitesse par tomographie avec agent de contraste: un problème inverse avec une équation aux dérivées partielles comme contrainte.

Dans ce chapitre, nous introduisons le problème inverse de la reconstruction de vitesse par tomographie avec un agent de contraste et la méthode de l'état adjoint. Nous présentons d'abord le principe des projections de Radon. Les conditions d'optimalité et l'algorithme d'optimisation sont ensuite présentés, ainsi que les détails des simulations. Les paramètres optimaux de simulations sont étudiés. Les résultats avec champs de vitesse stationnaires et non stationnaires sont présentés.

1.1 Tomographie

La tomographie est une technique d'imagerie médicale qui requiert des projections sous différents angles et basée sur l'atténuation des rayons X par les différents tissus du corps pour produire des section du corps humain. Les scanners usuels utilisent un tube de rayons X et une rangée de détecteurs. Les applications médicales sont nombreuses.

1.1.1 Principe des rayons X et de la tomographie

La radiographie est basée sur le fait que les rayons X sont plus ou moins absorbés en fonction de la densité des matériaux. L'agent de constraste permet une plus grande atténuation. La transmission des rayons X est décrite avec la loi de Beer-Lambert. Pour un matériau non homogène, avec une atténuation $A(x)$:

$$\frac{dI}{dx} = -A(x)I(x) \tag{1.1}$$

Si l'on note I_0 l'intensité du faisceau à la position x_0, I_1 celle à la position x_1 is denoted as I_1, on obtient pour un faisceau mono-énergétique:

$$ln(\frac{I_0}{I_1}) = \int_{x_0}^{x_1} A(x)dx \tag{1.2}$$

1.1.2 Transformée de Radon

Soit $\Sigma \in \mathbb{R}^2$ un domaine régulier, la transformée de Fourier d'une fonction f s'écrit:

$$Rf(\theta, s) = \int_{\Sigma \cap L(\theta,s)} f(\mathbf{x}) dl(\mathbf{x}) \tag{1.3}$$

La ligne $L(\theta, s)$ est déterminée par l'angle $\theta \in [0, \pi]$ et par la distance $s \in [-a, a]$ depuis l'origine comme présenté sur la figure 1.1. Un certain nombre d'angle de projections de Radon θ_i sont sélectionnés. Le tracé de la transformée de Radon en fonction de l'angle de projection θ s'appelle un sinograme.
Dans le problème de reconstruction considéré, le scanner tourne au cours du temps et les projections de Radon perpendiculaires au vaisseau sont acquises pour N_θ angles de projection distribués régulièrement dans la gamme $\Delta\theta(t)$. Pour chaque angle, N_p projections sont mesurées et les projections de Radon 2D sont obtenues pour Nz valeurs le long de l'axe z avec $z \in$[0, zmax].

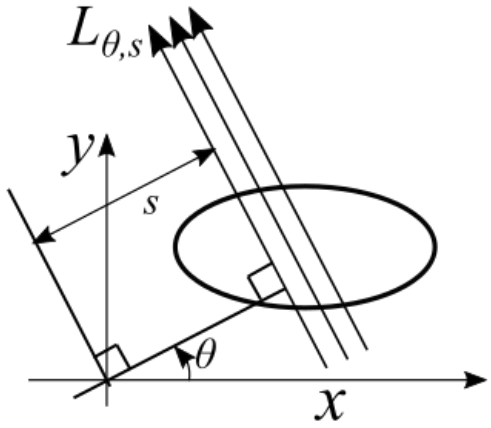

Figure 1.1: Principe de la transformation intégrale de Radon.

1.2 Problème inverse tomographique avec une équation aux dérivées partielles comme contrainte

Notre objectif est donc de reconstuire le champ de vitesse sanguin $\mathbf{V}$ à partir de projections de Radon d'un traceur et d'une équation aux dérivées partielles décrivant la propagation du traceur de densité f.

1.2.1 Problème inverse de la reconstruction du champ de vitesse

Notre but est de reconstruire le flux sanguin sur le fantôme de la Figure 1.4. Il s'agit d'un vaisseau avec une géométrie complexe et une bifurcation. Des projections 2D de Radon sont acquises perpendiculairement à l'axe du vaisseau dans le plan XY. La propagation de l'agent de contraste avec une concentration $f(\mathbf{x}, t)$ est modélisée avec une équation aux dérivées partielles basée sur le champ de vitesse $\mathbf{V}$ obtenu avec l'équation de Navier-Stokes. Nous notons Ω le domaine spatial, $[0, T]$ le domaine temporel et $Q = \Omega \times [0, T]$. Le tracer est injecté par la face d'entrée du vaisseau correspondant à $z = 0$. Nous supposons que les concentrations autres que celle du traceur peuvent être négligées. Nous avons étudié l'influence des paramètres de

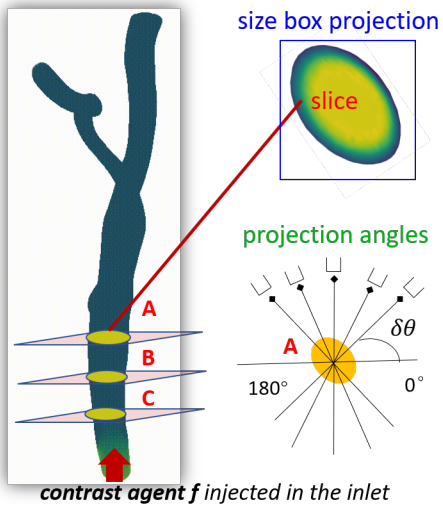

Figure 1.2: Vaisseau sanguin et paramètres utilisés dans les simulations.

simulation pour optimiser la reconstruction: taille de la zone de projection, nombre d'angles de projection, nombre de coupes comme montré sur la Figure 1.2. Dans la zone de projection, les projections de Radon sont obtenues avec une grille régulière. La propagation de l'agent de contraste dans le vaisseau est décrite par une équation de convection-diffusion.

1.2.2 Formulation du problème inverse de tomographie dynamique

Le problème inverse dynamique de tomographie que nous souhaitons résoudre peut s'écrire:

$$Rf(\theta, s, z, t) = p^{\delta}(\theta, s, z, t) \quad \forall\ \theta, s, z, t \tag{1.4}$$

où Rf est la transformée de Radon de la concentration du traceur f basée sur le champ de vitesse $\mathbf{V}$ du sang, p^{δ} sont les projections mesurées bruitées.

Les coordonnées s and z sont les coordonnées du détecteur, θ l'angle de projection et t le temps. Notre but est de trouver $f : [0, T] \rightarrow L_2(\Omega)$ à partir des équations linéaires précédentes1.4. puis le champ de vitesses $\mathbf{V}$ et nous allons ajouter une équation aux dérivées partielles pour décrire la propagation.

1.2.3 Formulation Variationelle

Une méthode variationelle est étudiée basée sur une fonction coût donnée par:

$$J(f, \mathbf{V}, \boldsymbol{\mu}) = \frac{1}{2}\int_0^T \|Rf(\theta, s, z) - p^{\delta}(t)\|_2^2 dt + \frac{\alpha_s}{2}\||\nabla \mathbf{V}|\|_2^2 \tag{1.5}$$

Cette fonction dépend de la concentration du traceur f, du champ de vitesse $\mathbf{V}$, et de paramètres $\boldsymbol{\mu}$. Le premier terme est un terme d'attache aux données qui mesure l'écart entre les projections mesurées et celles obtenues avec la concentration du traceur. Le second terme est un terme de régularisation pour la vitesse. Le premier terme est basé sur la norme L_2 définie sur $[0, \pi] \times [-a, a] \times [0, z_{\max}]$. Dans le terme de régularisation, $\||\nabla \mathbf{V}|\|_2$ dépend de la norme de Frobenius de la matrice jacobienne du champ de vitesse $\mathbf{V} = (u, v, w) : [0, T] \times \Omega \rightarrow \mathbb{R}^3$ combinée avec la norme $L_2(\Omega)$ du carré de chaque élément de la matrice. Le paramètre α_s est un paramètre de régularisation. L'ensemble des paramètres $\boldsymbol{\mu} = (\mu_1, \mu_2)$ est séparé en deux

sous-ensembles μ_1 et μ_2. Le premier sous-ensemble de paramètres μ_1 inclut la vitesse d'entrée et la pression de sortie dans l'équation de Navier-Stokes, μ_2 est défini comme l'ensemble des paramètres contenant la concentration initiale du traceur sur l'entrée du vaisseau, le coefficient de diffusion dans l'équation de transport présentée ci-dessous. Ces paramètres seront utiles au Chapitre 2 qui détaille la décomposition en composantes principales.

1.2.4 Formulation de type contrôle optimal avec une equation aux dérivées partielles.

Notre but est de minimiser la fonction coût précédente avec une contrainte donnée par une équation aux dérivées partielles. La propagation de l'agent de contraste dans le vaisseau est simulée par une équation de convection-diffusion avec un paramètre de diffusion D et une vitesse $\mathbf{V} = (u, v, w) : [0, T] \times \Omega \to \mathbb{R}^3$. Les champs de vitesses stationnaires ou dépendants du temps sont obtenus avec l'équation de Navier-Stokes dans le chapitre 3. Le champ de vitesse $\mathbf{V}$ est paramétré avec la première composante μ_1 de $\boldsymbol{\mu}$ liée aux conditions initiales et aux limites. Nous supposons que l'agent de contraste entre par un disque $(\mathcal{D})$ dans le plan $z = 0$. et que la valeur de f sur le disque $(\mathcal{D})$ est associée à la composante μ_2. L'équation de convection-diffusion s'écrit:

$$\begin{cases} e(f, \mathbf{V}, \boldsymbol{\mu}) = \frac{\partial f(\mathbf{x},t)}{\partial t} + u\frac{\partial f(\mathbf{x},t)}{\partial x} + v\frac{\partial f(\mathbf{x},t)}{\partial y} + w\frac{\partial f(\mathbf{x},t)}{\partial z} - D\triangle f(\mathbf{x}, t) = 0 \\ f(\mathbf{x}, t) = \mu_2 \quad \forall x \in (\mathcal{D}) \ \ \forall t \in [0, T] \\ f(\mathbf{x}, 0) = 0 \quad \forall x \in \Omega - (\mathcal{D}) \end{cases} \tag{1.6}$$

Nous supposons que la flux total sur la surface latérale est nul:

$$(-D\nabla f + fV).\mathbf{n} = 0 \ \ \forall t \in [0, T] \tag{1.7}$$

où $\mathbf{n}$ est la normale extérieure. Une condition de Neumann est imposée sur la face de sortie:

$$-D\nabla f.\mathbf{n} = 0 \ \ \forall t \in [0, T] \tag{1.8}$$

Cette équation sera utilisée comme contrainte de régularisation.

Le problème inverse peut être réécrit avec une fonctionelle réduite $\hat{J}$ dépendant uniquement du champ de vitesse $\mathbf{V}$ et formulé comme un problème de contrôle optimal:

$$\min_{\mathbf{V}, f \in U \times Y} J(f, \mathbf{V}, \boldsymbol{\mu}) = \min_{\mathbf{V} \in U} J(f(\mathbf{V}), \mathbf{V}, \boldsymbol{\mu}) = \min_{\mathbf{V} \in U} \hat{J}(\mathbf{V}, \boldsymbol{\mu}) \tag{1.9}$$

où U, Y sont les champs de vecteurs et concentrations admissibles. Le paramètre $\boldsymbol{\mu}$ sera utile pour la décompostion en composantes principales (POD).

1.3 Méthode de l'état adjoint pour le problème inverse

Afin de calculer le gradient de la fonctionelle réduite $\hat{J}$ et les conditions d'optimalité, nous considérons une variable duale $p : [0, T] \to L_2(\Omega)$, et un Lagrangian L combinant la fonctionelle précédente et l'équation aux dérivées partielles:

$$L(f, \boldsymbol{V}, p, \boldsymbol{\mu}) = J(f, \boldsymbol{V}, \boldsymbol{\mu}) + \beta \int_0^T < e(f, \boldsymbol{V}, \boldsymbol{\mu}), p(t) > dt \tag{1.10}$$

where β est un paramètre du Lagrangien et $< ., . >$ dénote le produit scalaire de $L_2(\Omega)$. Les conditions d'optimalité permettent d'obtenir les valeur optimales pour f, la vitesse $\boldsymbol{V}$, et la variable adjointe p.

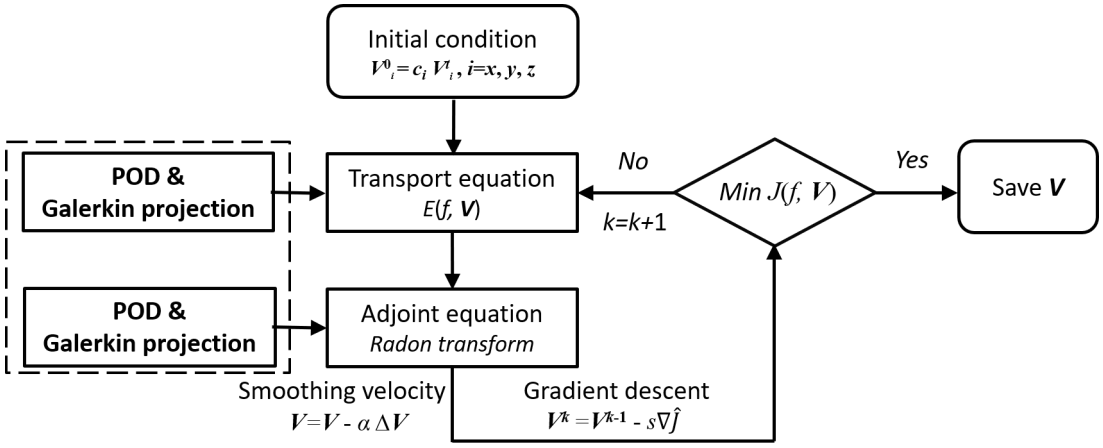

Figure 1.3: Résumé de la méthode itérative de l'état adjoint

1.3.1 Conditions d'optimalité

1.3.1.1 Condition d'optimalité pour la concentration du traceur et équation adjointe

Nous obtenons l'équation suivante pour la variable adjointe p:

$$\beta(\frac{dp}{dt} + \boldsymbol{V}.\nabla p + D\nabla.\nabla p) = R^t(Rf - g) \;\; with \;\; p(.,T) = 0 \tag{1.11}$$

1.3.1.2 Condition d'optimalité pour la vitesse

Pour la vitesse nous obtenons

$$-\alpha_s \triangle \boldsymbol{V} = \beta p \nabla f \;\; in \;\; \Omega \times [0,T] \tag{1.12}$$

Le gradient de la fonctionelle réduite est alors donné par:

$$\nabla\hat{J} = \int_0^T (\beta p \nabla f - \alpha_s \triangle \boldsymbol{V}) dt \tag{1.13}$$

1.3.2 Implémentation de la méthode de l'état adjoint

Après initialisation avec un champ de vitesse $\boldsymbol{V}_0$ et une concentration de traceur f_0, les étapes suivantes sont répétées pour chaque itération k:
(1) la concentration à l'itération k, $f_k(\mathbf{x}, t)$, est estimée avec l'équation de transport Eq.1.6 en utilisant la vitesse approchée $\boldsymbol{V}_k$.
(2) L'équation adjointe est utilisée pour calculer la variable adjointe p_k avec Eq.1.11.
(3) Le gradient de la fonctionnelle réduite $\nabla\hat{J}(\boldsymbol{V}_k)$ peut alors être obtenu. Le champ de vitesse $\boldsymbol{V}_k$ est mise à jour avec une descente de gradient Eq.1.13 et une méthode de recherche de pas de descente s.

Un résumé de la méthode est présenté sur la figure 1.3. La méthode de décomposition en composantes principale sera considérée par la suite. Pour chaque composante, nous avons

$$V_i^k = V_i^{k+1} - s\nabla\hat{J}_i, \;\; i = x, y, z \tag{1.14}$$

1.4 Détails de simulation

Nous avons utilisé des maillages non structurés avec des tétraèdres pour les simulations présentés Figure 1.4. Plus précisemment, le fantôme numérique utilisé est un vaisseau avec une bifurcation (géométrie 1). Il s'agit d'un vaisseau de 10 cm de long avec un diamètre transverse de 10 millimeters. Les simulations numériques avec des éléments finis ont été réalisées avec Fenics.

(a) Geometry 1 (b) Geometry 2

Figure 1.4: Maillages non structurés utilisés.

Nous discrétisons les valeurs des différents champs sur une grille de taille $N_t = 50$ pour le domaine temporel $[0, T]$ = [0s, 0.5s] avec un intervalle de temps $dt = 0.01$s. Une vitesse vérité terrain est obtenue en résolvant les équations de Navier-Stokes puis ce champ de vitesse est utilisé dans l'équation de transport pour le traceur qui sert de vérité terrain. Le problème inverse est résolu en utilisant la méthode de l'état adjoint en partant d'une approximation du champ de vitesse. Des différences finies en temps sont utilisées avec une méthode d'Euler explicite. La discrétisation spatiale consiste en 64000 noeuds avec des éléments finis de type $P1$. Les discrétisations en temps et en espace respectent les conditions de stabilité usuelles. Les champs de vitesses correspondent au régime laminaire. Nous avons testé la méthode de l'état adjoint avec deux types de champs de vitesses, stationnaires et non stationnaires obtenus avec les équations de Navier-Stokes. Nous avons utilisé les algorithmes proposés dans Fenics avec une discrétisation de Taylor-Hood ($P2 - P1$) pour les éléments finis et l'algorithme Incremental Pressure Correction scheme. Une condition de non glissement est appliquée sur la frontière latérale du vaisseau et en sortie une condition de pression nulle.

Le champ de vitesses non stationnaire est donné par:

$$\begin{cases} 0.4 + 0.4sin(\pi t) \quad for \;\; t \leq 0.5 \\ 0.4 + 0.4(3/2 - 0.5cos(2\pi(t - 0.5)) \quad for \;\; t \leq 0.5 \end{cases} \tag{1.15}$$

Pour le champ de vitesse stationnaire, la vitesse le long de l'axe z est de 0.4 m/s sur la face d'entrée avec un profil parabolique. Dans les simulations, la concentration initiale du traceur est $f^*(\mathbf{x}, z = 0) = 1$ pour tous les points de la surface et tous les temps. Les projections de Radon sont obtenues pour N_z valeurs le long de l'axe z. La concentration du traceur est projetée sur une grille rectangulaire régulière. L'opérateur de Radon et son adjoint sont estimés avec la librairie python Scipy. Les valeurs de $R^t(Rf - p)$ sont interpolées sur le maillage initial.

Pour les simulations, nous avons utilisé $N_z = 20$ ou $N_z = 40$ coupes. Pour chaque instant $t_p = pT/N_t$ dans le domaine temporel, $0 \leq t_p \leq T$, un nombre d'angles de projection N_θ a été considéré dans la gamme angulaire $\Delta\theta(t)$ ainsi qu'un nombre variable N_p de projections pour la discrétisation de l'opérateur de Radon. Nous avons aussi choisi différentes gammes d'angles $\Delta\theta(t) = [p\delta\theta, (p+1)\delta\theta]$ correspondant aux angles de mesure lors de la rotation du scanner avec un intervalle de mesure $\delta\theta$ dans la gamme 36, 45, 90 or 180°. Un bruit Gaussian avec un rapport signal sur bruit (PPSNR) entre 0 and 40 dB est ajouté aux projections de Radon pour étudier l'effet du niveau de bruit. Le rapport signal sur bruit est déterminé par:

$$PPSNR = 20log(\frac{S_{max}}{n_{max}}) \tag{1.16}$$

où S_{max} est l'amplitude maximale du signal et n_{max} l'amplitude maximale du bruit. Un optimum global du champ de vitesse ne peut pas être atteint par cet algorithme et les initialisations du traceur f_0 et du champ de vitesse$\mathbf{V}_0$ sont cruciales. Différentes initialisations ont été testées. Le paramètre de régularisation et le coefficient β sont obtenues pour avoir les meilleurs décroissances pour le terme d'attache aux données et le Lagrangien. Les itérations sont stoppées au minimum du terme d'attache aux données.
Nous avons calculé l'évolution des erreurs relatives de moindre carré (RMSE) en fonction de l'itération k pour plusieurs quantités en utilisant les normes $L2$. Ces quantités incluent le champ de vitesse V_k, ses composantes et la concentration reconstruite du traceur f_k. L'erreur pour la concentration du traceur est donnée par:

$$RMSE(f_k) = (\sum_{p=1}^{N_t} \|f_k(\mathbf{x}, t_p) - f^*(\mathbf{x}, t_p)\|^2_{L_2(\Omega)})^{1/2} / (\sum_{p=1}^{N_t} \|f^*(\mathbf{x}, t_p)\|^2_{L_2(\Omega)})^{1/2} \tag{1.17}$$

L'erreur pour la vitesse à l'itération k est:

$$\begin{aligned} RMSE(\mathbf{V}_k) = (\textstyle\sum_{p=1}^{N_t} \|u(\mathbf{x}, t_p) - u_k(\mathbf{x}, t_p)\|^2_{L_2(\Omega)} + \|v(\mathbf{x}, t_p) - v_k(\mathbf{x}, t_p)\|^2_{L_2(\Omega)} \\ + \quad \|w(\mathbf{x}, t_p) - w_k(\mathbf{x}, t_p)\|^2_{L_2(\Omega)})^{1/2} / (\textstyle\sum_{p=1}^{N_t} \|u(\mathbf{x}, t_p)\|^2_{L_2(\Omega)} + \|v(\mathbf{x}, t_p)\|^2_{L_2(\Omega)} + \|w(\mathbf{x}, t_p)\|^2_{L_2(\Omega)})^{1/2} \end{aligned} \tag{1.18}$$

où la somme est étendue à tous les instants. Pour les composantes du champ de vitesse, les définitions sont similaires.

1.5 Résultats de simulation pour la reconstruction du champ de vitesses sanguin

1.5.1 Champ de vitesses non stationnaires

La Figure 1.5 montre les courbes d'erreur de reconstruction pour différent niveaux de bruit Gaussien. On peut observer une décroissance de l'erreur pour la vitesse et la concentration du traceur. Quand le niveau de bruit augmente de 40 dB à 0 dB, ces erreurs de reconstruction ont tendance à augmententer. Les courbes d'erreur pour les composantes de la vitesse reconstruite sont présentées Figure 1.6.

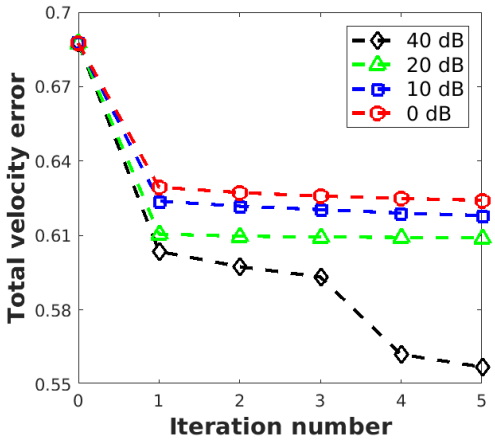

(a) Erreur pour la vitesse

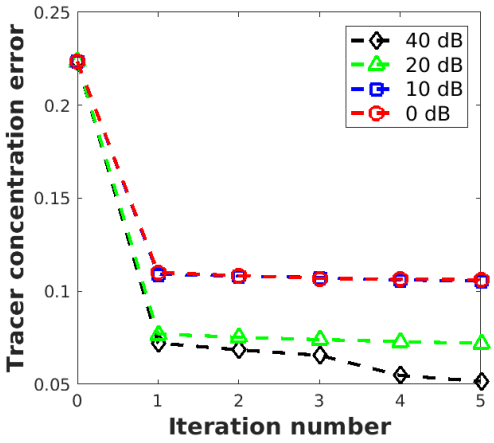

(b) Erreur pour la concentration du traceur

Figure 1.5: Courbes d'erreur de reconstruction pour les différentes composantes de la vitesse.

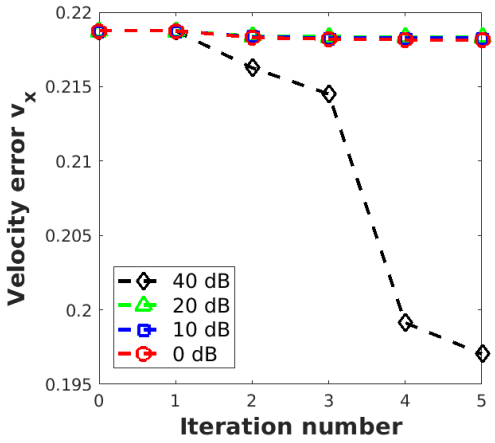

(a) Velocity error along x

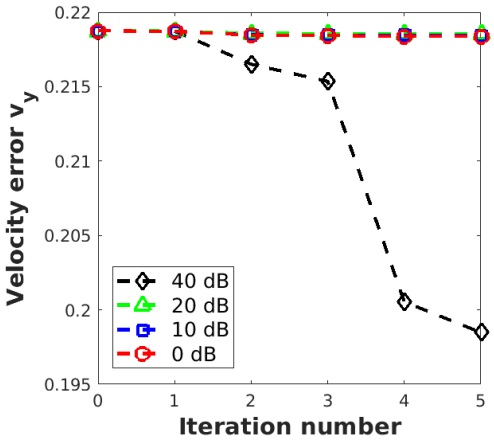

(b) Velocity error along y

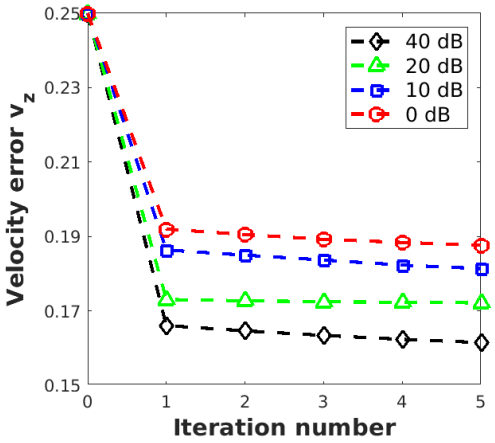

(c) Velocity error along z

Figure 1.6: Erreurs de reconstruction pour les composantes de la vitesse pour un champ de vitesses non stationnaire.

Sur cette figure, les erreurs de reconstruction selon x et y montrent une très légère décroissance en présence de bruit alors que la composante suivant z montre une décroissance régulière.

1.5.2 Examples de reconstructions du champ de vitesse et de la concentration du traceur.

1.5.2.1 Champ de vitesse non stationnaire

Champ de vitesse Nous étudions tout d'abord les composantes du champ de vitesse sanguin reconstruit selon les axes x, y et z.

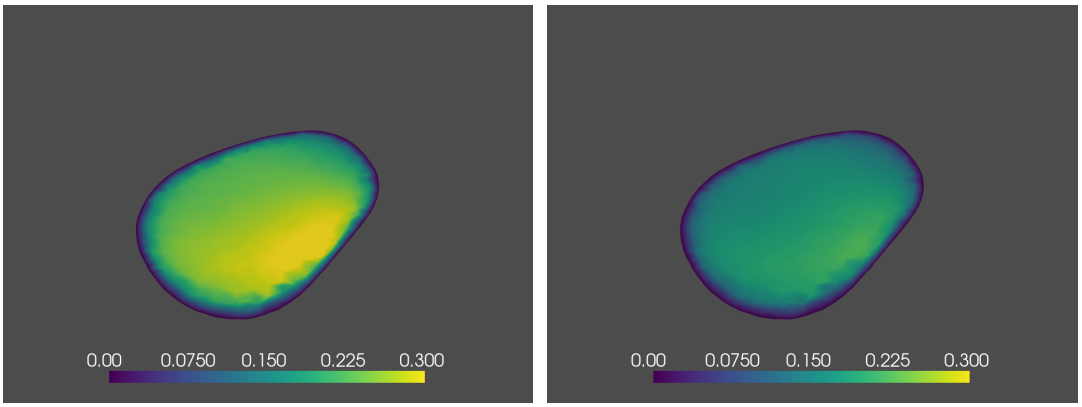

(a) Ground truth velocity along x (b) Reconstructed velocity along x

Figure 1.7: Champ de vitesse non stationnaire reconstruit selon x pour $z = 0.155$ et $t = 0.05$s, et pour un PPSNR = 40 dB.

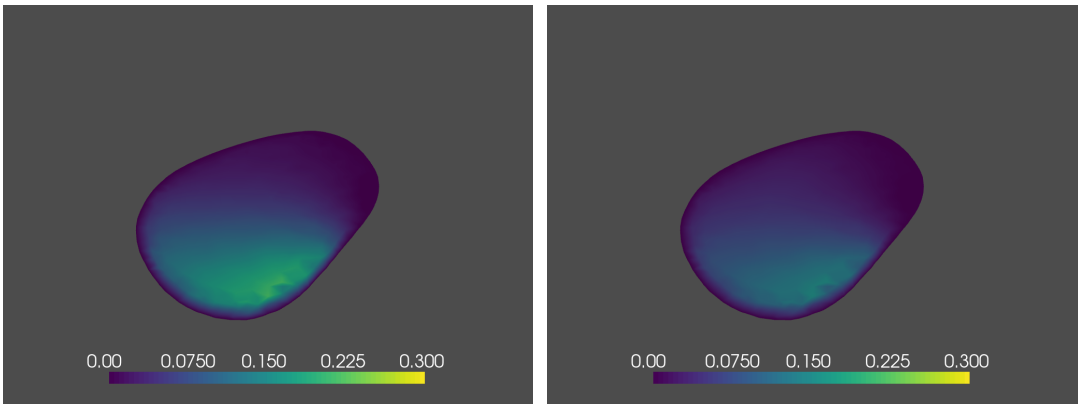

(a) Ground truth velocity along y (b) Reconstructed velocity along y

Figure 1.8: Champ de vitesse reconstruit selon y pour $z = 0.155$ et $t = 0.05$s, et pour un PPSNR = 40 dB.

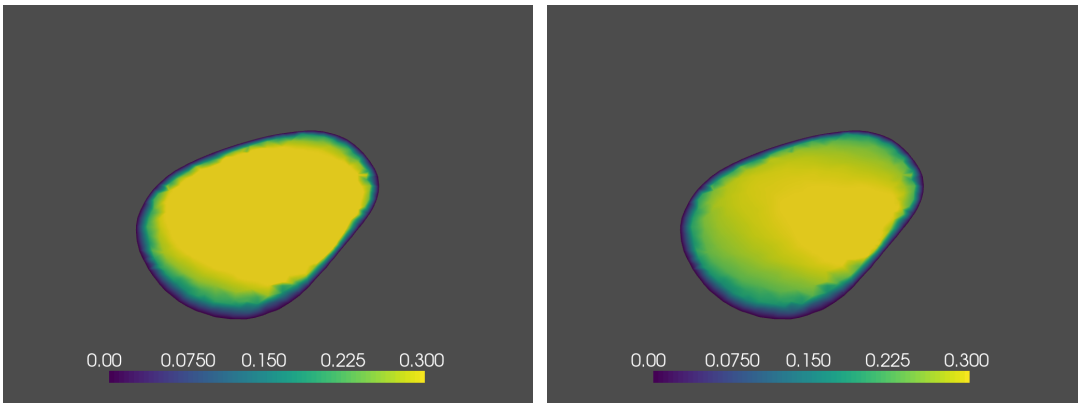

(a) Ground truth velocity along z (b) Reconstructed velocity along z

Figure 1.9: Champ de vitesse non stationnaire selon z pour $z = 0.155$ et $t = 0.05$s, et pour un PPSNR = 40 dB.

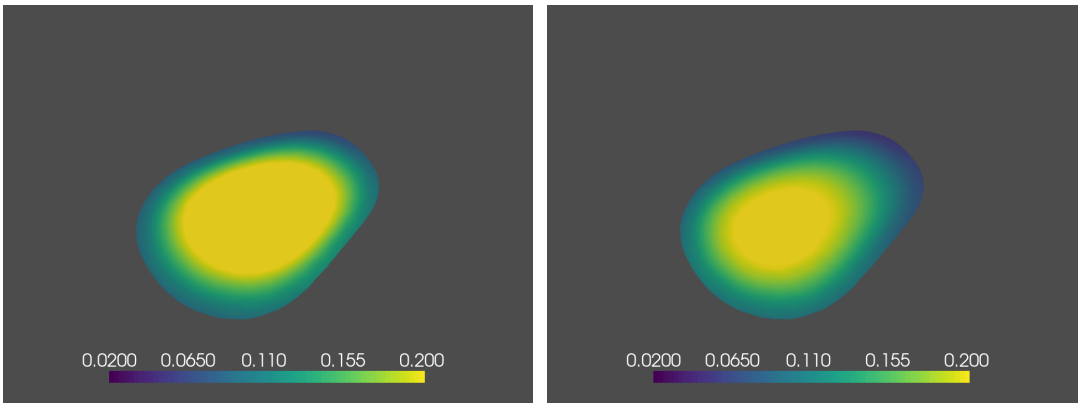

(a) Ground truth tracer concentration (b) Reconstructed tracer concentration

Figure 1.10: Concentration du traceur pour un champ de vitesse non stationnaire et $z = 0.155$ et $t = 0.05$s, pour un PPSNR = 40 dB.

Les figures présentées comparent les reconstructions et les vérités terrain pour z=0.155m, pour le champ de vitesse et la concentration, pour $t = 0.05s$. Sur les figures 1.7, 1.8, 1.9, on peut observer que la vitesse reconstruite et la vérité terrain sont très similaires.
Champ de concentration du traceur Pour la concentration du traceur sur la Figure 1.10, on peut voir que que les concentrations sont similaires.

1.6 Conclusion

Ce chapitre a donc présenté une nouvelle approche pour la reconstruction d'un champ de vitesse sanguin à partir de projections de Radon perpendiculaires à la direction principale du vaisseau. Une équation aux dérivées partielle de transport est utilisée pour régulariser la reconstruction. Les champs de vitesse sont obtenus par la méthode de l'état adjoint. La faisabilité de la méthode est montrée sur un vaisseau présentant une bifurcation. Des résultats

satisfaisants sont obtenus pour des champs de vitesse stationnaire et non stationnaires par la méthode de l'état adjoint. La composante axiale est la mieux reconstruite.

Chapter 2

Decomposition en modes propres orthogonaux pour accélérer la reconstruction du champ de vitesses.

2.1 Introduction

Dans le chapitre précédent, la méthode classique de l'état adjoint a été développée pour la reconstruction du champ de vitesse sanguin avec une équation de transport comme contrainte. Les temps de calcul restent très longs. Notre objectif est donc d'obtenir une reconstruction satisfaisante avec un temps de reconsruction raisonnable.

Avec une réduction du modèle, nous pouvons incorporer la structure du problème physique et les équations. Cette réduction est basée sur des fonctions de base qui encodent l'information sur la structure de la solution. La réduction de modèle peut être atteinte en couplant une décompostion en mode propres orthogonaux (POD) couplée avec une projection de Galerkin. Cette méthode permet de réduire les temps de calcul tout en prenant en compte le comportement décrit par les calculs avec le maillage initial. L'idée est d'obtenir une approximation de basse dimension en projetant le problème de grande dimension sur un sous-espace de dimension réduite. Cette réduction de modèle peut être considérée avec un ensemble de paramètres physiques et géométriques. Nous nous intéressons donc dans ce chapitre à un couplage entre la décomposition en mode propres orthogonaux et la méthode de l'état adjoint. Les variables prises en compte sont la vitesse, la concentration du traceur et les variables adjointes. Elles sont représentées par des ensembles de fonctions de bases qui sont obtenues à partir d'échantillons de ces distributions obtenus en faisant varier un certains nombre de paramètres physiques. L'efficacité de cette approche est illustrée sur des simulations numériques en utilisant des champs de vitesses stationnaire et non stationnaires et un fantôme réaliste. Nous présentons aussi une comparaison avec la méthode qui utilise le maillage de départ complet en termes de temps de calcul et d'erreurs de reconstruction.

2.2 Principe de la décomposition en modes propres orthogonaux.

Nous présentons la décomposition en modes propres orthogonaux (POD) pour la concentration du traceur à titre d'exemple. Des méthodes similaires peuvent être utilisées pour calculer les bases pour les composantes du champ de vitesse et la variable adjointe.

La base POD $\{\psi_{f,j}\}_{1\leq j\leq N_f}$ de rang N_f est obtenue avec des échantillons $\{y_j\}_{1\leq j\leq N_s} = \{f(\mu_j)\}_{1\leq j\leq N_s} \in \mathbb{R}^m$ et les paramètres du modèle $\{\mu_j\}_{1\leq j\leq N_s}$. Les bases réduites sont obtenues

à partir de la matrice des échantillons $Y = [y_1, ...y_{Ns}] \in \mathbb{R}^{m \times N_s}$ où les échantillons sont placés dans les colonnes. La décomposition en valeurs singulières de la matrice (SVD) s'écrit:

$$\Psi_f^t Y \Phi_f = \begin{pmatrix} D & 0 \\ 0 & 0 \end{pmatrix} = \Sigma \in \mathbb{R}^{m \times N_s} \tag{2.1}$$

où $D = \mathsf{diag}(\sigma_1, ..., \sigma_d) \in \mathbb{R}^{d \times d}$ contient les valeurs propres en ordre décroissant $\sigma_j \geq \sigma_{j+1} \geq 0$. La matrice Σ est une matrice de rang d. Les matrices $\Phi_f \in \mathbb{R}^{N_s \times N_s}$ et $\Psi_f \in \mathbb{R}^{m \times m}$ sont des matrices orthogonales avec des colonnes $\{\varphi_{f,j}\}_{1 \leq j \leq N_s}$ et $\{\psi_{f,j}\}_{1 \leq j \leq m}$ respectivement. Les vecteurs $\psi_{f,j}$ et $\varphi_{f,j}$ représentent les vecteurs propores des matrices de covariance YY^t and Y^tY avec les valeurs propres $\lambda_j = \sigma_j^2$ pour $j = 1, ...d$ et ils satisfont les relations:

$$Y\varphi_{f,j} = \sigma_j \psi_{f,j} \qquad Y^t \psi_{f,j} = \sigma_j \varphi_{f,j} \quad pour \quad j = 1, ...d \tag{2.2}$$

La base POD de rang N_f peut être obtenue avec le problème de valeurs propres:

$$Y^t Y \varphi_{f,i} = \lambda_i \varphi_{f,i} \ \ pour \quad i = 1, ...N_f \tag{2.3}$$

Les N_f vecteurs propres $\varphi_{f,1}$ ... $\varphi_{f,N_f} \in \mathbb{R}^{N_s}$ sont calculés et nous avons:

$$\psi_{f,i} = \frac{1}{\sqrt{\lambda_i}} Y \varphi_{f,i} \ \ pour \quad i = 1, ...N_f \tag{2.4}$$

Nous avons calculé plusieures bases réduites de rang N_f, N_V, et N_p pour la concentration du traceur f, les composantes du champ de vitesse V_x, V_y, V_z, et la variable adjointe p. Ces bases seront notés Ψ_f, Ψ_{V_x}, Ψ_{V_y}, Ψ_{V_z} et Ψ_p dans la suite.

2.3 Méthode POD-adjoint pour la résolution du problème inverse

La méthode de l'état adjoint présentée dans le premier chapitre est donc combinée avec une réduction POD pour différentes conditions paramétriques.

Le fantôme utilisé pour les simulations est le même que précédemment pour la méthode de l'état adjoint et présenté Figure 2.1. Le problème inverse est paramétré en employant un paramètre μ appartenant à un espace de paramètres $\mathcal{M}$. Cela nous conduit à reformuler le problème inverse et la méthode avec ce nouveau paramètre. La direction principale d'écoulement est la direction z et des projections de Radon perpendiculaires sont mesurées dans le plan xy. La propagation de l'agent de contraste avec la concentration $f(\mathbf{x}, t)$ est décrite avec une équation aux dérivées partielles basée sur un champ de vitesse réaliste obtenu avec l'équation de Navier-Stokes. Nous supposons que les concentrations des autres matériaux peuvent être ignorées. La propagation de l'agent de contraste est à nouveau décrite avec une équation de convection-diffusion avec un coefficient de diffusion D et une vitesse $\mathbf{V} = (u, v, w) : [0, T] \times \Omega \rightarrow \mathbb{R}^3$. Le champ de vitesse $\mathbf{V}$ est paramétré par la première composante μ_1 de μ reliée aux conditions initiales et aux limites. L'agent de contraste est injecté dans le vaisseau à travers un disque $(\mathcal{D})$ dans le plan $z = 0$. On suppose aussi que la valeur de la fonction f sur le disque $(\mathcal{D})$ est associée au paramètre μ_2 du problème inverse paramétré.

La méthode de réduction proposée dans ce travail est basée sur l'hypothèse que l'ensemble des solutions

$$\mathcal{M} = \{f(\mu), \mathbf{V}(\mu), p(\mu); \mu \in \mathcal{M}\} \tag{2.5}$$

Figure 2.1: Maillage du vaisseau utilisé pour les simulations.

peut être approximé par un sous-espace de basse dimension pendant une phase initiale. L'ensemble $\mathcal{M}$ est échantillonné avec un sous-ensemble discret de paramètres $\mathcal{M}_s \subset \mathcal{M}$ de cardinal $N_s = |\mathcal{M}_s|$. Un ensemble de solutions peut être défini pour les échantillons, $\{f(\mu), \mathbf{V}(\mu), p(\mu); \mu \in \mathcal{M}_s\}$. qui est une bonne représentation de $\{f(\mu), \mathbf{V}(\mu), p(\mu); \mu \in \mathcal{M}\}$. Les solutions obtenues par élément finis avec le maillage fin initial seront notées $\{f_{\mathcal{F}}(\mu), \mathbf{V}_{\mathcal{F}}(\mu), p_{\mathcal{F}}(\mu), \mu \in \mathcal{M}_s\}$. Les vecteurs de $\mathbb{R}^m$ ou $\mathbb{R}^{3m}$ pour la concentration du traceur, la variable adjointe ou les champs de vitesse, sont projetés sur des sous espaces de dimension finie en utilisant des bases réduites $(\Psi_{f,i})_{1\leq i\leq N_f}$, $(\mathbf{\Psi}_{V,j})_{1\leq j\leq N_v}$, $(\Psi_{p,k})_{1\leq k\leq N_p}$ de dimensions N_f, N_V^3 et N_p. Dans la sous-section 2.3.1, nous donnons une description de la méthode de construction des bases pour la vitesse, la concentration du traceur et la variable adjointe. Dans la sous-section 2.3.2, nous présentons la nouvelle méthodologie pour résoudre le problème inverse.

2.3.1 Etape initiale: construction des bases POD pour la concentration du traceur, la vitesse et la variable adjointe.

Des décompositions distinctes sont utilisées sur chacun des espaces de solutions: $\{f_{\mathcal{F}}(\mu_1), ...f_{\mathcal{F}}(\mu_{N_s})\}$, $\{\mathbf{V}_{\mathcal{F}}(\mu_1), ...\mathbf{V}_{\mathcal{F}}(\mu_{N_s})\}$, $\{p_{\mathcal{F}}(\mu_1), ...p_{\mathcal{F}}(\mu_{N_s})\}$ pour obtenir des espaces de faible dimension $Y_{N_f}, U_{N_V}, P_{N_p}$ de dimensions respectives N_f, N_V^3 et N_p. Le but de la méthode POD est d'extraire quelques vecteurs de base qui capturent l'information critique.

2.3.2 Deuxième étape en ligne: réduction de modèle POD pour le problème inverse.

Pendant la phase en ligne, une projection de $f(\mu), \mathbf{V}(\mu), p(\mu)$ est réalisée sur Y_{N_f}, U_{N_V} et P_{N_p} respectivement. Nous réécrivons les équations du modèle sous une forme réduite, et la

concentration du traceur est approximée dans la base POD:

$$f = \Psi_f \hat{f} \tag{2.6}$$

où $\Psi_f \in \mathbb{R}^{m \times N_f}$ la matrice constiutée des vecteurs de base pour la concentration du traceur, et $\hat{f}$ désigne les coefficients de la concentration dans cette base. Après projection de Galerkin, un opérateur linéaire est associé aux équations différentielles. Le modèle réduit peut être obtenu par:

$$\frac{d\hat{f}}{dt} = \hat{A}\hat{f} \tag{2.7}$$

avec $\hat{f}(0) = \Psi_f^t f(0)$. L'opérateur réduit est relié à l'opérateur de départ par $\hat{A} = \Psi_f^t A \Psi_f$. Nous allons résoudre cette équation par une méthode de différences finies en temps. Après avoir implémenté ces différences finies pour la discrétisation en temps,l'équation aux dérivées partielles $e(f, \mathbf{V}, \mu) = 0$ peut être réécrite

$$A^n f = f^n \tag{2.8}$$

avec

$$A^n f = f + (u^n \frac{\partial f}{\partial x} + v^n \frac{\partial f}{\partial y} + w^n \frac{\partial f}{\partial z} - D\triangle f)\delta t \tag{2.9}$$

où δt est le pas de temps de la discrétisation et f^n, u^n, v^n, et w^n sont la concentration du traceur et les composantes du champ de vitesse pour l'étape n approximés par projection sur les sous-espaces de dimension finie. Après projection, les N_f coefficients du dévelopement du traceur à l'instant $n+1$ sont calculés par résolution d'un système linéaire avec une matrice de $\mathbb{R}^{N_f \times N_f}$.

Nous avons aussi implémenté les réductions de modèle pour l'équation adjointe et le gradient de $\hat{J}$. Pour l'équation adjointe, nous pouvons obenir l'équation différentielle réduite avec la matrice Ψ_p générée par les échantillons de la variable adjointe. Le gradient de vitesse est projeté sur la base de la vitesse. Par exemple, nous notons $\nabla \hat{J}_x$ la composante le long de x du gradient obtenue selon la méthode expliquée au chapitre 1. Le gradient projeté est alors obtenu selon:

$$\nabla \tilde{J}_x = \Psi_{V_x} \Psi_{V_x}^t \nabla \hat{J}_x \tag{2.10}$$

On peut obtenir les composantes selon y et z du gradient réduit avec les matrices Ψ_{V_y} et Ψ_{V_z}. L'étape en ligne suit un schéma itératif similaire à celui de la méthode classique de l'état adjoint (Chapitre 1). La différence avec la méthode de l'état adjoint est la réduction POD et les projections pour l'équation de transport et l'équation adjointe.

2.4 Détails des simulations numériques

2.4.1 Construction des bases POD

Le problème inverse considéré repose sur un ensemble de paramètres μ. Les échantillons sont obtenus à la fois dans le temps et dans l'espace des paramètres avec une grille d'échantillonage régulière. Le paramètre μ_1 est relié aux conditions initiales et aux limites du champ de vitesse. Pour obtenir les échantillons pour le champ de vitesse, nous considérons des champs de vitesses stationnaires et non stationnaires obtenus avec les équations de Navier-Stokes. L'équation non stationnaire de Navier-Stokes s'écrit:

$$\begin{cases} \frac{\partial \mathbf{V}}{\partial t} + \mathbf{V}.\nabla\mathbf{V} + \nabla p - \nu\triangle\mathbf{V} = 0 \\ \nabla.\mathbf{V} = 0 \\ \mathbf{V} = \mathbf{V}_{\partial\Omega} \ \ on \ \ \partial\Omega \end{cases} \tag{2.11}$$

et l'équation stationnaire est donnée par:

$$\begin{cases} \mathbf{V}.\nabla\mathbf{V} + \nabla p - \nu\triangle\mathbf{V} = 0 \\ \nabla.\mathbf{V} = 0 \\ \mathbf{V} = \mathbf{V}_{\partial\Omega} \ \ on \ \ \partial\Omega \end{cases} \tag{2.12}$$

avec $\mathbf{V}_{\partial\Omega}$ le champ de vitesse sur la frontière $\partial\Omega$. La frontière $\partial\Omega = \Gamma_{in} \cup \Gamma_{out} \cup \Gamma_s$ du domaine spatial Ω inclut une zone d'entrée Γ_{in} sur le plan $z = 0$, une frontière de sortie Γ_{out} sur le plan de sortie et une frontière latérale Γ_s. La vitesse $\mathbf{V}_{\Gamma_{in}}$ sur la frontière d'entrée Γ_{in} et la pression $p_{\Gamma_{out}}$ sur la région de sortie Γ_{out} sont utilisées comme variables de contrôle. La condition de Dirichlet à l'entrée est donc $\mathbf{V} = \mathbf{V}_{\Gamma_{in}}$ sur le domaine Γ_{in}. Pour la sortie du vaisseau , nous considerons $\nu\partial_{\mathbf{N}}\mathbf{V} + p\mathbf{N} = \mathbf{0}$ où $\mathbf{N}$ est la normale unitaire et $\partial_{\mathbf{N}} = \mathbf{N}.\nabla$ désigne la dérivée normale. Nous choisissons un profil parabolique avec une valeur maximum $\mathbf{V}_{\Gamma_{in},max}$ sur le centre de la frontière d'entrèe. La vitesse stationnaire est donc paramétrée par $\mu_1 = (\mathbf{V}_{\Gamma_{in},max}, p_{\Gamma_{out}})$. Les échantillons du champ de vitesse sont obtenus avec une grille régulière de la vitesse d'entrée et de la pression de sortie. Pourla vitesse d'entrée, nous choisissons 10 valeurs entre 0.2 and 0.6 m/s, et pour la pression de sortie 10 valeurs entre 0 et 1000Pa. Pour le champ de vitesses non stationnaires, la vitesse d'entrée est donnée par:

$$\begin{cases} \mathbf{V}_{\Gamma_{in},max} + \mathbf{V}_{\Gamma_{in},max} sin(\pi t) \ \ for \ \ t \leq 0.5 \\ \mathbf{V}_{\Gamma_{in},max} + \mathbf{V}_{\Gamma_{in},max}(3/2 - 0.5cos(2\pi(t - 0.5)) \ \ for \ \ t \leq 0.5 \end{cases} \tag{2.13}$$

Le champ de vitesse non stationnaire est donc paramétré par $\mu_1 = (\mathbf{V}_{\Gamma_{in},max}, p_{\Gamma_{out}}, t_i)$, où $(t_i)_{1\leq i\leq 50}$ sont les temps de la simulation. Pour obtenir la base POD pour la concentration du traceur nous utilisons les solutions calculées avec l'équation de transport à différents instants, pour différents champs de vitesses, et pour différentes concentrations d'entrée du traceur. Le paramètre μ_2 dépend de la concentratoin du traceur sur la face d'entrée. Trois concentrations entre 0.5 et 1.5 kg/m^3 ont été considérées. Une approche similaire a été appliquée pour les échantillons de la variable adjointe. Les bases pour les différentes grandeurs sont calculées comme expliqué au dessus pour obtenir des espaces de dimension finie N_f, N_v^3 et N_p. L'erreur de projection est la some des carrés des valeurs singulières pour les valeurs singulières non contenues dans la base POD. Par exemple, l'erreur de projection pour la concentration du traceur est calculée par: $\sum_{i=N_f+1}^{N_s} \sigma_i^2$. Nous estimons la qualité des bases avec cette erreur de projection. Pour la concentration du traceur, un nombre d'élément dans la base est choisi avec une tolérance κ telle que:

$$\frac{\sum_{i=1}^{N_f} \sigma_i^2}{\sum_{i=1}^{N_s} \sigma_i^2} > \kappa \tag{2.14}$$

Nous avons choisi $\kappa = 1\%$. Nous considérons le même critère de sélection pour les champs de vitesses, la variable adjointe et la concentration du traceur. Dans nos simulations, nous avons choisi pour le cas non stationnaire$N_v = 6$, $N_f = 40$, et $N_p = 2$. Avec ces valeurs, les erreurs relatives de projection POD sont inférieures à 1%, Pour les champs de vitesses stationnaires, les bases pour la vitesse, la concentration du traceur et la variable adjointe sont obtenues en sélectionant 2, 75, ou 6 vecteurs propres. La dimension réduite totale est donc $2^3 * 75 * 6$. Nous avons donc obtenu des espaces de faible dimension qui permettent de maintenir une précision élevée pour la résolution du problème inverse.

2.5 Discussion des résultats de reconstruction du champ de vitesse sanguin

2.5.1 Comparaison de la méthode POD-adjoint avec l'approximation complète par éléments finis

Dans cette section, pour évaluer l'efficacité de la méthode POD-adjoint, nous utilisons les même cas pour comparer les deux méthodes pour des champs de vitesses stationnaires et non stationnaires. Les conditions initiales et aux limites choisies sont les suivantes: vitesse d'entrée 0.55m/s, pression de sortie 750Pa pour résoudre l'équation de Navier-Stokes, concentration de traceur injectée 1.1kg/m3 pour l'équation de transport.

2.5.1.1 Vitesse non stationnaire

Nous donnons ici les résulats de reconstruction pour une vitesse et une concentration correspondant à $\mu_1 = (0.55m/s, 500Pa)$ et une concentration sur l'entrée du vaisseau de $\mu_2 = 1.1kg/m^3$. Les évolutions avec les itérations des métriques d'erreur (RMSE) pour la vitesse et la concentration sont présentées Figure 2.2 pour différents niveaux de bruit et les deux méthodes. Les erreurs de reconstruction pour les champs de vitesse et la concentration du traceur sont remarquablement réduites avec l'approche POD-adjointe et elle améliore l'approximation complète par éléments finis (FOA).

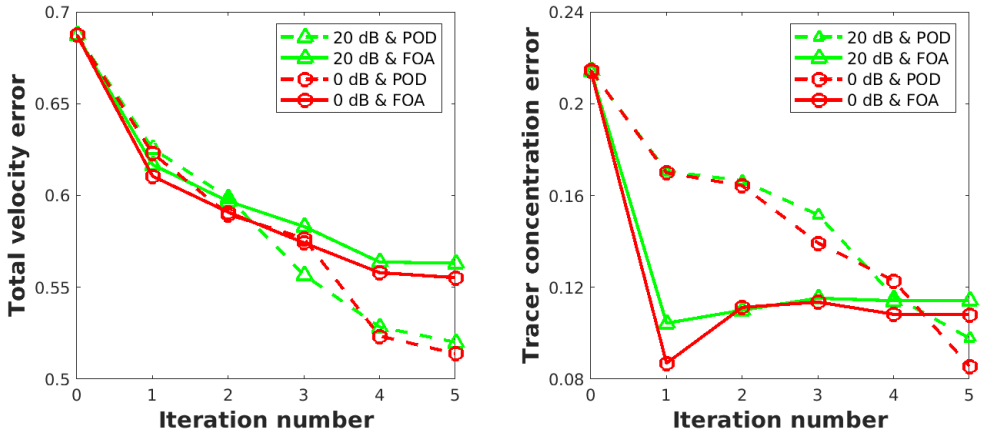

(a) Velocity error

(b) Erreur pour la concentration du traceur

Figure 2.2: Courbes d'erreur de reconstrution pour POD et FOA dans le cas d'une vitesse non stationnaire de 0.55 m/s, et pression de sortie 500 Pa.

Noise level (dB)	POD	FOA
0	0.086	0.108
20 dB	0.098	0.114

Table 2.1: Comparaison des erreur de reconstruction pour le traceur pour les méthodes POD-adjointe et FOA pour deux niveaux de bruit et des conditions de vitesse non stationnaires. Vitesse d'entrée de 0.55 m/s, pression de sortie 500 Pa.

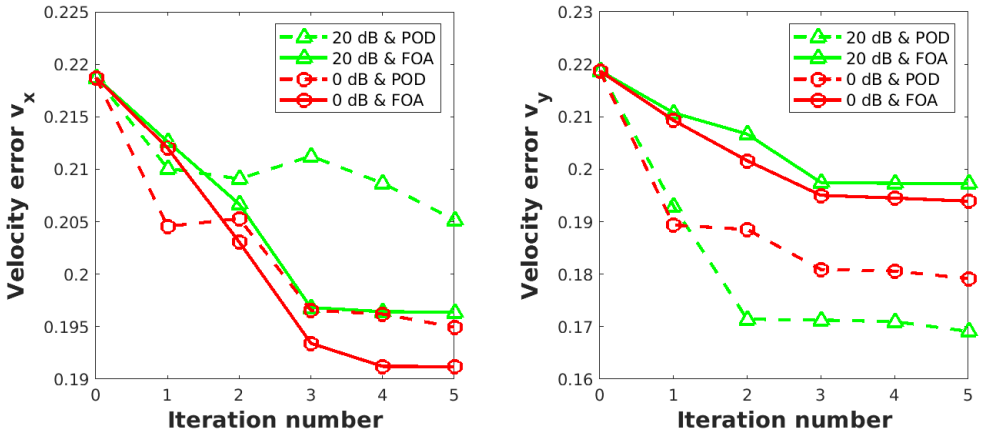

(a) Velocity error along x

(b) Velocity error along y

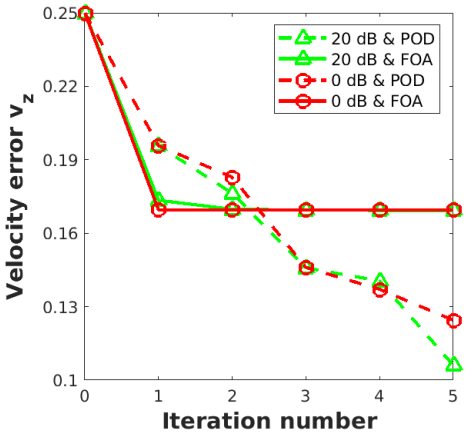

(c) Velocity error along z

Figure 2.3: Erreur de reconstruction pour les composantes du champ de vitesses pour les méthodes POD et FOA et un champ de vitesse non stationnaire.

Noise level (dB)	POD	FOA
0	0.514	0.555
20 dB	0.520	0.563

Table 2.2: Comparaison des erreurs de reconstruction pour la vitesse pour les méthodes POD et FOA pour deux niveaux de bruit et une vitesse non stationnaire. Vitesse d'entrée 0.55 m/s, pression de sortie 500 Pa.

Direction	Noise level (dB)	POD	FOA
X	0	0.195	0.191
X	20	0.205	0.196
Y	0	0.179	0.194
Y	20	0.169	0.197
Z	0	0.215	0.170
Z	20	0.106	0.169

Table 2.3: Comparaison de erreurs de reconstruction pour les composantes du champ de vitesse pour les deux méthodes POD et FOA et deux niveaux de bruit pour un champ de vitesses non stationnaire. Vitesse d'entrée 0.55 m/s, pression de sortie 500 Pa.

Sur la figure 2.3 a, on observe une reconstruction légèrement meilleure pour la méthode FOA selon l'axe x. La figure 2.3 b montre qu'en utilisant la méthode POD, on peut diminuer l'erreur de reconstruction selon l'autre axe y. La décroissance la plus nette est obtenue pour la composante z de la vitesse, Figure 2.3 c. Les erreurs de reconstruction sont résumées dans les tableaux 2.1, 2.2, et 2.3. La précision de la reconstruction de la composante suivant z de la vitesse et de la concentration du traceur dépend peu du niveau de bruit, pour les niveaux de bruit étudiés.

2.5.1.2 Champ de vitesse stationnaire

Les résultats présentés sont obtenus avec $\mu_1 = (0.55m/s, 500Pa)$ et une concentration de traceur en entrée $\mu_2 = 1.1kg/m^3$. Les figures2.4 and 2.5 montrent l'évolution avec les itérations des erreurs de reconstrution pour le champs de vitesse et ses composantes, ainsi que pour le traceur pour différents niveaux de bruit. Ces figures comparent les erreurs en fonction des itérations pour les méthodes POD et FOA.

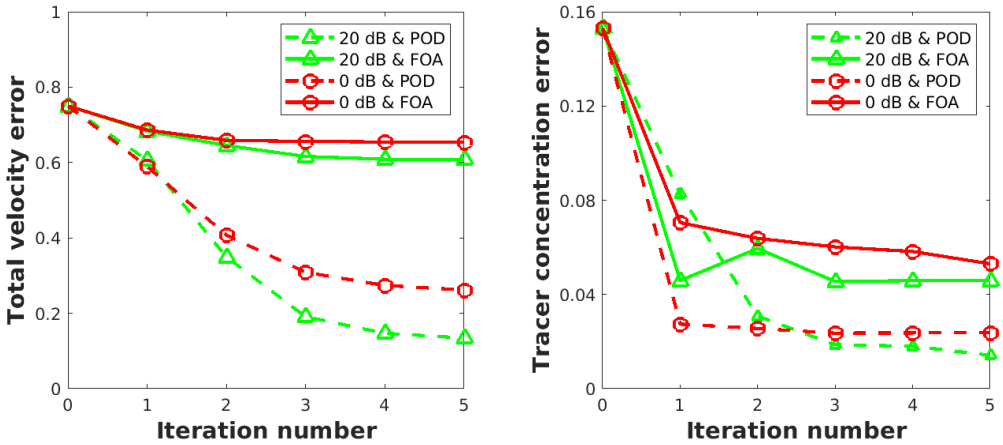

(a) Velocity error

(b) Tracer concentration error

Figure 2.4: Courbe d'erreur pour les méthodes POD et FOA pour un champ de vitesse stationnaire.

Nous résumons les erreurs de reconstruction dans les tableaux 2.4, 2.5,et 2.6 pour les deux niveaux de bruit et les deux approches. Des résultats similaires sont obtenus dans la gamme

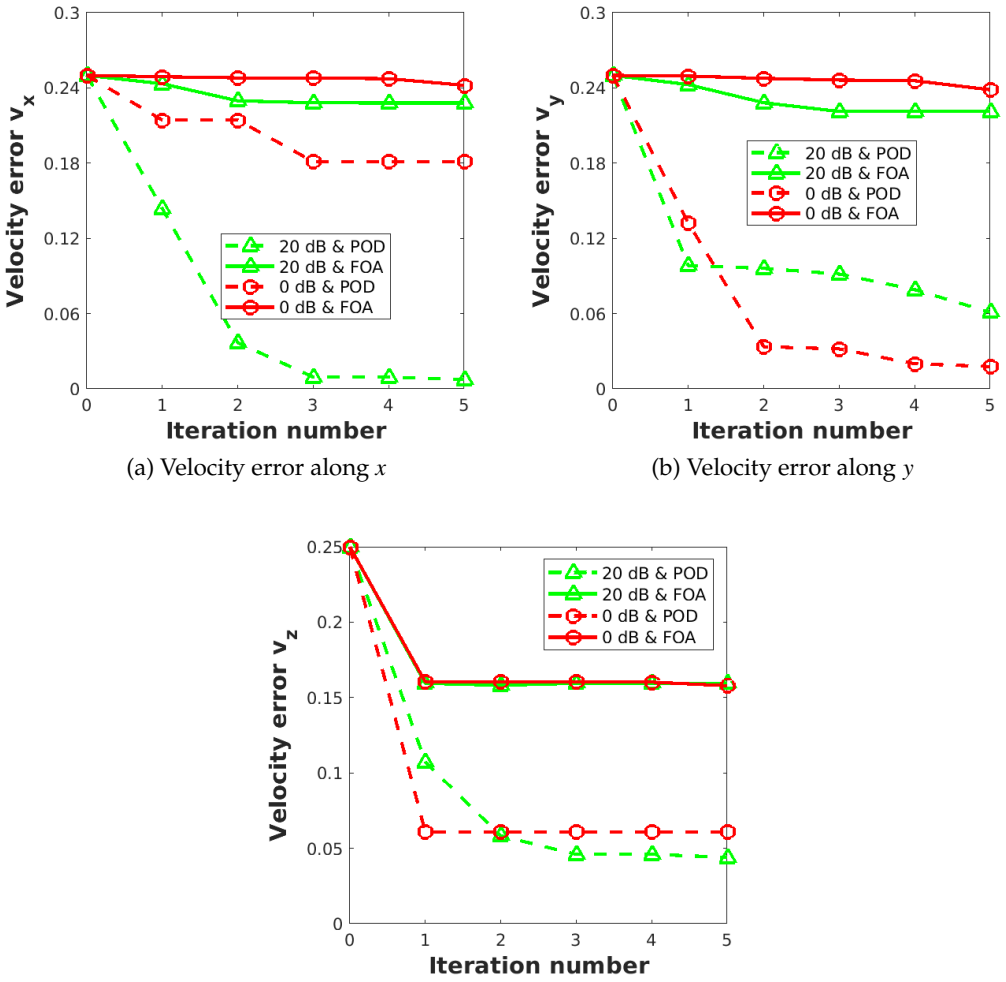

(a) Velocity error along x

(b) Velocity error along y

(c) Velocity error along z

Figure 2.5: Erreurs de reconstruction pour les composantes du champ de vitesse pour les méthodes POD et FOA, pour un champ de vitesses stationnaire.

de valeurs du paramètre μ étudié.

Noise level (dB)	POD	FOA
0	0.262	0.653
20	0.135	0.609

Table 2.5: Comparaison des erreurs de reconstruction pour les méthodes POD et FOA pour deux niveaux de bruit et des conditions de vitesse stationnaire. Vitesse d'entrée 0.55 m/s, pression de sortie 500 Pa.

Avec la méthode POD, les erreurs de reconstruction pour le traceur et la vitesse montrent une décroissance nette et rapide et la méthode est capable de donner une bonne approximation de ces champs inconnus. La précision de la reconstruction de la concentration du traceur et de la composante suivant z du champ de vitesse decroît quand le niveau de bruit sur les

Noise level (dB)	POD	FOA
0	0.024	0.053
20	0.014	0.046

Table 2.4: Comparaison des erreurs de reconstruction pour le traceur pour les méthodes POD et FOA pour deux niveaux de bruit et une vitesse stationnaire. Vitesse initiale 0.55 m/s, pression de sortie 500 Pa.

Direction	Noise level (dB)	POD	FOA
X	0	0.181	0.242
X	20	0.008	0.228
Y	0	0.018	0.239
Y	20	0.061	0.221
Z	0	0.061	0.158
Z	20	0.044	0.159

Table 2.6: Comparaison des erreurs de reconstruction pour les composantes du champ de vitesse pour les méthodes POD et FOA pour un champ de vitesse stationnaire et les deux niveaux de bruit.. Vitesse d'entrée 0.55 m/s, pression de sortie 500 pa.

projections de Radon augmente. De bon résultats de reconstruction sont obtenus pour les composantes transverses de la vitesse. Ces composantes sont moins sensibles au bruit sur les projections. Avec l'approche POD et l'équation aux dérivées partielles comme contrainte, il est possible d'obtenir une reconstruction simultanée des composantes axiales et transverses de la vitesse. Quand un nombre plus important de fonctions de base est pris en compte, l'erreur stagne et les bases peuvent être considérées comme optimales dans la gamme de paramètres μ étudiée. La méthode POD proposée améliore la méthode où le maillage entier est pris en compte. Les erreurs obtenues pour la concentration du traceur et le champ de vitesse sont plus faibles. Utiliser la méthode POD peut conduire à un temps de calcul initial élevé. Ce temps de calcul consiste à obtenir les solutions échantillons et à calculer les bases pour les différents champs inconnus. Sans une implémentation en parallèle, l'ensemble des calculs dure 20 h sur un cluster multi-processeurs.

Information	POD	FOA
Mesh size	-	56845
Degrees of freedom	3600	56845^5
Simulation time for transport equation (s)	10^{-2} (online)	0.9
Simulation time for adjoint method (s)	35	450

Table 2.7: La comparaison du nombre de degrés de liberté , du temps moyen de simulation pour l'équation de transport, et pour une itération du calcul en ligne, pour la méthode de l'état adjoint-POD et la méthode FOA et un champ de vitesse stationnaire.

Cependant, les temps de calcul sont beaucoup plus faibles pour l'étape en ligne avec la méthode POD. Le nombre de degré de liberté et le temps moyen de simulation requis pour l'équation de transport et pour une itération de la méthode de l'état adjoint sont résumés dans le tableau 2.7. Le facteur d'accélération est défini comme le rapport entre le temps de calcul

pour la solution FOA divisé par le temps de calcul pour la méthode POD. Il peut être évalué à 90 pour le problème direct et à 15 pour la méthode d'inversion avec une décroissance remarquable du nombre de degrés de liberté. La méthode POD est donc préférable pour des applications où le champ de vitesse doit être estimé plusieurs fois. Les résultats de cette section montrent clairement l'éfficacité de l'approche POD pour résoudre le problème inverse.

2.5.2 Discussion and conclusion

L'application de la méthode de l'état adjoint avec POD permet donc d'obtenir une prédiction très précise pour les champs de vitesses stationnaires et non stationnaires. Les caractèristiques essentielles du champ de vitesse peuvent donc être extraites même en présence de bruit. L'approche proposée permet de réduire les coûts de calcul de façon significative. On peut noter plusieurs limitations de l'approche POD. La transformations appliquée pour obtenir les coefficients est une transformation linéaire. Les méthodes de réduction basée un opérateur de projection linéaire peuvent ne pas être efficaces pour des écoulements complexes car le nombre de modes augmente significativement. Nous avons supposé que le sang est un fluide Newtonien. Cette hypothèse est valable dans des vaisseaux larges mais elle est plus discutable dans des artères plus petites. Des comportements physiques plus complexes devraient être pris en compte comme un comportement non Newtonien ou les propriétés visco-élastiques de la paroi artérielle. Nous n'avons pas considéré d'interaction entre le fluide et le vaisseau. L'approche précédente devrait pouvoir être appliquée pour des nombres de Reynolds plus élevés avec plus de coefficients POD. Il serait possible d'étendre l'approche avec une paramétrisation géométrique pour des domaines évoluant au cours du temps avec une interaction fluide-structure puisque la méthode est basée sur une formulation paramétrique du problème inverse. La méthode proposée pourrait être améliorée en utilisant les méthodes de deep learning et les auto-encodeurs qui permettent une approximation des solutions et une réduction de dimension non linéaires. Dans la suite, nous étudions des approches qui s'appuient sur un apprentissage à partir des données.

Chapter 3

Apprentissage profond pour la reconstruction du flux sanguin

Dans ce chapitre, nous nous intéressons à des approches deep learning ou apprentissage profond qui permettent souvent d'améliorer les approches variationnelles classiques en terme de convergence et de temps de calcul. Le deep learning ou apprentissage profond est une partie des méthodes d'apprentissage. Ces dernières années, les méthodes de deep learning ont été très étudiées notamment en imagerie médicale. Cependant, il n'existe pas d'application de ces techniques au problème de reconstruction d'un champ de vitesse d'un fluide à partir de mesures de tomographie.

Dans ce chapitre nous présentons deux architectures neuronales: un réseau POD-réseau complètement connecté, POD-FC (POD-Fully connected) et un réseau POD-convolutionel, POD-3D CNN. Les réseaux sont testés sur des vitesses stationnaires. Les résultats sont comparés avec la méthode POD-adjointe de façon plus quantitative.

3.1 Présentation du problème

Notre objectif est de combiner la réduction de modèle avec les méthode de deep learning pour apprendre une correspondance entre deux espaces de Hilbert, $\mathcal{L}_V = L_2(\Omega \to \mathbb{R}^3)$ pour le champ de vitesse V et $\mathcal{L}_p = L_2([0,T] \times [-a,a] \times [0,z_{max}] \to \mathbb{R})$ pour les projections de Radon$p$. Nous considérons uniquement des champs de vitesses stationnnaires mais nous avons à inclure le domaine temporel pour décrire l'évolution de la concentration du traceur et des projections de Radon. Dans la suite, la décomposition POD pour les projections inclut donc le domaine temporel. L'espace des vitesses $\mathcal{L}_V$ peut être considéré comme le produit de trois espaces $\mathcal{L}_V^x \times \mathcal{L}_V^y \times \mathcal{L}_V^z$ correspondants aux composantes du champ de vitesse. Nous avons $\mathcal{L}_V^x = \{V_x : \Omega \to \mathbb{R}\}$ pour la composante de vitesse selon x et des définitions similaires pour les autres directions. Notre but est de déterminer l'opérateur inverse non linéaire $\Psi = \Psi^x \times \Psi^y \times \Psi^z : \mathcal{L}_p \to \mathcal{L}_V$ à partir d'échantillons correspondant aux mesures de probabilité sur ces espaces. Avec ces notations, pour des projections de Radon p, les composantes du champ de vitesse sont données par $V_x = \Psi^x(p)$, $V_y = \Psi^y(p)$ et $V_z = \Psi^z(p)$. Cet opérateur est approximé par une classe d'opérateur $\Psi_\theta = \Psi_\theta^x \times \Psi_\theta^y \times \Psi_\theta^z : \mathcal{L}_p \times \mathbb{R}^D \to \mathcal{L}_V$ avec différentes architectures de réseaux de neurones, où $\theta \in \mathbb{R}^D$ représente l'ensemble des paramètres D du réseau de neurones. Cela correspond à l'apprentissage d'un opérateur inverse non linéaire. En pratique, un nombre fini N d'échantillons pour les projections de Radon et pour la vitesse sont disponibles $\{p_n\}_{1\le n\le N}$ et $\{V_n = \Psi(p_n)\}_{1\le n\le N}$ définissant des mesures empiriques. Donc le problème inverse se ramène à déterminer le paramètre optimal θ^*, pour une fonction coût $\mathcal{L}$

écrite:

$$\mathcal{L} = \frac{1}{N}\sum_{n=1}^{N} \frac{E_n^x + E_n^y + E_n^z}{\|\Psi^x(p_n)\|_2 + \|\Psi^y(p_n)\|_2 + \|\Psi^z(p_n)\|_2} \tag{3.1}$$

où $E_n^x = \left\|\Psi^x(p_n) - \Psi_\theta^x(p_n,\theta)\right\|_{L_2}^2$ est l'erreur de reconstruction le long de l'axe x et des définitions similaires sont utilisées pour les autres axes. En pratique, on obtient seulement une approximation de θ^* comme solution.

Afin d'obtenir une correspondance entre les deux espaces de Hilbert à partir des données, nous estimons d'abord des approximations de dimension finie sur ces espaces à partir des bases POD. Nous approchons les identités $I_{\mathcal{L}_p}$ et $I_{\mathcal{L}_V}$ par la composition de deux fonctions, un encodeur linéaire et un décodeur linéaire, définis et à valeur dans des espaces de dimension finie. Les sorties de dimension finie de l'encodeur sont appelées variables latentes et correspondent aux coefficients POD. Une fonction α va être construite entre ces codes latents. Nous notons $F_{\mathcal{L}_p}$: $\mathcal{L}_p \to \mathbb{R}^{N_R}$ et $G_{\mathcal{L}_p}$: $\mathbb{R}^{N_R} \to \mathcal{L}_p$ l'encodeur et le décodeur de l'espace $\mathcal{L}_p$, et N_R la dimension de l'espace réduit pour les projections de Radon. De façon similaire, $F_{\mathcal{L}_V}$ et $G_{\mathcal{L}_V}$ sont l'encodeur et le décodeur pour l'espace $\mathcal{L}_V$, avec une dimension réduite N_V pour chaque direction. Pour résumer, nous avons les approximations suivantes, $I_{\mathcal{L}_p} \simeq G_{\mathcal{L}_p} \circ F_{\mathcal{L}_p}$, $I_{\mathcal{L}_V} \simeq G_{\mathcal{L}_V} \circ F_{\mathcal{L}_V}$; $\Psi_\theta \simeq G_{\mathcal{L}_V} \circ \alpha \circ F_{\mathcal{L}_p}$. La combinaison des décompositions POD avec un réseau de neurones est la base de l'approche. Un diagramme avec les différentes fonctions est présenté Figure 3.1. Dans le cadre des approches de deep learning, la réduction de dimension n'est pas effectuée sur la densité, la variable adjointe et le champ de vitesse comme dans la méthode de l'état adjoint mais sur les projections de Radon et le champ de vitesses. Nous notons les dimensions réduite des projections de Radon et de la vitesse N_R et N_V^3 correspondant aux nombres d'éléments de la base. La décomposition POD pourrait être remplacée par un auto-encodeur non linéaire. La première étape des méthodes consiste à obtenir des approximations de dimension finie sur l'espace des vitesses et des projections de Radon. La décomposition POD présentée conduit à des bases orthonormales $\{\psi_{Rf,i}\}_{1\le i\le N_R}$ for $\mathcal{L}_p$ and $\{\psi_{V,i}\}_{1\le i\le N_V} = \{\psi^x_{V,i}\}_{1\le i\le N_V} \times \{\psi^y_{V,i}\}_{1\le i\le N_V} \times \{\psi^z_{V,i}\}_{1\le i\le N_V}$ pour $\mathcal{L}_V$ qui sont tronquées par les premiers N_R et N_V premier modes avant d'entrainer le réseau. Nous proposons deux architectures différentes pour les réseaux, POD-FC et POD-3D CNN.

a)POD-FC: (POD complètement connecté)
La méthode est basée sur un réseau complètement connecté (FC) et sera appelée POD-FC dans la suite. Etant donné les projections de Radon $p \in \mathcal{L}_p$, l'opérateur Ψ_θ est défini pour l'axe x par:

$$\Psi_\theta^x(p,\theta)(\boldsymbol{M}) = \sum_{j=1}^{N_v} \alpha_j^x(F_{\mathcal{L}p}(p),\theta)\psi^x_{V,j}(\boldsymbol{M}) \tag{3.2}$$

où $M \in \Omega$ pour les champs de vitesse stationnaires. Les fonctions $\alpha_j^x : \mathbb{R}^{N_R} \times \mathbb{R}^D \to \mathbb{R}$ pour $1 \le j \le N_V$, relient les coefficients POD de p, $F_{\mathcal{L}_p}(p) = \{(\psi_{Rf,i}, p)\}_{1\le i\le N_R}$ avec les coefficients correspondant au champ de vitesse selon x, $F^x_{\mathcal{L}_V}(V)$. Les autres définitions sont identiques pour les autres axes. La correspondance entrée-sortie avec la structure d'auto-encodeur du réseau est montrée dans la Figure 3.1.

b)POD-3D CNN: Nous proposons une seconde architecture neuronale qui est basée sur les réseaux de convolution ou Convolutional Neural Network (CNN) et qui sera appelée POD-CNN. Pour notre problème inverse, nous écrirons l'approximation de l'opérateur inverse pour la composante x sous la forme:

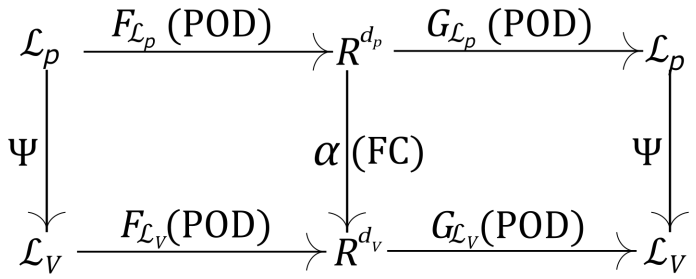

Figure 3.1: Structure du réseau POD-FC.

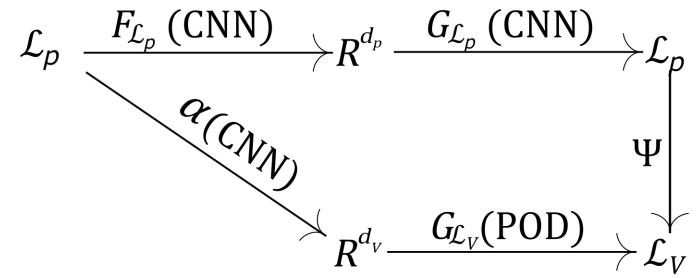

Figure 3.2: Structure du réseau POD-CNN.

$$\Psi_\theta^x(p,\theta)(\boldsymbol{M}) = \sum_{j=1}^{N_v} \alpha_j^x(p,\theta)\psi_{V,j}^x(\boldsymbol{M}) \tag{3.3}$$

avec des définitions similaires pour y et z. Il est important de noter que l'opérateur $F_{\mathcal{L}_p}$ et la décomposition sur l'espace de départ ne sont pas utilisés. La structure du réseau POD-CNN est présentée Figure 3.2. Les deux réseaux seront testés sur de nombreuses simulations numériques.

Afin d'étudier les deux réseaux, nous avons généré des ensembles de données et considéré les erreurs de reconstruction pour la vitesse et sa déviation standard. Nous avons optimisé les paramètres des réseaux comme le taux d'apprentissage, la taille de batch, le taux de 'dropout'. Nous avons étudié deux vitesses différentes pour comparer les reconstructions.

3.2 Méthodes de deep learning

Après la génération des données, nous présentons les architectures des réseaux et la méthode d'entrainement. Les calculs ont été effectués avec la bibliothèque Keras 2.2.5 et Tensorflow et implémentés sur un cluster hautes performances.

3.2.1 Architecture des réseaux

Nous considérons deux réseaux, le réseau POD-Fully connected(POD-FC) et le réseau POD-3D Convolutional Neural Network(POD-3D CNN). Les architectures sont présentées de manière schématique sur la Figure 3.3.

3.2.1.1 Réseau POD-Fully connected

L'architecture du réseau POD-Fully connected est présentée sur la Figure 3.3 a. Ce réseau comprend cinq parties: l'entrée, les coefficients POD de l'entrée, les couches complètement

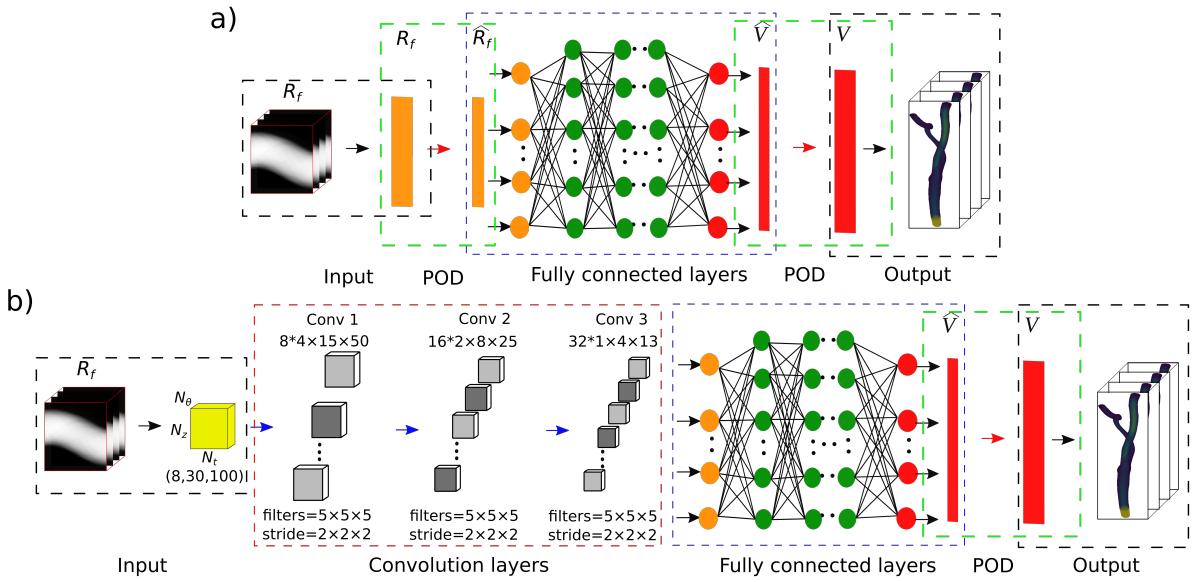

Figure 3.3: Architecture des réseaux.

connectées, une POD inversée, et la sortie. Les projections de Radon et les champs de vitesses correspondent à l'entrée et à la sortie respectivement. L'étape de décomposition POD connecte l'entrée et l'entée des couches complètement connectées alors que la POD inversée connecte la sortie et la sortie des couches complètement connectées.

3.2.1.2 Réseau de neurones POD-3D Convolutional Neural

In this second network shown in Figure 3.3 b, les couches de convolution sont ici utilisées à la place de la décomposiition POD pour réduire la dimension des projections de Radon. Dans ce dessin, N_t, N_θ, et N_z correspondent au nombre d'intervalles de temps, d'angles de projection, et de coupes selon z respectivement. Les données d'entrée correspondent à l'évolution dans le temps des projections de Radon, qui sont transformées avec les couches de convolution pour obtenir les coefficients latents similaires aux coefficients POD des projections de Radon. Cependant, la base POD des projections Radon n'est pas utilisée dans ce réseau et la transformation est apprise. Les autres parties sont similaires au premier réseau.

3.2.2 Details des réseaux

Pour entraîner ces réseaux, nous avons généré 800 échantillons pour le champ de vitesse et les projections de Radon correspondantes et nous avons estimé leur coefficients POD. Pour données test, nous utilisons 200 échantillons pour chaque niveau de bruit pour obtenir des estimations des erreurs et déviations standard. Pour comparer avec la méthode POD-adjointe, nous considérons 50 échantillons pour comparer les erreurs de reconstruction.

Pour le réseau POD-FC, nous obtenons les meilleurs résultats avec un réseau complètement connecté avec 4 couches internes de largeur (500, 1000, 1000, 1000) entre l'entée et la sortie et des activation de type ReLU sauf dans la dernière couche. Pour cette architecture, les résultats ont été obtenus avec une couche de dropout avec un taux entre 0 et 0.2 pour éviter un sur-ajustement après la première couche. Le réseau consiste en 3,550,506 paramètres ajustables, avec des poids entre -0.1017 to 0.1017. Pour le réseau POD-CNN, les opérations, tailles des filtres considérés sont résumées sur la Figure 3.3. L'entrée de chaque couche de convolution est un tenseur 4D, sauf pour la couche d'entrée qui est de taille (N_t, N_θ, N_z). La moyenne des projections le long

de la direction s est obtenue pour chaque angle θ. La couche L^{th} prend chaque tranche 3D du tenseur de la couche $L-1$ et la convolue avec tous les noyaux pour créer un tenseur 4D. Pour chaque couche de convolution L, nous notons k_L le nombre de canneaux caractéristiques. Les noyaux de taille $f_x \times f_y \times f_z$ peuvent être groupés en tenseur 4D $K_L \in R^{f_x \times f_y \times f_z \times k_L}$. Un dessin associé aux tailles (f_x, f_y, f_z, k_L) est donné dans la Figure 3.3. Ces trois couches de convolution de taille (f_x, f_y, f_z) = (5, 5, 5) et de pas (2,2,2) sont adoptées dans notre étude. Les couches de convolution 3D sont suivies par un réseau avec 300 neurones pour retourner un vecteur de caractéristiques $(\alpha_j^x)_{1\leq j\leq Nv} \times (\alpha_j^y)_{1\leq j\leq Nv} \times (\alpha_j^z)_{1\leq j\leq Nv}$. Les non linéarités dans ces réseaux sont associées à des fonctions d'activation ReLu. Le nombre de couches cachées, de poids par couche cachée, les fonction d'activation, la taille des lots pour une descente de gradient par mini-lots, et le nombre d'épochs pour l'entrainement du modèle ont été optimisés. Nous entrainons le réseau avec 100 épochs, un optimiseur Adam, et un taux d'apprentissage entre 10^{-3} et 10^{-4}. Au final, 92,762 paramètres ajustables dans la gamme -0.1394 à 0.1397 sont utilisés dans ce modèle.

3.2.3 Evaluation du modèle

Pour évaluer de façon précise et quantitative les performances de l'approche couplée POD-DL, les erreurs moyennes normalisées sont utilisées pour les champs de vitesse reconstruit sur 200 échantillons test. Cette métrique nous permet d'évaluer la précision des champs de vitesse reconstruits par rapport aux champs de vitesse vrais. Elle est définie de la façon suivante:

$$E(\mathbf{V}) = \frac{\|\mathbf{V} - \mathbf{V}_{\text{true}}\|_2}{\|\mathbf{V}_{\text{true}}\|} \tag{3.4}$$

où $\mathbf{V}$ est le champ de vitesse reconstruit et $\mathbf{V}_{true}$ le champ de vitesse vérité terrain. Nous pouvons estimer les erreurs normalisées pour les composantes selon x, y, et z de la vitesse. Les moyennes et écarts type pour les différentes erreurs peuvent être obtenues avec les formules classiques.

3.2.4 Comparaison avec la méthode POD-adjointe

Nous comparons les méthodes POD-DL et POD-adjoint par rapport au temps CPU hors-ligne et au temps en ligne CPU pour la reconstrution du champ de vitesse sanguin, les erreurs de reconstruction et leur déviation standard.

3.2.4.1 Etape hors-ligne

L'étape hors-ligne inclut le calcul des échantillons pour la vitesse $\mathbf{V}$, la concentration du traceur f, les projections de Radon Rf, et l'entrainement de la méthode POD-DL. Pour la méthode de l'état adjoint, nous avons besoin des échantilons de la vitesse $\mathbf{V}$, de la concentration du traceur f et de la variable adjointe p. Le tableau ci-dessous résume les informatons pour les temps CPU pour ces calculs. En particulier, il donne le temps requis pour estimer le champ de vitesse stationnaire, simuler la concentration du traceur pour un intervalle de temps unité et accomplir un pas de descente de gradient avec la variable adjointe. Pour la méthode POD-DL, le temps CPU correspond au calcul du champ de vitesse et des projections de Radon pour un intervalle de temps unité, à l'entrainement du modèle pour 800 snapshots pour 8 intervalles de temps.

Cette table indique que la méthode POD-DL améliore la méthode POD-adjointe avec un temps CPU hors ligne plus faible. Cependant le temps de cacul de nombreux échantillons sur un processeur unique reste très long. Nous travaillons actuellement sur une réduction du nombre de noeuds dans le maillage pour accélérer les calculs de ces échantillons.

Velocity	Tracer concentration	Adjoint variable	Gradient descent
8377.7s	54.3s	54.6s	5586.6s

Table 3.1: Temps CPU pour l'étape hors-ligne de la méthode adjoint

Velocity	Tracer concentration	Radon projection	DL model training
8377.7s	54.3s	2.13s	6042.8s

Table 3.2: Temps CPU hors-ligne pour la méthode POD-DL.

3.2.4.2 Etape en ligne

Les temps de reconstructoin sont 35s, 3.8×10^{-3}s et 9.6×10^{-4}s pour les méthodes POD-adjoint, POD-CNN, et POD-FC respectivement sur un échantillon test. En comparant les temps CPU en ligne, cela montre que les méthodes POD-DL permettent de reconstruire le champ de vitesse rapidement. Nous allons maintenant comparer les erreurs de reconstruction et leur déviation standard.

NMSE	PPSNR(dB)	POD-adjoint	POD-CNN	POD-FC
$\mathbf{V}$	20	0.061 (0.042)	0.025 (0.039)	0.011 (0.015)
$\mathbf{V}$	0	0.082 (0.061)	0.024 (0.035)	0.024 (0.033)
V_x	20	0.081 (0.085)	0.028 (0.044)	0.014 (0.021)
V_x	0	0.096(0.090)	0.025 (0.038)	0.027 (0.038)
V_y	20	0.070 (0.075)	0.029 (0.037)	0.019 (0.015)
V_y	0	0.082 (0.086)	0.026 (0.032)	0.029 (0.032)
V_z	20	0.051 (0.042)	0.024 (0.039)	0.010 (0.014)
V_z	0	0.074 (0.062)	0.022 (0.036)	0.029 (0.033)

Table 3.3: Comparaison des erreurs de reconstruction pour les méthode POD-adjoint, POD-CNN et POD-FC pour deux niveaux de bruit. La moyenne et l'écart type sont donnés pour chaque méthode et chaque niveau de bruit.

Les erreurs de reconstruction et leur déviation standard pour les différentes méthodes incluant les méthodes POD-adjoint, POD-CNN et POD-FC sont présentées sur le tableau 3.3. Nous pouvons observer qu'avec un niveau de bruit de 20 dB, on peut atteindre une erreur de reconstruction plus faible et une déviation standard plus faible avec la méthode POD-FC en comparaison avec la méthode POD-adjoint ou POD-CNN. Les deux méthodes POD-DL donnent des erreurs de reconstruction faibles et un écart type faible pour un bruit de 0 dB en comparaison avec la méthode de l'état adjoint classique.

Le taux de réduction de l'erreur par la méthode POD-DL peut être exprimé par:

$$I(E(\mathbf{V})) = |\overline{E(\mathbf{V})}_{DL} - \overline{E(\mathbf{V})}_{adj}|/|\overline{E(\mathbf{V})}_{adj}| \tag{3.5}$$

où $\overline{E(\mathbf{V})}_{DL}$ et $\overline{E(\mathbf{V})}_{adj}$ dénote l'erreur de reconstruction de la vitesse par les méthodes POD-DL et POD-adjoint respectivement. Le taux relatif de réduction de l'erreur le long de la composante x peut être écrit de façon similaire:

$$I(E(V_x)) = |\overline{E(V_x)}_{DL} - \overline{E(V_x)}_{adj}|/|\overline{E(V_x)}_{adj}| \tag{3.6}$$

L'erreur relative pour les autres composantes est similaire.

Reduction rate I	PPSNR(dB)	POD-CNN	POD-FC
$\mathbf{V}$	20	59.01%	81.96%
$\mathbf{V}$	0	70.73%	70.73%
V_x	20	65.43%	82.71%
V_x	0	73.95%	71.87%
V_y	20	58.57%	72.85%
V_y	0	68.29%	64.63%
V_z	20	52.94%	80.39%
V_z	0	70.27%	60.81%

Table 3.4: Taux de réduction des erreurs pour la vitesse et les méthodes POD-DL en comparaison avec la méthode POD-adjointe.

Le tableau 3.4 montre une réduction d'au moins 80 pourcent en utilisant la méthode POD-FC. Ces résultats montrent que les méthodes POD-DL permettent d'améliorer la reconstruction du flux sanguin avec un temps de calcul faible.

3.2.5 Application clinique et défis

Un grand nombre d'études ont montré le rôle décisif du flux sanguin et de la distribution des contraintes pour les maladies cardio-vasculaires. Les approches étudiées permettent d'obtenir une information plus détaillée sur le flux sanguin que les méthodes classiques de RMN et d'ultrasons avec une meilleure résolution spatiale. La précision des reconstructions des composantes longitudinales du champ de vitesse est améliorée. Dans le cadre de nos simulations, la résolution de la composante longitudinale de la vitesse peut être estimée avec la taille maximum du tétraèdre de la maille. La résolution estimée, 0.1mm, est meilleure que la résolution typique pour la RMN par constraste de phase. Les méthodes d'inversion développées peuvent estimer de façon assez précise les composantes tranverses du champ de vitesse. Cette étude montre donc la précision et l'efficacité de la reconstruction de la vitesse du sang par deep learning mais il reste des limitations pour une application clinique comme la mesure du champ de vitesse vérité terrain. Celui-ci pourrais être estimé par des simulations avec un jeu de données important.

Bibliography

Sixou, B. (2019). Contrast enhanced tomographic reconstruction of vascular blood flow with first order and second order adjoint methods. *Journal of Inverse and Ill-posed Problems*, 27(1):87–102. 2

Sixou, B., Boissel, L., and Sigovan, M. (2016). Contrast enhanced computerized tomography measurement of vascular blood flow. In *Journal of Physics: Conference Series*, volume 756, page 012003. IOP Publishing. 2

Sixou, B., Boussel, L., and Sigovan, M. (2018). Vascular blood flow reconstruction with contrast-enhanced computerized tomography. *Inverse Problems in Science and Engineering*, 26(6):855–876. 2

FOLIO ADMINISTRATIF

THESE DE L'INSA LYON, MEMBRE DE L'UNIVERSITE DE LYON

NOM : HUANG

DATE de SOUTENANCE : 25/01/2024

Prénoms : Shusong

TITRE : Blood velocity reconstruction with contrast enhanced X-ray CT

NATURE : Doctorat

Numéro d'ordre : 2024ISAL0009

Ecole doctorale : Électronique, Électrotechnique, Automatique (EEA)

Spécialité : Traitement du Signal et de l'Image

RESUME :

In this work, we aim to focus on blood flow reconstruction using the Computed Tomography (CT) technique. This non-destructive and non-invasive technique is broadly used in non-medical and medical clinical applications for the human body and brain. X-rays and Computed Tomography have been a breakthrough in the medical field to visualize the tissues and organs of a patient. However, in the past two decades, there are few research works concentrating on in vivo blood velocity measurement with X-ray CT. Blood flow velocity reconstruction with contrast enhanced X-ray CT is a complex inverse problem. The acquisition of 2D CT projections perpendicular to the major flow propagation direction is considered for the reconstruction of blood flow, with a tracer injected into the vessel. In order to solve the inverse problem of contrast-enhanced CT reconstruction of vascular blood flow, a function is minimized with a data term taken into account the projections coupled with a partial differential equation (PDE) describing the transport of the tracer used as a constraint. The PDE models the propagation of the contrast agent with a convection term depending on a flow velocity field.

The objectives of this work are blood velocity components reconstruction with X-ray CT with accelerated convergence, reduced calculation cost, and reduced radiation dose. To accomplish these objectives, the adjoint method is initially considered for solving the tomographic inverse problem with a constraint based on a PDE. Additionally, to accelerate convergence, the proper orthogonal decomposition (POD) method combined with the adjoint method is proposed in this work. Finally, the new Proper Orthogonal Decomposition-Deep Learning (POD-DL) approach for solving the considered inverse problem is investigated to reduce effectively the computation costs in our work. The effectiveness of proposed approaches for blood flow reconstruction is demonstrated by employing the blood velocity reconstruction in a simulation vessel.

MOTS-CLÉS : Hemodynamics, inverse problems, proper orthogonal decomposition, tomography

Laboratoire (s) de recherche : Centre de Recherche en Acquisition et Traitement de l'Image pour la Santé (CREATIS)

Directeur de thèse: Bruno SIXOU

Président de jury : Yuemin ZHU

Composition du jury :

Aurélia FRAYSSE	Maître de conférence HDR, Université Paris-Saclay	Rapportrice
Thomas RODET	Professeur, ENS Paris-Saclay	Rapporteur
Franck NICOUD	Professeur, Université de Montpellier	Examinateur
Yuemin ZHU	Directeur de recherche CNRS, INSA Lyon	Examinateur
Bruno SIXOU	Maître de conférence HDR, INSA Lyon	Directeur de thèse
Monica SIGOVAN	Chargés de recherche, CNRS	Co-Directrice de thèse